Virtual product development and testing for aerospace tube hydroforming industry: improved Non-linear solid-shell element

Thèse

Xavier Elie-Dit-Cosaque

Doctorat en génie mécanique
Philosophiae Doctor (Ph.D)

Québec, Canada

Résumé

Dans les recherches réalisées pour ce projet de thèse, il est démontré qu'une traverse existante de train d'atterrissage d'hélicoptère à patins fabriquée par pliage et érosion chimique, pourrait être remplacée par une autre traverse, dont la forme innovante est fabricable par le procédé d'hydroformage de tubes. Ce procédé présente par exemple l'avantage d'être plus respectueux de l'environnement que le procédé de fabrication actuel, car il ne nécessite pas l'utilisation de produits chimiques polluant. De plus, la méthodologie développée dans le cadre des recherches réalisées permet de prendre en compte l'histoire du matériau de la traverse dans toutes les étapes de son processus de fabrication. Les performances d'un train d'atterrissage équipé de la nouvelle traverse ont été évaluées numériquement. Des travaux, développés avec le logiciel de calculs par éléments finis ABAQUS, ont permis de mettre en évidence l'intérêt d'utiliser des éléments finis de coque solides fiables et précis. Ces éléments sont en effet capables de prendre en compte le comportement dans l'épaisseur de structures minces avec une seule couche d'éléments. Une nouvelle technique de lissage appelé «Smoothed finite element method» ou «SFEM» a retenu l'attention pour sa simplicité de mise en œuvre et son insensibilité à la distorsion de maillage parfois rencontrée dans les simulations de formage de formes complexes. Un élément de coque solide résultant linéaire développé en utilisant cette méthode SFEM pour traiter de la cinématique en membrane et en flexion a été testé avec succès au travers d'exemples classiques identifiés dans la littérature. Ce nouvel élément a montré un niveau de précision souvent supérieur à celui d'autres éléments déjà existants. En outre, un élément de coque solide à intégration réduite, capable de fonctionner avec la plupart des lois de comportement en trois dimensions et cela même en présence de structures minces a été développé. Cet élément, libre de tout blocage a montré un bon niveau de précision par rapport aux éléments existants dans le cas de problèmes implicites géométriquement linéaires et non-linéaires. L'élément a été étendu en formulation explicite puis couplé avec une loi de comportement hyper élastoplastique en trois dimensions. Il a enfin été testé dans une simulation d'hydroformage de tubes en présence de pressions élevées, de frottement et de grandes déformations.

Abstract

In the current work, it is shown that an existing helicopter skid landing gear cross tube, made by tube bending and chemical milling, could be replaced by another cross tube, whose innovative shape is producible by tube hydroforming. This method has for example the advantage of being more environmentally friendly than the current manufacturing process, because it does not require the use of hazardous chemicals. In addition, the methodology developed in this project takes into account the cross tube material's history throughout the manufacturing process. Moreover, the performance of a skid landing gear equipped with this new cross tube has been evaluated numerically. This thesis simulation work has been developed with the finite element analysis software ABAQUS. It highlights the potential gains of using a reliable and accurate solid-shell finite element which is capable to take into account the through-thickness behavior of thin structures with a single layer of elements. A new smoothing technique called «Smoothed finite element method» or «SFEM» has been considered for its simplicity and insensitivity to mesh distortion, sometimes encountered while simulating complex shapes forming. A new resultant linear solid-shell element using this SFEM to deal with membrane and bending kinematics has been developed and successfully tested through classical benchmark problems found in the literature. This new element has often shown much greater level of accuracy than other existing elements. In addition, a novel reduced integration solid-shell element, able to work with most three dimensions constitutive laws even in the presence of thin structures is also discussed. This element, free of locking, shows a good accuracy level with respect to existing elements in implicit geometrically linear and non-linear benchmark problems. Its extension to explicit formulation is coupled with a three dimensions hyper elastoplastic constitutive law and tested in a tube hydroforming simulation involving high pressures, friction and large deformations.

Table of content

List of tables

List of figures

Acknowledgements

I express my deepest gratitude to my PhD adviser Dr. Augustin Gakwaya for having accepted to integrate me in the CRIAQ's project 4.6. I did really appreciate your precious support during the research process, your advices in terms of finite element formulation and programming and your overall help for improving my knowledge in continuum mechanics. For this, many thanks Dr. Gakwaya!

I express my profound gratefulness to my PhD co-adviser Dr. Michel Guillot. I did really appreciate your advices on my research and especially in term of design and fabrication issues. For this, many thanks Dr. Guillot!

I sincerely acknowledge the other members of the jury Dr. Hakim Naceur from the University of Valenciennes, Dr. Mario Fafard, from Laval University and Dr Henri Champliaud, from École de Technologie Supérieure (ÉTS) for their very appreciated feedbacks and advice on my work.

I am very grateful to Dr. Julie Levesque for her precious support and partnership, her helpful discussions and her very appreciated readings. Thank you Dr. Levesque!

I am grateful to the CRIAQ for his support as well as to all of the partners of the CRIAQ's project 4.6 namely Université Laval, BHTC, Pratt and Whitney Canada, the NRC, the AMT, the NSERCC and ÉTS. I really appreciated the constructive interactions with the participants to the CRIAQ's project 4.6 and the CRIAQ staff. Thanks to all!

I thank all of the Do3M research team members for their partnership and for their friendship and more particularly Dr. Mihaita Matei for his support while combining our work, Jocelyn Blanchet-Letourneau, Jérémie Ouellet, and Dave Demers for the development of the hydroformable cross tube.

I acknowledge the Aluminum Research Center (REGAL) and the Martinique Regional Council associated with the European Social fund for supporting my research.

Finally, I am deeply grateful to my marvellous wife Nadia, my mother, father, grand-mother, David and Christophe, Ingrid and Zélika, who have always been beside me. Many thanks to all of you!

Sé green diri ka fe sak diri.

List of main abbreviations, operators and symbols

Abbreviations

2D	Two dimensions
3D	Three dimensions
BHTC	Bell Helicopter Textron Canada
ANS	Assumed natural strain
CRIAQ	Consortium for Research and Innovation in Aerospace in Québec / Consortium de Recherche et d'Innovation en Aérospatiale au Québec
EAS	Enhanced assumed strain
LHD	Limiting dome height
MPHD	Micro-plasto-hydrodynamic
MPHS	Micro-plasto-hydrostatic
SFEM	Smooth finite element method
THF	Tube hydroforming
Uel	User defined element
Umat	User defined material
Vuel	Vectorized user defined element
Vumat	Vectorized user defined material
CAD	Computer aided design
WMH	With material history
WOMH	Without material history
PEEQ	Equivalent plastic strain
IP	Integration point
UL	Updated lagrangian
TL	Total lagrangian
FLD	Forming limit diagram
FLC	Forming limit curve
SFLC	Stress forming limit curve
XSFLC	3D stress forming limit curve
Tol	Tolerance

Operators

$\nabla(\square)$	Gradient operator
$\Delta(\square)$	Difference operator or Gâteaux derivative
$\partial(\square)$ or $(\ )_{,x}$ or $(\ )_{,1}$	Partial derivative
$(\square)^T$	Vector or matrix transpose
$(\square)^{-1}$	Vector or matrix inverse
$(\dot{\square})$ or $\frac{D(\square)}{Dt}$	Time derivative
$(\ddot{\square})$	Second time derivative
$\min(\square)$	Minimum value of $\square$
$trace(\square)$	Trace of a matrix
$div(\square)$	Divergence
$\lvert\square\rvert$ or $\det(\square)$	Determinant
$\lVert\square\rVert$	Vector norm
$(\bar{\square})$	Assumed parameter
$sign(\square)$	Sign of $(\square)$
$\otimes$	Tensorial product

Coordinate systems definition

$\mathbf{X}^0\left(X^0,Y^0,Z^0\right)$ or $X_i^0,\quad i=1,2,3$	Global coordinates system, undeformed configuration
$\mathbf{X}(X,Y,Z)$ or $X_i,\quad i=1,2,3$	Global coordinates system, deformed configuration
$\left(\mathbf{e}_X,\mathbf{e}_Y,\mathbf{e}_Z\right)$	Global cartesian base vector
$\boldsymbol{\xi}\left(\xi^{0,1},\xi^{0,2},\xi^{0,3}\right)$ or $\boldsymbol{\xi}^{0,i},\quad i=1,2,3$	Natural coordinates system

$\xi\left(\xi^1,\xi^2,\xi^3\right)$ or $\xi^i, \quad i=1,2,3$	Natural coordinates system
$\left(\mathbf{G}_1,\mathbf{G}_2,\mathbf{G}_3\right)$	Natural base vector
$\left(\mathbf{g}_1,\mathbf{g}_2,\mathbf{g}_3\right)$	
$\mathbf{x}^0\left(x^0,y^0,z^0\right)$ or $x_i^0, \quad i=1,2,3$	Local coordinates system, undeformed configuration
$\mathbf{x}\left(x\ ,y\ ,z\ \right)$ or $x_i, \quad i=1,2,3$	Local coordinates system, deformed configuration
$\breve{\mathbf{x}}\left(\breve{x},\breve{y},\breve{z}\right)$ or $\breve{x}_i, \quad i=1,2,3$	Co-rotational coordinates system
$\left(\mathbf{R}_x,\mathbf{R}_y,\mathbf{R}_z\right)$	Local cartesian base vector
$\left(\mathbf{r}_x,\mathbf{r}_y,\mathbf{r}_z\right)$	
$\left(\mathbf{g}_1^{stab},\mathbf{g}_2^{stab},\mathbf{g}_3^{stab}\right)$	Natural base vector used for stabilization
$\left(\mathbf{r}_{1i}^{stab},\mathbf{r}_{2i}^{stab},\mathbf{r}_{3i}^{stab}\right)$ $i=1,2,3$	Local cartesian base vector used for stabilization
$\mathbf{Q}_1,\mathbf{Q}_2$ and $\mathbf{Q}^{stab}$	Rotation matrices
$\mathbf{T}$	$(6x6)$ transformation matrix from the natural coordinates system basis $\xi\left(\xi^1,\xi^2,\xi^3\right)$ to the local cartesian coordinates system $\left(\mathbf{g}_1,\mathbf{g}_2,\mathbf{g}_3\right)$
$\mathbf{T}^G$	$(6x6)$ transformation matrix from the natural coordinates system basis $\xi\left(\xi^1,\xi^2,\xi^3\right)$ to the local cartesian coordinates system $\left(\mathbf{G}_1,\mathbf{G}_2,\mathbf{G}_3\right)$
$\mathbf{J}$	Jacobian matrix
$\mathbf{j}$	Jacobian matrix inverse

<u>By order of use</u>

$\mathbf{U}\left(U,V,W\right)$ or $U_i, \quad i=1,2,3$	Global displacement vector

$\mathbf{u}(u,v,w)$ or $u_i, \quad i=1,2,3$	Local displacement vector
$\mathbf{h}_1, \mathbf{h}_2, \mathbf{h}_3, \mathbf{h}_4$	Degrees of freedom identifying hourglass modes
$\boldsymbol{\varphi}_1$ and $\boldsymbol{\varphi}_2$	Rotation vectors
$\mathbf{E}$	Green Lagrange strain field
E_v	Volumetric strain
K	Curvature variation
N_I with $I=4$	Shape functions for a quadrilateral
N_I with $I=8$	Shape functions for a hexahedron
$(\ )^l$	Linear
$(\ )^{nl}$	Non-linear
$\mathbf{B}^{dil}$	Dilatation part of the differential operator
$\overline{\mathbf{B}}^{dil}$	Dilatation part of the differential operator with the B-bar approach
$\mathbf{K}$	Stiffness matrix
$\mathbf{M}$	Mass matrix
μ_k	Dynamic friction coefficient
μ_s	Static friction coefficient
d_c	User-defined decay coefficient
$\dot{\gamma}_{eq}$	Slip rate
$(\square)^L$	Parameter at the lower surface of the element
$(\square)^U$	Parameter at the upper surface of the element
$\overline{\mathbf{X}}(\overline{X},\overline{Y},\overline{Z})$	Position vectors of the mid-surface
$\Delta\mathbf{X}(\Delta X,\Delta Y,\Delta Z)$	Nodal orientation vector pointing from lower to upper surface
$\overline{\mathbf{U}}(\overline{U},\overline{V},\overline{W})$	Displacement vectors of the mid-surface
$\Delta\mathbf{U}(\Delta U,\Delta V,\Delta W)$	Nodal orientation displacement vector pointing from lower to upper surface
$\breve{\mathbf{u}}(\overline{u},\overline{v},\overline{w},\Delta u,\Delta v,\Delta w)$	Displacements vector for the resultant theory

$\boldsymbol{\varepsilon}$ or ε_{ij}	Green-Lagrange strain tensor components regarding the deformed configuration
$(\ )^{\xi}$	Natural components
$(\ )^{m}$	Membrane components
$(\ )^{b}$	Bending components
$(\ )^{mb}$	Membrane and bending components
$(\ )^{\gamma}$	Transverse shear components
$(\ )^{zz}$	Transverse normal components
$\mathbf{B}$	Differential operator
$\mathbf{F}$	Deformation gradient
$(\ )^{e}$	Element variable
W	Total work
W_{int}	Internal work
W_{ext}	External work
S	Surface
V	Volume
ρ	Density
$\mathbf{f}_{v}$	Volume external forces
$\mathbf{f}_{s}$	Surface external forces
$\mathbf{f}_{ext}$	Vector of external forces
$\mathbf{f}_{\text{int}}$	Vector of internal forces
$\mathbf{f}_{\alpha}$	Vector of enhanced forces
$\boldsymbol{\sigma}$	Cauchy stress tensor
$\mathbf{H}$	Constitutive matrix
λ and μ	Lamé's coefficients
E	Young's modulus
ν	Poisson's ratio
$\mathbf{H}'$	Modified constitutive matrix

$\overline{\lambda}$	Modified Lamé's coefficient
δ_{ij}	Kronecker symbol
$\left(\tilde{\square}\right)$	Smoothed parameters
Γ_C	Length of the boundary of each cells
$\mathbf{S}$	Second Piola-Kirchhoff stress tensor
$\left(\ \right)^{\text{mod}}$	Modified expression
$\left(\ \right)^{\alpha}$	Enhanced assumed part
$\mathbf{k}$	Stiffness matrix
$\mathbf{k}_{uu}$	Compatible stiffness matrix
$\mathbf{k}_{mat}$	Material stiffness matrix
$\mathbf{k}_S$	Geometric stiffness matrix
$\mathbf{k}_{u\alpha}$, $\mathbf{k}_{\alpha u}$ and $\mathbf{k}_{\alpha\alpha}$	Enhanced stiffness variables
$\mathbf{b}_i$	Hallquist parameter
$\left(\hat{\square}\right)$	Mean form of a given parameter averaged on the element volume
$\mathbf{B}_{12}$	Un-stabilized part of the differential operator
$\mathbf{B}_{34}$	Stabilized part of the differential operator
$\left(\ \right)_{stab}$ or $\left(\ \right)^{stab}$	Stabilized terms
$\mathbf{\Lambda}_1^T$, $\mathbf{\Lambda}_2^T$, $\mathbf{\Lambda}_3^T$	Node coordinates in the natural coordinates system $\boldsymbol{\xi}\left(\xi^1,\xi^2,\xi^3\right)$
$\breve{\square}$	Parameters expressed in the co-rotational coordinates systems $\breve{\mathbf{x}}\left(\breve{x},\breve{y},\breve{z}\right)$
$q_{i\alpha}$	Generalized strain
rhs	Residue (Right hand side)
k	Iteration number
$\left(\ \right)_k$	Parameter at iteration k
$E_{\tan g}$	Tangent modulus
$\left(\breve{\square}\right)$	Rotated components
$\boldsymbol{\varepsilon}^{elast}$ or ε_{ij}^{elast}	Elastic part of the Green-Lagrange strain tensor components

$\boldsymbol{\varepsilon}^{plast}$ or ε_{ij}^{plast}	Plastic part of the Green-Lagrange strain tensor components
ε^{plast}	Equivalent plastic strain
$\bar{h}$	Mean hardening modulus
σ_H	Material hardening
$(\ )^{elast}$	Elastic component
$(\ )^{plast}$	Plastic component
$(\ )^{hydro}$	Hydrostatic
f	Load function
σ_y	Flow stress
θ	Back stress
$(\square)^{trial}$	Trial parameter
$\mathbf{R}$	Rotation tensor of the deformation gradient tensor $\mathbf{F}$
$\mathbf{U}$	Stretch tensor of the deformation gradient tensor $\mathbf{F}$
$\left(\lambda_{(1)}, \lambda_{(2)}, \lambda_{(3)}\right)$	Stretch tensor $\mathbf{U}$ eigenvalues
$\left(\mathbf{N}_{(1)}, \mathbf{N}_{(2)}, \mathbf{N}_{(3)}\right)$	Stretch tensor $\mathbf{U}$ eigenvectors
$\mathbf{P}\left(\mathbf{N}_{(1)}, \mathbf{N}_{(2)}, \mathbf{N}_{(3)}\right)$	Orthogonal eigenvector matrix
$\mathbf{C}$	Right Cauchy Green strain tensor
$\left(\mathbf{I}_1, \mathbf{I}_2, \mathbf{I}_3\right)$	Right Cauchy Green strain tensor invariants
t	Time
$(\ )_t$	Parameter at step time t

Chapter 1. General introduction

1.1. Context of the thesis

This research work has been performed in collaboration with industrial partners, universities and research centers involved in the Consortium for Research and Innovation in Aerospace in Québec (CRIAQ). Industrial partners for the research project include Pratt and Whitney Canada and Bell Helicopter Textron Canada (BHTC). The universities and research centers involved in this project are École de Technologie Supérieure, Université Laval and National Research Council / Institute for Aerospace Research, Aerospace manufacturing technology center and the Natural sciences and Engineering Research Council of Canada. The research work is related to CRIAQ's project 4.6, "Process modeling tools development for the virtual manufacturing of aerospace components by tube hydroforming".

In this dissertation work, the feasibility of replacing an existing expensive metal forming process in the aerospace industry by a more recent and efficient process is examined. For instance, the helicopter skid landing gear cross tubes are often manufactured by bending aluminum tubes with a circular cross section followed by chemical milling, further presented in Totten & MacKenzie (2003), to obtain a tube with variable thickness. This technique allows substantial weight reduction necessary in the aerospace industry. However, this technique has a long cycle time and requires the use of harmful chemicals. In order to reduce the cost and the waste of raw material, but also for environmental reasons, it becomes essential to replace the existing metal forming techniques presented above, by a more efficient and environmentally friendly one.

1.2. The tube hydroforming process (THF)

In this section, the general THF process is described. A special attention is given to the main parameters to manipulate in order to manufacture a defect-less part, such as pressure increase and end feeding. The major advantages and drawbacks of THF are then explained to better highlight its potential and its limits. The THF process often requires various pre-forming steps, like bending or crushing, which could have a direct impact on a given part's hydroformability. These steps are furthermore discussed in this chapter. This section also

emphasizes the essential role of the friction control as well as a fine material characterization. The material characterization is especially important in the aerospace industry because so little data is available today regarding the material behavior during the tube hydroforming.

1.2.1 The THF process definition

THF is a forming process used since the beginning of last century to manufacture various industrial parts. Since then, many research projects driven by industrial needs have been working on improving it. The main steps of the THF process, shown in Figure 1.1, can be described as follows. In a first step, the tube is positioned between dies. Then the dies are closed. A good description of this technology is presented by Koç (2008). During this step tube crushing could occur depending on the internal surface design of the dies. This could lead to the occurrence of defects if the tube is subjected to an inappropriate level of deformation. Ahmetoglu & Altan (2000) and Koç & Altan (2001) have proposed a complete overview of the THF process including its basic concepts, usable materials as well as their related formability and friction impact. The pre-forming requirement, used to prepare the tube for hydroforming, has been illustrated in some specific cases. Pre-forming is extensively employed in the automotive industry and has issues when dealing with complex parts and safety. In their work, Dohmann & Hartl (1997) have also made an excellent overview of the THF process in automobile industry, including various variants of THF processes with or without pre-forming and detailed the related encountered difficulties.

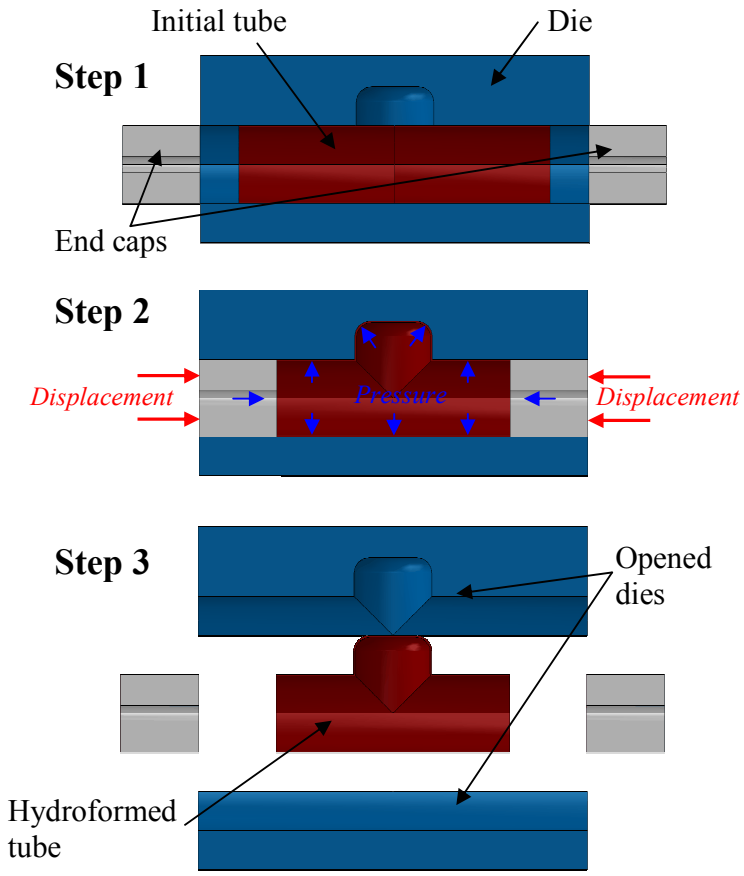

Figure 1.1: Hydroforming process sequence (sectional view)

Process control remains among the most important difficulty encountered in the THF process. Inappropriate process control parameters could induce some defects like buckling, wrinkling and bursting. In a first step, pre-forming like bending or the already cited crushing, is sometimes required to allow better tube positioning in between the hydroforming dies. Trana (2002) examined the effect of pre-forming which leaves residual stresses in the structure. These residual stresses could be eliminated by an annealing stage after hydroforming. This study highlights the importance of material history when modeling the fabrication of a part by means of hydroforming. Researchers like Coret & Combescure (2002) have developed complex constitutive laws taking into account the thermal effect, metallic microstructure and macroscopic stress and strain characteristics simultaneously in the forming process, as shown in Figure 1.2. In a second step, the

pressure of the fluid (liquid or gas) is increased inside the tube which forces deformation in the expansion zone, which is defined in section 1.2.3. The expansion period before any contact with the dies is called “free forming” and the period when contact occurs between the tube and the dies is called “calibration”. The tube ends can remain free or fixed as presented by Imaninejad et al. (2004). An axial feeding can also be provided during the pressure increase if necessary. In this specific case, applying a good loading path that makes an appropriate balance between pressure increase and axial feeding is one of the key prerequisites to obtain an acceptable part exempt of defect. For example, if the ratio between internal pressure and axial feeding is too large, bursting will occur. On the other hand, if this ratio is too small, buckling or wrinkling of the tube will occur as shown in Figure 1.3. Various researchers have examined this issue. For example, Aydemir et al. (2005) have illustrated an acceptable loading path region as shown in Figure 1.4. Once the part is hydroformed, the third and last step consist in opening the dies to free the hydroformed part which takes its final shape when the equilibrium is reached after springback.

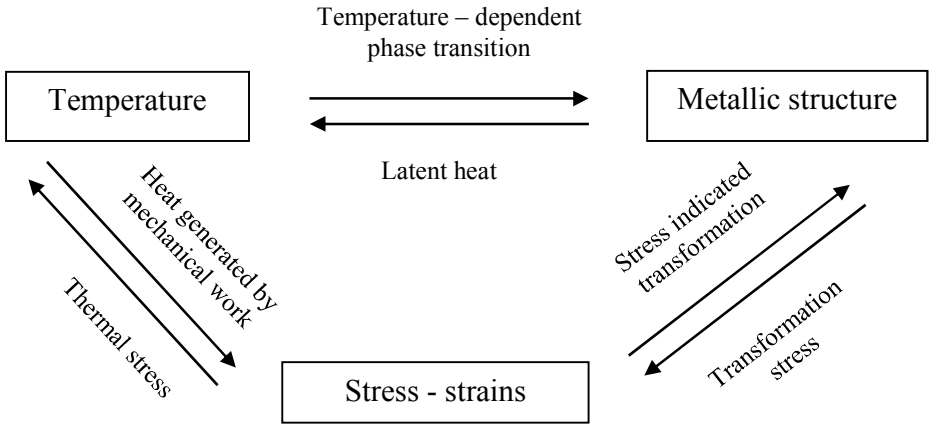

Figure 1.2: Coupling mechanism. Coret & Combescure (2002)

Wrinkling Bursting

Figure 1.3: Some THF defects

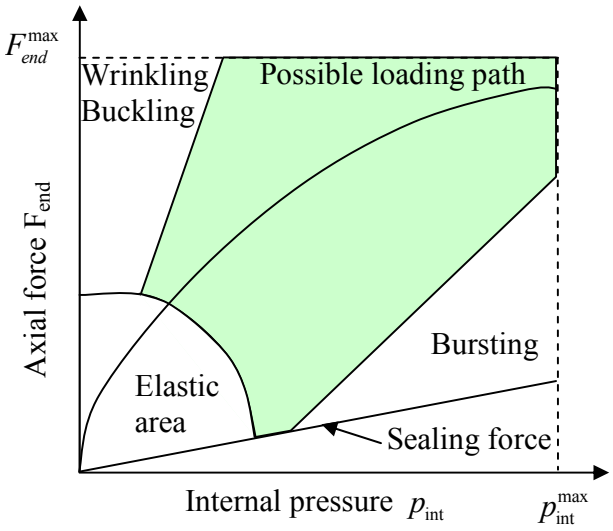

Figure 1.4: Admissible loading path Aydemir et al. (2005)

1.2.2 Pre-forming process: crushing, and bending

In some cases it is worth adding a pre-forming step before the THF process. In order to transform a circular section tube into a triangular section tube, Hwang & Altan (2002) have compared a manufacturing process including crushing and expansion steps with another

one including only one expansion step. Following this, Hwang & Altan (2003) have pursued their work by examining a rectangular section. The numerical results as well as the experimental observations confirmed the advantages of using crushing before THF. These advantages are namely: i) less pressure is required during THF; ii) Crushing force is lower than the required clamping force if crushing is not used; iii) It avoids excessive expansion and thinning and consequently provides a more uniform thickness in the final part cross section. Nevertheless, when the initial shape of the tube is deformed enough to fit the THF dies, the crushing step before THF process may not be required. This last observation is of interest to industrials since it could simplify the forming procedure, reducing in the same time the cost.

Indeed, industrials invest many resources to develop new reliable and cost effective fabrication processes. Reducing the number of preliminary steps before THF is an important improvement opportunity. Lee et al. (2005) have examined a typical multi-steps fabrication process for an automotive part which included bending, pre-forming and hydroforming steps. In their work, they have studied many parameters related to the rotary bending process of oval tubes in aluminum alloy Al6063. Using such initially oval tubes could diminish the need from using pre-forming to position the studied part inside the hydroforming dies. Moreover, they have observed that choosing an appropriate oval tube reduced the tube thinning and the tube plastic deformation outside of the bend. This last observation is interesting since it could decrease excessive thinning or bursting occurrence during THF.

Normani (2004) has made a helpful study of the pre-bending process which compares analytical and finite element analysis results to experimental results. A notable conclusion is that a pre-bending stage could induce some defects occurrence during the THF process. One of such defects is bursting which could happen because of both reduction in ductility available for the THF process and thinning of the wall section. However, our current knowledge about friction effects on pre-bending and THF processes is limited, which reduces the analytical and finite element analysis results accuracy. Besides, in all forming processes that induce some plastification, springback has a crucial influence on the final

part geometry. This phenomenon has then to be considered in the initial forming design to ensure that final part geometry is the one expected.

In order to obtain a final part within the expected specifications, it is necessary to consider springback. In a recent work presented in Zhan & Huang (2006) and Zhan et al. (2006), researchers have investigated on new analytical techniques to characterize the springback effect for thin structures. They have distinguished in their model two zones in a bent tube, the bending and the straight zones. The bending zone is the one subjected to large plastic deformation due to the dies and the straight zone is the remaining part of the tube. Thanks to comparisons between experimental data and numerical models they have identified parameters to characterize their models in these two zones.

1.2.3 Hydroforming tooling and friction problem

Tribology is one of the most fundamental parameter to be considered in metal forming operations, especially for the THF process, where a high level of internal pressure is applied in combination with axial feed. Researchers have identified three main contact regions in THF process: the guiding zone, the expansion zone and the transition zone. The guiding zone helps for tube positioning during hydroforming. The expansion zone is the part of the dies that provides to the tube its final shape after hydroforming. The transition zone is the zone between the guiding and the expansion one.

Many researchers have investigated techniques to find an appropriate friction coefficient in THF process. Vollertsen & Plancak (2002) have discussed on various ways to determine the friction coefficient. In particular, well known techniques such as the push through test have been used to determine the correct friction coefficient within the guiding zone. A tube upsetting method has been used to determine the friction coefficient in the expansion zone. In this relatively new method, a straight tube is positioned between rigid dies. The tube is then upset and in the same time the pressure increases inside the tube. Due to the friction coefficient between tube and dies, the tube wall thickness increases depending on the employed parameters. Among their interesting results, they have found a procedure to put in relation friction coefficient to tube wall thickness variation. Several diagrams have then been determined by finite element simulation runs with PAM-STAMP software.

Recently, Ngaile et al. (2004b) and Ngaile et al. (2004a) have studied lubrication and die coating influence specifically in expansion and transition zones. They have highlighted the complexity of determining an appropriate lubrication or die coating for a given THF process since some related parameters like material flow or relative velocity differ from one zone to another. For example, the relatively high velocity in the guiding zone encourages two important phenomena, the micro-plasto-hydrostatic (MPHS) and the micro-plasto-hydrodynamic (MPHD) when a liquid lubricant is used. MPHS, which occurs only if pressure is sufficiently high, shares the normal force between contacts asperities and lubricant and MPHD happens when the lubricant prevent dies and tubes from touching each other. None of these phenomena will generally happen in the transition or the expansion zones because of the relatively low velocity. In these last zones, they have observed that a dry film lubricant has appeared to be more appropriate. They have tested many lubricants properties in transition and expansion zones and have observed the related effects on final part geometry. The limiting dome height (LDH) has been used to evaluate lubricant potential in the transition zone and many tube expansions from round sections to triangular or square ones have been performed to evaluate lubricant performances in the expansion zone. They have compared for all these performed tests experimental to finite element analysis results from DEFORM 2D and PAM-STAMP software in order to determine some accurate friction coefficients to be used in their simulations.

Jansson et al. (2007b) have studied the impact of the friction coefficient on a hydroformed tube wall thickness. They have demonstrated that with only a simple biaxial test, it remains possible to get an accurate material characterization as well as a correct friction modeling in order to obtain a good constitutive model. These two parameters remain essential in the THF process since they control the instability pressure that possibly leads to tube bursting as well as the minimum tube wall thickness. Moreover, their study has also emphasized the direct relationship connecting the friction coefficient, particularly in the contact zone, between tube and dies and tube thickness after forming.

More recently, Luege & Luccioni (2008) have developed a contact model that considers friction film thickness and sliding velocity. They have implemented a model in the finite element code Stampack to perform some classic tests like the pear-shaped expansion. Their

model appears to provide results closer to experimental data than the classical Coulomb's friction law. This is mainly due to its ability to consider the velocity variation in the contact zones intrinsic data from the lubrication film.

1.2.4 Material modeling and characterization

In THF simulations, it is mandatory to use appropriate material properties depending on the type of simulation to be run. For this reason, many researchers have investigated constitutive modeling of aluminum alloys. Some of them like Hosford (1972), Hill (1990), Hill (1991) have developed criteria and formulations to accurately predict anisotropic material behavior in forming condition with plasticity.

In their work, Barlat et al. (2003) and Yoon et al. (2004) have proposed a new plane stress anisotropic yield formulation for aluminum alloy, the YLD2000-2d, that could be extended to other materials. In their formulation, they have solved various drawbacks encountered in the YLD96 formulation. On the top of them, there is the convexity of this new formulation that could be proven because it is based on linear transformations of the Cauchy stress. Moreover, the YLD2000-2d formulation has appeared to be simpler than YLD96, since only two principal stresses are required to deal with in-plane stress state. Few experimental tests have been necessary to calculate the new formulation coefficients, three uniaxial tensile tests and one biaxial bulge test. In addition, many experiments have exposed the advantage in term of accuracy of using the YLD2000-2d formulation in-plane stress finite element simulations of aluminum sheet metal forming process.

Jansson et al. (2005) have obtained very accurate results in THF simulations of tube in aluminum alloy AA6063-T4. The employed elastoplastic material has been based on the YLD2000-2d yield criterion formulation. The model calibration has been done with simple uniaxial tests and a biaxial test. They have observed that the anisotropic yield criterion used in this new formulation produced more accurate results as compared with the formulations classically used in the industry based on the yield criterion from Hill (1950) and Barlat & Lian (1989).

Korkolis & Kyriakides (2008) have compared various yield formulations with experimental data in the THF context for the AL-6260-T4 aluminum alloy. They have observed that

while the tested laws have generally remained accurate, the calculated strain at the start of rupture has usually been overestimated probably due to the yield surface formulation.

More recently Matei (2011) made a contribution to the field by developing a hyperelastoplastic material model based on the work of Simo & Hughes (1998) and capable of handling finite rotation problems and implemented in a co-rotational setting. Moreover, the hyperelastoplastic law is coupled with a ductile damage model detailed in Lemaître & Chaboche (2001). Since an explicit finite element formulation is employed, the resulting material model is implemented in ABAQUS software through its VUMAT facility and has been successfully calibrated with experimental data from several materials like the aluminum alloy 7075–W or the stainless steel grade 321.

1.2.5 Tube formability

A good overview of tube formability has been proposed by Green (2008). He has observed that each tube to be hydroformed has its own limits of formability influenced by various parameters such as: tube fabrication process, tube geometry, raw material properties and deformation history in a multi-steps fabrication process as pointed out in section 1.1. The forming limit diagram (FLD) is a tool extensively used in industry to assess the formability of tubes. This method, initially developed by Keeler (1961) and Goodwin (1968) is obtained under the assumption of strains being proportional to the loads although there may be no linear relationship between real strains and the applied load.

FLD diagram of sheet or tube material determines the state when localization of deformation and thinning of the material initiates during the forming operation Green (2008). It is usually expressed in terms of strain-based Forming Limit Curve (FLC) generated experimentally under the assumption of proportional loading and defined in terms of critical major and minor in-plane components of engineering strain. A FLD diagram comprises several curves named forming limit curves (FLC) that describe an admissible limit strain under which no necking is expected. Their inherent limitation of linear proportional loading and path dependence, make them unsuitable for predicting failure or forming severity, when applied to secondary forming operations involving pre-strain and non-linear loading paths Stoughton (2000), Kuwabara et al. (2003). In order to

recover path independence and be able to apply FLD to non-proportional loading and multi-steps forming processes, stress-based FLD's method were proposed in [Arrieux (1995), Stoughton & Zhu (2004)], who also give equations for the transformation of a strain-based FLD into the true principal stress space for several constitutive models (because they cannot be measured). Unfortunately, none of the above methods can be utilized for the failure prediction in straight and pre-bent tube hydroforming because both strain- and stress-based FLDs were derived according to through thickness plane stress assumptions. When a tube is expanded within a hydroforming die and if an important thinning is expected, the through-thickness stress component cannot be neglected, thus making the stress state 3D and invalidating application of strain- and stress-based FLDs. Hence, in [Koç (2008), chap5, "Hydroforming for advanced manufacturing", Woodhead Publishing Ltd., Cambridge, UK.], the suggested extended stress-based FLD (XSFLD), is applicable to the prediction of necking under 3D stress states. Although, recent studies indicate some path dependence of stress based FLD under certain conditions Koç (2008), it appears that this occurs primarily for severely non proportional loading histories where the initial pre-strain is in biaxial tension and where the material exhibits definite kinematics hardening effects. These experimental observations indicate that further work is required to establish a failure criterion that is unambiguous even under complex loading histories Koç (2008). For this reason, Simha et al. (2005) have extended the stress-based method by developing the XSFLC based on a 3D stress state instead of plane stress assumption and they observed that considering a 2D stress state instead of a 3D stress state could change the location of possible necking in THF simulations. Hence, it becomes necessary to use 3D solid elements compatible with 3D constitutive law while simulating THF process. However, for thin structures this is computational prohibitive Koç (2008). Therefore, using a solid-shell element, implementing a fully 3D constitutive law, requires only one element through the thickness and this could alleviate the need to use two or three standard continuum solid elements through the thickness in order to get accurate 3D stress field required to produce realistic limit diagram.

1.3. Problematic and research orientation

In the aerospace industry, it is still common to rely on empirical data, previously validated by aviation regulation authorities. In addition to this empirical knowledge, engineers use some safety factors in all new structural part developments in order to reach the required safety standard. However, in case of new technological advance, very few data exist to support such developments. Hence, two options arise while developing new parts. A first one is to fix the limitations of this development among the range of already proven product capabilities for then ensuring a prompt answer with low risks. However, because of cost and environmental reasons, it is not always possible to maintain the aforementioned old manufacturing processes. A second option is then to entirely rethink an approach to develop and to manufacture parts that is more appropriate to the new technology. It can be done so, for example by considering a larger variety of novel technologies regarding their potential and not only the related present available background. However, if this latter option provides a long term vision about the development of new products, the related required investments could be very high, eventually with at the end no guaranty to reach the final expected results.

In order to reduce those uncertainties, companies have found great support in computerized methods such as computer aided design and simulations based on the finite element method for example. In the latter, the accuracy of the simulation results and its ability to reproduce complex phenomena with good time efficiency are crucial issues. This is especially true while simulating THF process. As detailed in Koç (2008), the quality of several input data can influence the finite element method accuracy such as: Fine material parameters use. For example, characterizing the material properties from some tube specimens increases in the same time the material parameters fineness. Indeed, it allows considering the possible loss of formability due to the tube own fabrication process or considering its curvature; Adequate boundary conditions and loading, similar as those implemented experimentally.

Moreover, the phenomena encountered in THF process are more complex than those encountered in sheet metal forming. Koç (2008) have emphasized the necessity to consider the 3D stress field of a tube to be hydroformed in order to predict defect occurrence such as

necking already discussed. This implies the development of complex 3D constitutive models able to reproduce complex deformation pattern as presented in Matei (2011). However, the solid elements based on 3D formulations are generally time consuming. That is the reason why the THF industry commonly prefers using shell elements based on plane stress assumptions, prone to be more time efficient. The subsequent accuracy generally remains acceptable for simple cases but insufficient in case of tube hydroforming with complex shapes. In summary, the integrated virtual manufacturing tools need to evolve with the technology.

In order to respond to those knowledge gaps, the present work virtually develops and tests a method to improve a new part developing and manufacturing through a tube hydroforming process. More precisely, this research aims are: i) to develop an aerospace part new design which can be manufactured by tube hydroforming - This new design will be tested in in-service simulations to validate its ability to replace existing standard design; ii) to propose a virtual multi-steps fabrication process that keeps track of material history from the straight tube to the final, in-service conditions of the hydroformed part; iii) to develop solid-shell finite element formulations that are able to read most of the 3D constitutive laws with a competitive time efficiency. Accordingly, the developed element can benefit from the 3D constitutive law of Matei (2011).

1.4. Methodology and research objectives

The main objective of this thesis is thus to improve the efficiency of existing virtual tools for the tube hydroforming simulation process.

For years, the tube hydroforming process has been successfully used in the automotive industry. It indeed provides several advantages over conventional manufacturing techniques such as stamping and welding as presented in Ahmetoglu & Altan (2000). The benefits of the tube hydroforming process include: i) part consolidation; ii) weight reduction; iii) improved structural stiffness; iv) lower tooling cost; v) fewer secondary operations; and vi) tight dimensional tolerances. In spite of those advantages the tube hydroforming has some disadvantages which comprise in particular a long design cycle time and the need for expensive equipment to implement the process. The relative novelty of the tube hydroforming technology represents another drawback as compared with conventional metal forming processes, since there is still a lack of knowledge base about process and tool design. Consequently, there is a growing need for improved expertise as well as for more systematic approaches in order to respond to the needs of the aerospace industry in this area.

Indeed, as the aerospace industry is less familiar with such technology, it is willing to explore its potential benefits. Although tube hydroforming has been used in this domain before, some important issues have inhibited a broader diffusion of the technique. It still remains difficult, for instance, to obtain a helicopter cross tube of skid type landing gear with a variable thickness from a tube with a constant thickness only by hydroforming. In order to do so, a new skid landing gear cross tube design needs to be developed. This will help in producing a hydroformable tube with acceptable mechanical properties. Moreover, to hydroform a tube, a pre-form step is sometimes required depending on the geometry of the final shape. As a result, the initial material properties of the tube will change based on the level of plasticity in the pre-formed shape.

Accordingly, this work first aims at developing a methodology that quantifies and takes into account the impact of material loading history from the initial straight tube to the test

of the fully assembled skid landing gear equipped with a hydroformed cross tube in hard landing conditions.

One of the main difficulties in the tube hydroforming process is the defect detection and correction during the process. Four major types of defects can occur during tube hydroforming: buckling, wrinkling, necking and bursting. Several researchers have been working on the adaptive simulation method for buckling and winkling detection based on specific identification criteria. For example, the energy balance method is generally used to determine the buckling criteria and the plastic bifurcation method is generally used to determine the wrinkling criteria Lundqvist (2004). However, no reliable wrinkling indicator has been developed so far for more complex parts and processes, especially for those parts involving pre-forming operations. In this field, research is not as advanced as for necking detection which generally precedes bursting. As a consequence, a number of unresolved issues continue to emerge. What criteria may be more helpful for necking detection in a tube hydroforming process? Will those criteria be efficient enough to quantify the necking defect? It is necessary to determine new parameters in order to observe and to analyze, so that a relation can be made between this defect occurrence and the criteria.

The second objective of this work is to present the new smoothed finite element method through the development of a 3D resultant solid-shell element. The presentation of this element helps emphasizing its potential advantages in a near future. However, at this stage of its development, this newly developed element is not ready to simulate tube hydroforming process.

As a third objective, this work aims at understanding and at developing a reduced integration solid-shell finite element representing shell structures embedded in a 3D formulation. This element will eventually be combined with a 3D hyperelastoplastic constitutive law coupled with damage criteria as part of another task in the same CRIAQ project 4.6.

1.5. Required tasks to reach research objectives

In order to reach the three aforementioned research objectives, the necessary main tasks are articulated as follows:

- Development of a new cross tube design with a hydroformable geometry, which offers mechanical properties that are comparable with those of the standard existing design in hard landing conditions.

- Development of a methodology for multi-steps fabrication process including bending, crushing, tube hydroforming and heat treatment that takes into account material history from the straight tube to the tests in hard landing conditions.

- Investigation of recently developed finite element formulations that may be useful in THF simulations.

- Formulation and implementation of a non-linear solid-shell element based on a 3D constitutive law that is possibly efficient in forming process.

- Combination of the explicit formulation of the developed solid-shell element with a 3D hyperelastoplastic constitutive law.

- Check of the ability of this improved element in the tube hydroforming context.

1.6. Main contribution of the thesis

In view of the above work and planned methodology, a series of original contributions to research and development can be identified as follows:

- Development of a hydroformable helicopter skid landing gear cross tube. This innovative part has successfully been tested in hard landing conditions simulations regarding the FAR § 27.725 requirements in the software ABAQUS/Explicit.

- Development of a methodology that considers material history during a multi-steps fabrication process of an aerospace part including bending, aging and hydroforming.

- Development and implementation of an implicit 3D fully integrated resultant solid-shell element using the new SFEM technique to deal with membrane and bending modes for small deformation problems. The element has been implemented and validated in the ABAQUS finite element commercial code as UEL subroutines.

- Formulation of an implicit, 3D reduced integration solid-shell finite element with physical stabilization, called here SH8RSe, for large strain problem. The element has been implemented in the commercial FE code ABAQUS/Implicit with the via its UEL subroutines facilities. Its performance is established against a number of relevant benchmark problems.

- Formulation and implementation of an explicit SH8RSe, 3D reduced integration solid-shell finite element with stabilization for large strain problem. The element is implemented in ABAQUS/Explicit FE commercial code via its VUEL subroutines.

- Combination of the developed solid-shell element SH8RSe with a 3D hyperelastoplastic constitutive law provided as an ABAQUS/VUMAT like subroutine from Matei's thesis work (See Matei (2011)). The combined formulation has then successfully been tested in the tube hydroforming context in ABAQUS/Explicit.

Chapter 2. Literature review

A review of the most popular finite elements used in the tube hydroforming process is proposed in this Chapter 2. The description of shell element formulations that could be employed in the tube hydroforming process is proposed with emphasis on eight-node solid-shell elements that combine the advantages of shell elements in their ability to simulate thin structures and solid elements embedded in a 3D formulation. Some of the advantages of this type of formulation are then presented together with existing methods used to tackle the associated drawbacks.

2.1. Process modeling using finite element analysis

The finite element analysis method is a widely accepted in industry as a design tool that can be applied to develop rapidly new products with minimum waste for increased competitiveness. This last point is much appreciated while working with expensive materials such as those encountered in the aerospace industry. Indeed, the finite element method helps reducing the number of prototypes necessary to determine final part specifications. The main advantages of this method are that:

- It reduces the number of experimental tests which require a lot of time and huge investments;
- It allows part and device numerical optimizations, therefore reducing the need to manufacture expensive physical prototypes. In the same time, it can give an idea on production feasibility;
- It provides a rapid overview of what is required for a specific production process or of the specifications of parts to be processed.

Lundqvist (2004) has given an overview of a typical virtual verification methodology. It appears that irrespective of the quality of the code, data collection as well as pre-processing remains crucial steps since they are largely responsible for simulation results accuracy. In the data collection step, some experiments are usually necessary to fine tune material characterization since the employed constitutive laws may depend on a given problem

configuration. With the finite element method, the pre-processing step also remains fundamental. The element choice is set depending on the problem parameters. For more than thirty years, many researchers have been working on various element formulations to decrease the computation time and to increase in the same time their accuracy. Due to some computer limitations, shell elements have been preferred to solid elements. In other words, by making some simplifying assumptions, computation time remained acceptable with an acceptable level of accuracy. Since then, much development has been made on finite element in implicit as well as in explicit formulations. For hydroforming simulations, in spite of progress made in computer efficiency, the shell elements combined with explicit formulation are frequently chosen to save time.

The use of finite element analysis for THF process is still challenging in various aspects as for example the numerical material characterization or the adaptive process simulation methodology. In their work, Kim et al. (2003) have presented a multi-steps simulation of an automotive part including bending, pre-forming and THF steps with the finite element software HydroFORM-3D. They have underlined the benefits of using the finite element analysis method mainly to reduce time and cost, in the THF industry.

One of the main challenges with the THF process is that it is not easy to determine an appropriate loading path. Trial and error method is generally used, which is not optimal. In this approach, a run is submitted with a specific loading path and when a potential defect is detected, it is stopped. Then, the loading path is changed based on the experience of the designer. Another run is then submitted with the latest loading path. And the process continues until an acceptable response is obtained. The finite element analysis is helpful because it allows implementing many iterations numerically before any heavy investments on THF press.

Differently, Koç & Altan (2002) have compared experimental data with numerical results for the hydroforming of simple axisymmetric shapes to establish some guidelines while dealing with the THF process. Their numerical models have used 2D elements of the software Deform 2D. They have observed that, even though using 2D elements provides less accuracy than 3D elements, it remains useful at the beginning of a project

development. Indeed, the accuracy is adequate regarding the rapidity of a simulation completion time.

In another study from Lang et al. (2004), the LS-Dyna 2D software has been used in 2D to investigate the bending and unbending effects on an aluminum tube wall thickness during the THF process. The authors have also studied some parameters responsible of wrinkling in order to create some useful wrinkling during the THF process. Interestingly, they have emphasized the beneficial properties of the wrinkling effect during that process. They have further observed that a wrinkling from a pre-forming - stage which is soft enough to be flattened during the THF process with the pressure applied - could facilitate the shape formability. However, they have also observed that strong wrinkling need to be avoided during the pre-form stage to circumvent final shape defects. The obtained simulation results with 2D models are in good correlation with experimental data. Nevertheless, 2D models still remain a preliminary step before implementing 3D models. This method allows reducing computation time of a given project since 2D simulations are usually faster than 3D simulations.

More recently, Ray & Mac Donald (2005) have studied the hydroformability of X- and T-branch tubes using the LS-Dyna 3D explicit software. They have meshed the tubes with the Belytschko Wong Chiang shell element. The formulation of this element allows observing the thickness variation. The numerical results are consistent with experimental data. However, the element has been fully integrated and fine meshes were used which induced small step time increments. Consequently, it has been mandatory to use a mass scaling parameter to reduce the computation time together with increased model accuracy.

Other researchers such as Abrantes et al. (2005) and Kang et al. (2005) have simulated the THF process using the LS-Dyna software. In the later work, the authors have examined the influence of the diameter of a straight tube on its hydroformability. They did so using different loading paths to produce a vehicle bump rail. The exciting point is that the whole study has been performed numerically. They have meshed the tube with Belytschko–Lin–Tsai shell elements. Furthermore, they have observed that using the largest initial diameter possible increases the hydroformability of a tube. Additionally, a particular loading path should be determined for each geometry.

As mentioned before, the trial and error method is not cost efficient due to the required number of iterations. In order to increase the computer time efficiency, some researchers have developed an adaptive method. In this method, a failure indicator is initially selected. If this criterion is satisfied during calculation, the initial loading path is automatically adjusted and as a consequence the tube can continue to expand while avoiding defects. Strano et al. (2001) have successfully determined a geometric wrinkling indicator for the THF process. This geometric indicator is a ratio between the surface and the volume of the hydroformed shape. A wrinkled part has for example a large area / volume indicator value. Other wrinkling indicators exist like the one based on the slope of the profile. A change of the slope indicates a possible wrinkling occurrence.

Furthermore, Ray & Mac Donald (2004) have proposed an indicator based on the bending strain difference. A large in-plane strain difference between the inside and the outside of the tube could indicate a wrinkling occurrence. They have successfully determined an appropriate loading path to hydroform “T” and “X” shapes from a straight tube. The tube has been meshed with four-node 3D shell elements and simulations have been performed on Ansys / LS-Dyna code.

In a more recent work presented in Jansson et al. (2007a), it has been proposed a methodology to estimate the THF process parameters for a conical shape. The authors have implemented adaptive simulation using the bending strain wrinkling indicator previously cited. The tube was in aluminum alloy 6063-T4 using the YLD2000 yield criterion and meshed with Belytschko Tsay Belytschko et al. (1984) elements from the explicit code LS-Dyna. They have observed the efficiency of the adaptive method in finding an appropriate loading path to hydroform a tube using conical dies. However, some drawbacks needed to be pointed out from this method. First, implementing a wrinkling indicator remains mathematically complicated. Second, as the adaptive method is mainly based on the indicator estimation, an inappropriate indicator leads to inaccurate results.

Various researchers have tried to find the best way to get optimized loading parameters. For example, Fann & Hsiao (2003) have developed an optimization method for a T-shaped metal tube based on the conjugate gradient method. They have compared two optimization procedures: the batch and the sequential modes. In the batch mode, all design variables are

optimized at the same time according only to the end results. In the sequential mode, the design variables are optimized according to intermediate results at the end of each sequence. According to their work, the batch mode gives more accurate results.

Matei (2011) has developed an adaptive approach based on evaluating the material behavior of the structure to determine in real time an appropriate loading path for the THF process. The calculated pressure and axial feeding have been both related to material parameters like material limit flow and plasticity. He has combined two user's subroutines of ABAQUS/Explicit software in explicit, namely ABAQUS/VUMAT and ABAQUS/VDLOAD. His work has been validated against experimental examples from the literature and has offered competitive time efficiency.

2.2. Shell element formulations

Regarding the above literature review, shell finite elements are mainly preferred in the THF process simulations. Among the reasons for this preference, the simulated structures wall thickness remains relatively thin. However, such elements have some limitations, especially in THF simulations involving high pressure level and where an accurate contact definition is fundamental. Moreover, these elements are not compatible with a 3D stress state generally required in such simulation as presented in section 1.2.5. This section set an overview of the main characteristics of shell elements along with a summary of existing shell elements that may be useful in the THF process. The most important problems generally related with the use of these elements are presented in the present work together with some techniques to tackle them. The Kirchhoff-Love and Reissner-Mindlin plate theories described in the following section 2.2.1 are the basis of the most popular shell element formulations.

2.2.1 Kirchhoff-Love and Reissner-Mindlin plate theories

Choosing the most appropriate shell models depends on the type of structures they are supposed to describe. The Kirchhoff-Love plate theory is used to describe thin structures. One of the key hypothesis is that a straight line l_0 normal to the mid-surface of the structure before deformation remains straight and normal (see l_1) to the deformed mid-surface of the structure after deformation, as illustrated in Figure 2.1.

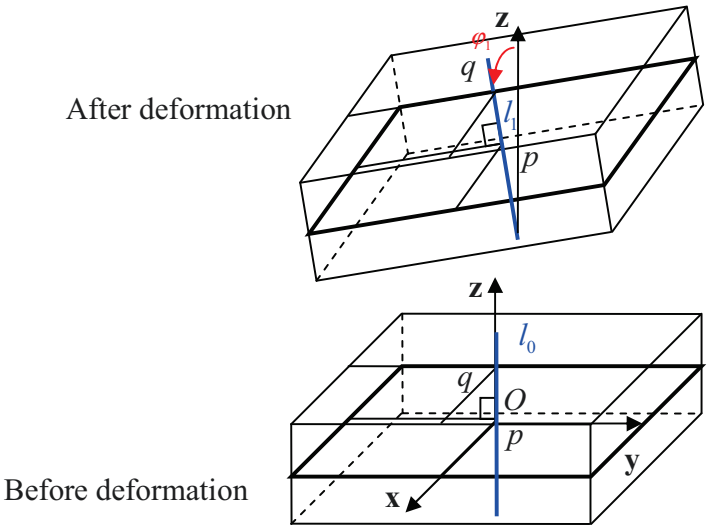

Figure 2.1: Kirchhoff-Love plate theory

In contrast with the Kirchhoff-Love plate theory, the Reissner-Mindlin plate theory is used to describe thick structures. One of the key assumptions is that a straight line l_0 normal to the mid-surface of the structure before deformation remains straight - but not necessarily normal - to the deformed mid-surface of the structure after deformation, as illustrated in Figure 2.2.

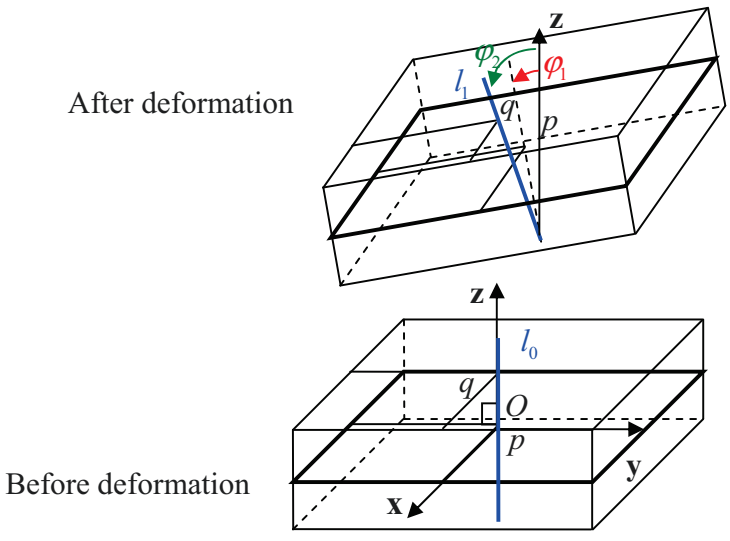

Figure 2.2: Reissner-Mindlin plate theory

As a consequence, in kinematics terms, the displacement of a point q of the structure can be described for these two approaches as:

$$\mathbf{u}_q = \mathbf{u}_p + \mathbf{z} \times \boldsymbol{\varphi}_2 \tag{2.1}$$

where $\mathbf{u}_p$ is the displacement vector of a point p located on the mid-surface of the structure and $\boldsymbol{\varphi}_2$ is the rotation vector of the straight line initially normal to the mid - surface.

2.2.2 Degenerated or classical shell elements

A degenerated shell element or classical shell element is an isoparametric or 3D continuous degenerated element. One of the key points of this category of elements is the plane stress hypothesis, which is used to avoid some thickness locking while dealing with thin structures. This is the reason why the term "degenerated" is adopted, since it reduces a 3D theory into a planar theory. Among the first to develop a degenerated shell element, Ahmad et al. (1970) have provided a detailed work on the subject limited to linear problem.

This element family concept is based on a four-node curved element with five degrees of freedoms per node (three displacements and two rotations) which can deal with large displacement as well as large rotation problems. As they mix two different types of degree of freedoms, they are usually named "mixed" elements. Malkus & Hughes (1978) have made a valuable work that presents the equivalence between some mixed elements and displacement based elements with reduced integration. Many researchers as Dvorkin & Bathe (1984) and Bathe & Dvorkin (1985) have developed such elements for the robustness they could offer. Besides, Parisch (1978), Parisch (1979), Bathe & Bolourchi (1980), Brendel & Ramm (1980) and Hughes & Liu (1981) have extended this shell element theory to non-linear problems. Belytschko et al. (1984) further developed an explicit algorithm now implemented in the explicit code LS-Dyna. Following those works on degenerated shell elements development based on a 3D continuum mechanics theory, this type of element has become more and more efficient to deal with a range of problems larger than those generally restricted to shell elements. However, as highlighted by Bathe (1982) and Bathe et al. (1983), such elements commonly have some shear locking while dealing with

thin structures in constant bending condition, because the transverse shear strains components cannot be set to zero. In this last study, the proposed element did not present any transverse shear locking even for thin structures thanks to a separate interpolation of strain components. This technique appeared to be more efficient for dealing with non-linear problems than the reduced order integration discussed in Macneal (1978). As this family of elements remains time efficient and provides an acceptable accuracy, which is well appreciated by the industry, it has been extensively developed by many other researchers like Simo & Fox (1989), Batoz & Dhatt (1992), Bucalem & Bathe (1993), Bathe et al. (2000), César de Sá et al. (2002) and Chapelle et al. (2003).

Notwithstanding, the fundamental plane stress hypothesis of this category of elements makes it impossible to get a 3D stress field in the structure. This limitation makes degenerated shell elements inadequate for various forming process of thin structures where through thickness information remains a critical issue. In order to remedy this drawback, researchers have been working on the implementation of 3D behavior laws in such elements. In this context, one can cite the contribution of Betsch et al. (1996), Bischoff & Ramm (1997), Brank et al. (2002), Cardoso & Yoon (2005), Lu et al. (2006), Klinkel et al. (2008) and Kim & Bathe (2008).

2.2.3 Solid-shell elements locking overview

Solid-shell element introduction

During the past two decades, 3D solid-shell elements using only displacement type degrees of freedom have been enhanced thanks to the interest of many researchers as well as the industrial community. One great advantage of solid-shell elements is that a 3D solid geometry can be meshed. Indeed, solid-shell elements have inner and outer nodes that can lay on a surface structure. As a result, the contact between parts is explicit. In addition, as a solid-shell element formulation only uses displacement degrees of freedom, it remains easier to develop than mixed elements. This also allows meshing complex parts that contain both thick and thin wall thickness regions.

Among the pioneer who developed this method, Parisch (1995) have proposed two solid-shell element versions, one with eight nodes and another with sixteen nodes. Their

integrations have been performed on the element mid-surface as for a classical 2D element. Though, they have coupled it with an explicit through the thickness integration at each integration points. From these elements have arisen encouraging results while dealing with thin structures in linear as well as non-linear problems. However, Simo, et al. (1990) have pointed out possible issues with the stiffness matrix ill-conditioning. This problem arises in thin structures because of a stiffness growth in the thickness direction in the same time as wall thickness decay. A detailed formulation of displacement based solid-shell element is proposed in Hauptmann & Schweizerhof (1998) as well as an overview of related locking problems. A locking overview, inspired from the work of Nguyen (2009) is presented below.

Solid-shell element locking phenomena

Using low-order interpolation solid-shell elements remains very popular since it tends to reduce computation time. However, some low-order solid-shell elements are exposed to various locking phenomenon Hauptmann et al. (2001). A solid-shell element is a solid type element which includes shell properties, which allows it to be used in thin wall problems. As a result, it remains exposed to locking that generally influence solid elements like shear locking, volumetric locking, Poisson thickness locking and curvature (or trapezoidal) locking. It is also subject to locking, which is generally encountered in shell-like elements as transverse shear locking and membrane locking. In order to better understand the locking phenomenon, which could occur in solid type as well as shell type elements, let us consider the eight-node isoparametric element presented in Figure 2.3. The displacements field $\mathbf{U}(U_1, U_2, U_3)$ at an arbitrary point q within the element in the global coordinates system $(\mathbf{X}, \mathbf{Y}, \mathbf{Z})$ can be linearly interpolated using the classical tri-linear shape functions as detailed in Chapter 4.

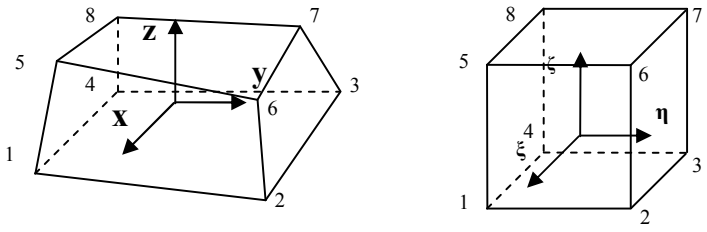

Figure 2.3: Standard eight - node geometry

The tri-linear displacements field can then take the following form:

$$u_i = a_{0i} + a_{1i} \times X + a_{2i} \times Y + a_{3i} \times Z + c_{1i} \times h_1 + c_{2i} \times h_2 + c_{3i} \times h_3 + c_{4i} \times h_4, \quad (i = 1, \ldots, 3) \tag{2.2}$$

in which

$$h_1 = \eta \times \zeta, \; h_2 = \zeta \times \xi, \; h_3 = \xi \times \eta, \; h_4 = \xi \times \eta \times \zeta \tag{2.3}$$

As in Nguyen (2009) equation (2.2) is alleviated in the subsequent development, considering that the element remains perfectly rectangular prismatic. This induces the alignment of the global cartesian coordinates system $\mathbf{X}(X, Y, Z)$ with the natural coordinates system $\xi(\xi^1, \xi^2, \xi^3)$.

The Green Lagrange strain field is then:

$$\mathbf{E}(\mathbf{u}) = \begin{bmatrix} E_{xx} \\ E_{yy} \\ E_{zz} \\ 2 \times E_{xy} \\ 2 \times E_{yz} \\ 2 \times E_{xz} \end{bmatrix} = \begin{bmatrix} u_{1,1} & + & \frac{1}{2}\left[\left(u_{1,1}\right)^2 + \left(u_{2,1}\right)^2 + \left(u_{3,1}\right)^2 \right] \\ u_{2,2} & + & \frac{1}{2}\left[\left(u_{1,2}\right)^2 + \left(u_{2,2}\right)^2 + \left(u_{3,2}\right)^2 \right] \\ u_{3,3} & + & \frac{1}{2}\left[\left(u_{1,3}\right)^2 + \left(u_{2,3}\right)^2 + \left(u_{3,3}\right)^2 \right] \\ u_{1,2} + u_{2,1} & + & \left(u_{1,1} \times u_{1,2} + u_{2,1} \times u_{2,2} + u_{3,1} \times u_{3,2} \right) \\ u_{2,3} + u_{3,2} & + & \left(u_{1,2} \times u_{1,3} + u_{2,2} \times u_{2,3} + u_{3,2} \times u_{3,3} \right) \\ \underbrace{u_{1,3} + u_{3,1}}_{linear(l)} & + & \underbrace{\left(u_{1,1} \times u_{1,3} + u_{2,1} \times u_{2,3} + u_{3,1} \times u_{3,3} \right)}_{nonlinear(nl)} \end{bmatrix} \tag{2.4}$$

In the following, only the linear part of the Green Lagrange strain field will be considered in order to explain locking troubles for reasons of simplicity.

Transverse shear locking

The denomination “shear locking” is generally used in case of solid element since there is no preferential direction in this element type. In case of solid-shell element, this locking phenomenon is commonly called “transverse shear locking” since this element type identifies thickness orientation. In this work, this last denomination is adopted since it is

about solid-shell elements. Transverse shear locking could occur when a thin structure is subjected to pure bending. In this special situation, shear strain E_{xy} should vanish. Introducing equation (2.2) into the shear strain expression E_{xy} of equation (2.4) leads to the developed expression:

$$\begin{aligned} E_{xy}^{l} &= u_{1,2} + u_{2,1} \\ &= \left(a_{21} + c_{11} \times Z + c_{31} \times X + c_{41} \times X \times Z\right) + \left(a_{12} + c_{22} \times Z + c_{32} \times Y + c_{42} \times Y \times Z\right) \\ &= \left(a_{21} + a_{12}\right) + \left(c_{11} + c_{22}\right) \times Z + c_{31} \times X + c_{32} \times Y + c_{41} \times X \times Z + c_{42} \times Y \times Z \end{aligned} \quad (2.5)$$

Thus, it appears that $E_{xy}^{l} = 0$ only in the following conditions are fulfilled:

$$a_{21} + a_{12} = 0 \; ; + c_{11} + c_{22} = 0 \quad (2.6)$$

$$c_{31} = 0 \; ; c_{32} = 0 \; ; c_{41} = 0 \; ; + c_{42} = 0 \quad (2.7)$$

If the condition in equation (2.6) can be satisfied, the condition in equation (2.7) cannot be reached since they are required to define the tri-linear displacements field described in equation (2.2). These last terms $c_{31} \; ; c_{32} \; ; c_{41} \; ; c_{42}$ are identified as “inconsistency” terms Chandra & Prathap (1989).

Volumetric locking

The volumetric locking occurs when the employed material is nearly incompressible or incompressible. It is dependent on material behavior parameters. In order to avoid volumetric locking, the required condition is the volumetric strain E_v vanishing. This parameter corresponds to the trace of the linear strain field. Introducing the equation (2.2) into the volumetric strain E_v, leads to:

$$\begin{aligned} E_v &= u_{1,1} + u_{2,2} + u_{3,3} \\ &= \left(a_{11} + c_{21} \times Z + c_{31} \times Y + c_{41} \times Y \times Z\right) + \left(a_{22} + c_{12} \times Z + c_{32} \times X + c_{42} \times X \times Z\right) + \ldots \\ &\ldots + \left(a_{33} + c_{13} \times Y + c_{23} \times X + c_{43} \times X \times Y\right) \\ &= \left(a_{11} + a_{22} + a_{33}\right) + \left(c_{32} + c_{23}\right) \times X + \left(c_{13} + c_{31}\right) \times Y + \left(c_{21} + c_{12}\right) \times Z + \ldots \\ &\ldots + c_{41} \times Y \times Z + c_{42} \times X \times Z + c_{43} \times X \times Y \end{aligned} \quad (2.8)$$

The volumetric locking condition $E_v = 0$ leads to the subsequent equalities:

$$a_{11} + a_{22} + a_{33} = 0 \; ; c_{32} + c_{23} = 0 \; ; c_{13} + c_{31} = 0 \; ; c_{21} + c_{12} = 0 \tag{2.9}$$

$$c_{41} = 0 \; ; c_{42} = 0 \; ; c_{43} = 0 \tag{2.10}$$

Hence, it clearly appears from the relations (2.9) that locking free conditions occur when $a_{11} = -\left(a_{22} + a_{33}\right)$, $c_{32} = -c_{23}$, $c_{13} = -c_{31}$ and $c_{21} = -c_{12}$. Nevertheless, relations (2.10) obtained from the isolated terms c_{41} ,c_{42} *and* c_{43} cannot be encountered since these isolated terms remain essential to define the tri-linear displacements field presented in equation (2.2). This results in an additional stiffness which leads to the well known volumetric locking.

Poisson thickness locking

When the strain field in the thickness direction is not appropriate, the Poisson thickness locking can occur. The strain in the thickness direction E_{zz} can be evaluated introducing equation (2.2) into equation (2.4) as follows:

$$\begin{aligned} E_{zz}^{l} &= u_{3,3} \\ &= a_{33} + c_{13} \times Y + c_{23} \times X + c_{43} \times X \times Y \end{aligned} \tag{2.11}$$

In problems dominated by bending, analytic through - thickness strain field linear changes with the thickness are expected. This last observation results in that the thickness strain E_{zz} determined in equation (2.11) is not appropriate since it remains constant through the thickness.

Curvature or trapezoidal locking

When an element is used to mesh curved geometry like tubes, its edges through the thickness do not remain perpendicular to its mid-surface as illustrated in Figure 2.4. This deformed configuration can in some cases add some unphysical strain to the thickness strain E_{zz} conducting to locking.

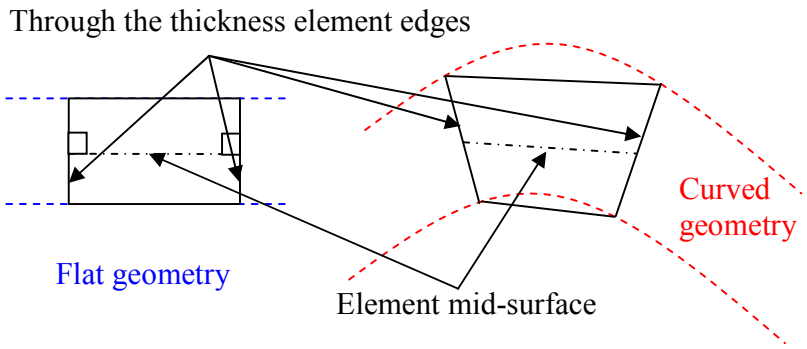

Figure 2.4: Curvature or trapezoidal locking

Membrane locking

The membrane locking phenomena occurs mainly when curved structures subjected to inextensional bending problems are subjected to an abnormal significant membrane strain compared with the curvature variation. The term inextensional refers to the specific condition in which membrane strains remain very low compared with the bending strains in thin type structures. As membrane stiffness is much higher than bending stiffness, this membrane strain could then lead to locking. In inextensional bending problems, some conflicts can occur between in plane and transverse strains. Extensional bending situation happens when a thin structure is affected simultaneously by both significant membrane and bending strains. In the literature, arches elements are usually preferred over shell elements to explain membrane locking phenomena as in Cook et al. (2001). Considering an arched geometry as in Figure 2.5, the tangential strain E^s at an arbitrary q point on the geometry takes the form:

$$E^s = E^m + Z \times K \tag{2.12}$$

where

$$E^m = u_{,s} + \frac{w}{R} \tag{2.13}$$

$$K = \frac{u_{,s}}{R} - w_{,ss} \tag{2.14}$$

with E^m being the membrane strain along the mid-line which depends on membrane force and K is the curvature variation which depends on bending.

As for a beam element, the membrane and transverse displacements take the form:

$$u = a_1 + a_2 \times s \tag{2.15}$$

$$w = a_3 + a_4 \times s + a_5 \times s^2 + a_6 \times s^3 \tag{2.16}$$

where $a_i, (i = 1, \ldots, 6)$ are the generalized degrees of freedom.

Introducing equations (2.15) and (2.16) into equations (2.13) and (2.14), the membrane strain and curvature variation are derived as:

$$\begin{aligned} E^m &= a_2 + \frac{1}{R} \times \left(a_3 + a_4 \times s + a_5 \times s^2 + a_6 \times s^3 \right) \\ &= \left(a_2 + \frac{1}{R} \times a_3 \right) + \frac{1}{R} \times \left(a_4 \times s + a_5 \times s^2 + a_6 \times s^3 \right) \end{aligned} \tag{2.17}$$

$$K = \left(\frac{a_2}{R} - a_5 \right) - a_6 \times s \tag{2.18}$$

In inextensional bending conditions, the membrane strain E^m is supposed to vanish which leads to the following equalities:

$$a_2 + \frac{1}{R} \times a_3 = 0 \tag{2.19}$$

$$a_4 = 0, a_5 = 0, a_6 = 0 \tag{2.20}$$

However, the above equations (2.20) cannot be verified since the coefficients a_4, a_5 and a_6 are required to define the structure kinematics. This phenomenon creates an additional membrane deformation leading to locking.

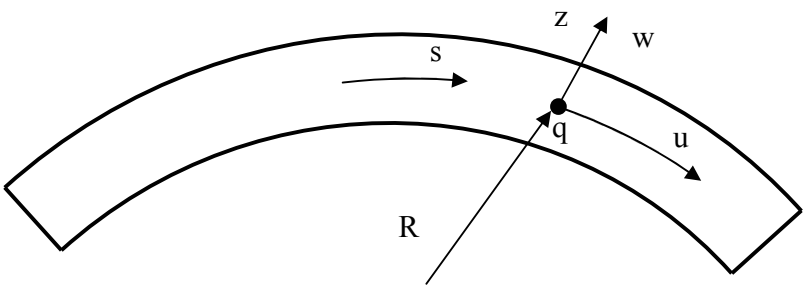

Figure 2.5: Membrane locking

2.2.4 EAS elements

Researchers have developed different models to handle the locking issues discussed above, resulting in the rise in a number of solid-shell finite element families. Two of these, the enhanced assumed strain (EAS) elements and the assumed natural strain (ANS) elements models, are particularly well suited for THF because they work well with thin structures and are computationally efficient.

The EAS method, similar to the incompatible modes theory proposed by Taylor et al. (1976) and Wilson & Ibrahimbegovic (1990), is based on assumed strain parameters. EAS elements have been extensively and successfully used to overcome locking problems. This technique, initially presented in Simo & Rifai (1990) takes its foundation in the three field Hu-Washizu variational principle and results in enriching the deformation modes of the strain field that are exposed to locking with zero energy modes. EAS elements are known to provide accurate results even with coarse mesh. A drawback of EAS elements is that they can be time consuming depending on the number of enhanced parameters employed. Moreover, EAS elements do not stay accurate with a highly distorted mesh or while dealing with thin structures. Some elements theories usually combine ANS and EAS methods to deal with persistent locking issues. The EAS method has been extended to geometrically non-linear problems by Simo & Armero (1992). The key concept of the EAS non-linear formulation results in the same additive decomposition of the Green Lagrange strain tensor $\mathbf{E}$ as for the linear case. The variational formulation of EAS element is further detailed

within the following chapters through the presentation of the new SH8RSe solid-shell element formulation.

2.2.5 ANS elements

In this method, the strain field is calculated at the boundary of the domain and then interpolated at the calculation points. The ANS method has been pioneered by Hughes & Tezduyar (1981), Macneal (1982) and Dvorkin & Bathe (1984). The mixed interpolation of tensorial components (MITC) is a similar method, initially proposed by in Dvorkin & Bathe (1984), Bathe & Dvorkin (1985). Note that unlike the EAS method, using the ANS method does not imply the use of any spurious zero energy modes. The ANS method has not been developed initially as a pure mathematical theory. Since the first contribution on the subject, it was only during the nineties that a variational formulation has been proposed in Militello & Felippa (1990a) and Militello & Felippa (1990b). However, this rationalized variational formulation of the ANS method has limitations. It is used to cure only shear locking as emphasized in Nguyen (2009). Some details on the subject are presented in the other chapters.

2.2.6 Locking correction for solid-shell elements

Section 2.2.3 details some of the most severe locking issues that may appear while using low-order solid-shell elements. An overview of the methods to solve each of these issues is provided below.

Transverse shear locking

Alves de Sousa et al. (2003) and Fontes Valente et al. (2004) have developed a solid-shell element entirely based on the EAS concept for both small and large deformation problems. They have also enriched the formulation with some bubble function displacements. The bubble function concept corresponds to assuming that the displacements field of an arbitrary point in the element is the sum of the displacements field of the classical node added with the displacements field of a fictive bubble function displacement. Bubble functions displacements do not increase the degrees of freedom and vanish on the element boundary. The element modeled with the addition of bubble function displacements have produced reliable results in various popular benchmark problems and have not presented

any transverse shear or volumetric locking. Another method to get rid of transverse shear locking is the ANS method first introduced by Hughes & Tezduyar (1981) and Dvorkin & Bathe (1984) in four node plate and shell elements. The ANS method has then been extended to solid-shell elements as in Domissy (1997) or in Hauptmann et al. (2000) who have implemented the ANS method to eradicate the transverse shear locking. Based on their results, the EAS method has provided more accurate results as compared with the ANS method while solving problems involving transverse shear locking problem. They have also used the EAS method to suppress Poisson thickness locking. Other contributions related to solving the shear locking issue are Sze & Yao (2000), and more recently Kim et al. (2005) and Hannachi (2007).

Volumetric locking

Hughes (1980) has separated the strain matrix operator $\mathbf{B}$ into a deviatoric and a dilatation parts. In their proposed B-bar approach, they have observed that an improvement $\overline{\mathbf{B}}^{dil}$ of the strain matrix operator dilatation part $\mathbf{B}^{dil}$ remains necessary when the material remains nearly incompressible or incompressible. They have then presented different options to calculate $\overline{\mathbf{B}}^{dil}$. A first method based on the reduced integration concept evaluates $\overline{\mathbf{B}}^{dil}$ at the element center while another method estimates a mean value of $\mathbf{B}$. Andelfinger & Ramm (1993) have studied the influence of the number of EAS parameters on the locking issue. They have observed that if 15 EAS parameters significantly improved the element membrane behavior, at least 21 EAS parameters have been necessary to tackle volumetric locking. However, De Souza Neto et al. (1995) have highlighted some drawbacks of the method in large compressive strain situation. More recently, an element formulation that is free of volumetric locking has been presented in Alves de Sousa et al. (2003) in small deformation problems and was extended to large deformation problems by Fontes Valente et al. (2004). Liu et al. (1998) and many other researchers like Duarte Filho & Awruch (2004), Alves de Sousa et al. (2006) and Cardoso et al. (2008) have introduced the B-bar approach to cure volumetric locking in solid-shell elements.

Poisson thickness locking

In the work of Büchter et al. (1994), one enhanced parameter has been introduced successfully to ensure a linear thickness strain without any modification of the employed

3D law. Their proposed element performed well in linear as well as in non-linear problems and even with thin structures. Following the same idea Domissy (1997), Lemosse (2000) and Hannachi (2007) have developed fully integrated implicit elements using the ANS and the EAS methods.

Curvature or trapezoidal locking

Betsch et al. (1996) have applied the ANS concept in order to overcome the trapezoidal locking. The normal strain components are calculated at the corner of the element mid-surface and then interpolated at the element integration points using the classical bilinear shape functions. This method has then been extensively used and introduced in solid type elements integration scheme as in Kim et al. (2005) and Hannachi (2007).

Membrane locking

Miehe (1998) has proposed an eight-node brick element with an enhanced parameter to overcome membrane and bending locking. They have also used the EAS method to tackle Poisson thickness locking. The ANS method has then been implemented to deal with the transverse shear as well as the trapezoidal locking. Recently, the strain smoothing concept from mesh free method, initially introduced by Chen et al. (2001), has been combined with the finite element method. From this original combination, Liu et al. (2007) and Liu et al. (2007) have developed the smoothed finite element method (SFEM). The key point of this concept is that the domain is divided in smoothing cells and the integration is set on the boundary of each of them. Nguyen-Thanh et al. (2008) have used the SFEM to deal with the membrane and the bending effects in a four-node shell element. In their contribution, Nguyen-Xuan (2008) have proposed a summary of two as well as 3D elements using the SFEM.

Reduced integration

Another technique to alleviate locking is the reduced integration. This method has initially been introduced by Zienkiewicz et al. (1971). This alternative technique consists in integrating the element using fewer points than for the fully integrated elements. However, to under integrate an element introduces zero energy modes called “hourglass modes” that need to be stabilized. Various stabilization techniques exist such as the selective integration detailed in the work of Hughes et al. (1978) and Hughes (1980). A different stabilization

technique introduced by Flanagan & Belytschko (1981), in the same inspiration as the one used in the present work, is implemented by introducing stabilization terms in the stiffness matrix. These calculated terms are then determined in a co-rotational frame in order to simplify the formulation. The SHB8PS element is a reduced integration element that uses a Hu-Washizu variational formulation. Its stabilization, based on the work of Belytschko & Bindeman (1993), avoids hourglass modes from happening. Since then, developments have been made. Among the more recognized contributions, there is Legay & Combescure (2003) in implicit or Abed-Meraim & Combescure (2002) in explicit. Abed-Meraim & Combescure (2009) have developed the expression of the stabilization matrix by projecting the gradient operator into a co-rotational sub-space. This improvement has eliminated some persistent locking encountered in the previous versions of their model and performs well for elastic as well as plastic problems with competitive time efficiency.

Other researchers have combined successfully the reduced integration and the EAS methods. As Duarte Filho & Awruch (2004) in their eight-node brick element model, Reese (2005) and then Reese (2007) have proposed a reduced integration element based on a Taylor expansion of the first Piola-Kirchhoff stress tensor with only three enhanced parameters to avoid the thickness locking. Their proposed element remains competitive for a large range of problems even with distorted elements. However, in bending dominated problems at least two elements are required through the thickness. If this element is indeed a good alternative to a shell element, it does not remain competitive in case of extremely thin structures. The actualization of the stabilization matrix for explicit problems is also subject to investigation due to the high number of time step increments. In the same idea Alves de Sousa et al. (2005) and Alves de Sousa et al. (2006) have developed the RESS element coupling reduced integration and EAS method. This element offers the option to use several integration points through the thickness and stays time efficient. Shear hourglass modes can also occur in non-linear applications, since the employed stabilization does not include the shear aspect. Afterwards, Alves de Sousa et al. (2007) have successfully evaluated the RESS element in forming process of sheet metal forming using 3D plastic behavior laws. Moreover, Cardoso et al. (2008) have improved this last element incorporating the ANS method to increase transverse shear efficiency and called it M-RESS. More recently Schwarze & Reese (2009) and Schwarze & Reese (2011) have

developed a new solid-shell element inspired by the work of Reese (2007). Among the upgrades of this new formulation, there is the use of the ANS technique to tackle shear locking and trapezoidal effect. To do so, they adopted an enriched ANS concept which considers not only the element mid-surface, but also two other mid-surfaces normal to the two remaining principal directions as presented in Chapter 5. The proposed improved formulation remains time efficient and exhibits a better hourglass stabilization.

2.3. Conclusion and scientific approach

Even though the tube hydroforming process is used in various industrial activities, our knowledge on this process still needs some improvements to take advantage of its potential. Because of the complexity that may exist around this process implementation, the finite element method is a well appreciated numerical tool which helps saving time and money. Shell finite elements with plane stress hypothesis remain very popular to simulate THF process due to their robustness and time efficiency. However, these elements cannot be used to simulate FLD based on a 3D stress state, which is essential in order to detect possible defect occurrences like necking or bursting, due to the plane stress hypothesis. Another limitation is, for some elements, a sensitivity to mesh distortion. The development of more suitable elements then appeared to be an important issue. Moreover, the influence of material history is not generally considered in the process. This last observation may then induce some inaccuracy in the finite element method regarding experimental data while simulating a hydroformed part in in-service conditions. The development of a new methodology that considers material history during a tube hydroforming process and then which considers the impact of subsequent plastification in the material properties of the fabricated part would then be useful for the industry.

As seen above, several problems still exist while developing parts fabricated by tube hydroforming. In light of this literature review, this thesis is characterized by:

- The development of a new helicopter skid landing gear cross tube fabricated by tube hydroforming considering material history from the straight tube to hard landing conditions simulations.

- A variational formulation using the recent smoothing technique for an eight-node resultant solid-shell element.

- A variational formulation of an eight-node reduced integration solid-shell element compatible with a wide range of classical 3D constitutive laws and efficient while dealing with thick as well as with thin geometries.

- The application of this element in the THF context.

Chapter 3. Hydroformable skid landing gear cross tube design investigation and rotorcraft crashworthiness

Chapter 3 develops a methodology to simulate the tube hydroforming process in the aerospace context using the commercial software ABAQUS/Explicit. As an example, a skid landing gear cross tube is virtually fabricated in multiple steps process and aged. The cross tube has been specifically redesigned to allow its fabrication by tube hydroforming. The landing gear equipped with this new cross tube is then tested in various hard landing configurations in compliance with the Federal Aviation Regulations requirements. The hydroforming process is less polluting than the chemical milling usually used to fabricate the standard cross tube design. The proposed hydroformable cross tube offers capabilities comparable, in hard landing simulations, to those exhibited by the standard one but with a reduced weight. Another important contribution is the successful development of a methodology that takes into account material history of the hydroformed cross tube in the final hard landing simulations. This methodology includes implicit and explicit simulations. The additional benefit of having a non-linear solid-shell element efficient in tube hydroforming process as well as in hard landing contexts and which provides accurate results in a competitive amount of time has then arisen.

3.1. Introduction: statement of the problem to be solved

Currently, the studied light helicopter model standard landing gear cross tube is manufactured by bending a tube with a circular cross section, which is followed by chemical milling to obtain a tube with variable thickness so as to reduce its weight. The main drawbacks of this process are the cost, the cycle time and the use of chemical contaminants. New environmental regulations are strongly driven toward a greener and less material consuming process. The authors of the present work believe that tube hydroforming (THF) could be this process. Currently THF process is being used successfully in the automotive industry for several advantages over conventional manufacturing processes including: i) part consolidation; ii) weight reduction; iii) improved structural stiffness; iv) lower tooling cost; v) fewer secondary operations; and vi) tight dimensional tolerances. Some of its disadvantages include slow design cycle time and

expensive equipment. The novelty of the THF technology compared with conventional metal forming processes represents another drawback as the existing knowledge base for process and tool design is insufficient. Hence, there is a growing need for enhanced expertise that would satisfy industrial needs and establish systematic approaches in this area. This last observation is even more applicable to the aerospace industry which remains less familiar with such technology and is willing to explore its potential benefits.

It is usually necessary to perform some pre-forming operations like tube bending before actual THF. However, such multi-steps fabrication processes often induce significant impacts in the final part properties. Trana (2002) has contributed in our understanding of the impact of residual stresses induced by pre-forming steps on tube formability during THF process. As a consequence, the new cross tube design fabricated by tube hydroforming examined in the present work, considers its fabrication history in the subsequent hard landing simulations.

Dutton et al. (1999) have studied a methodology to account for thickness changes and strain hardening in a car component generated within a forming analysis. They have followed the analysis with a crashworthiness simulation involving the fabricated component. Both forming and crash simulation have been performed with Ls-Dyna, taking advantage of its ability to transfer data from one model to another. Similarly, Lee et al. (2001) have performed the sheet metal forming simulation of an automotive part on the simulation software Es-form and the crash simulations on Ls-Dyna. The proposed methodology to transfer the current state after forming at the beginning of the crash simulation has been successfully performed with a limited amount of errors. A similar approach has been performed by Kim et al. (2003) who studied the effect of material history on a car component behavior, fabricated by sheet metal forming within crash test simulations. More recently, Oliveira et al. (2006) have studied the effect of tube bending process on a crash test of an s-rail structure. An initial aluminum alloy EN-AW5018 straight tube has been bent in two locations with a mandrel-rotary draw bending device and the obtained part has then been tested in an impact test. Besides, the researchers have performed the corresponding numerical models on the explicit code Ls-Dyna within the following sequence: i) first bent in explicit; ii) springback after first bent in implicit; iii) second bent

in explicit; iv) springback after second bent in implicit and crashworthiness in explicit. They have meshed the tube with the four node reduced integration Belytschko-Lin-Tsay Belytschko et al. (1984) and a fully integrated shell elements and have kept the mesh deformation, the stress as well as the plastic strain level from one step to another. Interestingly, they observed that ignoring these two changes in the following tube crush tests could lead to underestimating the energy absorption and the peak force up to 30%. Further details on this issue are given in Grantab (2006). Moreover, Oliveira et al. (2007) have examined the influence of tube bending on subsequent THF process. They observed that the pre-bending of a tube in aluminum alloy EN-AW5018 could induce some thinning and consume part of the material ductility. As a consequence, this last point reduces in the same time the hydroformability of the bent tube in the subsequent THF process. Interestingly, they also revealed that a bending boost could reduce these effects. Williams et al. (2007) have proceeded to dynamic crush tests of hydroformed tubes in aluminum alloys using the explicit code Ls-Dyna. They have emphasized the necessity to account for thickness changes as well as plastification, which could occur within the forming operations in the subsequent crash simulations. Other authors like Grolleau et al. (2008) have emphasized the necessity of considering material history from metal forming in impact simulations.

When a new skid landing gear is developed, the finite element method is well exploited to rapidly verify its potential in hard landing conditions. However, there is little information available in the literature on the subject. In Bianchi et al. (2001), the hard landing conditions simulations have been made with an assembly of rigid elements with the explicit finite element software Adams. Each cross tube has been divided into eight main parts, connected together with a rotational degree of freedom and a rotational spring. Each of those eight parts has also been divided into two parts linked together with a translational degree of freedom and a translational spring. However, it appeared that these models were not accurate enough in the non-linear range. More recently, Cheng-Ho et al. (2003) have developed a complete methodology to simulate skid landing gear hard landings and have compared simulation results with experimental data in various configurations. Their models, meshed with hollow rectangular beam elements on the explicit finite element software Ls-Dyna, gave results consistent with experimental data with competitive time

efficiency. Shrotri (2008) has tested hard landing performances of a skid landing gear using composite materials. The employed element to mesh cross tube was the four-node reduced integration shell element of the finite element software ABAQUS. To our knowledge, Élie-Dit-Cosaque et al. (2009a) were the first to initiate a methodology which considered material history in a helicopter skid landing gear. They then emphasized the effect of a multi-steps bending process to fabricate a helicopter skid landing gear cross tube on its final specifications. They used the eight-node solid-shell element SC8R of the finite element software ABAQUS to mesh their models.

In summary, regarding the above introduction, the following points could be highlighted:

- Forming process like sheet metal forming, bending or THF process could induce wall thickness variation of the fabricated part as well as material properties changes.
- Numerical methodologies that consider material history from forming to crashworthiness simulation exist and remain necessary to provide an acceptable simulation level of accuracy.
- A variety of models can be employed to simulate skid landing gear hard landing.

However, it emerges that some other issues still require some further development:

- Improving our knowledge on THF process using aerospace material.
- Accounting for material condition change required between forming and hard landing simulations.

This chapter has multiple objectives. A new design of the light helicopter model forward cross tube has been developed in order to come up with a hydroformable tube with acceptable properties, similar to those of the standard design produced by chemical milling. A first objective of the present work is to propose a methodology to determine, in the early stages of development, the validity of the design of a new skid landing gear in term of structural behavior. The characteristics of the new design are checked and compared with those of the standard one. A second objective is to develop and implement a methodology

that considers material history similar to Élie-Dit-Cosaque et al (2009a). The key point here remains in the addition of a virtual ageing. This provides to the hydroformed cross tube material properties which depend on the plastification level after fabrication.

The outline of this chapter is as follows. Section 3.1 introduces this study's context. Section 3.2 gives an overview of the hydroformed cross tube design. The employed methodology to simulate multi-steps fabrication process is presented in sections 3.3 and 3.4 as well as some key details on the proposed THF process simulation models and related results. Section 3.5 then details simulation models for skid landing gear hard landing conditions simulations. In-service capabilities of a landing gear equipped with the hydroformable forward cross tube are compared with those of a landing gear equipped with the standard forward cross tube in four hard landing configurations from FAR § 27.725 (1965).

3.2. Preliminary product design for THF

3.2.1 Problematic: Manufacturability study of existing model

The geometry of the skid landing gear studied in this work is presented in Figure 3.1. Two skids provide contact with the ground, forward and aft cross tube absorb the energy during hard landing. Some skid attachments link skids and cross tubes together. The fuselage attachments link the forward and aft cross tubes to the helicopter fuselage. Even if their designs are simplified, these attachments offer comparable capabilities during hard landing simulations compared with the standard ones. The forward cross tube, in particular, is realized with a multi-steps fabrication process. First, a tube with an exterior diameter of 57.15 mm and a wall thickness of 8.128 mm is bent. Then the tube wall thickness is progressively reduced by chemical milling from 8.128 mm at the center to 3.81 mm near its ends respectively from "a" to "b" as illustrated on Figure 3.2. However, the cross tube extremities keep the same exterior diameter and wall thickness as for the initial tube from "b" to "c" allowing its assembly on the skid landing gear. One of the objectives of the CRIAQ 4.6 project is to investigate the forward cross tube feasibility using THF process. Nevertheless, the standard design could hardly be hydroformed because of its large wall thickness variation. Moreover, the sudden wall thickness variation at cross tube extremities in "b" remains to our knowledge unfeasible with THF process. An entire redesign of the forward cross tube appears necessary to ease the fabrication by THF. The THF process

itself has the potential to improve the skid landing gear characteristics. A good knowledge of the standard forward cross tube is essential. The employed numerical methodology presented in Élie-Dit-Cosaque et al. (2008) and further emphasized in Blanchet-Létourneau (2010) consisted in loading the standard cross tube with similar maximum loads as during drop test to obtain maximum stress and displacement values. New models with some hydroformable designs using various optimization parameter values have been implemented with the objective to get analogous results as for the standard reference results.

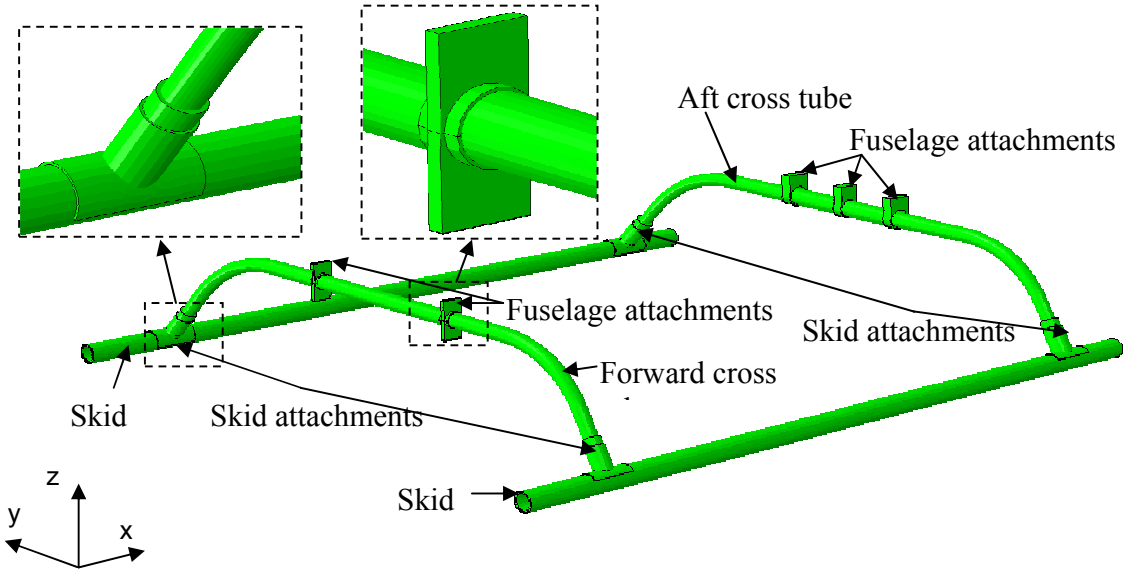

Figure 3.1: Standard skid landing gear geometry

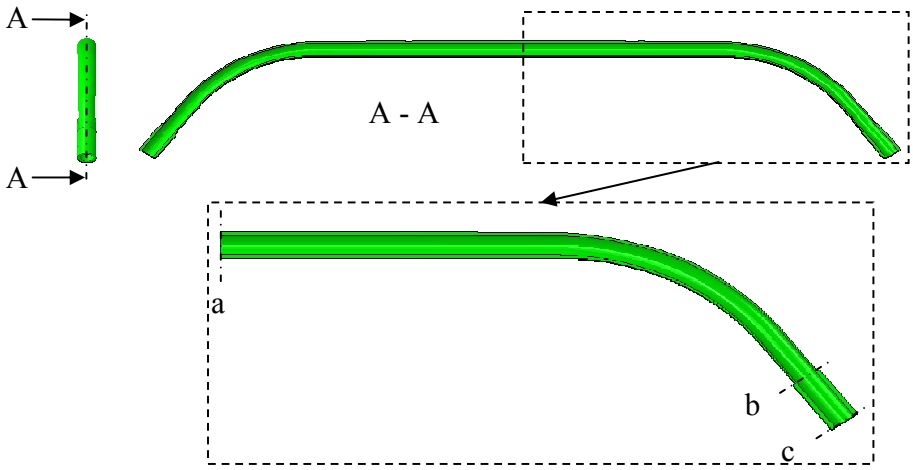

Figure 3.2: Standard forward cross tube geometry

3.2.2 New design process and objectives

It should have been possible to fabricate the new cross tube design presented in this work by bending metallic aluminum sheets and welding. However, this choice would have introduced some weakness along the weld seam, possibly critical in hard landing conditions as those studied below. Fabricating the new design by THF from an extruded tube has appeared to be a relevant solution since it avoids introducing weld seam. The chosen optimization parameters of the hydroformable cross tube design are the wall thickness, the weight, the energy absorption, the stress field distribution and the strain field distribution. One has to note that it remains possible to get a hydroformable cross tube with variable thickness using initial variable thickness straight tubes for THF process. However, a tube with constant wall thickness is chosen for the new design to reduce the number of forming operations. A constant cross section perimeter is then required along the cross tube to avoid possible thinning or thickening due to the tube expansion inside the THF dies.

Importantly, in the aerospace industry, weight is a fundamental parameter. Hence, changing a standard design with a lighter one, may provide notable advantages. That is why one of the goals of this study is to create a new cross tube design at least 15 % lighter than the standard one. Moreover, in case of hard landing, the forward cross tube deforms and

absorbs a part of the energy by plastification. The new design had to absorb a similar amount of energy as the standard one. The stress distribution had then to be as smooth as possible to avoid creating some local effects in the structure. This last point induced smooth section changes along the tube. After choosing the optimization parameters, it was essential to determine the cross tube dimensions allowed or not allowed to change according to BHTC specifications in order to ensure that the new design could be assembled with the other existing parts of the skid landing gear. The dimensions not allowed to change from standard to hydroformable design were L which is half of the distance between skids, H which directly impact the distance between the belly and the ground and L_c which indicates the fuselage attachments position. The region between fuselage attachments remains essential in case of hard landing because it absorbs the major part of energy by plastification. These parameters are illustrated in Figure 3.3 and further detailed in Blanchet-Létourneau (2010).

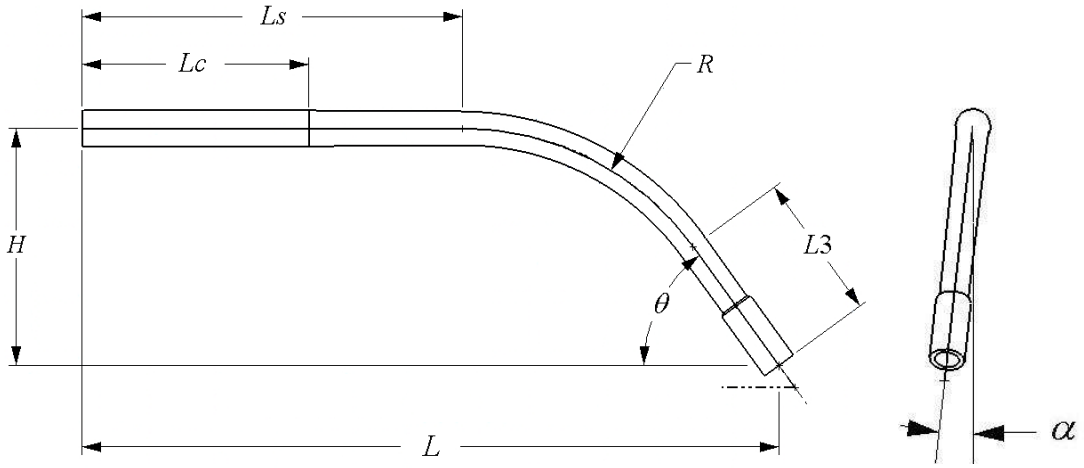

Figure 3.3: Standard forward cross tube dimensions Blanchet-Létourneau (2010)

3.2.3 New Section properties

The kind of section adopted for the new cross tube is a square like section with a constant thickness. The initial extruded tube used for the new cross tube design is thinner than the initial tube used to fabricate the standard cross tube one, and this, exhibiting a larger diameter. These new characteristics have been chosen in order to lower the forming

pressure necessary to hydroform the new design. Howard et al. (2002) observed in their work that using a non-symmetric cross tube cross section geometry or a non-symmetric cross tube cross section material could have the advantage of decoupling the effective vertical stiffness from the effective longitudinal stiffness. These stiffnesses can then be modified independently by modifying the cross tube cross sections.

In the present work, a non- symmetric cross tube cross section material could be expected depending on the level of plasticity accumulated during manufacturing. Eleven variable rectangular like sections were used along the neutral fiber of half of the cross tube to provide to the new cross tube a smooth geometry (twenty two along the whole neutral fiber). The modifiable parameters of the new sections presented in Figure 3.4 are h_i, b_i, r_i and t where $i = 1,\ldots,11$ represents sections number.

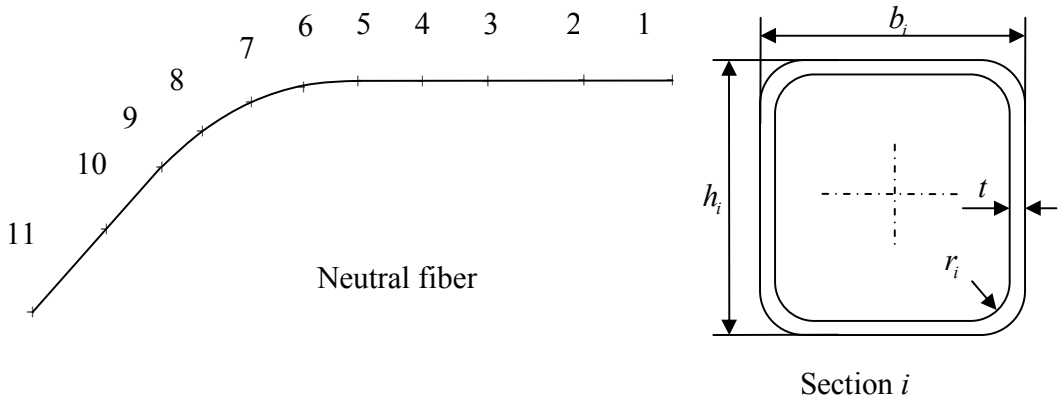

Figure 3.4: Hydroformable cross tube section shape Blanchet-Létourneau (2010)

An optimization process detailed in Blanchet-Létourneau (2010) based on an intern application developed by Professor Michel Guillot of Laval University consisted in finding, in the elastic range, the section dimensions that guarantee in each of them a stress level under the allowed maximum values for various loading cases. This optimization process is briefly recalled below:

First, an elastic static model analysis has been performed with the standard cross tube design as illustrated in Figure 3.5. Due to the symmetry of the model, at point O, only half

of it has been considered. Some forward and vertical displacements limitations have been used at point A to represent the fuselage attachments resistance. F_v, F_S and F_D represent the forces applied at point B in agreement with the specifications. The maximum Von Mises equivalent stress has then been observed at the positions of the eleven section planes shown in Figure 3.4. These stresses have then been considered as the allowable stress level that must not be exceeded for each section of the hydroformable design.

In the present work, the eleven sections have adopted a similar square shape with a constant wall thickness which facilitates the THF step. Second, the inertias of these sections have been calculated analytically together with the Von Mises equivalent stress.

Third, the dimensions of each section have been optimized by making sure that the related Von Mises equivalent stress stays below the allowable stress level. Among the constraint parameters of the sections design, the area of each section remains unchanged and the radius in each section remains under 12.7 mm.

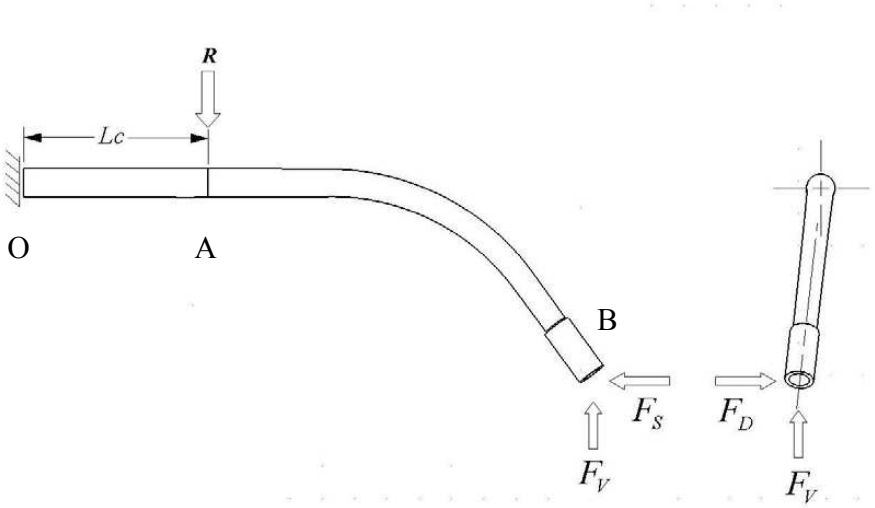

Figure 3.5: Simplified elastic static model with the standard design, Blanchet-Létourneau (2010)

The hydroformable design after optimization presented in Figure 3.6(a) adopts the dimensions detailed in Table 3.1 and Table 3.2. This new design is then approximately 30% lighter than the standard one. The analytical validations performed in Blanchet-Létourneau (2010) have shown a good stress distribution along the cross tube compared with the standard design with comparable stress levels. The numerical validation in plastic range has been performed in various hard landing configurations as presented in section 3.5.

Besides, the present fuselage and skid attachments also needed to be modified to fit the hydroformable cross tube. Some basic fuselage attachments are then developed for numerical models with appropriate specifications as shown in Figure 3.6(b). Among the main ones the fuselage attachments needed to maintain the forward cross tube but letting it free to rotate around x – axis (See Figure 3.1 for axis definition). Its central part is then able to absorb some energy dissipated during hard landing conditions by plastification.

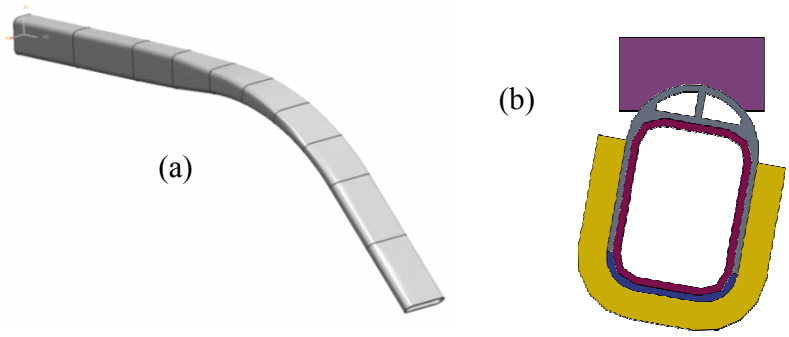

Figure 3.6: (a) Half hydroformable cross tube Élie-Dit-Cosaque et al. (2008), (b) fuselage attachments Élie-Dit-Cosaque et al. (2009b)

i	h_i (mm)	r_i (mm)	b_i (mm)
1	76.2	12.7	54.41
2	76.2	12.7	54.41
3	76.2	12.7	54.41
4	71.1	12.7	54.41
5	50.8	12.7	79.81
6	40.6	12.7	89.97
7	33.0	12.7	97.59
8	25.4	12.7	105.21
9	25.4	12.7	105.21
10	25.4	12.7	105.21
11	25.4	12.7	105.21

Table 3.1: Sections dimensions

Parameters	Values
θ (degrees)	48
α (degrees)	10
L (mm)	1118
Ls (mm)	567
L3 (mm)	298
R (mm)	470
H (mm)	377

Table 3.2: Neutral fiber dimensions

The following sections 3.3 and 3.4 detail the multi-steps forming process simulation of the new design by bending and THF. Section 3.5 then presents the obtained results of hard landing simulations with the skid landing gear equipped with the hydroformable forward cross tube.

3.3. Bending

3.3.1 Bending steps description

At the beginning of the fabrication process, the tube is straight with a circular section. Nevertheless, it is necessary to bend the tube in order to be able to position it between the hydroforming press dies. The bending machine that has been considered for this work is a ram bending machine as shown in Figure 3.7(a).

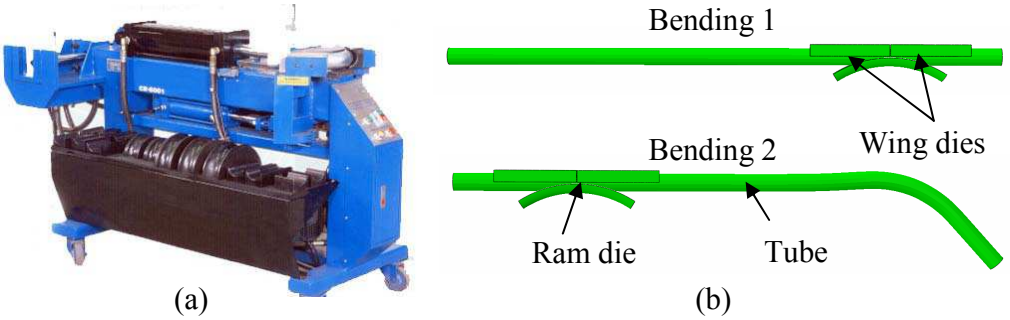

Figure 3.7: (a) Ram bending machine, (b) Ram bending models

This machine includes three main parts: one actuator set up with a ram die on the top and two wing dies. During the bending process, the tube is placed between the wing dies and the ram die perpendicular to the actuator extension direction. The internal shapes of the dies have a circular section that closely fit the exterior shape of the tube. When the actuator is activated, the ram die translates and forces the tube between the wing dies. In the same time, the wing dies rotate around their axis and a mechanism creates on them an opposite force to the movement which guarantees a permanent contact with the tube. As the tube needs to be bent in two different locations, two sequential bendings are made, both of them followed by a springback step. The two bending runs are implemented in explicit and the two springback runs in implicit. It remains necessary to drive the actuator translation with an appropriate value that provides to the bent tube a correct angle after springback regarding the THF dies. The sequence of the tube bending simulation is detailed in Figure 3.8.

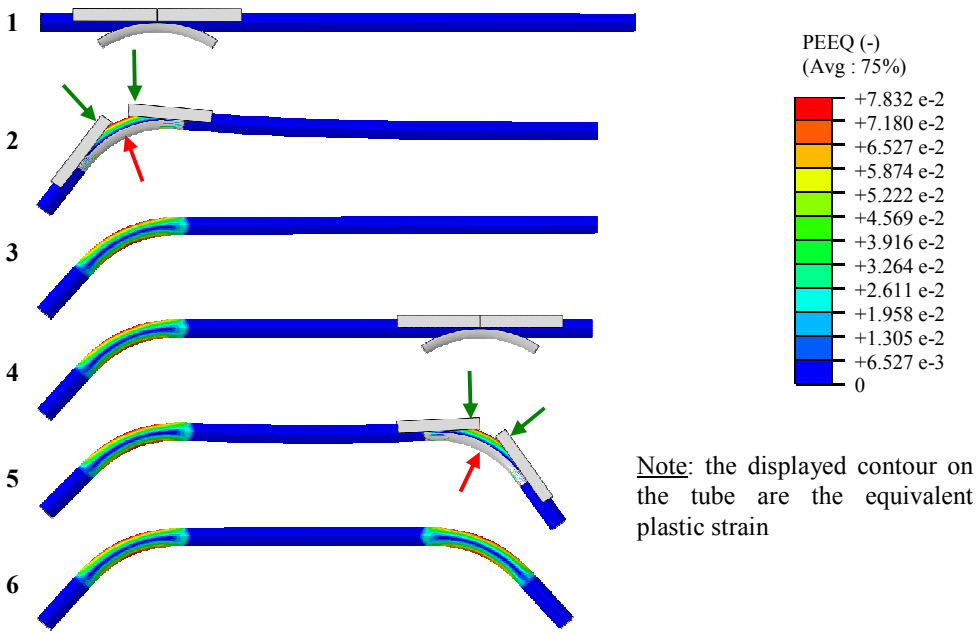

1. The initial straight tube is placed between the bending dies before the first bending.
2. The ram die moves forward, forcing the tube against the wing dies. (First bending in explicit).
3. The dies are removed allowing the first springback. (First springback, in implicit).
4. The bent tube is placed between the bending dies before the second bending.
5. The ram die moves forward, forcing the tube against the wing dies. (Second bending in explicit).
6. The dies are removed allowing the second springback. (Second springback, in implicit).

Figure 3.8: Bending sequence

3.3.2 Bending model description

The initial straight tube dimensions were: a length of 2.52 m, a diameter of 76,2 mm and a thickness of 3,18 mm. It is meshed with the ABAQUS reduced integration solid element, the C3D8R. The elements size is chosen to insure at least two elements in the radii of each section while keeping an aspect ratio below 1/10. A convergence study has proven that two layers of elements in the thickness direction are sufficient enough to provide acceptable results accuracy as presented in Table 3.3. However, in this study, the tube was meshed with three elements layers in the thickness direction since it remains the minimum number of elements layers in the thickness direction that provides acceptable results in hard landing simulations.

Number of elements in the thickness direction	Normalized max plastic dissipation
1	-
2	1
3	0.9982
4	0.9997

Table 3.3: Bending: convergence study

The tube is made of aluminum alloy AA7075-W (solution heat treated and quenched) with a density of $\rho = 2823\, kg/m^3$, a Young's modulus of $E = 74531$ Mpa a Poisson's ratio of $\nu = 0.3$ and a yield stress of $\sigma_y = 446\, Mpa$. Its elastoplastic properties, determined by Dr. Julie Levesque Research Associate at Laval University, are shown in Table 3.4.

Aluminum alloy 7075-W			
True stresses (Mpa)	True strains	True stresses (Mpa)	True strains
445.93	0	501.10	0.02
446.23	0.0001	525.18	0.03
446.53	0.0002	547.19	0.04
446.83	0.0003	567.30	0.05
447.13	0.0004	585.68	0.06
447.43	0.0005	602.49	0.07
447.73	0.0006	617.84	0.08
448.03	0.0007	631.88	0.09
448.33	0.0008	644.71	0.1
448.63	0.0009	656.43	0.11
448.93	0.001	667.15	0.12
451.90	0.002	676.94	0.13
454.85	0.003	685.89	0.14
457.77	0.004	694.07	0.15
460.66	0.005	701.55	0.16
463.53	0.006	708.38	0.17
466.38	0.007	714.63	0.18
469.19	0.008	720.34	0.19
471.98	0.009	725.56	0.2
474.75	0.01		

Table 3.4: Aluminum alloy 7075-W material properties

As material history is considered, the first bent area is already plastified at the beginning of the second bending sequence (see in Figure 3.7(b)). Ram die and wing dies are considered rigid and meshed with R3D4 ABAQUS rigid elements.

In term of boundary conditions, the ram die has a translation of 109.95 mm and the wing dies are only able to rotate around they axis of rotation. A force of 117.88 N opposite to the movement is applied on each wing dies. A *surface to surface penalty contact is applied for every contact areas with a friction coefficient of 0.05 which supposes the use of a dry lubricant. During springback simulation, no force is applied and only one node is fixed to avoid rigid body's motion.

3.3.3 Bending numerical results

The bending sequence needs to consider springback in order to give a final angle α to the bent part well-suited to the THF dies. Figure 3.9 is the deformed tube shape after bending process. With a shorter angle it would not have been possible to place the bent tube in the THF dies. On the contrary, it would not have been possible to close the THF dies with a larger angle. This emphasizes the necessity to consider springback in forming simulation.

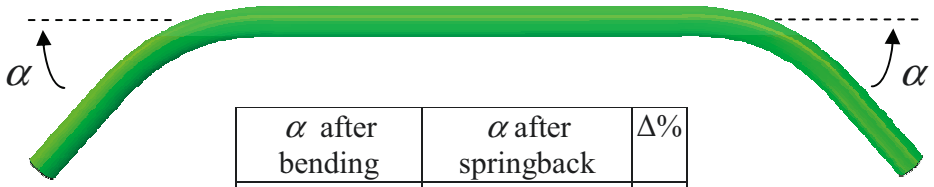

α after bending	α after springback	Δ%
52.6º	47.8 º	10

Figure 3.9: Deformed shape after bending operation

Moreover, as emphasized in Chapter 1, bending process could induce some thickness changes. Hence, the implemented models predict some thickness variations fully located in the bent area as illustrated in Figure 3.10. In order to verify this last point, the thickness is checked on two paths along the tube. Path 1 is outside the bend along the tensile area and path 2 is inside the bend along the compressive area. It appears that thickness decreases on path 1 down to -3.8% and increases on path 2 up to 5.96%.

Figure 3.11 to Figure 3.15 present the stress and plastic strain distributions on the tube at different steps of the bending process. The maximum Von Mises equivalent stresses level drops from approximately 608 MPa after the first or after the second bending to 329 MPa after the first or after the second springback. It also appears on Figure 3.11 and Figure 3.12 that the region far from the bent area recovers its straight geometry after springback. A similar observation can be made while observing Figure 3.13 and Figure 3.14. A reason for this is that the plastification occurs mainly in the bent area as shown in Figure 3.15. Note that the maximum of equivalent plastic strain (PEEQ) is 7.83 % and remains located in the tensile zone of the bent area.

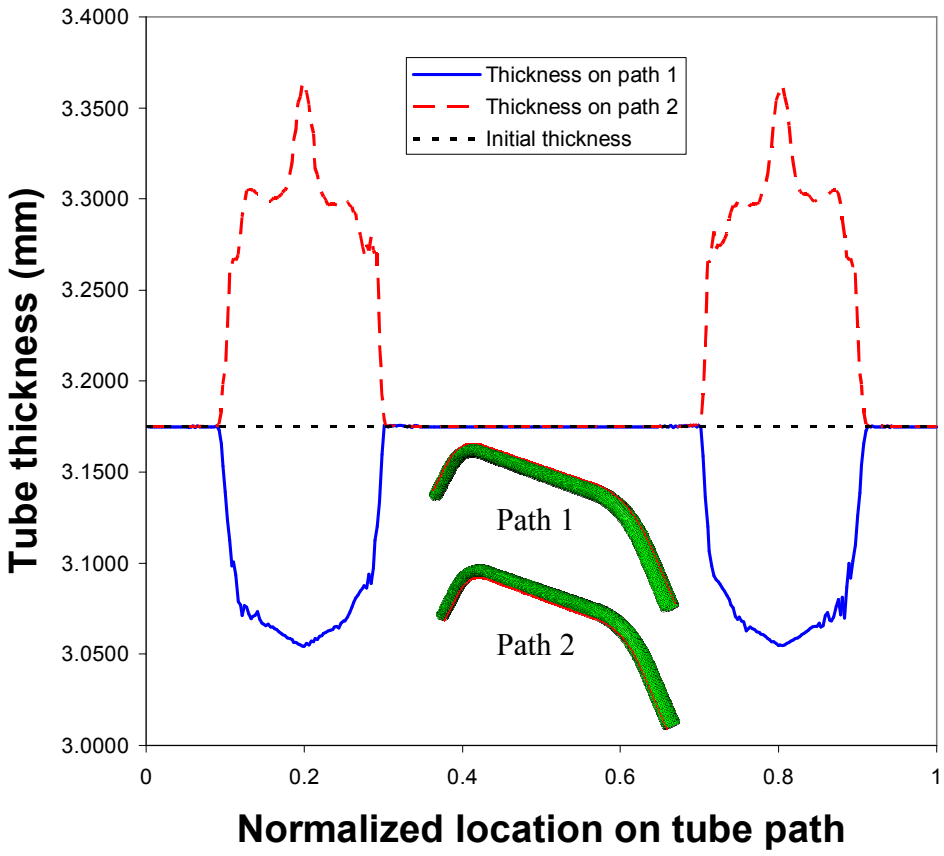

Figure 3.10: Tube thickness along path after bending

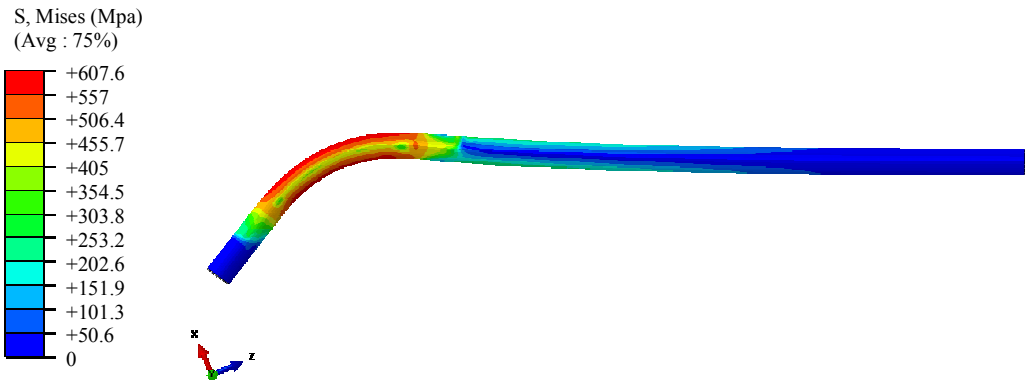

Figure 3.11: Equivalent Von Mises stresses distribution before first springback

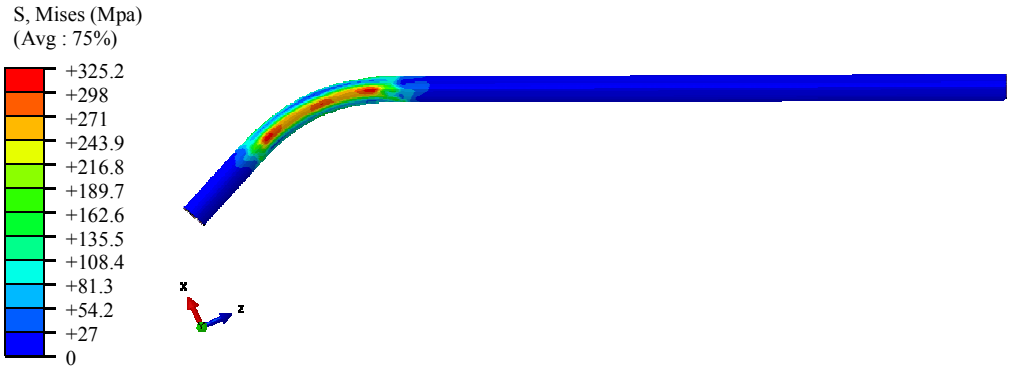

Figure 3.12: Equivalent Von Mises stresses distribution after first springback

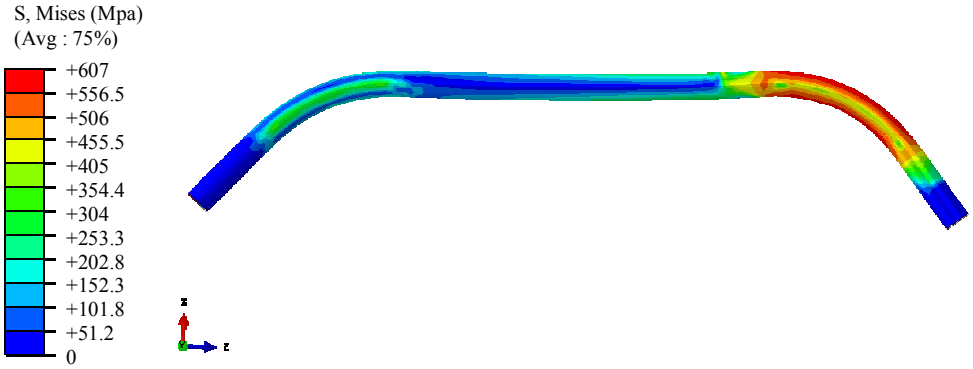

Figure 3.13: Equivalent Von Mises stresses distribution before second springback

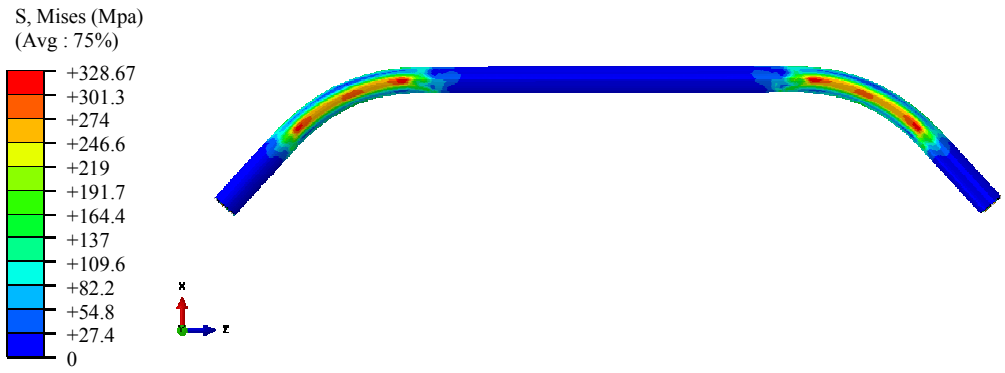

Figure 3.14: Equivalent Von Mises stresses distribution after second springback

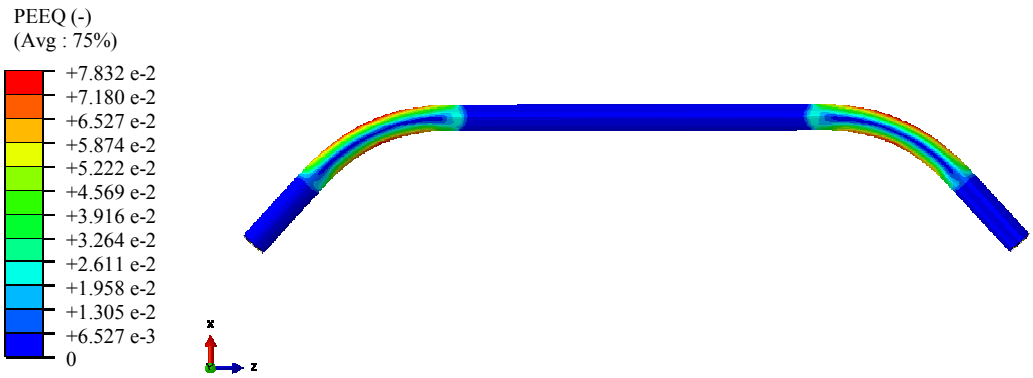

Figure 3.15: Equivalent plastic strains distribution after second springback

The final tube geometry after the bending process simulations yields in a tube with two bent areas. The geometry has a variable thickness since a thinning can be observed in the tensile zone and a thickening can be observed in the compressive zone of these bent areas. The plastification has occurred within these bent areas and some residual stresses are still present even after the second springback. This part is the one used in the subsequent THF process simulation in order to fabricate numerically the hydroformable forward cross tube.

3.4. THF

3.4.1 THF steps description

The bent tube obtained by tube bending simulation discussed above is used at the input of the THF process. The material history as well as the obtained geometry are kept. This geometry offers proper angle that matches with the dies used in the THF process.

Figure 3.16 presents the THF sequence used in this work. The bent tube is positioned between the THF dies. Then, the central part of the die is closed by translation. As a consequence, the tube is crushed from a circular to a round rectangular section. After that, the two lateral areas of the tube are crushed from a circular to a flat section. Once entirely closed, the pressure is increased inside the tube forcing it to take the shape of the inner part of the dies. As the springback effect is not considered in the die design geometry presented in this work, the THF simulation described below is not followed by a springback step.

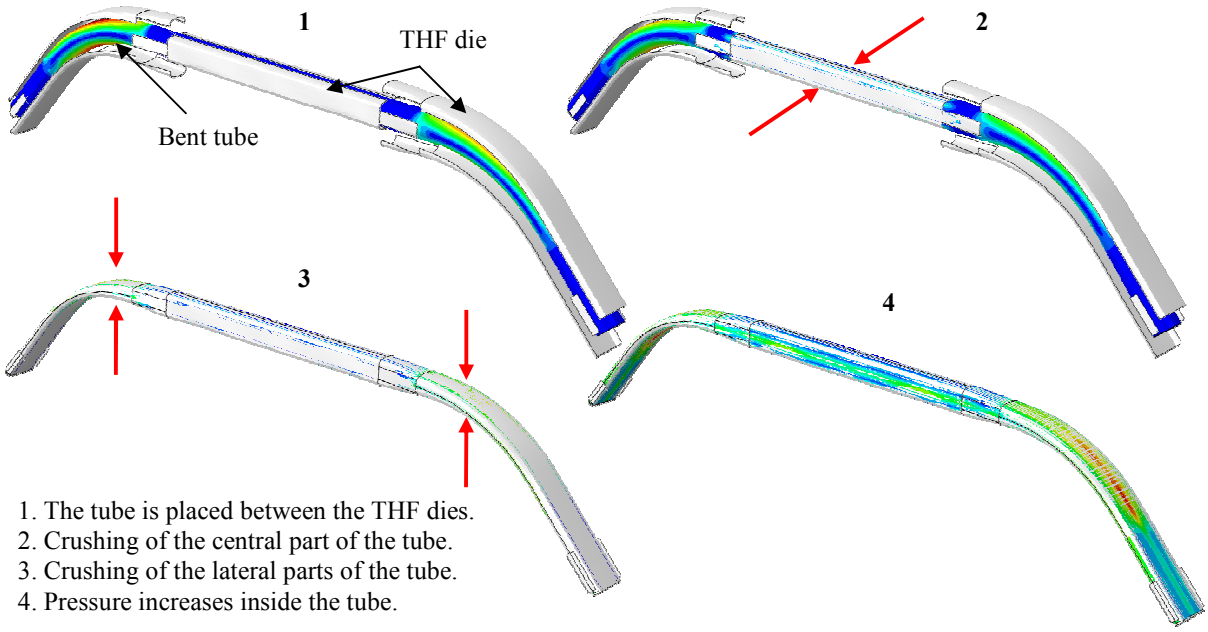

Figure 3.16: THF sequence

3.4.2 THF process model description

In the present case, the geometry after THF and before springback is used. The bent tube is placed between the THF dies with the same geometry, mesh and material properties as after the springback which occurs after the second bending. The elastoplastic properties of the part are those of the aluminum alloy 7075 in "W" condition presented in Table 3.4 with the added plastification from the bending sequence. The THF dies includes six parts, all of them considered rigid and meshed with R3D4 rigid elements. A *general contact with a friction coefficient of 0.05 is applied for every contact areas. The THF process, presented in Figure 3.16, consists of two crushing followed by a linear pressure increase inside the tube with a maximum value of 206.8 MPa, sufficient enough to fill the THF dies cavity.

3.4.3 THF numerical results

Figure 3.17(a) presents the deformed geometry of the tube after hydroforming and Figure 3.17 (b) presents half of its geometry with some cross sections shapes.

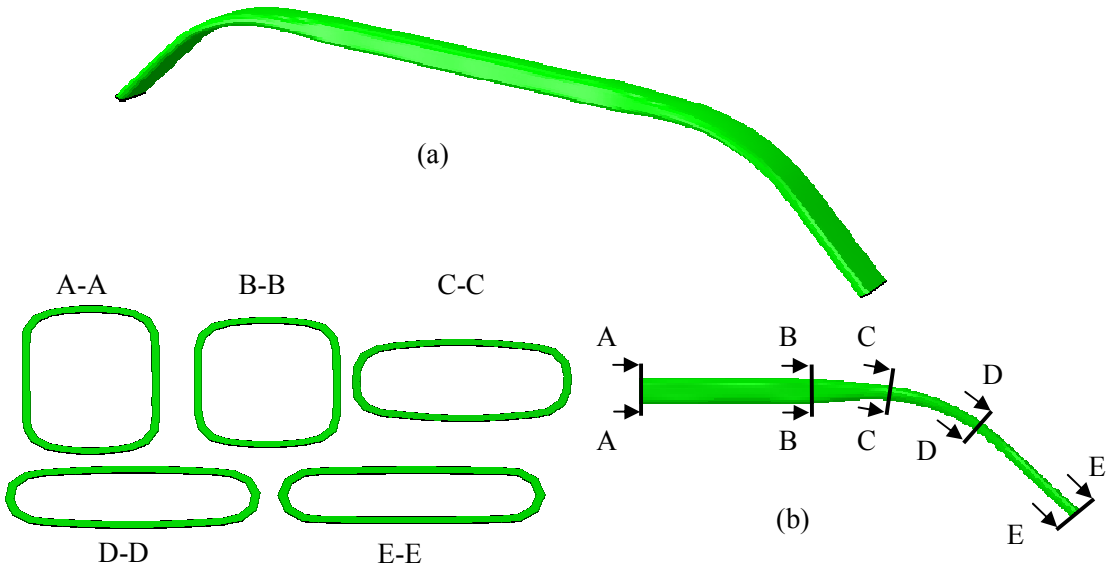

Figure 3.17: (a) Deformed shape and (b) cross section shapes after THF operation

It appears that the tube wall thickness does not remain constant along the tube after bending and THF processes. Figure 3.18 illustrates this last observation by showing the tube thickness along the same paths as in Figure 3.10. Tube thicknesses after bending and after THF process are then plotted on the same graph. Between these two fabrication steps, the

major trends in term of thickness variations are: i) an important drop of the wall thickness in the compressive area; ii) a moderate increase of the wall thickness in the tensile area; and iii) a thickness decrease in the central part of the tube. This diversity of thickness variations could be due to the accumulated plastic strain as well as the severity of the crushing and the THF steps.

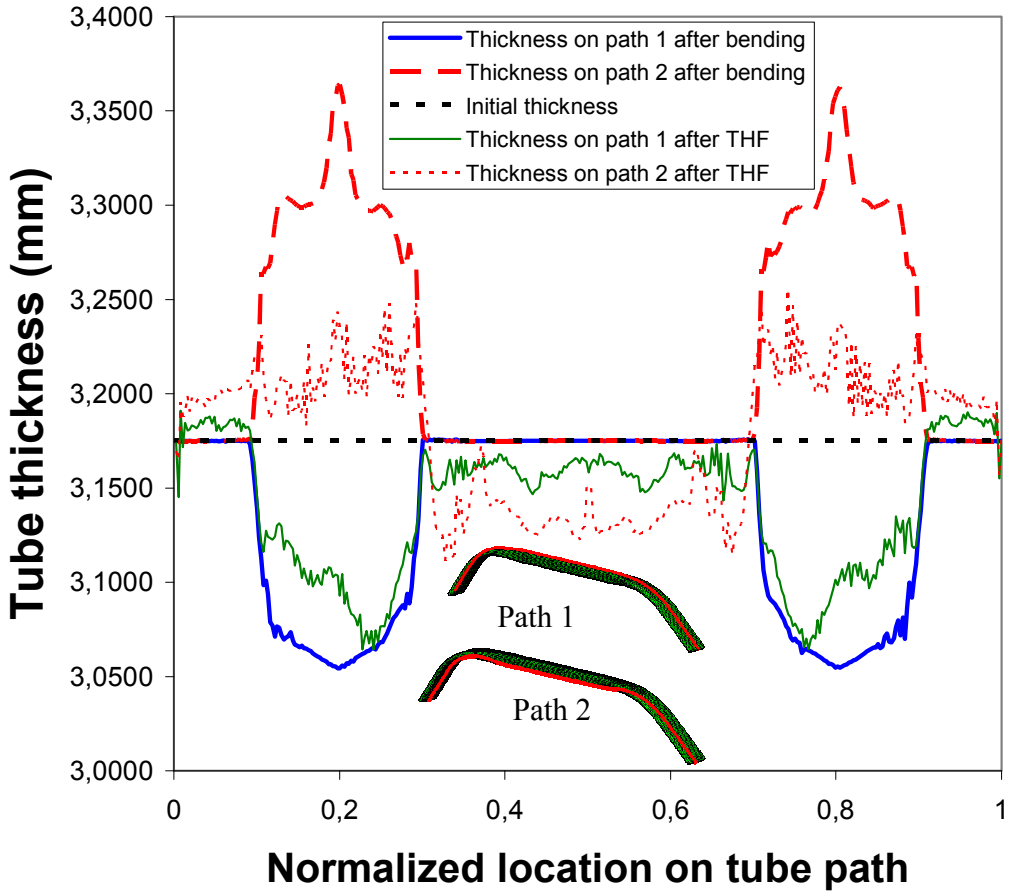

Figure 3.18: Tube thickness along path after THF

The maximum of equivalent plastic strain 14.8 % is located in the tensile area of the bend. Figure 3.19 to Figure 3.26 present the stress and plastic strain distributions on the tube at different steps of the THF process. Due to the apparent symmetry of the model, only half of the tube is presented on these figures. It appears that the two crushing operations induce a non negligible equivalent plastic strain within the tube. The maximum equivalent plastic

strain is 7.8% after bending, 9.6% after the first crushing in the center part of the tube and 14.75% after the second crushing in the bent area as illustrated respectively in Figure 3.20, Figure 3.22 and Figure 3.24. The maximum equivalent plastic strain remains similar before and after the pressure increase inside the tube as shown in Figure 3.26. As the tube circumference remains the same during the process, the tube deformation remains limited. Figure 3.26 also highlights the plastification level throughout the tube after hydroforming as this should be considered in subsequent simulations.

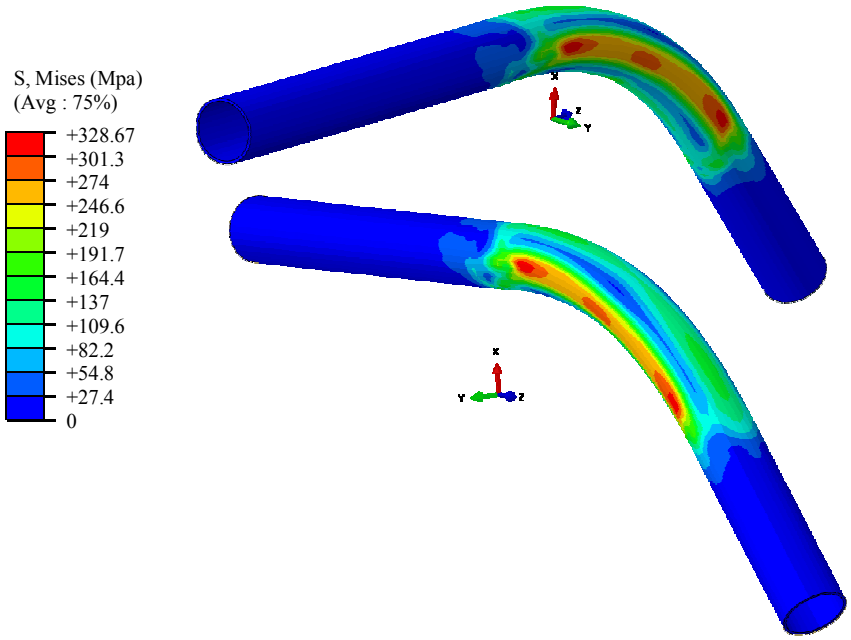

Figure 3.19: Equivalent Von Mises stresses distribution before THF process

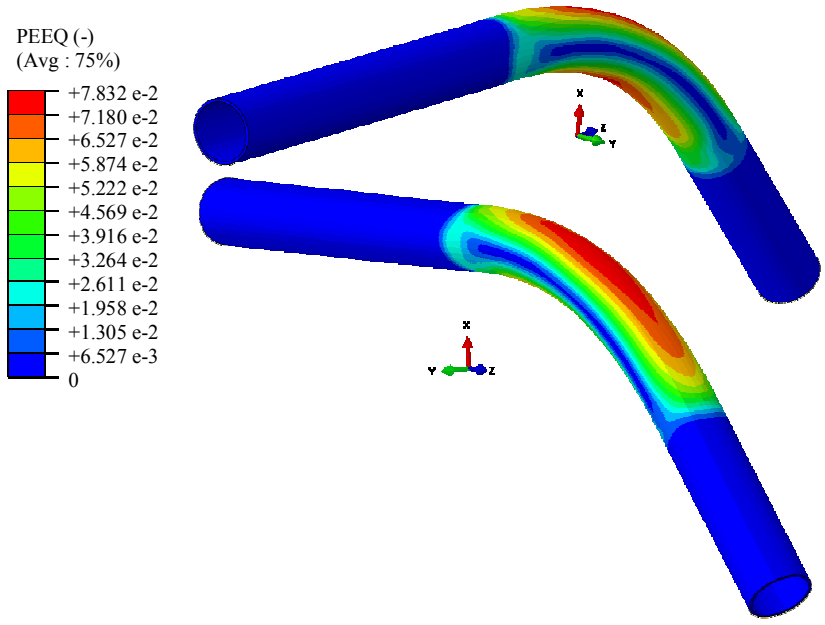

Figure 3.20: Equivalent plastic strains distribution before THF process

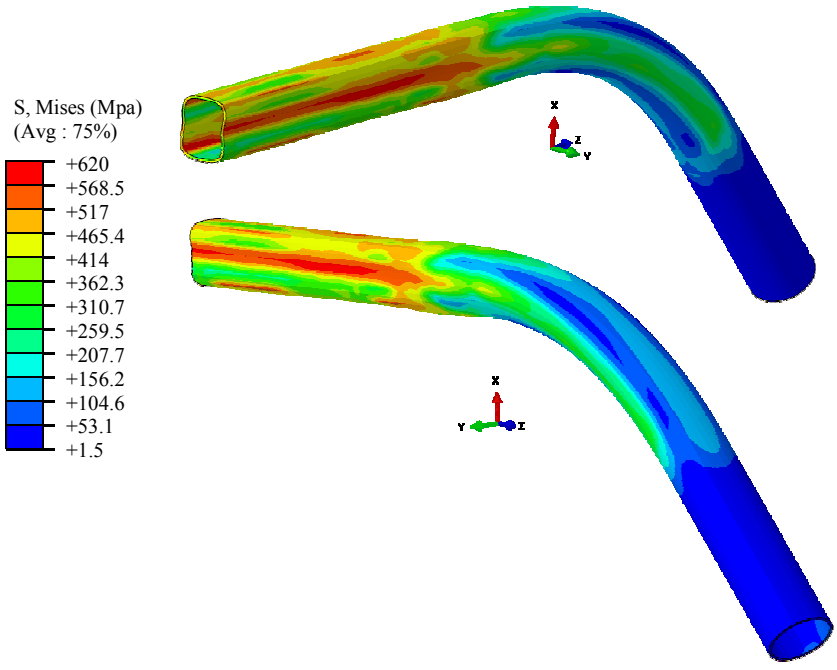

Figure 3.21: Equivalent Von Mises stresses distribution after first crushing

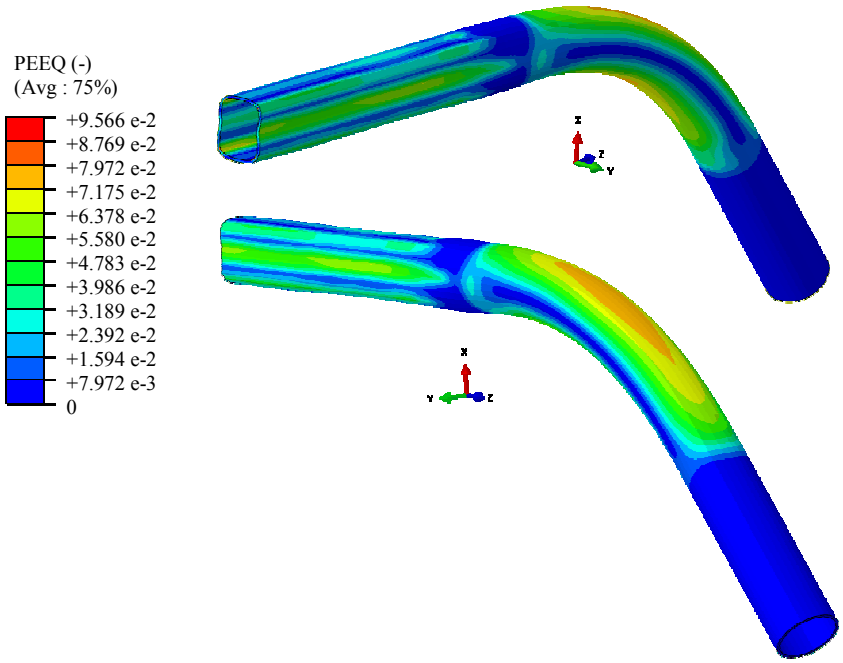

Figure 3.22: Equivalent plastic strains distribution after first crushing

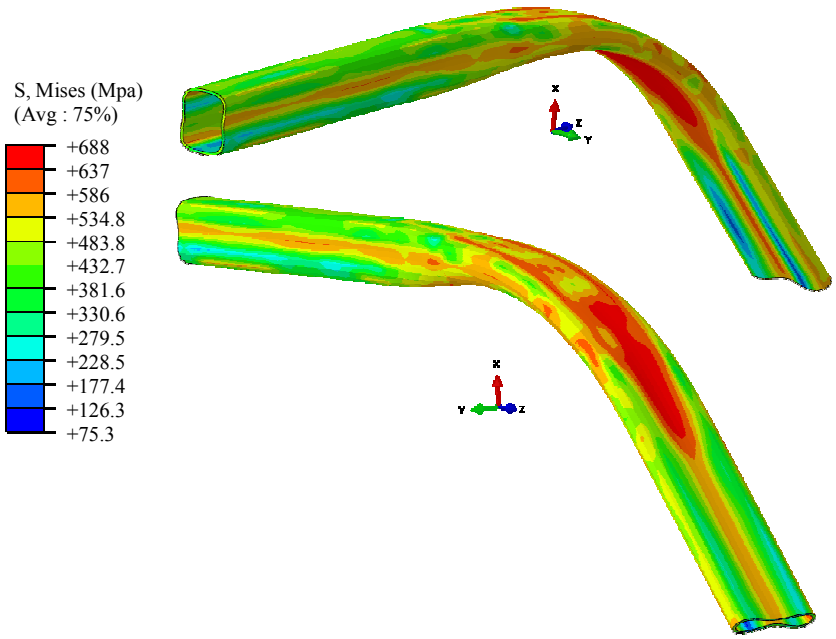

Figure 3.23: Equivalent Von Mises stresses distribution after second crushing

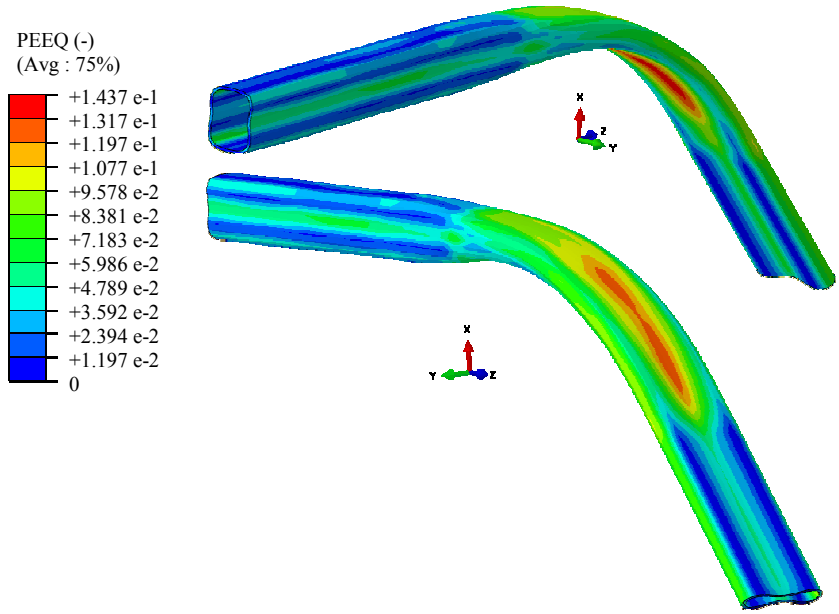

Figure 3.24: Equivalent plastic strains distribution after second crushing

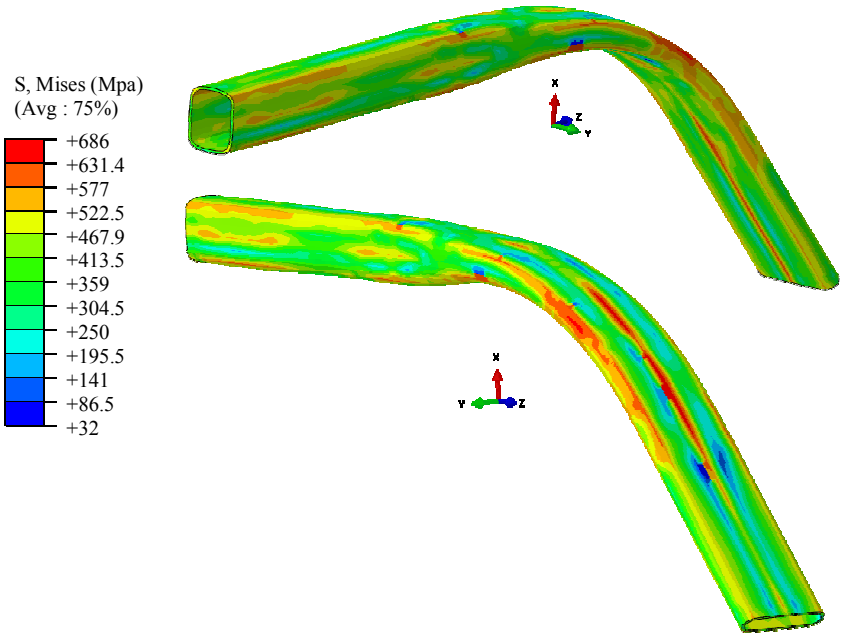

Figure 3.25: Equivalent Von Mises stresses distribution after pressure increase

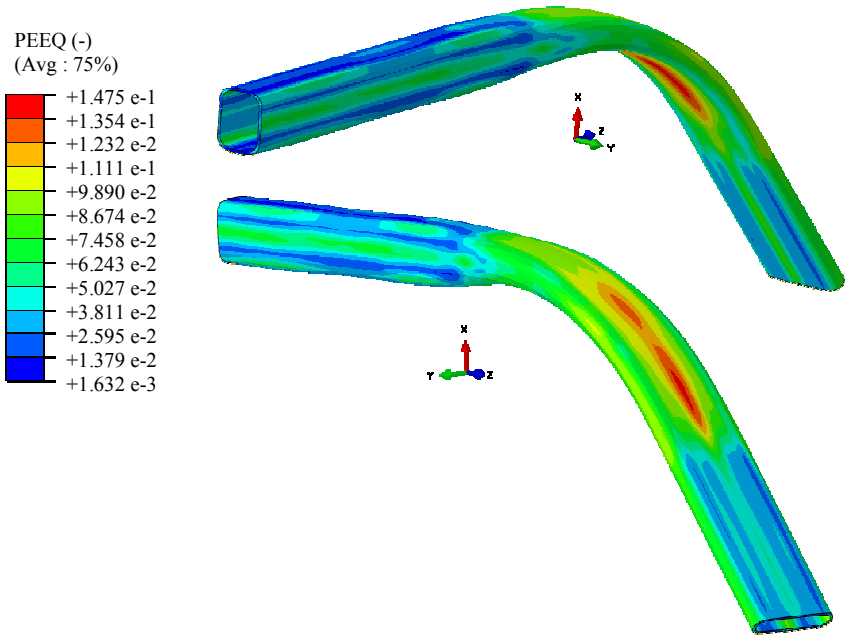

Figure 3.26: Equivalent plastic strains distribution after pressure increase

3.5. Hard landing simulations

3.5.1 Federal Aviation Regulations (FAR)

When a new landing gear is designed, its performances have to fulfill the FAR requirements § 27.725 (See Appendix A). BHTC uses two different design criteria for the light helicopter model standard landing gear, the limit drop test and the reserve energy drop test configurations. In the limit drop test configuration, the drop height is eight inches and the rotor lift does not completely compensate the helicopter weight (0.667 time the helicopter weight). In the reserve energy configuration, the drop height is twelve inches and the rotor lift completely compensates for the helicopter weight. Each skid landing gear has to withstand these tests without collapsing. In the reserve energy drop configuration, the initial impact speed is around 22% higher than for the limit energy configuration, generally making the reserve energy drop test configuration the hardest requirement to satisfy for the light helicopter model standard landing gear. As a result, the performance of the new hydroformable design is only checked in the reserve energy drop test configuration.

A helicopter is likely to encounter various ground and landing configurations during its life. For sake of simplicity, the loads are different than those of the FAR requirements but inspired form them. The four loading conditions considered in this work are then depicted below:

- Level landing configuration: the helicopter lands on a horizontal ground with only a vertical speed.

- Level landing with drag configuration: the helicopter lands on a horizontal ground with vertical and forward horizontal speeds. The forward horizontal speed is 50% of the vertical speed.

- Level landing with side load configuration: the helicopter lands on a horizontal ground with vertical and transverse horizontal speeds. The transverse horizontal speed is 25% of the vertical speed.

- One skid landing configuration: the helicopter lands on a ground with only a vertical speed and hit the ground with only one skid.

The skid landing gear has to be stiff enough to prevent a part of the fuselage to hit the ground during the hard landing simulations, and this, in all the configurations above. Moreover, it has to absorb a maximum amount of energy in order to keep the helicopter integrity. The skid landing gear cross tubes absorb a part of this energy by plastification. The variable thickness of the standard forward cross tube allows for a smooth and continuous stress and plastic strain distribution along its length. The hydroformable cross tube studied in this research project has a constant thickness, but the variable rectangular section allows influencing the stress and plastic strains distributions along the forward cross tube. Another issue is the resonance phenomenon attenuation which is not studied in this contribution. BHTC usually uses some additional damper devices like a rocker beam to deal with this aspect. However, some researchers postulate that a square section could allow optimizing the ground resonance placement by decoupling the directional stiffnesses (Cheng-Ho et al. (2003)).

3.5.2 Hard landing model description

Material characterization

The aluminum alloy used in the hard landing simulations of the landing gear equipped with the standard cross tube is characterized for its specific geometry. However, it is necessary to characterize the material for the tube geometry to be hydroformed, which is thinner with a larger diameter than for the standard design. The tube material used in bending and THF simulations detailed in the previous sections is an aluminum alloy 7075 in W condition which is prone to provide a good formability during bending as well as THF processes. However, before assembly of the landing gear, an artificial ageing is required to shift the aluminum properties from W to T73 condition (Artificially aged). During the experiments and materials characterization performed by Dr. Julie Levesque Research Associate at Laval University, it has been observed that forming the material in the W condition changes its final mechanical properties after ageing. Thus, the material properties will be heterogeneous in the cross tubes depending on the level of plastification reached during forming process shown in Figure 3.26. It is then necessary to characterize the material with different thermo-mechanical treatments to be able to predict numerically the T73 condition for the hydroformed cross tube. To do so, tensile tests have been performed using large tensile specimens machined from tubes with the same initial diameter and thickness as the one used during the forming process. The tensile specimen extremities have been flattened in order to offer an appropriate grip section during deformation. They have then been deformed with various pre-deformation conditions. Afterwards, they have been artificially aged in T73 condition. Smaller samples have been cut from the large deformed and aged ones. The new obtained specimens have then been tested in order to obtain the final properties. One of the main observations is the decrease of material properties after ageing in T73 condition when pre-deformation is used in W condition. The Voce-type hardening law presented in equation (3.1) has been used to express the hardening behavior of the aluminum alloy in T73 condition:

$$\sigma = A - B \times e^{\left(-C \times \varepsilon^{P}\right)} \tag{3.1}$$

where A, B and C are functions of the equivalent plastic strain obtained during pre-deformation step. More details on these parameters are on an oncoming publication from Dr. Julie Levesque Research Associate at Laval University. Regression using the least square method has been used with the previously obtained experimental results to calibrate it.

Model description

The skid landing gear assembly has various parts linked together that are presented below. The most critical parts are the cross tubes since they are the only one authorized to plastify during the hard landing simulations presented here according to the FAR requirements. The light helicopter model standard landing gear cross tubes, presented in Figure 3.27(a) are meshed with the ABAQUS solid element with reduced integration (C3D8R) since it has a variable thickness through its length. The vertical displacement on the fuselage attachments has been checked for three mesh densities of the standard cross tube. The results presented in Table 3.5 shows a difference less than 3% between two and three layers of C3D8R elements in the thickness direction. Three layers of C3D8R elements are then used in the thickness direction to mesh the standard cross tubes.

Number of elements in the thickness direction	m	Δ%
1	-2.56E-01	-
2	-2.42E-01	5.57
3	-2.35E-01	2.85

Table 3.5: Hard landing, standard cross tube: convergence study

The light helicopter model landing gear hydroformable forward cross tube presented in Figure 3.27(b), from the earlier detailed bending + THF runs, has a thin constant theoretical thickness. It is then possible to mesh it with an ABAQUS four nodes shell element with reduced integration (S4R). However, in the present model set-up, C3D8R elements are also used to mesh the hydroformable forward cross tube since it is more convenient than the S4R element to deal with some thickness variations that could occur during hydroforming problems. The vertical displacement on the fuselage attachments has been checked for four mesh densities of the hydroformable cross tube. The results presented in Table 3.6 show a difference of about less than 1% between two and three layers of C3D8R elements in the

thickness direction. Three layers of C3D8R elements are then used in the thickness direction to mesh the hydroformable cross tubes.

Number of elements in the thickness direction	m	Δ%
1	-2.83E-01	-
2	-2.41E-01	14.89
3	-2.41E-01	0.12
4	-2.39E-01	0.50

Table 3.6: Hard landing, hydroformable cross tube: convergence study

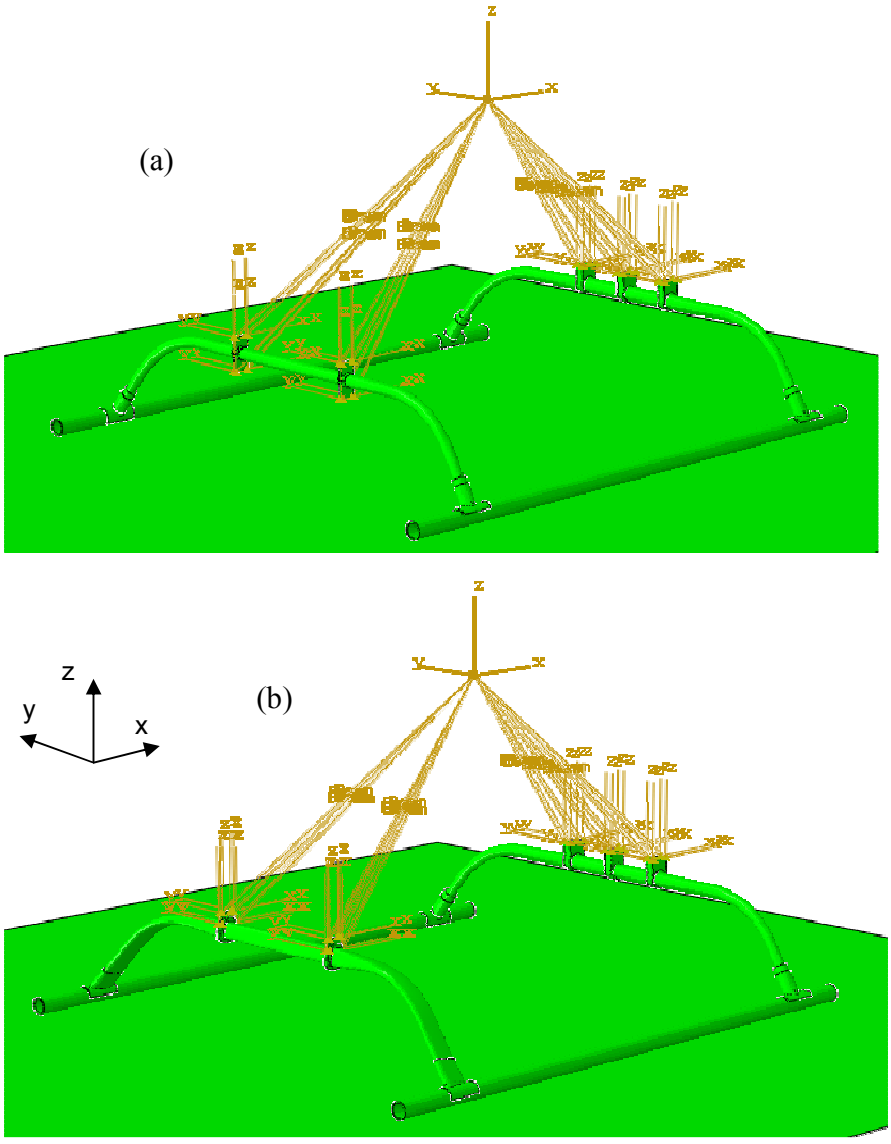

Figure 3.27: Skid landing gear geometry, equipped with (a) standard or (b) hydroformable forward cross tube

The hydroformable cross tube is in aluminum alloy AA7075-T73 with a density of $\rho = 2823\, kg/m^3$, a Young's modulus of $E = 71705.48$ Mpa a Poisson's ratio of $\nu = 0.3$ and a yield stress of $\sigma_y = 432.8\, Mpa$. Its elastoplastic properties at areas without initial plastification are shown in Table 3.7.

Aluminum alloy 7075-T73	
True stresses (Mpa)	True strains
432.79	0
440.31	0.0025
447.43	0.005
460.58	0.01
472.40	0.015
483.02	0.02
515.75	0.04
537.09	0.06
550.99	0.08
560.05	0.1
575.01	0.2

Table 3.7: Aluminum alloy 7075-T73 material properties

Usually, when a new design is developed, its geometry is created on a computer aided design (CAD) system before being used in hard landing runs. However, because this geometry is "perfect" compared with one that would be fabricated, test results could suffer from some inaccuracy. For these reasons, two configurations are compared for the hydroformable cross tube: one using an aluminum alloy 7075-T73 that does not consider material history with a perfect CAD geometry and another using a set of aluminum alloys 7075-T73 that takes into account material history during fabrication process with the geometry from the previously detailed THF process. The methodology of this last configuration is presented in the next section. The fuselage attachments are designed to prevent bending from occurring around the "x" and the "y" axes. Only the contact areas, usually named bearing plates, and the fuselage attachments were represented. This model allows recording and examining some interesting information such as the fuselage reaction forces. Only elastic properties with a large Young's modulus are used for the material properties of fuselage attachments.

The fuselage center of gravity has a mass of 2495 Kg and inertia properties from experimental data. This center of gravity is linked to the fuselage attachments with rigid connectors that can transmit the three displacements and the three rotations to the skid landing gear. The surface to surface contacts are defined without fiction in the fuselage attachments. Two nodes (one on the forward cross tube center and one on the aft cross tube center) are constrained in displacement with the same transversal displacement (y direction) as the center of gravity. Moreover, the bearing plates are tied to the cross tubes.

The skids, which are supposed to be the only parts in contact to the ground, are meshed with the ABAQUS solid element with reduced integration, the C3D8R. The skids are in aluminum alloy AA7075-T6 (Aged) with a density of $\rho = 2823\, kg/m^3$, a Young's modulus of $E = 71016\,\text{Mpa}$ a Poisson's ratio of $\nu = 0.3$ and a yield stress of $\sigma_y = 443\, Mpa$. Its elastoplastic properties, determined by Dr. Julie Levesque Research Associate at Laval University, are shown in Table 3.8.

Aluminum alloy 7075-T6	
True stresses (Mpa)	True strains
443.03	0
478.01	0.001237
497.56	0.002944
509.01	0.004761
522.23	0.00852
530.26	0.012336
539.23	0.0171
546.47	0.021864
552.33	0.026624
556.43	0.031385
575.44	0.059556

Table 3.8: Aluminum alloy 7075-T6 material properties

Four skid attachments linked the forward and aft cross tube to the skids with a tied contact. Their design provided in the same time an appropriate angle to the cross tubes plan. C3D8R elements and the elastoplastic properties of the aluminum alloy 7075-T73 are used to model these parts.

The fixed ground is a rigid surface meshed with only one element R3D4. The ground is supposed to be the master surface in the surface to surface contact with the skids to be sure that they do not get through. The friction coefficient between the ground and the skids is calculated with the following formula also used by Cheng-Ho et al. (2003).

$$\mu = \mu_k + (\mu_S - \mu_k) e^{-d_c \dot{\gamma}_{eq}} \tag{3.2}$$

where μ_k is the dynamic friction coefficient, μ_s is the static friction coefficient, d_c is a user-defined decay coefficient and $\dot{\gamma}_{eq}$ is the slip rate as presented in Abaqus, V6.9 (2007). This formula is illustrated in Figure 3.28.

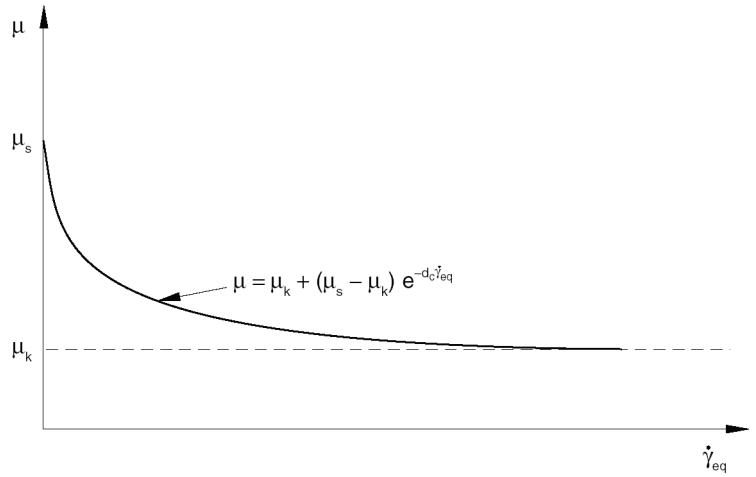

Figure 3.28: Exponential decay friction model Abaqus, V6.9 (2007)

The following parameters is used: the static friction $\mu_s = 0.5$, the dynamic friction $\mu_k = 0.35$ and the exponential decay coefficient $d_c = 0.05$.

When simulation starts, a gap of $2.54e^{-2}$ mm (1/1000 inch) exists so that the skids and the ground are not in contact. This gap does not affect the result and is useful to verify lift and weight equilibrium. All simulations are made in the reserve energy condition. An initial velocity is applied to the skid landing gear as specified in section 3.5.3. Lift and weight are then equal by applying on the center of gravity upward and downward forces of 24.5 KN.

Four hard landing configurations are simulated with the new design and are presented below.

3.5.3 Hard landing numerical results

The ABAQUS/Explicit models are initially compared and validated using the Ls-Dyna BHTC reference model in level landing configuration. A convergence study based on the maximum deflection and the total energy has been made to determine an acceptable mesh refinement for the ABAQUS models. Once the ABAQUS modelization is validated in level landing configuration, the four landing load configurations are then implemented and compared on ABAQUS for the landing gear equipped with a standard forward cross tube, a hydroformable cross tube with material history (WMH) and a hydroformable cross tube without material history (WOMH). For a convenient reading of the graphic, a Butterworth with a frequency of 20 Hz filter is applied in some figures. Note that 1,2 and 3 correspond to directions x, y and z in the following figures.

Level landing configuration

In the level landing configuration, only a fall speed of 2.45 m/s (corresponding to a drop height of 0.3 m) is applied to the skid landing gear. Figure 3.29 shows the center of gravity vertical displacements. During landing in level landing configuration, the results are very similar for the standard and the hydroformable models. Moreover, the center of gravity vertical accelerations presented in Figure 3.30 are also very similar. The load factors (Appendix A) are thus acceptable for the skid landing gear with the hydroformable cross tube (WMH: 3.86 g and WOMH: 3.85 g) as for the skid landing gear with the standard cross tube (3.82 g).

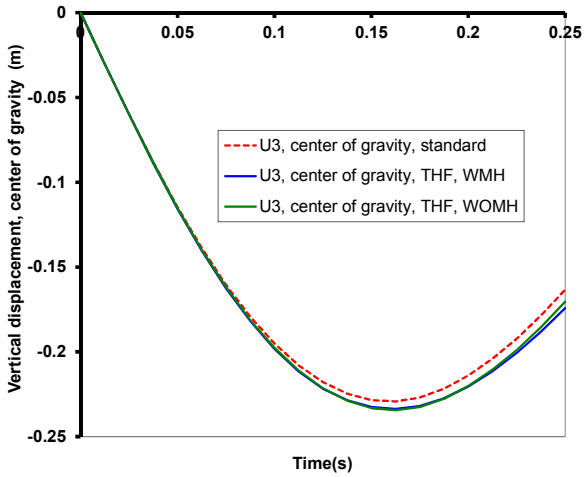

Figure 3.29: Center of gravity vertical displacement, level landing

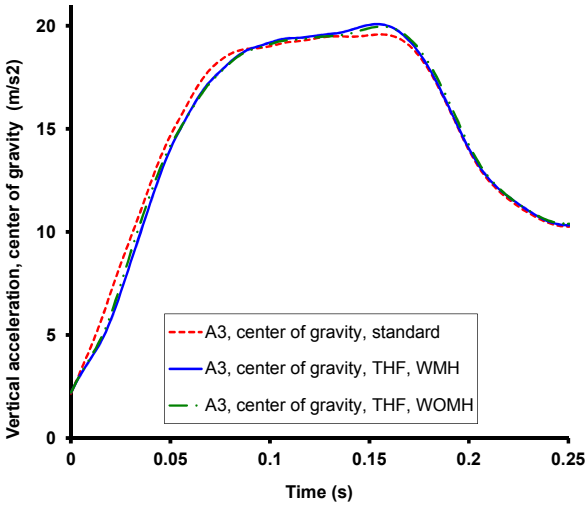

Figure 3.30: Center of gravity vertical acceleration, level landing (Butterworth, 20 Hz)

Besides, as illustrated in Figure 3.31**,** the vertical reaction forces at skids are also very similar for both standard and hydroformable models. Only the right skid is analyzed due to model symmetry.

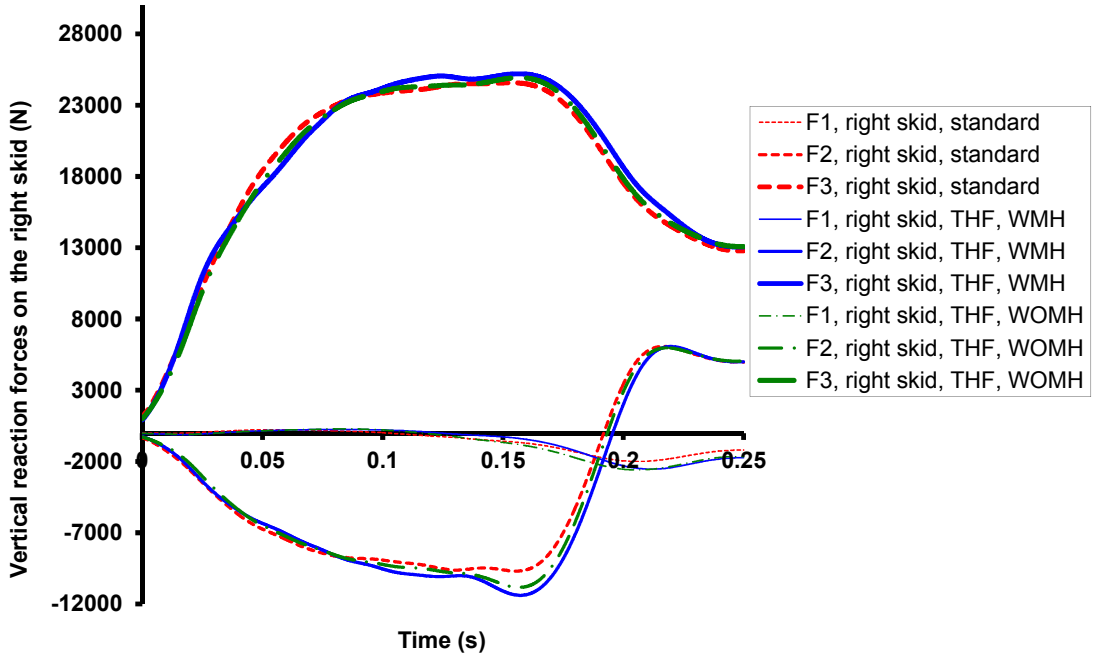

Figure 3.31: Vertical reaction forces, level landing (Butterworth, 20 Hz)

Level landing with drag configuration

In the level landing configuration with drag, a fall speed of 2.45 m/s (corresponding to a drop height of 0.3 m) and a forward velocity of 1.22 m/s (50% of the seek speed) are applied to the skid landing gear. Figure 3.32 shows the center of gravity vertical displacements. During landing in level landing configuration with drag, the results are also similar for the standard and the hydroformable models. Moreover, the center of gravity longitudinal and vertical accelerations presented in Figure 3.33 are also comparable. The load factors (Appendix A) are thus acceptable for the skid landing gear with the hydroformable cross tube (WMH: 3.71 g and WOMH : 3.70 g) as for the skid landing gear with the standard cross tube (3.68 g).

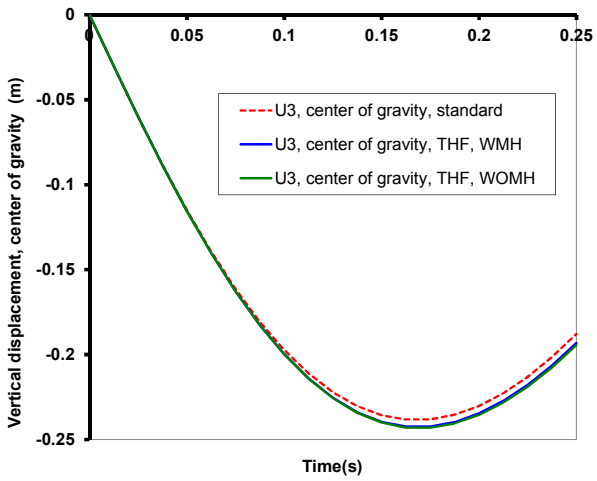

Figure 3.32: Center of gravity vertical displacement, level landing with drag

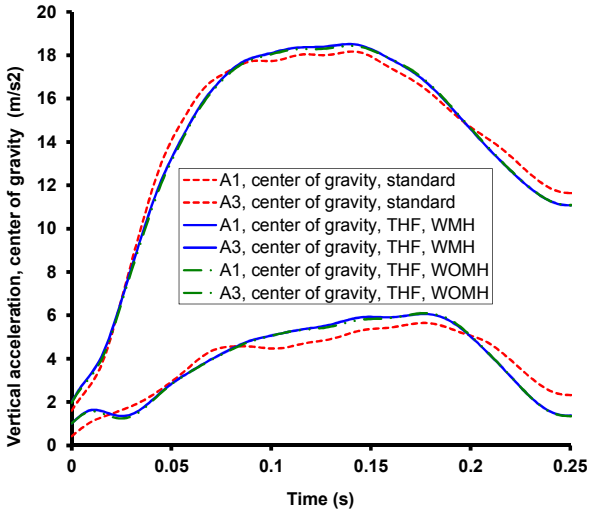

Figure 3.33: Center of gravity vertical acceleration, level landing with drag (Butterworth, 20 Hz)

Besides, as illustrated in Figure 3.34**,** the vertical reaction forces at skids are also very similar for both standard and hydroformable models. However, the maximum vertical force is slightly higher for the case WMH. Only the right skid is analyzed due to model symmetry.

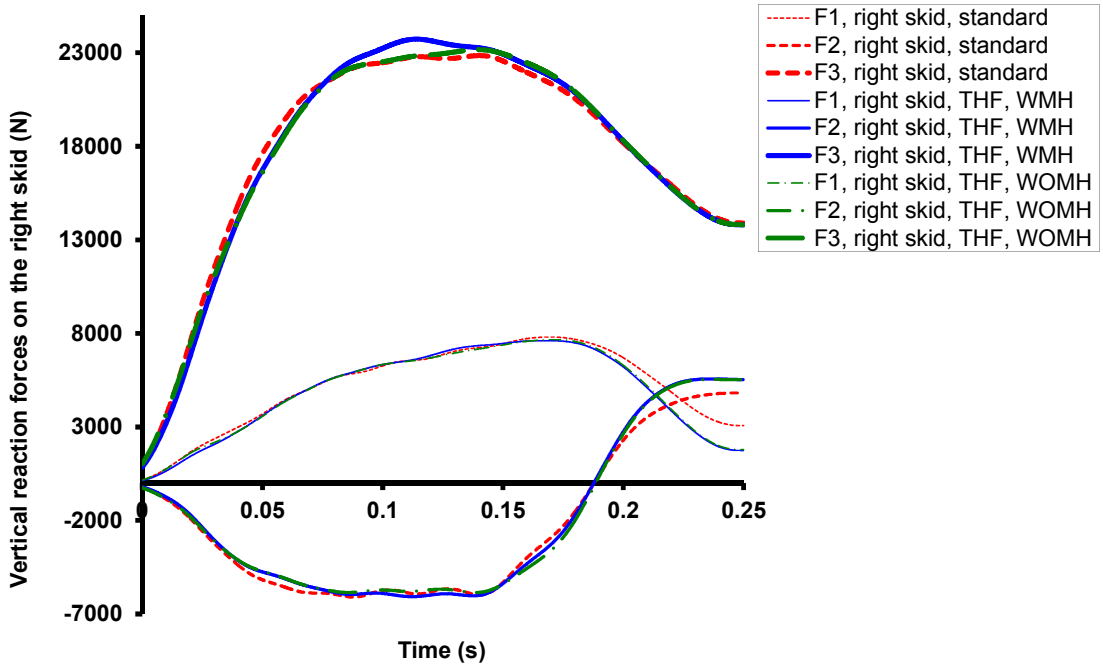

Figure 3.34: Vertical reaction forces, level landing with drag (Butterworth, 20 Hz)

Level landing with side load configuration

In the level landing with side load configuration, a fall speed of 2.45 m/s (corresponding to a drop height of 0.3 m) and a transverse velocity in the "y" direction of 0.61 m/s (25 % of the seek speed) are applied to the skid landing gear. The velocity transverse component could be calculated thanks to the velocity diagram when the impacted surface had an angle of 6.4º. Figure 3.35 shows the center of gravity vertical displacements. During landing in level landing configuration with side load, the results are also similar for the standard and the hydroformable models. Moreover, the center of gravity side and vertical accelerations presented in Figure 3.36 are also comparable. The load factors (Appendix A) are thus acceptable for the skid landing gear with the hydroformable cross tube (WMH: 3.73 g and WOMH : 3.72 g) as for the skid landing gear with the standard cross tube (3.73 g).

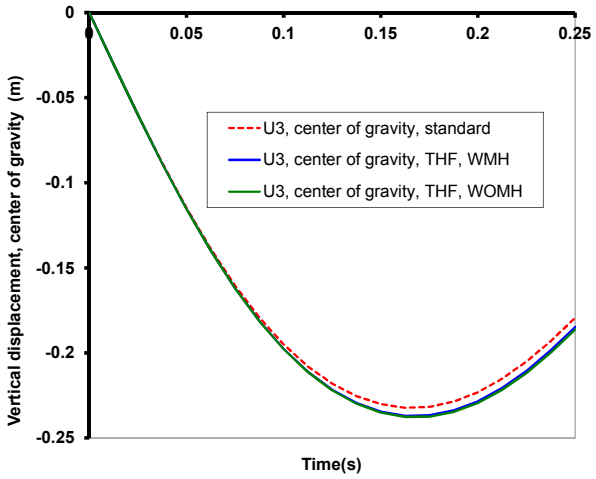

Figure 3.35: Center of gravity vertical displacement, level landing with side load

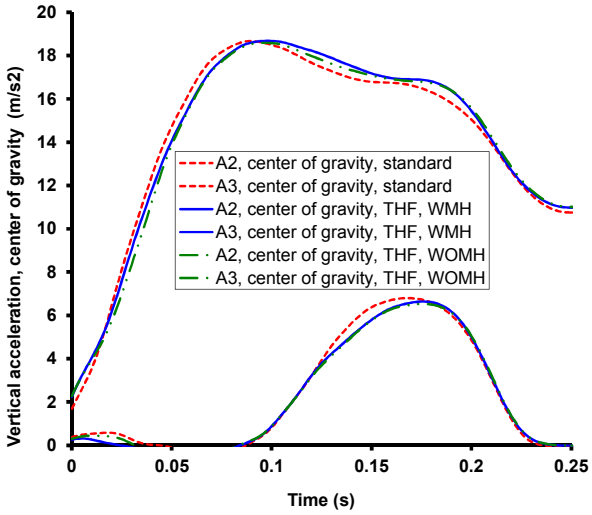

Figure 3.36: Center of gravity vertical acceleration, level landing with side load (Butterworth, 20 Hz)

Besides, as illustrated in Figure 3.37 and Figure 3.38**,** the side and vertical reaction forces at skids were also very similar for both standard and hydroformable models.

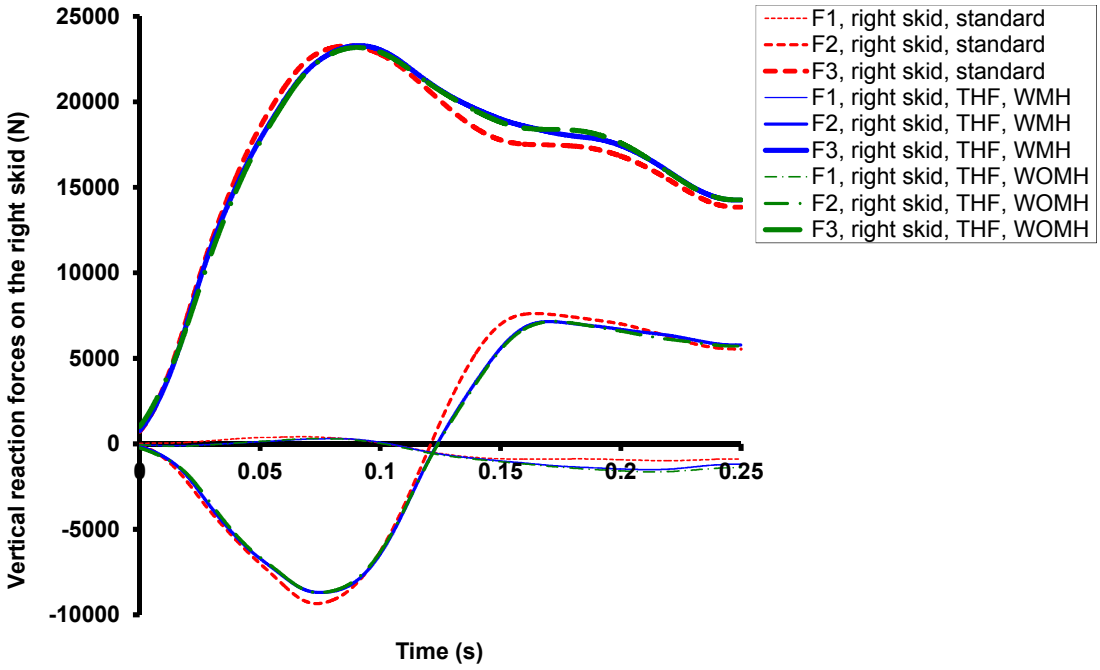

Figure 3.37: Vertical reaction forces, level landing with side load, right skid (Butterworth, 20 Hz)

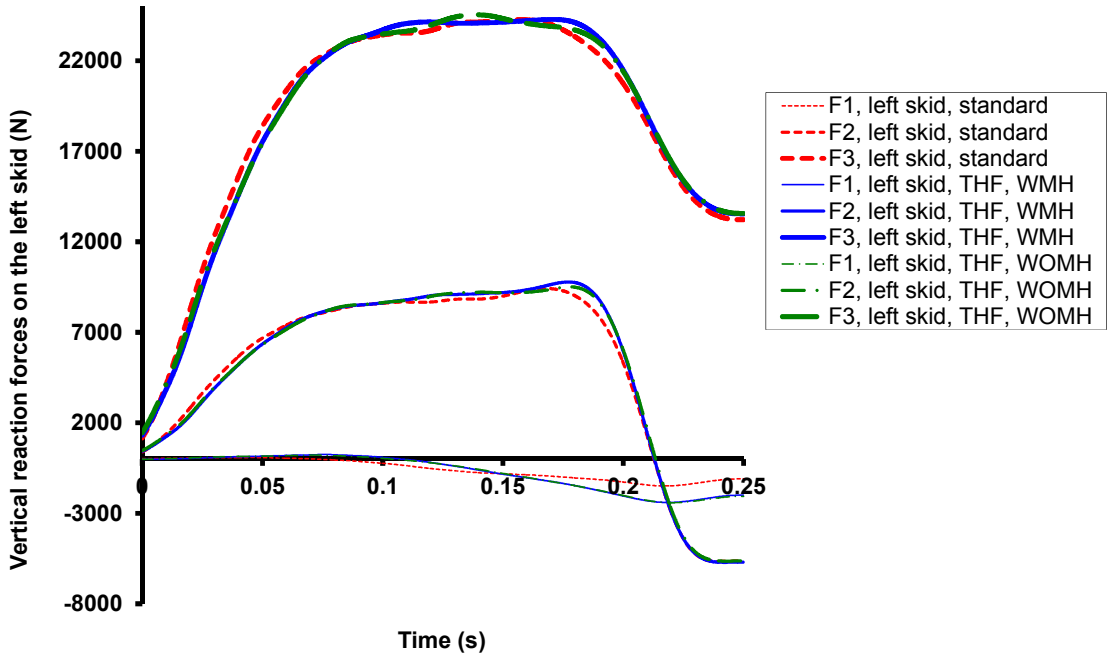

Figure 3.38: Vertical reaction forces, level landing with side load, left skid (Butterworth, 20 Hz)

One skid landing configuration

In the one skid landing configuration, a fall speed of 1.22 m/s is applied to the skid landing gear. Only the right skid hit the impacted surface. Figure 3.39 shows the center of gravity vertical displacements. During landing in one skid landing configuration, the results are very similar for the standard and the hydroformable models. Moreover, the center of gravity vertical accelerations presented in Figure 3.40 are also very similar. The load factors (Appendix A) were thus acceptable for the skid landing gear with the hydroformable cross tube (WMH: 2.84 g and WOMH : 2.85 g) as for the skid landing gear with the standard cross tube (2.85 g).

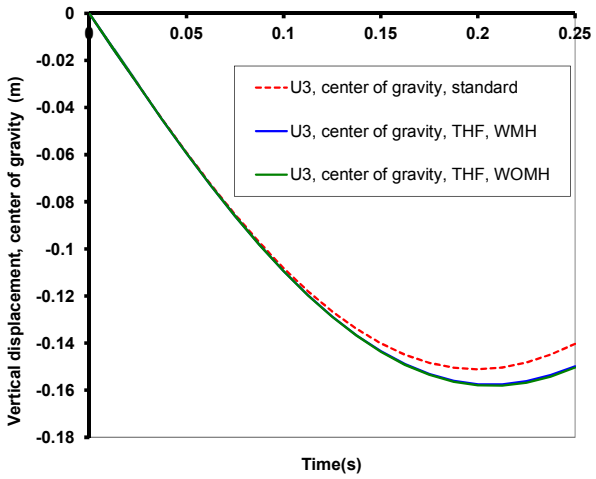

Figure 3.39: Center of gravity vertical displacement, one skid landing

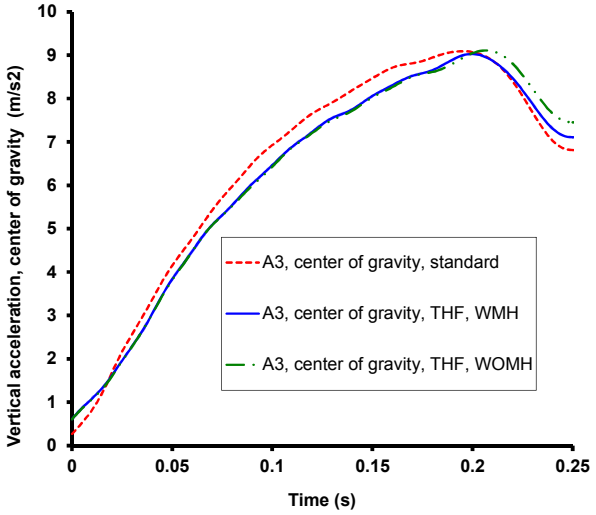

Figure 3.40: Center of gravity vertical acceleration, one skid landing (Butterworth, 20 Hz)

Besides, as illustrated in Figure 3.41**,** the vertical reaction force at right skid is also very similar for both standard and hydroformable models.

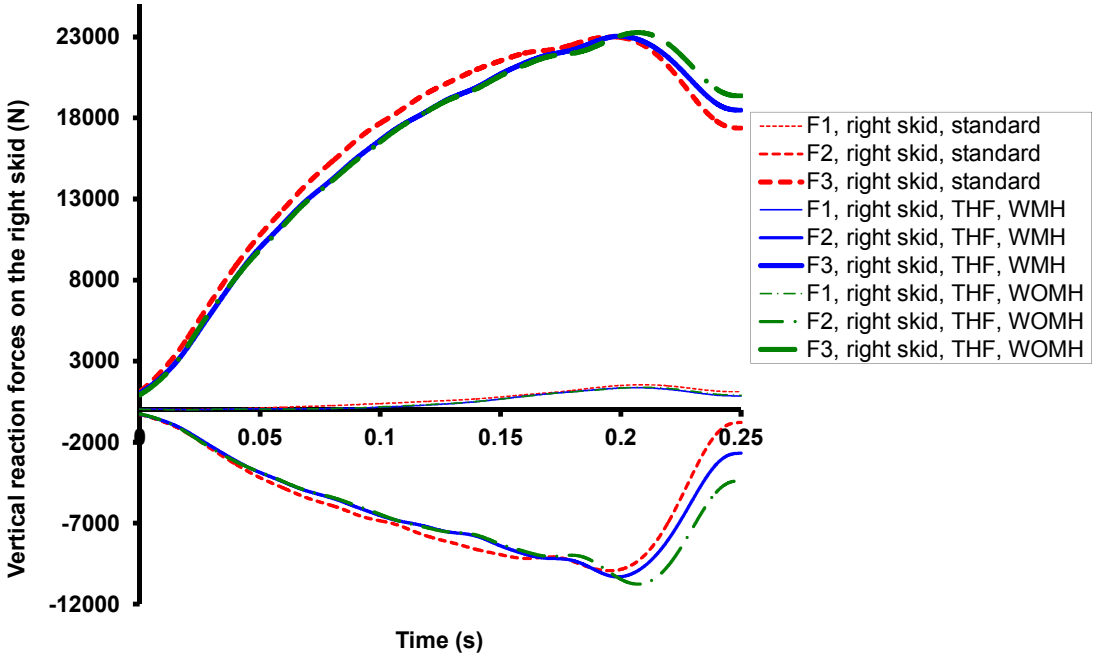

Figure 3.41: Vertical reaction forces, one skid landing (Butterworth, 20 Hz)

General observations

In this section, the level of plasticity of the forward cross tube is analyzed excluding the regions close to the fuselage attachments. The maximum value of the equivalent plastic strain is generally higher for the hydroformable cross tubes, as illustrated in Table 3.9. This could be due to its square geometry which tends to localize the highest stresses in the corner of the sections. Besides, comparing PEEQ for the hydroformable designs, it appears that the level of plasticity for the case WOMH is higher than WMH in the four tested drop loads. A reason to this could be that the fabrication process has strengthened the cross tube material properties in the case WMH.

	Standard	WMH	WOMH	Δ% (Standard - WMH)	Δ% (WMH - WOMH)
Level	7.28E-03	9.10E-03	9.59E-03	-24.89	-5.38
Drag	9.86E-03	1.06E-02	1.16E-02	-7.59	-9.43
Side	8.51E-03	1.06E-02	1.12E-02	-24.17	-5.66
One	3.22E-03	2.61E-03	3.19E-03	18.74	-22.22

Table 3.9: Forward cross tube maximum equivalent plastic strain (PEEQ)

In order to emphasize the influence of material history in the new design during hard landing conditions, Figure 3.42 defines the main zones to be observed on the hydroformable cross tube. The maximum Von Mises equivalent stress, S_{Mises} max and the maximum equivalent plastic strain, PEEQ max are listed for the four studied drop load conditions from Table 3.10 to Table 3.15. The analysis of the results reveals that if the maximum Von Mises equivalent stresses, S_{Mises} max remain generally similar WMH and WOMH, the maximum equivalent plastic strains, PEEQ max are significantly higher in the case WOMH with a difference of up to 22%. Moreover, in the one skid landing condition, zone 3 is more critical than zone 2 in the case WMH while zone 2 is more critical than zone 3 in the case WOMH. In other words, the position of the critical zones may change if material history is considered depending on the level of plasticity generated by the fabrication process.

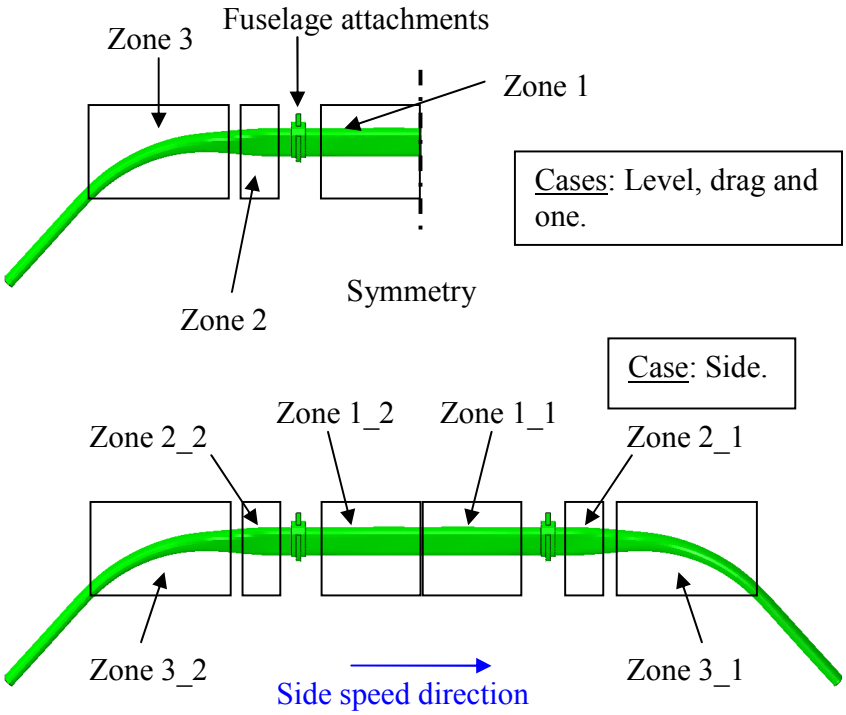

Figure 3.42: Zones definition on the hydroformable cross tube

S_{Mises} max (Mpa)	WMH	WOMH	Δ% (WMH - WOMH)
Level	456.08	456.55	-0.10
Drag	459.70	461.65	-0.42
Side	457.73	460.04	-0.51
One	439.88	440.43	-0.12

Table 3.10: Hydroformable cross tube maximum Von Mises equivalent stress zone 1

PEEQ	WMH	WOMH	Δ% (WMH - WOMH)
Level	9.10E-03	9.59E-03	-5.38
Drag	1.06E-02	1.16E-02	-9.43
Side	1.06E-02	1.12E-02	-5.66
One	2.61E-03	3.19E-03	-22.22

Table 3.11: Hydroformable cross tube maximum equivalent plastic strain zone 1

S_{Mises} max (Mpa)	WMH	WOMH	Δ% (WMH - WOMH)
Level	445.86	444.72	0.25
Drag	457.26	454.82	0.53
Side (Zone 2_1)	446.12	445.00	0.25
One	437.36	437.33	0.01

Table 3.12: Hydroformable cross tube maximum Von Mises equivalent stress zone 2

PEEQ	WMH	WOMH	Δ% (WMH - WOMH)
Level	0.00525583	0.00493173	6.17
Drag	0.00980106	0.00894075	8.78
Side (Zone 2_1)	0.00619037	0.00553714	10.55
One	0.00205212	0.00193926	5.50

Table 3.13: Hydroformable cross tube maximum equivalent plastic strain zone 2

S_{Mises} max (Mpa)	WMH	WOMH	Δ% (WMH - WOMH)
Level	445.03	443.25	0.40
Drag	455.65	454.76	0.20
Side (Zone 3_2)	451.02	451.05	-0.01
One	435.86	436.21	-0.08

Table 3.14: Hydroformable cross tube maximum Von Mises equivalent stress zone 3

PEEQ	WMH	WOMH	Δ% (WMH - WOMH)
Level	0.00498273	0.00421758	15.36
Drag	0.0093579	0.00885111	5.42
Side (Zone 3_2)	0.00763731	0.00764131	-0.05
One	0.00206614	0.00162233	21.48

Table 3.15: Hydroformable cross tube maximum equivalent plastic strain zone 3

3.6. Concluding remarks

The light helicopter landing gear standard forward cross tube is currently manufactured by bending tubes with circular cross section followed by chemical milling. This fabrication process is not only damaging to the environment, but also wastes valuable aerospace grade material. The THF process solves both those issues. A complete rethinking of the design is proposed, since it would have been difficult to hydroform thick tubes such as those used in the standard design. The hydroformable design is 30% lighter than the standard design, while greatly reducing material waste which is highly appreciated while using expensive aerospace materials. The hydroformable design also offered properties similar to those attained with the standard design in four severe drop loads configurations. A full simulation methodology that takes into account material history during cross tube multi-steps fabrication process is successfully developed and applied. In the presented work, the complete material history is considered in the hydroformable cross tube. It has been observed numerically that results for this new design WMH and WOMH are very similar regarding the skid landing gear general behavior. However, it has been observed after hard landing that the plastification level is significantly higher in the case WOMH than in the case WMH. Moreover, it is likely that this trend increases if more complex hydroformable designs, which generate lager deformation during the forming process, are used. It then appears to be crucial to take account of material history in fatigue life prediction studies as it has direct effect on the plasticity level in the hydroformable cross tube as well as in the critical zone position. Depending on the complexity of the geometry to be hydroformed, some mesh distortion could appear. Moreover, in the THF simulation process, it is important to know the structure behavior through the thickness. Hence, the tube is meshed with three C3D8R ABAQUS solid elements. However, it has been observed that this mesh refinement induces long computation time. Hence use of solid shell elements that require one layer of elements in the thickness direction could help to reduce the computational costs. Since existing solid shell elements available to us were not accurate enough, some developments of a new solid-shell elements based on a 3D variational formulation was required in order to provide an acceptable accuracy. The following chapters thus present developments on solid-shell elements as well as investigations on a new technique, known

as the smooth finite element method that is prone to be insensitive to mesh distortion and time efficient.

Chapter 4. Smoothed finite element method implemented in a resultant eight-node solid-shell element for geometrical linear analysis

A new approach combining finite element and mesh free formulations, named smooth finite element method (SFEM) is presented. It offers some interesting properties such as insensitivity to mesh distortion and simplicity of the formulation. These advantages are possibly beneficial in the tube hydroforming process. However, to the best knowledge of the authors, no solid-shell element using this technique exists. The variational formulation of a resultant solid-shell element using the SFEM is thus presented. The formulation is only used to model membrane and bending aspects. This linear resultant element has been developed in implicit on ABAQUS/Standard, using the ABAQUS/UEL subroutine. The advantages of the SFEM are demonstrated and an operation count helps to note the simplicity and efficiency of the approach. No additional stabilization of the membrane and bending parts are necessary to keep the presented formulation efficient. Its accuracy is compared favorably to the accuracy of other equivalent elements in various benchmark problems.

4.1. Introduction

In finite element method (FEM), a lot of work dealing with thin shell structures has been accomplished, led by industry needs. This category of three dimensional (3D) shell structures is useful in many industrial activities, like those involved in the aerospace industry. It is characterized by the existence of a small dimension in one direction, identified as the shell thickness, when compared to the two remaining directions.

The many existing shell element formulations can be grouped into three main classes: i) Classical shell elements depicted into plate elements and shell elements. Plate elements combine membrane as well as bending characteristics and hence include in-plane and out-of-plane theories. For each node, they use translational as well as rotational degrees of freedom. They are widely used in practice because they have a simple formulation and exhibit attractive time efficiency. Shell elements have the same characteristics as plate elements except for the fact that they also remain accurate in arbitrary shapes contexts. The

readers can consult Betsch et al. (1996), Bischoff & Ramm (1997) and Cardoso & Yoon (2005); ii) Degenerated shell elements based on a 3D variational formulation as for solid elements have a kinematics expressed on the shell mid-surface exhibiting translational and rotational degrees of freedom. For more details on this topic one can consults among others the following authors: Ahmad et al. (1970), Parisch (1978), Dvorkin & Bathe (1984), Belytschko et al. (1984), Bathe & Dvorkin (1985), Simo & Fox (1989), Simo & Rifai (1990) and César de Sá et al. (2002); iii) Solid-shell elements, which are among the most recent shell elements developments, are 3D shell elements.

Some advantages of solid-shell compared with shell elements formulations are: i) the capability of modeling 3D geometries comprising both thin and thick portions without any need for special transition elements; ii) the boundaries modeling without any extra kinematics assumptions. Since physical nodes are located on the bottom and the top surface of the shell structure, the contact definition with associated friction phenomenon can be dealt with easily; iii) the kinematics description remains simple since their formulation uses only displacement degree of freedoms avoiding the complicated updating of rotation vector in non-linear problems. See Parisch (1995), Hauptmann & Schweizerhof (1998) and Hauptmann et al. (2000) for details.

Independently from the above classification, shell elements can be separated into two categories: i) Thin shell elements described by Kirchhoff–Love plate theory, which neglects transverse shear deformation, are described in Timoshenko & Woinowsky-Krieger (1959). The elements using this theory require a C^1 displacement continuity; ii) Thick shell elements described by Reissner-Mindlin plate theory which considers transverse shear, (see Timoshenko & Woinowsky-Krieger (1959)) and used in Bathe & Dvorkin (1985). However, solid-shell elements using only displacements degrees of freedom and based in particular on the Reissner-Mindlin theory, use shape functions that are not able to describe the kinematics induced by bending in the thickness direction which may be responsible for locking occurrences. The main locking problems comprise: transverse shear locking cited above, volumetric locking, Poisson thickness locking, curvature or trapezoidal locking and membrane locking. The transverse shear locking may occur when a shell element with a thickness tending to zero is subject to bending.

Among the most popular methods to solve transverse shear locking is the Assumed Natural Strain (ANS) method, used for example in Dvorkin & Bathe (1984) to remedy to transverse shear locking in shell elements. Then, Klinkel et al. (2006), Kim et al. (2005) and more recently Hannachi (2007) introduced it in solid-shell elements. According to ANS method, the natural transverse shear strains are calculated in four sampling points located at the center of the element mid-surface edges. The transverse shear strain is then calculated at element integration points by interpolating the strains evaluated at the element mid-surface. However, the four sampling points used above are sufficient only in fully integrated elements to provide a good accuracy. An extended ANS method using eight sampling points initially introduced in Cardoso et al. (2008) and also used in Schwarze & Reese (2009) and Nguyen (2009) is however preferred for reduced integration elements.

Another popular technique, used to eliminate transverse shear locking is the enhanced assumed strain (EAS) method which consists in adding, in the deformation field, a field of internal variables that creates additional modes of deformation. The EAS approach is employed for example in the work of Andelfinger & Ramm (1993), Alves de Sousa et al. (2003) and in the work of Wriggers et al. (1996), Alves de Sousa et al. (2005), Li et al. (2011) and Fontes Valente et al. (2004) for small and for large deformations, respectively. The volumetric locking can occur when a given material remains nearly incompressible or incompressible. Simo & Rifai (1990) have demonstrated that applying the EAS method is a way to reduce the volumetric locking issue. The Poisson thickness locking may take place when the hypothesis of a linear displacement variation is considered in thickness direction, and thus when the thickness strain remains constant. In this last case, inconsistencies may arise since the thickness strain varies linearly as a combination between Poisson's effect and in-plane strain (Büchter et al. (1994)). More recently Schwarze & Reese (2009) have successfully used this EAS technique in an eight-node solid shell element in a full 3D integration context in order to avoid the Poisson thickness locking. The curvature or trapezoidal locking may appear when an element is used to mesh curved structures and thus when an edge in the thickness direction of a given element is not perpendicular to its mid-surface. Following the same idea as for transverse shear locking treatment, Betsch et al. (1996) applied the ANS method to tackle curvature locking. Accordingly, the natural thickness strain is calculated in four sampling points located at the corners of the element

mid-surface. It is then interpolated at the integration points. The membrane locking could emanate from a configuration whereby membrane strains remain very small as compared with bending strains in thin structure bending problems. Moreover, mesh distortion may also be responsible for membrane locking. In order to overcome membrane locking issues, Miehe (1998) developed a solid type element using one enhanced parameter.

In spite of the prolific and insightful prior research aiming at improving the FEM, there are still some unresolved issues such as those related to element distortion and numerical integration. In an effort to enhance the accuracy of numerical solutions for irregular meshes, an approximation method named the smoothed finite element method (SFEM) was recently proposed by Liu, Dai, et al. (2007) - Liu, Nguyen, et al. (2007). This method integrates the conventional FEM technology and the strain smoothing technique that was introduced by Chen et al. (2001) while devising a stabilized nodal integration scheme in mesh-free methods (element free Galerkin method). Essentially, the SFEM consists in dividing each element into smoothing cells over which a strain smoothing operation is performed and the strain energy in each smoothing cell is expressed as an explicit form of the smoothed strain. A subsequent use of the divergence theorem allows then the integration to be transformed into integration on the cell boundary with no more requirements to use shape function derivative. In Liu, Dai, et al. (2007), the SFEM was applied to a two dimensional static continuum element and implemented in a four-node quadrilateral and polygonal elements. Compared with standard FEM method, the work of Liu, Dai, et al. (2007) and Liu, Nguyen, et al. (2007) indicate that SFEM has interesting features such as: i) simplicity of the method, since no cartesian derivatives of shape functions are used; ii) elimination of the inverse of the jacobian matrix; iii) apparent insensitivity of the SFEM to mesh distortion. This thus makes finite elements based on this technique more attractive in situations requiring convergence for very complex mesh and / or adaptive meshing when standard finite elements are used; iv) compared with standard finite elements, the proposed SFEM elements appear to be more accurate and significantly more attractive in terms of computer time efficiency. Results accuracy could also be increased by using more smoothing cells.

The variational weak form used in SFEM can be derived from the Hu-Washizu three-fields variational principle or by the assumed strain method proposed by Simo & Hughes (1986). Liu, Nguyen, et al. (2007) then detailed the SFEM theory and found that it remains equivalent to standard FEM theory for one dimension as well as for two dimensional (2D) triangular elements contrasting with quadrilateral elements. Moreover, they investigated on the variational consistency of this last type of element regarding the number of smoothing cells used. They observed that if the formulation remains variationally consistent with one cell, this observation does not hold in case of multiple cells use. However, when using the same set of shape functions for a given element, the formulation still remains energy consistent since the element nodal displacements remain continuous. Nguyen-Xuan et al. (2008) and Bordas & Natarajan (2009), in their theoretical study of convergence, accuracy and properties of SFEM technique, also contributed to a better understanding of SFEM and gave a good overview of the SFEM driving concept as well as some interesting results obtained with a SFEM quadrilateral shell element. The SFEM applied previously to static problems was extended to 2D dynamic problems in Dai & Liu (2007a) and in Dai & Liu (2007b). It is demonstrated in these papers that the approach yields better results than standard quadrilateral finite elements. The SFEM was initially used with conventional isoparametric elements in Liu, Dai, et al. (2007). An extension of the method to polygonal elements is then performed in Dai et al. (2007) and further extended to node-centered (Liu et al. (2009)) and edge-centered (Nguyen-Thoi et al. (2011)). It is observed that SFEM for general n-sided polygonal elements works well and yield very accurate results, especially in case of heavily distorted meshes. However, due to the corresponding high computational cost induced by the higher number of nodes inherent to the technique, they suggest to use a combination of nSFEM and quadrilateral SFEM elements to respectively mesh the exterior and the interior of a part. Nguyen-Thanh et al. (2007) investigated on some methods to cure shear as well as incompressible locking problems for quadrilateral SFEM elements. They successfully presented three selective integration schemes. Scheme 1 is based on the decomposition of the material matrix into two parts; one containing the shear modulus or μ terms and another containing the remaining terms. Scheme 2 is based on the B-bar approach of Hughes (1980) to overcome volumetric locking. Scheme 3, used to overcome shear locking, consists in using different smoothing cell numbers for each stiffness matrix

contribution. However, this last scheme does not seem to be attractive compared with standard finite elements, since shear stiffness matrix still needs Gauss integration points to be determined. Then, various developments have been made on SFEM quadrilateral plate and shell elements. For example, H. Nguyen-Xuan et al. (2008) developed a four node plate element using the SFEM to deal with membrane and bending stiffness matrix components. Their proposed element exhibited good accuracy and time efficiency compared with equivalent standard element. Nguyen-Thanh et al. (2008) then extended this work to quadrilateral flat shell elements and emphasized the high potential capabilities of the SFEM. Unlike the MITC4 element which uses an isoparametric mapping, their proposed element calculates the membrane and bending parts of the stiffness matrix directly in the local cartesian coordinates system. As a matter of fact, it remains accurate even with a distorted mesh. Moreover, this new element is found to be insensitive to mesh distortion when compared to the standard MITC4 element. The extension of SFEM to 3D solid continuum elements is proposed by Nguyen-Xuan (2008) and Bordas et al. (2010). In their work, they used a stabilization technique to avoid membrane and volumetric locking. This is consistent with the stabilization technique used in mesh free method proposed by Puso & Solberg (2006). In order to reduce computation time, their 3D stiffness matrix is calculated using reduced integration on each facet of the element cells, instead of a standard 2×2 Gauss quadrature formula. However, in order to keep some element efficiency and to eliminate the zero energy modes, a stabilization strategy was developed. This method results in considering the stiffness matrix as a linear combination of the one subcell element and the four or eight subcell element. Due to the relative novelty of the SFEM, its non-linear development and associated applications still remain limited. Cui et al. (2008) developed quadrilateral non-linear SFEM plate and shell elements. They then illustrated their good accuracy as well as their rapid convergence compared with the analytic solutions. Moreover, Liu et al. (2010) successfully compared a quadrilateral shell element using SFEM with classical finite element through non-linear examples using plastic materials. More recently, Élie-Dit-Cosaque et al. (2011) developed a non-linear resultant eight-node solid-shell element. Their proposed element gives encouraging results but some developments are still required in order to improve its accuracy in non-linear applications. One should also mention a method called the partition element method (PEM) detailed in

Rashid & Sadri (2012). In this method, similarly to SFEM, an element is divided into quadrature cells over which the shape functions are piecewise linear. The averaged strain operators are then calculated in each cell. A major difference between the PEM and the SFEM is that the PEM method allows arbitrary cells definition which gives it greater flexibility.

In summary, previous works on the SFEM have observed the following main features of the method:

- Simple implementation.
- Insensitivity to mesh distortion.
- Better accuracy as well as convergence compared with standard equivalent finite element in many cases.
- Time efficiency.

However, to the best of our knowledge, the following issues are either scarce or did not receive much attention:

- A full assessment of the theoretical basis of the stabilization techniques proposed in Nguyen-Xuan (2008) and Bordas et al. (2010) is still an open issue.
- The performance of the eight-node solid element using the SFEM in case of distorted mesh.
- Application of SFEM shell elements formulation to geometric and material non-linear problems.
- Implementation of the SFEM approach in solid-shell elements.

In the present chapter, the SFEM is applied to an eight node resultant solid-shell element presented in Kim et al. (2005) as an extension of the classical resultant shell theory and in Simo et al. (1993), in order to evaluate the membrane and bending element stiffness. The strain smoothing method is then applied in a way similar to that applied to a quadrilateral

shell element (Nguyen-Thanh et al. (2008)) without any use of stabilization since no reduced integration is required. A preliminary simplified version of this work has already been proposed in Élie-Dit-Cosaque et al. (2011). A complete development of the smoothing technique is proposed in the following sections. In order to get rid of element locking problems inherent to the proposed solid-shell element extended to SFEM formulation, the well-known ANS method is applied, in a way that is similar to the procedure proposed in Bordas et al. (2010). The trapezoidal effect is also eliminated by using the ANS technique. Special care has been taken in order to adequately explain how the SFEM is applied to a resultant solid-shell formulation. This chapter is organized as follows. In sections 4.2, 4.3 and 4.4, the geometric description, the kinematics and the finite element approximation of the resultant solid-shell element are presented. The related virtual work principle is then presented in section 4.5. The SFEM approximation applied to solid-shell element and its parameters are then discussed in section 4.6. The details of SFEM discretization of the weak form and the computer implementation including detailed element stiffness matrix structures are then given. Various benchmark examples for geometrically linear problems are presented in section 4.7 to validate the approach. Finally, a conclusion is given in the last section.

4.2. Geometric description

A solid-shell element based on Reissner-Mindlin kinematics is considered and represented parametrically as in Figure 4.1 and for which only three displacement degrees of freedom are introduced at each node as in a standard solid element Hauptmann & Schweizerhof (1998).

In order to describe the shell-like behavior of the eight-node solid element, it is useful to introduce a set of three coordinates systems as shown in Figure 4.2 inspired from Vu-Quoc & Tan (2003) and further detailed in Table 4.1: a global cartesian coordinates system $\mathbf{X}(X,Y,Z)$, a convected coordinates system $\boldsymbol{\xi}(\xi^1,\xi^2,\xi^3)$ and a local cartesian coordinates system $\mathbf{x}(x\ ,y\ ,z\ )$ whose orientation changes with the configuration. The latter is set up in the element mid-surface in order to be able to handle shell features such as membrane, bending and shear behavior of thin shell structures. The relationships between the different

coordinates basis are given in several monographs and papers as in Domissy (1997) and Hannachi (2007).

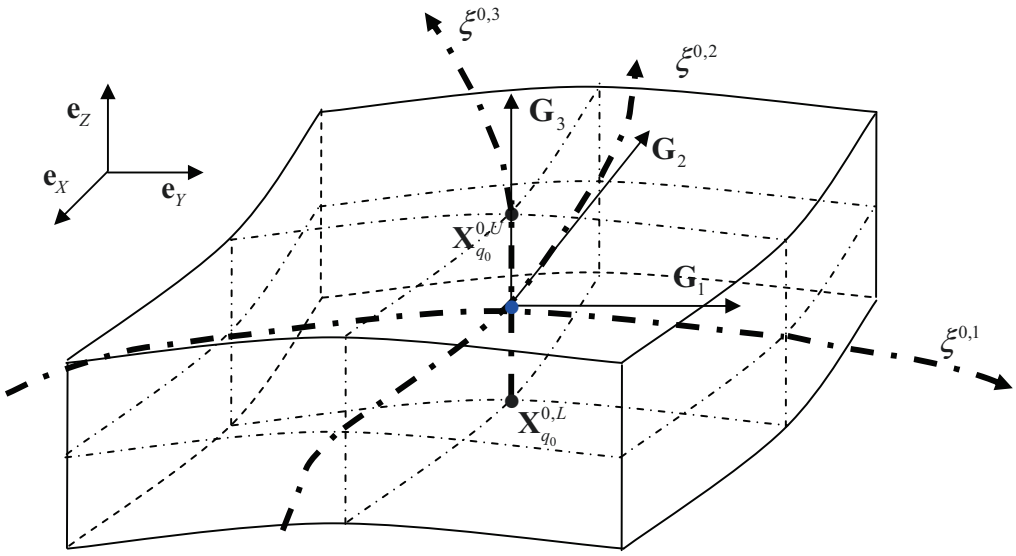

Figure 4.1: Solid-shell element parametrization, undeformed configuration

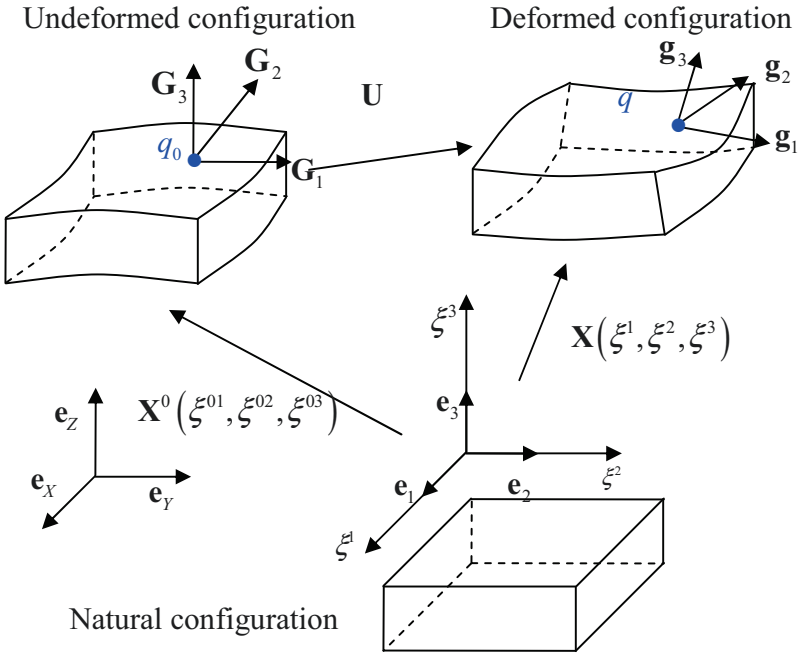

Figure 4.2: Solid-shell element configurations

Table 4.1: Coordinates systems definition		
Level	Base vectors	Coordinates
Global cartesian	$\left(\mathbf{e}_X, \mathbf{e}_Y, \mathbf{e}_Z\right)$	$\mathbf{X}^0\left(X^0, Y^0, Z^0\right)$ or $\mathbf{X}_i^0, \quad i=1,2,3$ undeformed configuration
		$\mathbf{X}\left(X, Y, Z\right)$ or $\mathbf{X}_i, \quad i=1,2,3$ deformed configuration
Natural	$\left(\mathbf{G}_1, \mathbf{G}_2, \mathbf{G}_3\right)$ $\left(\mathbf{g}_1, \mathbf{g}_2, \mathbf{g}_3\right)$	$\xi\left(\xi^{0,1}, \xi^{0,2}, \xi^{0,3}\right)$ or $\xi^{0,i}, \quad i=1,2,3$
		$\xi\left(\xi^1, \xi^2, \xi^3\right)$ or $\xi^i, \quad i=1,2,3$
Local cartesian	$\left(\mathbf{R}_x, \mathbf{R}_y, \mathbf{R}_z\right)$ $\left(\mathbf{r}_x, \mathbf{r}_y, \mathbf{r}_z\right)$	$\mathbf{x}^0\left(x^0, y^0, z^0\right)$ or $\mathbf{x}_i^0, \quad i=1,2,3$ undeformed configuration
		$\mathbf{x}\left(x, y, z\right)$ or $\mathbf{x}_i, \quad i=1,2,3$ deformed configuration

The coordinates of an arbitrary point q_0 on the solid-shell structure in the undeformed configuration can then be defined in term of the position vector represented parametrically by:

$$\mathbf{X}_{q_0}^0\left(\xi^1, \xi^2, \xi^3\right) = \frac{(1+\xi^3)}{2} \times \mathbf{X}^{0,U}(\xi^1, \xi^2) + \frac{(1-\xi^3)}{2} \times \mathbf{X}^{0,L}(\xi^1, \xi^2) \qquad \left(-1 \le \xi^1, \xi^2, \xi^3 \le 1\right) \tag{4.1}$$

which after introducing the mid-surface concepts and considering the parameter ξ^3 as the thickness direction (see Figure 4.3), can also be written as :

$$\mathbf{X}_{q_0}^0\left(\xi^1, \xi^2, \xi^3\right) = \bar{\mathbf{X}}^0\left(\xi^1, \xi^2\right) + \xi^3 \times \Delta\mathbf{X}^0\left(\xi^1, \xi^2\right), \quad \left(-1 \le \xi^1, \xi^2, \xi^3 \le 1\right) \tag{4.2}$$

where, $\mathbf{X}^{0,L}$ and $\mathbf{X}^{0,U}$ are respectively the position vector of a point on the lower and on the upper surface in the global cartesian coordinates system $\mathbf{X}^0\left(X^0, Y^0, Z^0\right)$ of the undeformed

configuration, $\bar{\mathbf{X}}^0 = \dfrac{\mathbf{X}^{0,U} + \mathbf{X}^{0,L}}{2}$ is the position vector of the mid-surface and $\Delta\mathbf{X}^0 = \dfrac{\mathbf{X}^{0,U} - \mathbf{X}^{0,L}}{2}$ a director vector pointing from the lower to the upper surface.

In the deformed configuration, the coordinates of an arbitrary point q in the global cartesian coordinates system $\mathbf{X}(X,Y,Z)$ can similarly be represented as:

$$\mathbf{X}_q\left(\xi^1,\xi^2,\xi^3\right) = \bar{\mathbf{X}}\left(\xi^1,\xi^2\right) + \xi^3 \times \Delta\mathbf{X}\left(\xi^1,\xi^2\right), \quad \left(-1 \le \xi^1,\xi^2,\xi^3 \le 1\right) \tag{4.3}$$

By introducing the displacements field vector $\mathbf{U}_q$, the undeformed and the deformed configurations are related by the standard mapping at point q, as:

$$\mathbf{X}_q\left(\xi^1,\xi^2,\xi^3\right) = \mathbf{X}^0_{q_0}\left(\xi^1,\xi^2,\xi^3\right) + \mathbf{U}_q\left(\xi^1,\xi^2,\xi^3\right) \tag{4.4}$$

in the global cartesian coordinates system $\mathbf{X}(X,Y,Z)$. Similarly, as in equations (4.2) and (4.3), by using mid-surface related parameters, the displacement vector in equation (4.4) can be written as:

$$\mathbf{U}_q\left(\xi^1,\xi^2,\xi^3\right) = \bar{\mathbf{U}}\left(\xi^1,\xi^2\right) + \xi^3 \times \Delta\mathbf{U}\left(\xi^1,\xi^2\right), \quad \left(-1 \le \xi^1,\xi^2,\xi^3 \le 1\right) \tag{4.5}$$

where $\bar{\mathbf{U}}$ and $\Delta\mathbf{U}$ are defined as $\bar{\mathbf{U}} = \dfrac{\mathbf{U}^U + \mathbf{U}^L}{2}$ and $\Delta\mathbf{U} = \dfrac{\mathbf{U}^U - \mathbf{U}^L}{2}$, with $\mathbf{U}^L$ and $\mathbf{U}^U$ are respectively the displacement vector of a point on the lower and on the upper surface of the shell structure.

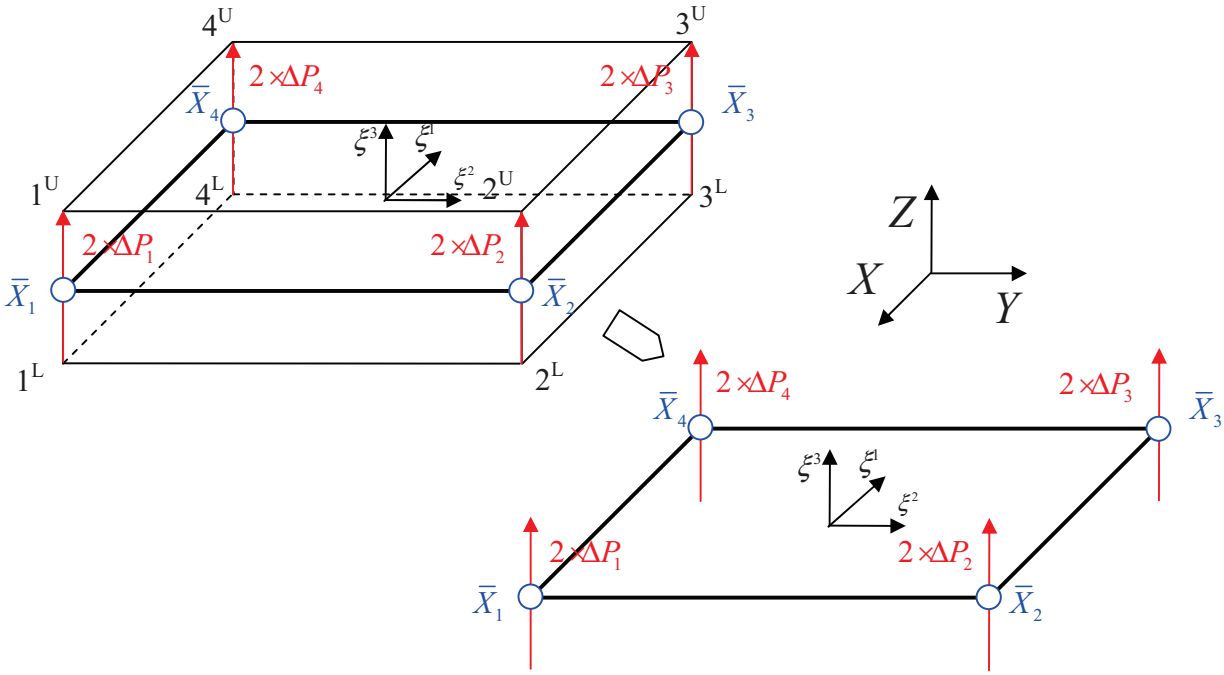

Figure 4.3: Resultant eight-node solid-shell element geometry and mid-surface concept

The covariant base vectors $\left(\mathbf{G}_1,\mathbf{G}_2,\mathbf{G}_3\right)$ respectively the contravariant base vectors $\left(\mathbf{G}^1,\mathbf{G}^2,\mathbf{G}^3\right)$ in the undeformed configuration take the forms:

$$\mathbf{G}_i=\frac{\partial \mathbf{X}^0}{\partial \xi^i},\quad i=1,2,3 \tag{4.6}$$

$$\mathbf{G}^i=\frac{\partial \xi^i}{\partial \mathbf{X}^0},\quad i=1,2,3 \tag{4.7}$$

In the same idea, the covariant base vectors $\left(\mathbf{g}_1,\mathbf{g}_2,\mathbf{g}_3\right)$, respectively the contravariant base vectors $\left(\mathbf{g}^1,\mathbf{g}^2,\mathbf{g}^3\right)$ in the deformed configuration take the forms:

$$\mathbf{g}_i=\frac{\partial \mathbf{X}}{\partial \xi^i},\quad i=1,2,3 \tag{4.8}$$

$$\mathbf{g}^i = \frac{\partial \xi^i}{\partial \mathbf{X}}, \quad i = 1,2,3 \tag{4.9}$$

The local cartesian base vectors are defined in the undeformed configuration from the covariant base vectors as :

$$\mathbf{R}_z = \frac{\mathbf{G}_1 \wedge \mathbf{G}_2}{\left\| \mathbf{G}_1 \wedge \mathbf{G}_2 \right\|} \tag{4.10}$$

$$\mathbf{R}_x = \frac{\mathbf{G}_1}{\left\| \mathbf{G}_1 \right\|} \tag{4.11}$$

$$\mathbf{R}_y = \mathbf{R}_z \wedge \mathbf{R}_x \tag{4.12}$$

Similarly, the local cartesian base vectors are defined in the deformed configuration from the covariant base vectors as :

$$\mathbf{r}_z = \frac{\mathbf{g}_1 \wedge \mathbf{g}_2}{\left\| \mathbf{g}_1 \wedge \mathbf{g}_2 \right\|} \tag{4.13}$$

$$\mathbf{r}_x = \frac{\mathbf{g}_1}{\left\| \mathbf{g}_1 \right\|} \tag{4.14}$$

$$\mathbf{r}_y = \mathbf{r}_z \wedge \mathbf{r}_x \tag{4.15}$$

So, the local cartesian coordinates $\mathbf{x}\left(x, y, z\right)$ are related to the global cartesian coordinates $\mathbf{X}\left(X, Y, Z\right)$ through the transformation matrix $\mathbf{Q}_1 = \left[\mathbf{r}_x \quad \mathbf{r}_y \quad \mathbf{r}_z \right]$ such that the local components of a position or displacement vector $\mathbf{u}_q = \left\langle \mathbf{u} \quad \mathbf{v} \quad \mathbf{w} \right\rangle$ of an arbitrary point q are given by:

$$\mathbf{x}_q = \mathbf{Q}_1^T \times \mathbf{X}_q \tag{4.16}$$

$$\mathbf{u}_q = \mathbf{Q}_1^T \times \mathbf{U}_q \tag{4.17}$$

For sake of simplify, the subscript $\left(\right)_q$ is omitted in the subsequent developments.

4.3. Kinematics of shell deformation

The Green-Lagrange strain tensor components ε_{kl}^{ξ}, oriented in the natural coordinates system $\xi\left(\xi^1,\xi^2,\xi^3\right)$ are (see Vu-Quoc & Tan (2003) for more detail):

$$\varepsilon_{kl}^{\xi}=\frac{1}{2}\left(\mathbf{g}_i\frac{\partial\mathbf{u}}{\xi^j}+\frac{\partial\mathbf{u}}{\xi^i}\mathbf{g}_j+\frac{\partial\mathbf{u}}{\xi^i}\frac{\partial\mathbf{u}}{\xi^j}\right),\quad i,j=1,2,3 \tag{4.18}$$

Considering only the linear terms, the above equation (4.18) yields in:

$$\varepsilon_{kl}^{\xi}=\frac{1}{2}\left(\mathbf{g}_i\frac{\partial\mathbf{u}}{\xi^j}+\frac{\partial\mathbf{u}}{\xi^i}\mathbf{g}_j\right),\quad i,j=1,2,3 \tag{4.19}$$

Considering equation (4.19) components by components, the components of ε_{kl}^{ξ} are then:

$$\begin{aligned}
\varepsilon_{11}^{\xi}&=\mathbf{g}_1\times\frac{\partial\mathbf{u}}{\partial\xi^1} & \varepsilon_{22}^{\xi}&=\mathbf{g}_2\times\frac{\partial\mathbf{u}}{\partial\xi^2} & \gamma_{12}^{\xi}&=\mathbf{g}_1\times\frac{\partial\mathbf{u}}{\partial\xi^2}+\mathbf{g}_2\times\frac{\partial\mathbf{u}}{\partial\xi^1}\\
\gamma_{13}^{\xi}&=\mathbf{g}_1\times\frac{\partial\mathbf{u}}{\partial\xi^3}+\mathbf{g}_3\times\frac{\partial\mathbf{u}}{\partial\xi^1} & \gamma_{23}^{\xi}&=\mathbf{g}_2\times\frac{\partial\mathbf{u}}{\partial\xi^3}+\mathbf{g}_3\times\frac{\partial\mathbf{u}}{\partial\xi^2} & \varepsilon_{33}^{\xi}&=\mathbf{g}_3\times\frac{\partial\mathbf{u}}{\partial\xi^3}
\end{aligned} \tag{4.20}$$

The Green-Lagrange strain tensor $\boldsymbol{\varepsilon}$, can be formulated in the directions of the local cartesian base vectors as:

$$\boldsymbol{\varepsilon}=\varepsilon_{ij}\mathbf{r}_i\otimes\mathbf{r}_j,\quad i,j=1,2,3 \tag{4.21}$$

It can also be formulated in the directions of the contravariant base vector $\left(\mathbf{g}^1,\mathbf{g}^2,\mathbf{g}^3\right)$ defined in equation (4.9) as:

$$\begin{aligned}
\boldsymbol{\varepsilon}&=\varepsilon_{kl}^{\xi}\mathbf{g}^k\otimes\mathbf{g}^l\\
&=\varepsilon_{kl}^{\xi}\frac{\partial\xi^k}{\partial x_i}\mathbf{r}_i\otimes\frac{\partial\xi^l}{\partial x_j}\mathbf{r}_j\\
&=\varepsilon_{kl}^{\xi}\frac{\partial\xi^k}{\partial x_i}\frac{\partial\xi^l}{\partial x_j}\mathbf{r}_i\otimes\mathbf{r}_j,\quad i,j,k,l=1,2,3
\end{aligned} \tag{4.22}$$

Identifying the terms of equations (4.21) and (4.22), the transformation between the local cartesian and the natural components of the Green-Lagrange strain tensor respectively ε_{ij} and ε_{kl}^{ξ} is:

$$\varepsilon_{ij} = \varepsilon_{kl}^{\xi} \frac{\partial \xi^k}{\partial x_i} \frac{\partial \xi^l}{\partial x_j}, \quad i,j,k,l = 1,2,3 \tag{4.23}$$

Starting from the deformation gradient $\mathbf{F}$ defined in term of the displacements field described in equation (4.5) as $\mathbf{F} = \frac{\partial \mathbf{x}}{\partial \mathbf{X}} = \mathbf{I} + \nabla_X \mathbf{u}$, the Green-Lagrange strain tensor $\boldsymbol{\varepsilon}$ oriented in the local cartesian coordinates system can be written as:

$$\boldsymbol{\varepsilon} = \frac{1}{2}\left(\mathbf{F}^T\mathbf{F} - \mathbf{I}\right) = \frac{1}{2}\left\{\left(\nabla_X \mathbf{u}\right) + \left(\nabla_X \mathbf{u}\right)^T + \left(\nabla_X \mathbf{u}\right)^T \left(\nabla_X \mathbf{u}\right)\right\} \tag{4.24}$$

Limiting the following development to the linear strain components as for the natural expression of the Green-Lagrange strain tensor gives:

$$\boldsymbol{\varepsilon} = \frac{1}{2}\left\{\left(\nabla_X \mathbf{u}\right) + \left(\nabla_X \mathbf{u}\right)^T\right\} \tag{4.25}$$

Following the concepts introduced in equation (4.5), the displacements vector can also be written as:

$$\mathbf{u} = \left\langle \mathbf{u} \quad \mathbf{v} \quad \mathbf{w} \right\rangle^T = \left\langle \overline{\mathbf{u}} + \xi^3 \times \Delta\mathbf{u} \quad \overline{\mathbf{v}} + \xi^3 \times \Delta\mathbf{v} \quad \overline{\mathbf{w}} + \xi^3 \times \Delta\mathbf{w} \right\rangle^T \tag{4.26}$$

with $\overline{\mathbf{u}} = \begin{Bmatrix} \overline{u} \\ \overline{v} \\ \overline{w} \end{Bmatrix}$ as the displacement mean value on the mid-surface and $\Delta\mathbf{u} = \begin{Bmatrix} \Delta u \\ \Delta v \\ \Delta w \end{Bmatrix}$ as the through-thickness relative displacement vector.

Separating the in-plane and the out-of-plane degrees of freedoms from this latter, the displacements vector for the resultant theory can then be defined as:

$$\breve{\mathbf{u}} = \left\langle \overline{u} \quad \overline{v} \quad \overline{w} \quad \Delta u \quad \Delta v \quad \Delta w \right\rangle^{T} \tag{4.27}$$

Then, using the displacement vector defined as in equation (4.5), the linear terms of the Green-Lagrange strain tensor can be expressed in the local cartesian coordinates system $\mathbf{x}\left(x\ ,y\ ,z\ \right)$ as:

$$\begin{aligned}
\varepsilon_{xx} &= \frac{\partial u}{\partial x} = \frac{\partial \overline{u}}{\partial x} + \xi^3 \times \frac{\partial \Delta u}{\partial x}; \qquad \varepsilon_{yy} = \frac{\partial v}{\partial y} = \frac{\partial \overline{v}}{\partial y} + \xi^3 \times \frac{\partial \Delta v}{\partial y}; \\
\gamma_{xy} &= \frac{\partial u}{\partial y} + \frac{\partial v}{\partial x} = \frac{\partial \overline{u}}{\partial y} + \frac{\partial \overline{v}}{\partial x} + \xi^3 \times \left(\frac{\partial \Delta u}{\partial y} + \frac{\partial \Delta v}{\partial x} \right) \\
\varepsilon_{zz} &= \frac{\partial w}{\partial z} = \frac{\partial \overline{w}}{\partial z} + \frac{\partial \xi^3}{\partial z} \times \Delta w + \xi^3 \times \frac{\partial \Delta w}{\partial z} \\
\gamma_{yz} &= \frac{\partial v}{\partial z} + \frac{\partial w}{\partial y} = \frac{\partial \overline{v}}{\partial z} + \frac{\partial \overline{w}}{\partial y} + \xi^3 \times \left(\frac{\partial \Delta v}{\partial z} + \frac{\partial \Delta w}{\partial y} \right) + \frac{\partial \xi^3}{\partial z} \times \Delta v \\
\gamma_{xz} &= \frac{\partial u}{\partial z} + \frac{\partial w}{\partial x} = \frac{\partial \overline{u}}{\partial z} + \frac{\partial \overline{w}}{\partial x} + \xi^3 \times \left(\frac{\partial \Delta u}{\partial z} + \frac{\partial \Delta w}{\partial x} \right) + \frac{\partial \xi^3}{\partial z} \times \Delta u
\end{aligned} \tag{4.28}$$

Developing the terms of equation (4.23) and reorganizing the obtained equations in tensor and matrix forms, the transformation of the Green-Lagrange strain tensor components from the natural to the local coordinates system can be expressed as:

$$\begin{Bmatrix} \varepsilon_{xx} \\ \varepsilon_{yy} \\ \varepsilon_{zz} \\ \gamma_{xy} \\ \gamma_{yz} \\ \gamma_{xz} \end{Bmatrix} = \mathbf{T} \times \begin{Bmatrix} \varepsilon_{11}^{\xi} \\ \varepsilon_{22}^{\xi} \\ \varepsilon_{33}^{\xi} \\ \gamma_{12}^{\xi} \\ \gamma_{23}^{\xi} \\ \gamma_{13}^{\xi} \end{Bmatrix} \tag{4.29}$$

where

$$\mathbf{T}=\begin{bmatrix} j_{11}^2 & j_{21}^2 & j_{31}^2 & j_{11}j_{21} & j_{21}j_{31} & j_{11}j_{31} \\ j_{12}^2 & j_{22}^2 & j_{32}^2 & j_{12}j_{22} & j_{22}j_{32} & j_{12}j_{32} \\ j_{13}^2 & j_{23}^2 & j_{33}^2 & j_{13}j_{23} & j_{23}j_{33} & j_{13}j_{33} \\ 2j_{11}j_{12} & 2j_{21}j_{22} & 2j_{31}j_{32} & j_{12}j_{21}+j_{11}j_{22} & j_{22}j_{31}+j_{21}j_{32} & j_{12}j_{31}+j_{11}j_{32} \\ 2j_{12}j_{13} & 2j_{22}j_{23} & 2j_{32}j_{33} & j_{23}j_{12}+j_{22}j_{13} & j_{23}j_{32}+j_{22}j_{33} & j_{13}j_{32}+j_{12}j_{33} \\ 2j_{11}j_{13} & 2j_{21}j_{23} & 2j_{31}j_{33} & j_{23}j_{11}+j_{21}j_{13} & j_{23}j_{31}+j_{21}j_{33} & j_{13}j_{31}+j_{11}j_{33} \end{bmatrix} \quad (4.30)$$

with $j_{ij}=J_{ij}^{-1}=\left(\mathbf{g}_i \times \mathbf{r}_j\right)^{-1}$ the inverse of the components of the matrix $\mathbf{J}$ such that $\mathbf{J}=\mathbf{g}_i \otimes \mathbf{r}_j$. Equation (4.30) expressed on the mid-surface $\xi^3=0$ simplifies to $\mathbf{T}_{\xi^3=0}$:

$$\mathbf{T}_{\xi^3=0}=\begin{bmatrix} j_{11}^2 & j_{21}^2 & 0 & j_{11}j_{21} & 0 & 0 \\ j_{12}^2 & j_{22}^2 & 0 & j_{12}j_{22} & 0 & 0 \\ 0 & 0 & j_{33}^2 & 0 & 0 & 0 \\ 2j_{11}j_{12} & 2j_{21}j_{22} & 0 & j_{12}j_{21}+j_{11}j_{22} & 0 & 0 \\ 0 & 0 & 0 & 0 & j_{22}j_{33} & j_{12}j_{33} \\ 0 & 0 & 0 & 0 & j_{21}j_{33} & j_{11}j_{33} \end{bmatrix} \quad (4.31)$$

However, the calculations required for evaluating the terms of the inverse $\mathbf{J}^{-1}$ of the jacobian matrix may be laborious and are likely to induce matrix transformations that are potentially computational time consuming, as illustrated in Kim et al. (2005). Nevertheless, introducing the strain smoothing techniques in the context of finite element or SFEM technique to calculate membrane and bending components helps avoiding such calculations as their integration is made in the local cartesian coordinates system $\mathbf{x}\left(x\ ,y\ ,z\ \right)$ after smoothing operation which eliminates the calculation of Cartesian derivatives of shape functions. Those techniques are presented in the following sections.

Separating the strain tensor components of equations (4.28) into membrane-bending $\boldsymbol{\varepsilon}^{mb}$, transverse shear $\boldsymbol{\gamma}$ and transverse normal $\boldsymbol{\varepsilon}^{zz}$, the linear strain vector can be written in line with the work proposed in Kim et al. (2005) in compact form as:

$$\boldsymbol{\varepsilon}=\begin{Bmatrix} \boldsymbol{\varepsilon}^{mb} \\ \boldsymbol{\gamma} \\ \varepsilon_{zz} \end{Bmatrix}=\begin{Bmatrix} \boldsymbol{\varepsilon}^{m}+\xi^3 \times \boldsymbol{\varepsilon}^{b} \\ \boldsymbol{\gamma} \\ \varepsilon_{zz} \end{Bmatrix} \quad (4.32)$$

In equation (4.32), $\boldsymbol{\varepsilon}^{mb}$ is the combination of the membrane and the bending strains components, $\boldsymbol{\varepsilon}^{m}$ respectively $\boldsymbol{\varepsilon}^{b}$ such that $\boldsymbol{\varepsilon}^{mb} = \begin{Bmatrix} \boldsymbol{\varepsilon}_{xx} \\ \boldsymbol{\varepsilon}_{yy} \\ \boldsymbol{\gamma}_{xy} \end{Bmatrix} = \boldsymbol{\varepsilon}^{m} + \xi^{3} \times \boldsymbol{\varepsilon}^{b}$. Writing equations (4.28) in matrix form:

$$\boldsymbol{\varepsilon}^{m} = \begin{Bmatrix} \dfrac{\partial \overline{u}}{\partial x} \\ \dfrac{\partial \overline{v}}{\partial y} \\ \dfrac{\partial \overline{u}}{\partial y} + \dfrac{\partial \overline{v}}{\partial x} \end{Bmatrix} = \mathbf{B}^{m} \times \breve{\mathbf{u}} \tag{4.33}$$

with membrane strain operator defined as:

$$\mathbf{B}^{m} = \begin{bmatrix} \dfrac{\partial}{\partial x} & 0 & 0 & 0 & 0 & 0 \\ 0 & \dfrac{\partial}{\partial y} & 0 & 0 & 0 & 0 \\ \dfrac{\partial}{\partial y} & \dfrac{\partial}{\partial x} & 0 & 0 & 0 & 0 \end{bmatrix} \tag{4.34}$$

and where:

$$\boldsymbol{\varepsilon}^{b} = \begin{Bmatrix} \dfrac{\partial \Delta u}{\partial x} \\ \dfrac{\partial \Delta v}{\partial y} \\ \dfrac{\partial \Delta u}{\partial y} + \dfrac{\partial \Delta v}{\partial x} \end{Bmatrix} = \mathbf{B}^{b} \times \breve{\mathbf{u}} \tag{4.35}$$

with bending strain operator defined as:

$$\mathbf{B}^b = \begin{bmatrix} 0 & 0 & 0 & \dfrac{\partial}{\partial x} & 0 & 0 \\ 0 & 0 & 0 & 0 & \dfrac{\partial}{\partial y} & 0 \\ 0 & 0 & 0 & \dfrac{\partial}{\partial y} & \dfrac{\partial}{\partial x} & 0 \end{bmatrix} \tag{4.36}$$

From equations (4.28), the matrix expressions of the transverse shear strain $\boldsymbol{\gamma}$ and the transverse normal strain ε_{zz} are also obtained:

The transverse shear strains $\boldsymbol{\gamma} = \begin{Bmatrix} \gamma_{yz} \\ \gamma_{xz} \end{Bmatrix}$ can be written in matrix form as:

$$\begin{Bmatrix} \gamma_{yz} \\ \gamma_{xz} \end{Bmatrix} = \begin{Bmatrix} 0 & \dfrac{\partial \overline{v}}{\partial z} & \dfrac{\partial \overline{w}}{\partial y} & 0 & \xi^3 \times \dfrac{\partial \Delta v}{\partial z} + \dfrac{\partial \xi^3}{\partial z} \times \Delta v & \xi^3 \times \dfrac{\partial \Delta w}{\partial y} \\ \dfrac{\partial \overline{u}}{\partial z} & 0 & \dfrac{\partial \overline{w}}{\partial x} & \xi^3 \times \dfrac{\partial \Delta u}{\partial z} + \dfrac{\partial \xi^3}{\partial z} \times \Delta u & 0 & \xi^3 \times \dfrac{\partial \Delta w}{\partial x} \end{Bmatrix} = \mathbf{B}^{\gamma} \times \breve{\mathbf{u}} \tag{4.37}$$

where $\mathbf{B}^{\gamma}$ is:

$$\mathbf{B}^{\gamma} = \begin{bmatrix} 0 & \dfrac{\partial}{\partial z} & \dfrac{\partial}{\partial y} & 0 & \xi^3 \times \dfrac{\partial}{\partial z} + \dfrac{\partial \xi^3}{\partial z} & \xi^3 \times \dfrac{\partial}{\partial y} \\ \dfrac{\partial}{\partial z} & 0 & \dfrac{\partial}{\partial x} & \xi^3 \times \dfrac{\partial}{\partial z} + \dfrac{\partial \xi^3}{\partial z} & 0 & \xi^3 \times \dfrac{\partial}{\partial x} \end{bmatrix} \tag{4.38}$$

The transverse normal strain ε_{zz} can be written in matrix form as:

$$\varepsilon_{zz} = \begin{bmatrix} 0 & 0 & \dfrac{\partial \overline{w}}{\partial z} & 0 & 0 & \xi^3 \times \dfrac{\partial \Delta w}{\partial z} + \dfrac{\partial \xi^3}{\partial z} \times \Delta w \end{bmatrix} = \mathbf{B}^{zz} \times \breve{\mathbf{u}} \tag{4.39}$$

where $\mathbf{B}^{zz}$ is:

$$\mathbf{B}^{zz} = \begin{bmatrix} 0 & 0 & \dfrac{\partial}{\partial z} & 0 & 0 & \xi^3 \times \dfrac{\partial}{\partial z} + \dfrac{\partial \xi^3}{\partial z} \end{bmatrix} \tag{4.40}$$

4.4. Finite element approximation

4.4.1 Strain finite element approximation

In terms of finite element, the standard trilinear shape functions of the hexahedral element can be defined in terms of standard bilinear shape functions as in Sze & Yao (2000) combined with a parameterization in the thickness direction. The resultant solid-shell geometry is thus defined in terms of shape functions defined on the shell mid-surface combined with a thickness parameterization as:

$$\mathbf{x}\left(\xi^1, \xi^2, \xi^3\right) = \sum_{I=1}^{4} N_I\left(\xi^1, \xi^2\right) \times \left(\overline{\mathbf{x}}_i + \xi^3 \times \Delta \mathbf{x}_i\right), \quad \left(-1 \le \xi^3 \le 1\right) \tag{4.41}$$

where $N_I, \quad I = 1, \cdots, 4$ are the standard bilinear shape functions of a quadrilateral element, $\overline{\mathbf{x}}_i = \left(\overline{x}_{i1}, \overline{x}_{i2}, \overline{x}_{i3}, \overline{x}_{i4}\right), \left(i = 1, \ldots, 3\right)$ are the position vectors of the element mid-surface corners and $\Delta \mathbf{x}_i = \left(\Delta x_{i1}, \Delta x_{i2}, \Delta x_{i3}, \Delta x_{i4}\right), \left(i = 1, \ldots, 3\right)$ are the orientation vectors at the element mid-surface corners.

The displacements field expressed in equation (4.5) can be approximated in finite element form, $\mathbf{u} \approx \mathbf{u}^e$. For sake of simplicity the superscript $(\ )^e$ is omitted in this last expression, such that the nodal displacements field $\mathbf{u}$ is:

$$\begin{aligned} \mathbf{u}\left(\xi^1, \xi^2, \xi^3\right) &= \sum_{I=1}^{4} N_I\left(\xi^1, \xi^2\right) \times \left(\frac{\left(1 + \xi^3\right)}{2} \times \mathbf{u}_i^U + \frac{\left(1 - \xi^3\right)}{2} \times \mathbf{u}_i^L \right) \\ &= \sum_{I=1}^{4} N_I\left(\xi^1, \xi^2\right) \times \left(\overline{\mathbf{u}}_i + \xi^3 \times \Delta \mathbf{u}_i\right) \qquad , \quad \left(-1 \le \xi^3 \le 1\right) \end{aligned} \tag{4.42}$$

where $\bar{\mathbf{u}}_i = \left(\bar{u}_{i1}, \bar{u}_{i2}, \bar{u}_{i3}, \bar{u}_{i4}\right), \left(i = 1, \ldots, 3\right)$ are the displacement vectors of the element mid-surface corners and $\Delta\mathbf{u}_i = \left(\Delta u_{i1}, \Delta u_{i2}, \Delta u_{i3}, \Delta u_{i4}\right), \left(i = 1, \ldots, 3\right)$ are the rotation vectors at the element mid-surface corners. They are defined at each corners I similarly as in equation (4.5).

The finite element approximation of the membrane and bending strain field, defined respectively in equations (4.33) and (4.35) then becomes:

$$\boldsymbol{\varepsilon}^m = \sum_{I=1}^{4} \mathbf{B}_I^m . \breve{\mathbf{u}}_I \tag{4.43}$$

where $\breve{\mathbf{u}}_I = \left\langle \bar{u}_I \quad \bar{v}_I \quad \bar{w}_I \quad \Delta u_I \quad \Delta v_I \quad \Delta w_I \right\rangle^T$ for each corner I,

with

$$\mathbf{B}_I^m = \begin{bmatrix} N_{I,x} & 0 & 0 & 0 & 0 & 0 \\ 0 & N_{I,y} & 0 & 0 & 0 & 0 \\ N_{I,y} & N_{I,x} & 0 & 0 & 0 & 0 \end{bmatrix}, \quad I = 1, \cdots, 4 \tag{4.44}$$

and

$$\boldsymbol{\varepsilon}^b = \sum_{I=1}^{4} \mathbf{B}_I^b . \breve{\mathbf{u}}_I \tag{4.45}$$

with

$$\mathbf{B}_I^b = \begin{bmatrix} 0 & 0 & 0 & N_{I,x} & 0 & 0 \\ 0 & 0 & 0 & 0 & N_{I,y} & 0 \\ 0 & 0 & 0 & N_{I,y} & N_{I,x} & 0 \end{bmatrix}, \quad I = 1, \cdots, 4 \tag{4.46}$$

The detailed smoothing procedure to calculate this membrane and bending element strain fields $\boldsymbol{\varepsilon}^m$ and $\boldsymbol{\varepsilon}^b$ as well as the corresponding strain operator $\mathbf{B}_I^m$ and $\mathbf{B}_I^b$ in their smoothed form are given in section 4.6.1.

Developing equation (4.37) in the element mid-surface, at $\xi^3 = 0$, the element transverse shear components can be expressed as:

$$\boldsymbol{\gamma} = \mathbf{T}^{\gamma}_{\xi^3=0} \times \boldsymbol{\gamma}^{\xi} \tag{4.47}$$

where the natural transverse shear strain $\boldsymbol{\gamma}^{\xi}$ in matrix form is obtain by developing equation (4.20) as:

$$\boldsymbol{\gamma}^{\xi} = \begin{Bmatrix} \gamma^{\xi}_{23} \\ \gamma^{\xi}_{13} \end{Bmatrix} = \sum_{I=1}^{4} \mathbf{B}^{\gamma,0}_{I} \times \breve{\mathbf{u}}_{I} \tag{4.48}$$

with the transverse shear strain operator $\mathbf{B}^{\gamma,0}_{I}$, expressed in the element mid-surface $\xi^3 = 0$ by:

$$\mathbf{B}^{\gamma,0}_{I} = \begin{bmatrix} 0 & 0 & \dfrac{\partial N_I}{\partial \xi^2}\mathbf{g}^T_3 & 0 & N_I \mathbf{g}^T_2 & 0 \\ 0 & 0 & \dfrac{\partial N_I}{\partial \xi^1}\mathbf{g}^T_3 & N_I \mathbf{g}^T_1 & 0 & 0 \end{bmatrix}, \quad I = 1, \cdots, 4 \tag{4.49}$$

and $\mathbf{T}^{\gamma}_{\xi^3=0}$ is a sub-transformation matrix extracted from equation (4.31) as:

$$\mathbf{T}^{\gamma}_{\xi^3=0} = \begin{bmatrix} j_{22}j_{33} & j_{12}j_{33} \\ j_{21}j_{33} & j_{11}j_{33} \end{bmatrix} \tag{4.50}$$

Using equation (4.39), the element normal strain finite element approximation evaluated on the element mid-surface $\xi^3 = 0$ then becomes:

$$\varepsilon_{zz} = j^2_{33} \times \varepsilon^{\xi}_{33} \tag{4.51}$$

where the natural normal strain in matrix form is obtained by developing equation (4.20) as in equation (4.52):

$$\varepsilon_{33}^{\xi} = \sum_{I=1}^{4} \mathbf{B}_I^{\zeta\zeta} \times \tilde{\mathbf{u}}_I \tag{4.52}$$

where the normal strain operator $\mathbf{B}_I^{\zeta\zeta}$, evaluated on the element mid-surface $\xi^3 = 0$ is expressed as:

$$\mathbf{B}_I^{\zeta\zeta} = \left\langle 0 \quad 0 \quad 0 \quad 0 \quad 0 \quad N_I \mathbf{g}_3^T \right\rangle, \quad I = 1, \cdots, 4 \tag{4.53}$$

4.4.2 Transverse shear locking

In order to tackle the transverse shear locking when evaluating the transverse shear stiffness using first order shell theory (Reissner-Mindlin assumption), the ANS technique initially introduced by Hughes & Tezduyar (1981) and then developed by other researchers like Batoz & Dhatt (1992), as Q4-gama element, remains an efficient strategy. Since first order shear deformable shell formulation yield constant transverse shear strain through the shell thickness, this may be a good approximation for very thin shell but not necessary appropriate for thick shell. Then in order to handle the thick shell case, the natural shear strains evaluated at four points $\left(A_1, A_2, B_1, B_2\right)$ located in the middle of the mid-surface edge as illustrated in Figure 4.4. These four points are used to evaluate the actual transverse shear strain anywhere on the element.

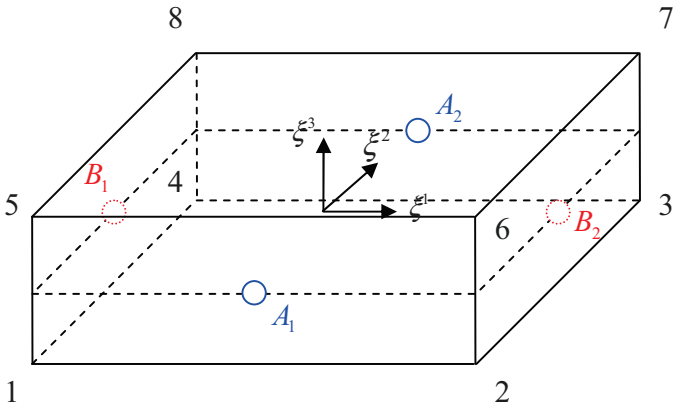

Figure 4.4: Eight-node shell element, ANS method for transverse shear locking

This is done by calculating the element shear strain used in actual shear stiffness computation from the interpolation of the element natural strains defined in equation (4.48) at points A_1, A_2, B_1 and B_2 as:

$$\gamma_{13}^{\xi,A_1} = \gamma_{13}^{\xi}\Big|_{\xi^1=0,\,\xi^2=-1,\,\xi^3=0} \qquad (4.54)$$

$$\gamma_{13}^{\xi,A_2} = \gamma_{13}\Big|_{\xi^1=0,\,\xi^2=1,\,\xi^3=0} \qquad (4.55)$$

$$\gamma_{23}^{\xi,B_1} = \gamma_{23}^{\xi}\Big|_{\xi^1=-1,\,\xi^2=0,\,\xi^3=0} \qquad (4.56)$$

$$\gamma_{23}^{\xi,B_2} = \gamma_{23}^{\xi}\Big|_{\xi^1=1,\,\xi^2=0,\,\xi^3=0} \qquad (4.57)$$

Equations (4.54) to (4.57) are then used to obtain an improved interpolated shear strain using linear interpolation functions:

$$\gamma_{13}^{\xi,ANS} = \frac{1-\xi^2}{2}\gamma_{13}^{\xi,A1} + \frac{1+\xi^2}{2}\gamma_{13}^{\xi,A2} \qquad (4.58)$$

$${}^{0}\gamma_{23}^{\xi,ANS} = \frac{1-\xi^1}{2}\gamma_{23}^{\xi,B1} + \frac{1+\xi^1}{2}\gamma_{23}^{\xi,B2} \qquad (4.59)$$

where $-1 \le \xi^1, \xi^2 \le 1$.

4.4.3 Trapezoidal effect or curvature thickness effect

In FEM approximation, simulation accuracy is dependent on the mesh quality. However, it remains common to use some trapezoidal elements to mesh curved structures like tubes. In case of bending dominated problems, such trapezoidal shape may be responsible for the trapezoidal effect occurrence since it may provide additional through-the-thickness strain. Betsch et al. (1996) were among the first to apply the ANS method in order to get rid of this type of locking. In their work, the natural thickness strains are evaluated at the four corners of the element mid-surface (C, D, E, F) as illustrated in Figure 4.5.

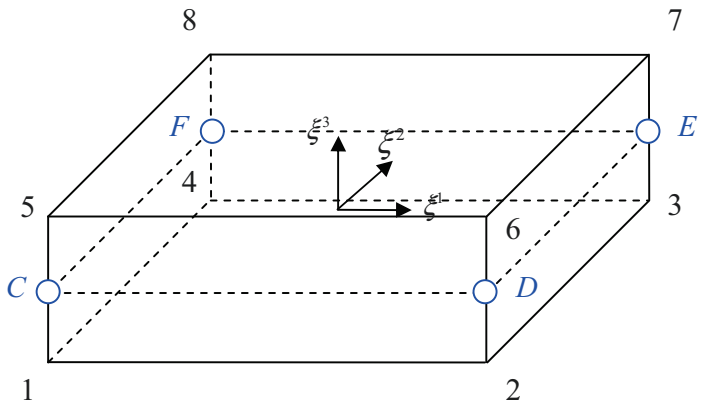

Figure 4.5: Eight-node shell element, ANS method for trapezoidal effect treatment

The thickness strain used in actual thickness stiffness calculation is then obtained by interpolation of these natural thickness strains.

The normal strains at the four corners of the mid-surface are then obtained from equation (4.52) as:

$$\varepsilon_{33}^{\xi,C} = \varepsilon_{33}^{\xi}\Big|_{\xi^1=-1,\xi^2=-1} \quad (4.60) \qquad \varepsilon_{33}^{\xi,D} = \varepsilon_{33}^{\xi}\Big|_{\xi^1=1,\xi^2=-1} \quad (4.61)$$

$$\varepsilon_{33}^{\xi,E} = \varepsilon_{33}^{\xi}\Big|_{\xi^1=1,\xi^2=1} \quad (4.62) \qquad \varepsilon_{33}^{\xi,F} = \varepsilon_{33}^{\xi}\Big|_{\xi^1=-1,\xi^2=1} \quad (4.63)$$

And equations (4.60) to (4.63) are used to obtain an improved interpolated transverse normal strain using bilinear interpolation functions of the standard mid-surface Q4 element.

$$\begin{aligned}\varepsilon_{33}^{\xi,ANS} = {} & \frac{1}{4}\times\left(1-\xi^1\right)\times\left(1-\xi^2\right)\times\varepsilon_{33}^{\xi,C} + \frac{1}{4}\times\left(1+\xi^1\right)\times\left(1-\xi^2\right)\times\varepsilon_{33}^{\xi,D} \\ & + \frac{1}{4}\times\left(1+\xi^1\right)\times\left(1+\xi^2\right)\times\varepsilon_{33}^{\xi,E} + \frac{1}{4}\times\left(1-\xi^1\right)\times\left(1+\xi^2\right)\times\varepsilon_{33}^{\xi,F}\end{aligned} \quad (4.64)$$

where $-1 \le \xi^1, \xi^2 \le 1$.

4.5. Principle of virtual work

In the present contribution, a mixed variational formulation based on the three-field variables (u,ε,σ), is used. As a consequence, the decomposition of this formulation in terms of effects remains simple. The weak form expression of the virtual work principle can be written as detailed in Hodge (1970):

$$\delta W = \delta W_{\text{int}} - \delta W_{ext} = 0 \tag{4.65}$$

where the internal and the external work expressions are given by:

$$\delta W_{\text{int}} = \int_V \delta\boldsymbol{\varepsilon}^T : \boldsymbol{\sigma}\ dV \tag{4.66}$$

$$\delta W_{ext} = \int_V \delta\breve{\mathbf{u}}^T \times \mathbf{f}_v dV + \int_s \delta\breve{\mathbf{u}}^T \times \mathbf{f}_s dS \tag{4.67}$$

with the stress field $\boldsymbol{\sigma}$ and the constitutive parameter $\mathbf{H}'$ are assumed to be related by the following constitutive equation:

$$\boldsymbol{\sigma} = \mathbf{H}' \times \boldsymbol{\varepsilon} \tag{4.68}$$

Separating the membrane and bending stresses from the transverse shear stresses and the through-the-thickness stress, the stress-strain relations can be decomposed as follows:

$$\begin{aligned} \boldsymbol{\sigma}^{mb} = \mathbf{H}'^{mb} \times \boldsymbol{\varepsilon}^{mb} = \mathbf{H}'^{mb}\left(\boldsymbol{\varepsilon}^m + \xi^3 \times \boldsymbol{\varepsilon}^b\right) = \boldsymbol{\sigma}^m + \xi^3 \times \boldsymbol{\sigma}^b \\ \boldsymbol{\sigma}^{\gamma} = \mathbf{H}'^{\gamma} \times \boldsymbol{\varepsilon}^{\gamma} \\ \sigma^{zz} = H'^{zz} \times \varepsilon^{zz} \end{aligned} \tag{4.69}$$

where $\boldsymbol{\sigma}^m = \mathbf{H}'^{mb}\boldsymbol{\varepsilon}^m$ and $\boldsymbol{\sigma}^b = \mathbf{H}'^{mb} \times \boldsymbol{\varepsilon}^b$ and where $\mathbf{H}'^{mb}$, $\mathbf{H}'^{\gamma}$ and H'^{zz} are constitutive matrices having for an isotropic elastic material, the following form in 3D:

$$\mathbf{H}'^{mb} = \begin{bmatrix} \bar{\lambda}+2\mu & \bar{\lambda} & 0 \\ \bar{\lambda} & \bar{\lambda}+2\mu & 0 \\ 0 & 0 & \mu \end{bmatrix} \qquad \mathbf{H}'^{\gamma} = \begin{bmatrix} \mu & 0 \\ 0 & \mu \end{bmatrix} \qquad H'^{zz} = E$$

(4.70) (4.71) (4.72)

in which the modified Lamé's coefficients are $\bar{\lambda} = \dfrac{E.\nu}{\left(1-\nu^2\right)}$ and $\mu = \dfrac{E}{2.\left(1+\nu\right)}$ with E the Young's modulus and ν the Poisson's ratio.

According to the adopted kinematics decomposition for shell formulation and following Domissy (1997) and Hannachi (2007), it is possible to decompose the weak form of the internal virtual work δW_{int}, defined in equation (4.66), into membrane-bending, transverse shear and normal components as:

$$\begin{aligned} \delta W_{\text{int}} &= \delta W_{\text{int}}^{mb} + \delta W_{\text{int}}^{\gamma} + \delta W_{\text{int}}^{zz} \\ &= \int_V \left(\delta\boldsymbol{\varepsilon}^{mb}\right)^T : \boldsymbol{\sigma}^{mb} dV + \int_V \delta\boldsymbol{\gamma}^T : \boldsymbol{\sigma}^{\gamma} dV + \int_V \left(\delta\boldsymbol{\varepsilon}^{zz}\right)^T : \boldsymbol{\sigma}^{zz} dV \end{aligned} \tag{4.73}$$

Introducing equation (4.69) in the above equation (4.73) gives:

$$\begin{aligned} \delta W_{\text{int}} &= \delta W_{\text{int}}^{mb} + \delta W_{\text{int}}^{\gamma} + \delta W_{\text{int}}^{zz} \\ &= \int_V \left(\delta\boldsymbol{\varepsilon}^{mb}\right)^T \times \mathbf{H}'^{mb} \times \boldsymbol{\varepsilon}^{mb} dV + \int_V \delta\boldsymbol{\gamma}^T \times \mathbf{H}'^{\gamma} \times \boldsymbol{\varepsilon}^{\gamma} dV + \int_V \left(\delta\varepsilon_{zz}\right)^T \times H'^{zz} \times \varepsilon_{zz} dV \end{aligned} \tag{4.74}$$

Then, using equation (4.74) and separating integration into thickness and mid-surface integrations gives:

$$\begin{aligned} \delta W_{\text{int}} &= \delta W_{\text{int}}^{mb} + \delta W_{\text{int}}^{\gamma} + \delta W_{\text{int}}^{zz} \\ &= \int_S \left(\delta\boldsymbol{\varepsilon}^{m}\right)^T \times \mathbf{A} H \times \boldsymbol{\varepsilon}^{m} dS + \int_S \left(\delta\boldsymbol{\varepsilon}^{b}\right)^T \times \mathbf{D} H \times \boldsymbol{\varepsilon}^{b} dS + \cdots \\ &\quad \cdots + \int_S \delta\boldsymbol{\gamma}^T \times \bar{\mathbf{A}} H \times \boldsymbol{\gamma} dS + \int_S \left(\delta\varepsilon_{zz}\right)^T \times E H \times \varepsilon_{zz} dS \\ &= \delta\breve{\mathbf{u}}^T \times \Big[\int_S \left(\mathbf{B}^m\right)^T \times \mathbf{A} H \times \mathbf{B}^m dS + \int_S \left(\mathbf{B}^b\right)^T \times \mathbf{D} H \times \mathbf{B}^b dS + \cdots \\ &\quad \cdots + \int_S \left(\mathbf{B}^{\gamma}\right)^T \times \bar{\mathbf{A}} H \times \mathbf{B}^{\gamma} dS + \int_S \left(\mathbf{B}^{zz}\right)^T \times E H \times \mathbf{B}^{zz} dS \Big] \times \breve{\mathbf{u}} \end{aligned} \tag{4.75}$$

where h is the shell thickness and $\mathbf{A}H$, $\mathbf{B}H$, $\mathbf{D}H$, $\bar{\mathbf{A}}H$ and EH are through-the-thickness integrated material parameters thus defining the new resultant constitutive law expressed as:

$$\mathbf{A}H = \int_{-h/2}^{h/2} \mathbf{H}'^{mb}_{ij} d\xi^3 = h \times \mathbf{H}'^{mb} \quad (4.76) \qquad \mathbf{D}H = \int_{-h/2}^{h/2} \left(\xi^3\right)^2 \times \mathbf{H}'^{mb} d\xi^3 = \frac{h^3}{12} \times \mathbf{H}'^{mb} \quad (4.77)$$

$$\bar{\mathbf{A}}H = \int_{-h/2}^{h/2} \mathbf{H}'^{\gamma} d\xi^3 = h \times \mathbf{H}'^{\gamma} \quad (4.78) \qquad EH = \int_{-h/2}^{h/2} H'^{zz} d\xi^3 = h \times H'^{zz} \quad (4.79)$$

Introducing the finite element approximation, the element internal virtual work δW^e_{int} in equation (4.73) can be expressed as:

$$\begin{aligned}
&\delta W^e_{\text{int}} = \delta W^{e,mb}_{\text{int}} + \delta W^{e,\gamma}_{\text{int}} + \delta W^{e,zz}_{\text{int}} \\
&= \int_{-1}^{1}\int_{-1}^{1} \sum_{I=1}^{4} \left(\delta \boldsymbol{\varepsilon}^m_I + \xi^3 \times \delta \boldsymbol{\varepsilon}^b_I\right)^T : \boldsymbol{\sigma}^{mb} \left|\mathbf{J}\right| d\xi d\eta + \int_{-1}^{1}\int_{-1}^{1} \sum_{I=1}^{4} \delta \boldsymbol{\gamma}^T_I : \boldsymbol{\sigma}^{\gamma} \left|\mathbf{J}\right| d\xi d\eta + \int_{-1}^{1}\int_{-1}^{1} \sum_{I=1}^{4} \left(\delta \boldsymbol{\varepsilon}_{zz}\right)^T_I : \boldsymbol{\sigma}^{zz} \left|\mathbf{J}\right| d\xi d\eta \\
&= \delta \breve{\mathbf{u}}^T_I \times \int_{-1}^{1}\int_{-1}^{1} \left[\sum_{I=1}^{4} \left(\mathbf{B}^m_I + \xi^3 \times \mathbf{B}^b_I\right)^T \times \boldsymbol{\sigma}^{mb} \left|\mathbf{J}\right| + \sum_{I=1}^{4} \left(\mathbf{B}^{\gamma}_I\right)^T \times \boldsymbol{\sigma}^{\gamma} \left|\mathbf{J}\right| + \sum_{I=1}^{4} \left(\mathbf{B}^{zz}_I\right)^T \times \boldsymbol{\sigma}^{zz} \left|\mathbf{J}\right| \right] d\xi d\eta \\
&= \delta \breve{\mathbf{u}}^T_I \times \mathbf{f}_{\text{int}}
\end{aligned} \quad (4.80)$$

where $\left|\mathbf{J}\right|$ is the determinant of $\mathbf{J}$ and

$$\mathbf{f}_{\text{int}} = \int_{-1}^{1}\int_{-1}^{1} \left[\left(\mathbf{B}^m_I + \xi^3 \times \mathbf{B}^b_I\right)^T \times \boldsymbol{\sigma}^{mb} + \left(\mathbf{B}^{\gamma}_I\right)^T \times \boldsymbol{\sigma}^{\gamma} + \left(\mathbf{B}^{zz}_I\right)^T \times \boldsymbol{\sigma}^{zz} \right] \times \left|\mathbf{J}\right| d\xi d\eta \quad (4.81)$$

The finite element approximation of the weak form of the internal virtual work $\Delta\delta W^e_{\text{int}}$ expressed in equation (4.75) then yields in (See Kim et al. (2005)):

$$\begin{aligned}
\delta W^e_{\text{int}} = \delta \breve{\mathbf{u}}^T_I \times \int_{-1}^{1}\int_{-1}^{1} \Bigg[&\sum_{I=1}^{4} \left(\mathbf{B}^m_I\right)^T \times \mathbf{A}H \times \mathbf{B}^m_I \times \left|\mathbf{J}\right| + \sum_{I=1}^{4} \left(\mathbf{B}^b_I\right)^T \times \mathbf{D}H \times \mathbf{B}^b_I \times \left|\mathbf{J}\right| + \cdots \\
\cdots + &\sum_{I=1}^{4} \left(\mathbf{B}^{\gamma}_I\right)^T \times \bar{\mathbf{A}}H \times \mathbf{B}^{\gamma}_I \times \left|\mathbf{J}\right| + \sum_{I=1}^{4} \left(\mathbf{B}^{zz}_I\right)^T \times EH \times \mathbf{B}^{zz}_I \times \left|\mathbf{J}\right| \Bigg] d\xi d\eta \times \Delta \breve{\mathbf{u}}_I \\
&= \delta \breve{\mathbf{u}}^T_I \times \mathbf{k} \times \Delta \breve{\mathbf{u}}_I
\end{aligned} \quad (4.82)$$

where the element stiffness matrix $\mathbf{k}$ is:

$$\mathbf{k} = \mathbf{k}^{mb} + \mathbf{k}^{\gamma} + \mathbf{k}^{zz} \tag{4.83}$$

with

$$\mathbf{k}^{mb} = \int_{-1}^{1}\int_{-1}^{1}\sum_{I=1}^{4}\left[\left(\mathbf{B}_I^m\right)^T \times \mathbf{A}H \times \mathbf{B}_I^m + \left(\mathbf{B}_I^b\right)^T \times \mathbf{D}H \times \mathbf{B}_I^b\right] \times \left|\mathbf{J}\right| d\xi d\eta \tag{4.84}$$

$$\mathbf{k}^{\gamma} = \int_{-1}^{1}\int_{-1}^{1}\sum_{I=1}^{4}\left(\mathbf{B}_I^{\gamma}\right)^T \times \bar{\mathbf{A}}H \times \mathbf{B}_I^{\gamma} \times \left|\mathbf{J}\right| d\xi d\eta \tag{4.85}$$

$$\mathbf{k}^{zz} = \int_{-1}^{1}\int_{-1}^{1}\sum_{I=1}^{4}\left(\mathbf{B}_I^{zz}\right)^T \times EH \times \mathbf{B}_I^{zz} \times \left|\mathbf{J}\right| d\xi d\eta \tag{4.86}$$

4.6. Smoothed finite element method

4.6.1 Smoothed strain field FEM formulation

At this stage, the standard FEM and the SFEM formulations share the same shell kinematics and variational principles. A fundamental difference will however result from the introduction, in the SFEM, of the smoothed strain obtained from a strain smoothing operation introduced in Liu, Dai, et al. (2007), Dai & Liu (2007) or Nguyen-Thanh et al. (2008) and defined as:

$$\tilde{\varepsilon}_{ij}\left(\mathbf{x}_c\right) = \int_{\Omega^h} \varepsilon_{ij}\left(\mathbf{x}\right) \times \varphi\left(\mathbf{x} - \mathbf{x}_c\right) d\Omega \tag{4.87}$$

where φ is a smoothing function with $\varphi\left(\mathbf{x} - \mathbf{x}_c\right) = \begin{cases} 1/S_c & \mathbf{x} \in \Omega_c \\ 0 & \mathbf{x} \notin \Omega_c \end{cases}$ *and* $S_c = \int_{\Omega_c} d\Omega$ is the area of the smoothing cell Ω_c and $\mathbf{x}_c$ the position vector of a point on the shell structure. This operation is very similar to the mean dilatation procedure used to deal with the incompressibility in non-linear mechanics. It has also been used in weak-form mesh less method based on nodal integration.

Applying the strain smoothing concepts to the deformation gradient, the smoothed deformation gradient can be written as:

$$\tilde{F}_{ij}\left(\mathbf{x}_c\right)=\frac{1}{S_C}\int_{\Omega_C}\left[\frac{\partial u_i}{\partial x_j}+\delta_{ij}\right]d\Omega \tag{4.88}$$

By applying the divergence theorem, $\int_{\Omega_C}\left[\frac{\partial u_i}{\partial x_j}\right]d\Omega=\int_{\Gamma_C}\left(u_i \times n_j\right)d\Gamma$, the smoothed strain formulation is then expressed as an integration of the strain matrix on the cell boundary and equation (4.88) becomes:

$$\tilde{F}_{ij}\left(\mathbf{x}_c\right)=\tilde{e}_{ij}\left(\mathbf{x}_c\right)+\delta_{ij} \tag{4.89}$$

where

$$\tilde{e}_{ij}\left(\mathbf{x}_c\right)=\frac{1}{S_C}\int_{\Gamma_C}\left(u_i \times n_j\right)d\Gamma \tag{4.90}$$

Hence the associated smoothed Green-Lagrange strain $\tilde{\varepsilon}$ becomes:

$$\tilde{\varepsilon}_{ij}=\frac{1}{2}\left(\tilde{F}_{ik}\tilde{F}_{kj}-I_{ij}\right)=\frac{1}{2}\left[\left(\tilde{e}_{ik}+\delta_{ik}\right)\left(\tilde{e}_{kj}+\delta_{kj}\right)-\delta_{ij}\right] \tag{4.91}$$

In the previous equation, Γ_C is the cell boundary and $\mathbf{n}_j$ the outward normal of the considered cell boundary.

In the concept presented here, the mid-surface of the shell is first identified. Then, the length of its boundary Γ_c, the normal vectors of its boundary $\mathbf{n}$ and its area S_C are determined as illustrated in Figure 4.6.

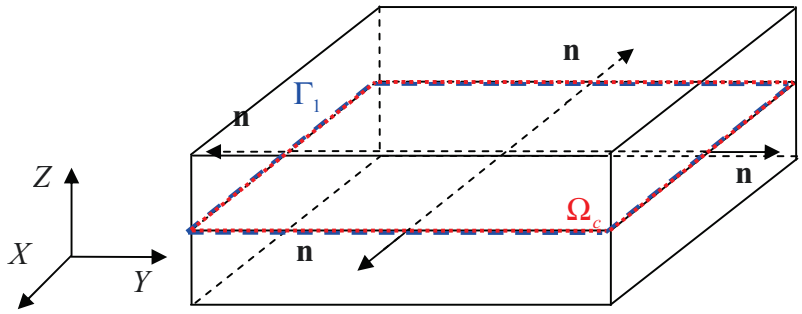

Figure 4.6: Smoothing concept: Mid-surface identification

Considering only the linear part, the smoothed strain becomes after simplification:

$$\tilde{\varepsilon}_{ij}^{l} = \frac{1}{2}\left[\tilde{e}_{ij} + \tilde{e}_{ji}\right] \tag{4.92}$$

Introducing the local displacements field $\mathbf{u}\left(\xi^1,\xi^2,\xi^3\right) = \bar{\mathbf{u}}\left(\xi^1,\xi^2\right) + \xi^3 \times \Delta\mathbf{u}\left(\xi^1,\xi^2\right)$, then the deformation gradient can be written as:

$$\begin{aligned}\tilde{F}_{ij}\left(\mathbf{x}_c\right) &= \frac{1}{S_C}\int_{\Omega_C}\left[\frac{\partial\left[\bar{u}_i\left(\xi^1,\xi^2\right) + \xi^3 \times \Delta u_i\left(\xi^1,\xi^2\right)\right]}{\partial x_j} + \delta_{ij}\right] d\Omega \\ &= \tilde{e}_{ij}\left(\mathbf{x}_c\right) + \delta_{ij}\end{aligned} \tag{4.93}$$

with

$$\tilde{e}_{ij}\left(\mathbf{x}_c\right) = \frac{1}{S_C}\int_{\Gamma_C}\left(\bar{u}_i \times \mathbf{n}_j + \xi^3 \Delta u_i \, \mathbf{n}_j\right) d\Gamma \tag{4.94}$$

Separating the strain field into membrane-bending, transverse shear and transverse normal components gives:

$$\tilde{\varepsilon}_{ij} = \tilde{\varepsilon}_{ij}^{m} + \tilde{\varepsilon}_{ij}^{b} + \tilde{\varepsilon}_{ij}^{\gamma} + \tilde{\varepsilon}_{ij}^{zz} \tag{4.95}$$

The smoothed element formulation is here applied for the numerical integration of the membrane and bending parts of the strain field on the mid-surface boundary for the resultant eight-node solid-shell element.

From equations (4.84) and (4.94) it is possible to deduce the continuous smoothed form of the membrane and bending stiffness matrix $\tilde{\mathbf{k}}^{mb}$:

$$\tilde{\mathbf{k}}^{mb} = \sum_{c=1}^{n_c} \left[\left(\tilde{\mathbf{B}}_c^m \left(x_c \right) \right)^T \times \mathbf{A} H \times \tilde{\mathbf{B}}_c^m \left(x_c \right) + \left(\tilde{\mathbf{B}}_c^b \left(x_c \right) \right)^T \times \mathbf{D} H \times \tilde{\mathbf{B}}_c^b \left(x_c \right) \right] \times S_c \tag{4.96}$$

where the smoothed strain-displacement matrix operators are determined similarly as in N. Nguyen-Thanh et al. (2008):

$$\tilde{\mathbf{B}}_c^m \left(x_c \right) = \frac{1}{S_c} \times \sum_{b=1}^{4} \sum_{I=1}^{4} \begin{bmatrix} N_I \times n_x & 0 & 0 & 0 & 0 & 0 \\ 0 & N_I \times n_y & 0 & 0 & 0 & 0 \\ N_I \times n_y & N_I \times n_x & 0 & 0 & 0 & 0 \end{bmatrix} \times l_b^c \tag{4.97}$$

$$\tilde{\mathbf{B}}_c^b \left(x_c \right) = \frac{1}{S_c} \times \sum_{b=1}^{4} \sum_{I=1}^{4} \begin{bmatrix} 0 & 0 & 0 & N_I \times n_x & 0 & 0 \\ 0 & 0 & 0 & 0 & N_I \times n_y & 0 \\ 0 & 0 & 0 & N_I \times n_y & N_I \times n_x & 0 \end{bmatrix} \times l_b^c \tag{4.98}$$

From equation (4.96) to (4.98), I is the mid-surface node label from 1 to 4; x_c is the unique gauss point along element edge and l_b^c the length of Γ_b^c; n_x and n_y are the components of the sub cell border outward normal vectors $\mathbf{n}$; S_c is the area of the sub cell c; n_c is the total cell number; N_I, the shape functions at the integration point and b is the edge number of cell c going from 1 to 4. One of the main advantages of the SFEM is that N_I, l_b^c, $\mathbf{n}$ and S_c are directly calculated from the real structure geometry as presented in Figure 4.7.

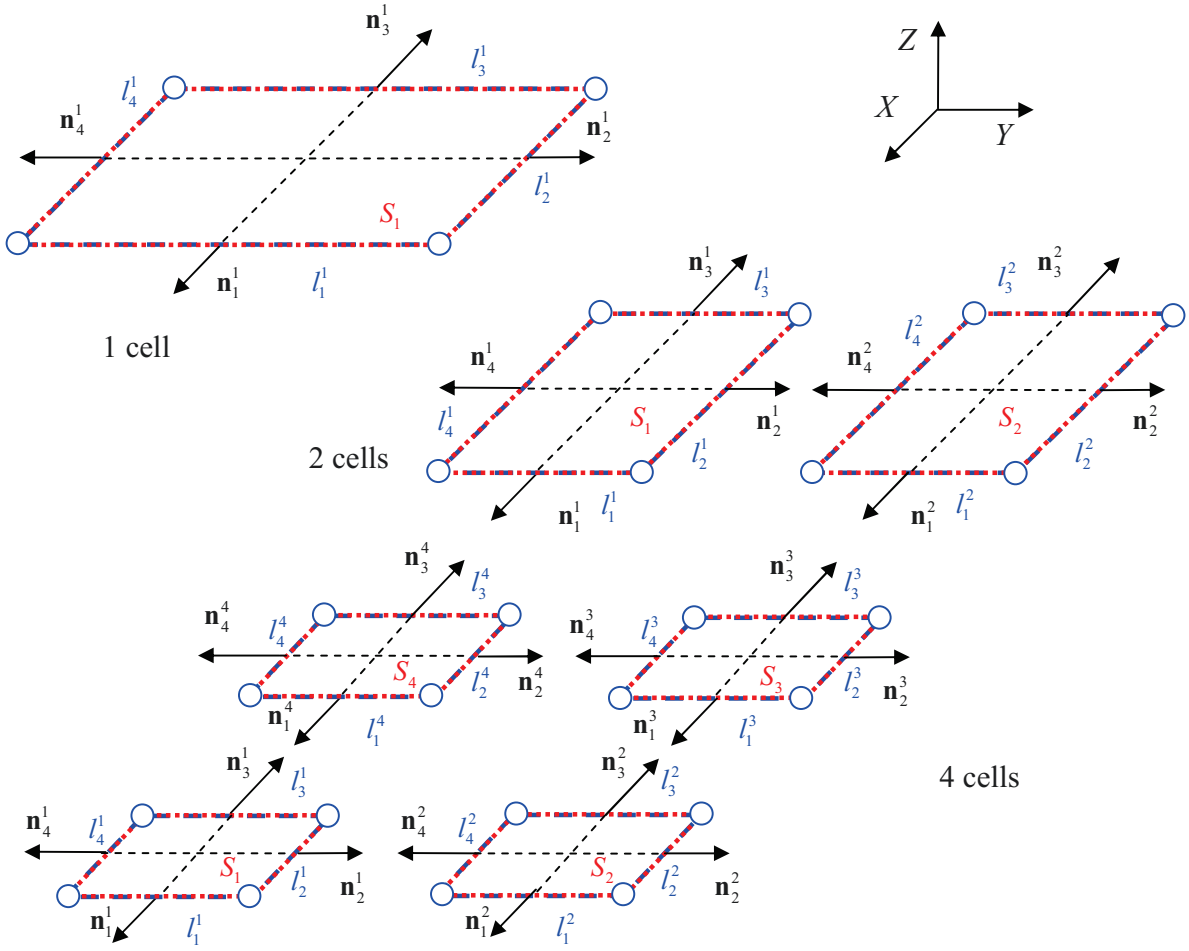

Figure 4.7: Mid-surface partition in cells

As a result the expression of the total element stiffness matrix, expressed in equation (4.83), can take the smoothed form in the local cartesian coordinates system $\mathbf{x}\left(x\ ,y\ ,z\ \right)$:

$$\tilde{\mathbf{k}}\ =\tilde{\mathbf{k}}^{mb}+\mathbf{k}^{\gamma}+\mathbf{k}^{zz} \tag{4.99}$$

The approximation of the shear strain field presented in section 4.4.2 is used to determine the shear strain matrix $\mathbf{B}^{ANS,\gamma}$. This matrix is then used in the numerical integration of the transverse shear stiffness at four classical Gauss points. A 2x2 integration scheme is adopted in the element mid-surface. The transverse shear stiffness, evaluated at the

geometry mid-surface and free of transverse shear locking, is then calculated introducing equations (4.58) and (4.59) into equation (4.48) to give:

$$\mathbf{k}^{ANS,\gamma} = \sum_{I=1}^{4} \left(\mathbf{B}_I^{ANS,\gamma} \right)^T \times \bar{\mathbf{A}} H \times \mathbf{B}_I^{ANS,\gamma} \times \left| \mathbf{J} \right| \tag{4.100}$$

Moreover, the approximation of the transverse normal strain field presented in section 4.4.3 is used to determine the transverse normal strain matrix $\mathbf{B}^{ANS,zz}$. It is this later which is used in the numerical integration of the through-the-thickness normal stiffness equations (4.64) defined as:

$$\mathbf{k}^{ANS,zz} = \sum_{I=1}^{4} \left(\mathbf{B}_I^{ANS,zz} \right)^T \times EH \times \mathbf{B}_I^{ANS,zz} \times \left| \mathbf{J} \right| \tag{4.101}$$

The adopted integration scheme is 2×2.

The total local element stiffness matrix then becomes:

$$\tilde{\mathbf{k}}^{ANS} = \tilde{\mathbf{k}}^{m} + \tilde{\mathbf{k}}^{b} + \mathbf{k}^{ANS,\gamma} + \mathbf{k}^{ANS,zz} \tag{4.102}$$

The local to global stiffness matrix transformation presented in Appendix B is similar to the method used in Kim et al. (2005).

4.6.2 Operation count

A quick overview of the integration scheme used in the SFEM is given in this section. It is compared with the integration scheme used in a classical eight-node resultant shell element to deal with the membrane and bending effects as illustrated in Figure 4.8.

In the classical scheme, the intrinsic shape function and shape function derivatives are calculated at the four integration points located in the element mid-surface. Then the jacobian matrix $\mathbf{J}$ and its determinant $\left|\mathbf{J}\right|$ are calculated. As the element is integrated in local cartesian coordinates system $\mathbf{x}\left(x\ ,y\ ,z\ \right)$, the cartesian shape function derivatives, required to define the strain operators $\mathbf{B}^m$ and $\mathbf{B}^b$, are computed by multiplying the

intrinsic derivative with the inverse of the jacobian matrix $\mathbf{J}^{-1}$. Then the stiffness matrix $\mathbf{K}^{mb}$ is calculated at each integration point and assembled with corresponding element vector and matrices.

In the SFEM, there is no need to calculate the intrinsic shape function derivatives. At the beginning of the integration, each element is subdivided into n_c subcells and over each cell a smoothed strain is used, which is a constant integrand, and the integral over each cell is evaluated over the cell boundary. Geometric parameters such as the length of the four edges of each cells l_b^c, cell areas S_c and cell edge normals $\mathbf{n}$ are calculated depending on the number of partitioning cells used within the element. In the present study, even if the number of cells remains limited to one, two or four, it is possible to increase this number depending on the level of the required accuracy. In order to get familiar with the calculated geometric parameters, let us consider for example one cell for the element integration.

As presented in section 4.6.1, only lengths l_1^1, l_2^1, l_3^1 ,l_4^1 and normals $\mathbf{n}_1^1$, $\mathbf{n}_2^1$, $\mathbf{n}_3^1$, $\mathbf{n}_4^1$, of four edges are calculated as well as one area A_1, all of them calculated in the local cartesian coordinates system $\mathbf{x}\left(x\ ,y\ ,z\ \right)$. Mathematically, the length of the four edges of each cell l_b^c corresponds to the jacobian used in the loop on cell edges integration. The intrinsic shape functions are calculated in the center of each cell boundary. Then, the jacobian matrix $\mathbf{J}$ and its determinant $\left|\mathbf{J}\right|$ are evaluated in the center of each cell located in the element mid-surface. As no cartesian derivatives of the shape function are calculated, there is no need to calculate the inverse of the jacobian matrix $\mathbf{J}^{-1}$ to determine the smoothed operator $\tilde{\mathbf{B}}^{mb}$ as presented in equations (4.97) and (4.98). Then the smoothed stiffness matrix $\tilde{\mathbf{K}}^{mb}$ is calculated and summed on each cell if more than one cell is used for the integration. The smoothing method simplifies the expression of the integration terms and is very attractive especially when only one cell is used since the number of operations remains small.

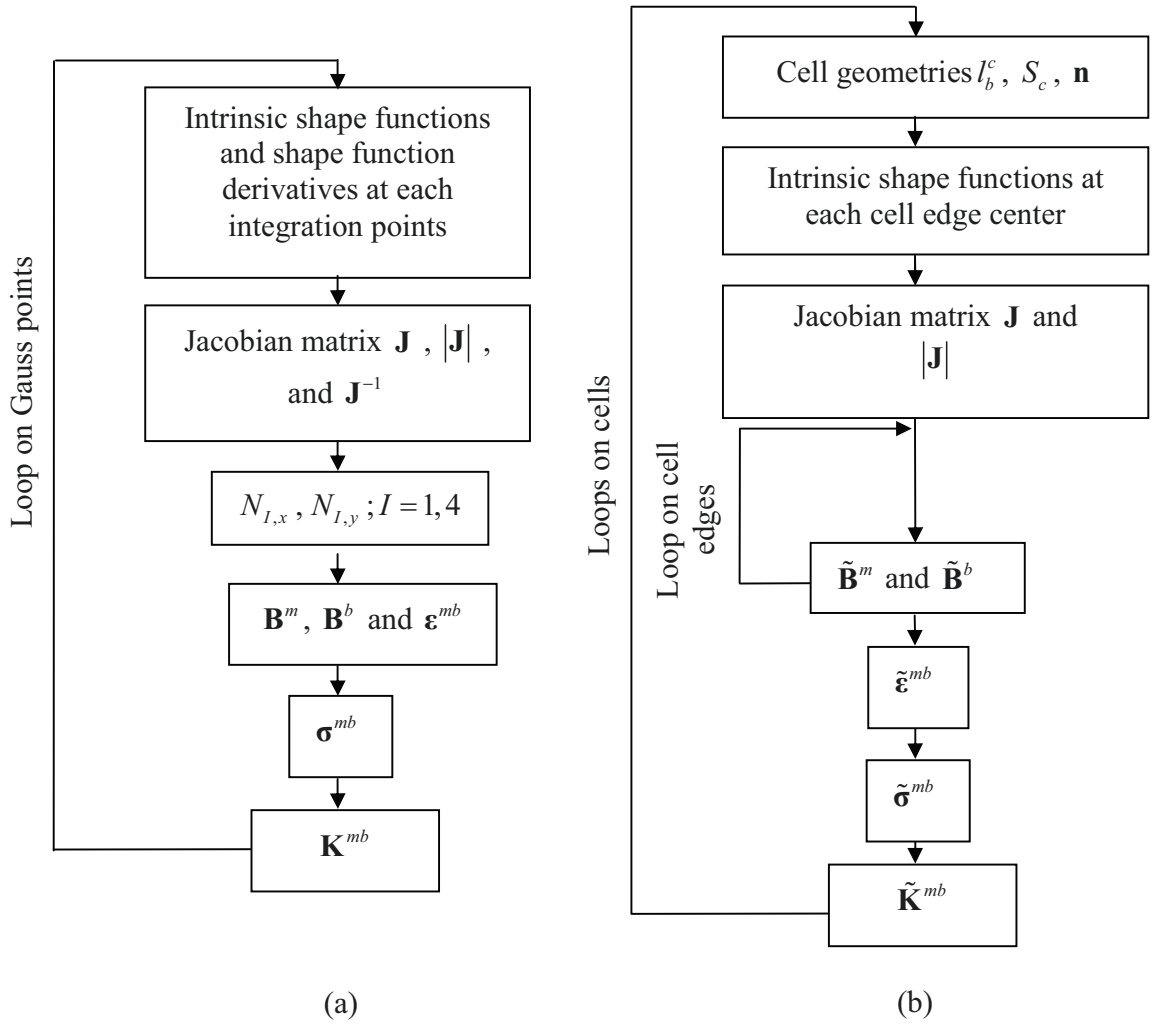

Figure 4.8: Membrane / bending integration scheme per element; (a) classical and (b) SFEMs

4.7. Benchmark problems

The proposed eight-node solid-shell element is named RH8s-X (Resultant hexahedra eight nodes smoothed with X smoothing cells) where X represents the number of smoothing cells dividing its mid-surface, 1, 2 or 4. Its capabilities have been compared in typical benchmark problems with other eight-node fully integrated elements presented in the following list:

SH8 – eight-node element with ANS and EAS equivalent to the SCH8 element from Hannachi (2007).

SC8R – eight-node element with reduced integration and plane stress assumption Abaqus user's manual, ver 6.8, (2007).

RH8 – resultant eight-node element with ANS.

Xsolid85 – resultant eight-node element with ANS and plane stress assumption Kim et al. (2005).

RH8s-X (X = 1, 2 or 4) – present eight-node resultant element.

Sch2009 –Schwarze & Reese (2009) : reduced integration eight – node solid-shell element with ANS and EAS.

All results have been normalized compared to the exact reference solution of each problem.

4.7.1 Cook's membrane problem

This benchmark problem is usually considered to check the ability of an element to handle membrane problems. Moreover, the irregular mesh helps verifying in the same time the accuracy of the isoparametric jacobian transformation matrix calculation. A plate, with the geometry presented in Figure 4.9 is clamped on the left side and subjected to a shear load F = 1 on the right side. The Young's modulus is $E = 1$ and the Poisson's ratio is $\nu = 0.33$. The vertical displacement of point A, located at the right side center, is compared to the exact reference solution $U_y = 23.91$ in Figure 4.10 and Table 4.2.

For very coarse mesh, at least two cells seem to be necessary to provide sufficient accuracy to the problem. The current element shows good performance. Even if the SC8R element has the best convergence, the RH8s-1 and RH8s-2 remain the most accurate elements.

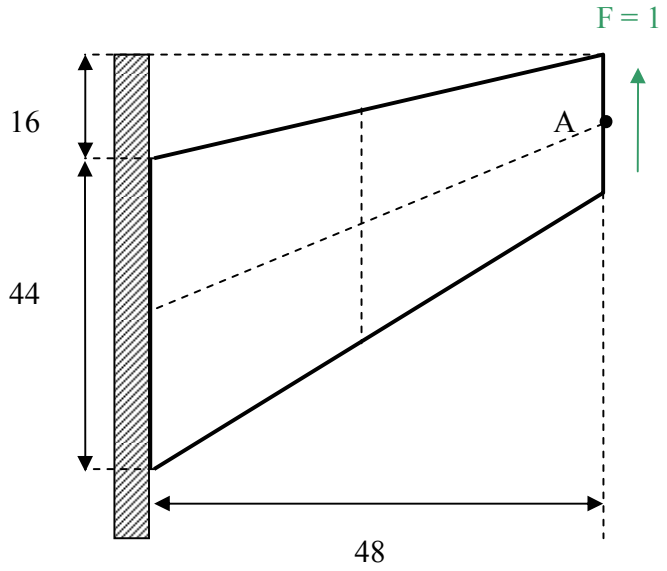

Figure 4.9: Cook's membrane problem

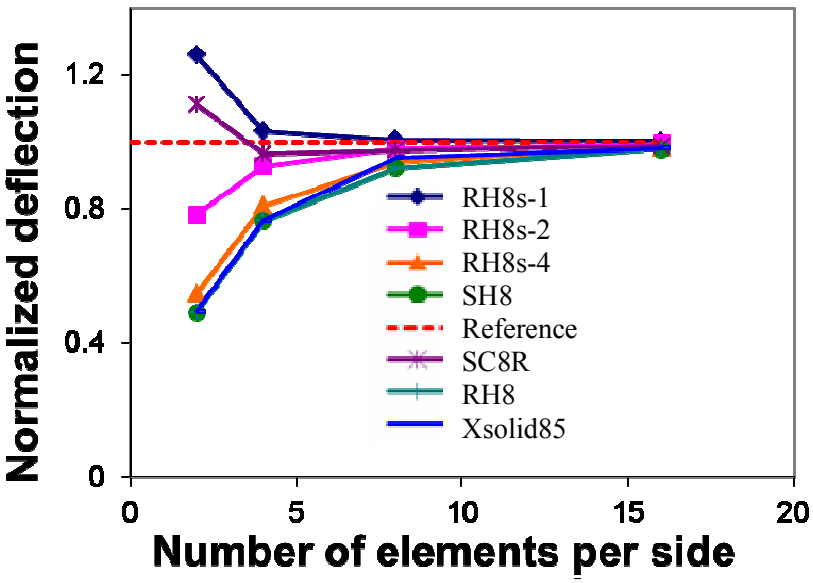

Figure 4.10: Cook's membrane problem normalized results

Table 4.2: The normalized results of Cook membrane problem

Element number	SC8R	Xsolid85	SH8	RH8	**RH8s-1**	**RH8s-2**	**RH8s-4**
2x2	1.112	0.495	0.492	0.492	**1.259**	**0.784**	**0.547**
4x4	0.963	0.765	0.763	0.763	**1.032**	**0.928**	**0.810**
8x8	0.974	0.953	0.922	0.922	**1.008**	**0.980**	**0.941**
16x16	0.987	0.98	0.979	0.979	**1.003**	**0.995**	**0.985**

4.7.2 Pinched cylinder with end diaphragm problem

In the pinched cylinder problem, a cylinder with an end diaphragm is subjected to a concentrated load at is center top surface A. Its geometry parameters, presented in Figure 4.11(a) are a length L = 600, a radius R = 25 and a thickness t = 0.25. Due to the symmetry of the model, only a quarter is considered for simulations. The Young's modulus is $E = 3e-6$ and the Poisson's ratio is $\nu = 0.3$. This typical benchmark problem is very useful, in that it helps to determine the capability of an element to deal with inextentional bending modes and complex membrane states. The vertical displacement of point A is compared to the reference solution $U_y = 1.8248\, e^{-5}$. Irregular meshes, like in Figure 4.11(b), created using a technique presented in Nguyen-Thanh et al. (2008) are also studied. Results for different mesh sizes are presented in Table 4.3 and in Figure 4.12.

In terms of result accuracy, the proposed element remains the best for regular mesh if all the element formulations are considered and also the best resultant shell element for irregular mesh. Thus, RH8s-1 is here again the best configuration of the proposed elements. It is worth noting that the RH8 element remains slightly more sensitive to mesh distortion than the RH8s-X elements providing lowest precision in case of irregular mesh.

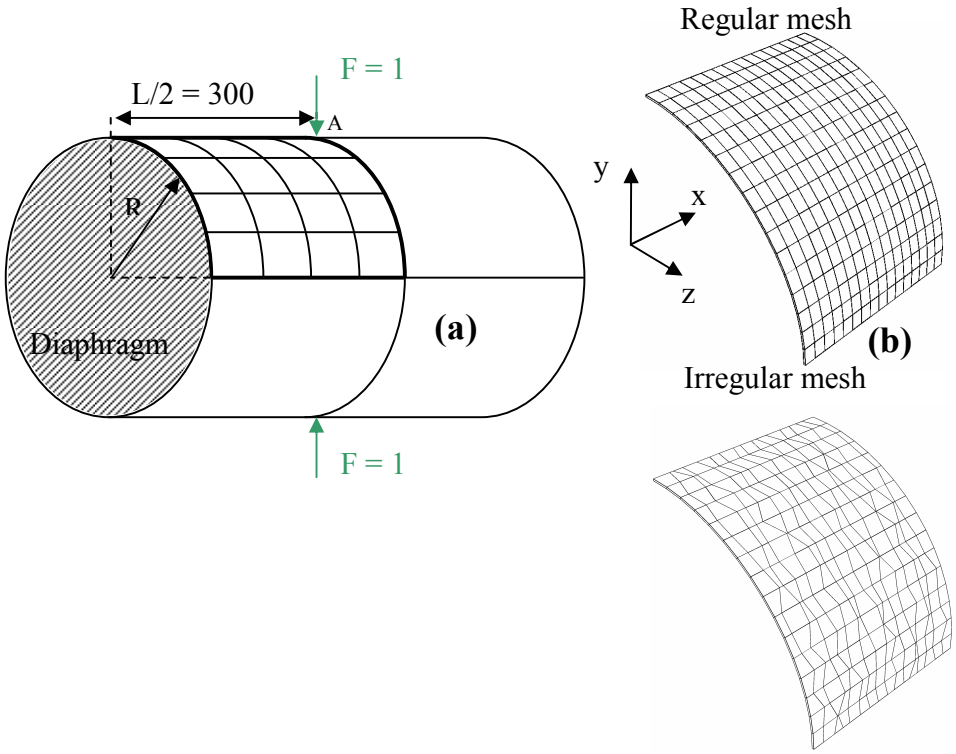

Figure 4.11: Pinched cylinder with end diaphragm problem

Table 4.3: The normalized results of pinched cylinder with end diaphragm problem

Regular mesh							
Element number	SC8R	Xsolid85	SH8	RH8	**RH8s-1**	**RH8s-2**	**RH8s-4**
4x4	0.453	0.382	0.383	0.375	**0.478**	**0.417**	**0.392**
8x8	0.785	0.751	0.75	0.746	**0.81**	**0.782**	**0.758**
16x16	0.945	0.932	0.935	0.929	**0.955**	**0.945**	**0.934**
32x32	0.995	0.991	0.989	0.989	**0.997**	**0.993**	**0.99**
Irregular mesh							
Element number	SC8R		SH8	RH8	**RH8s-1**	**RH8s-2**	**RH8s-4**
4x4	0.458		0.369	0.361	**0.461**	**0.4**	**0.377**
8x8	0.784		0.742	0.739	**0.811**	**0.775**	**0.751**
16x16	0.953		0.928	0.927	**0.963**	**0.948**	**0.933**
32x32	0.999		0.988	0.988	**0.997**	**0.994**	**0.989**

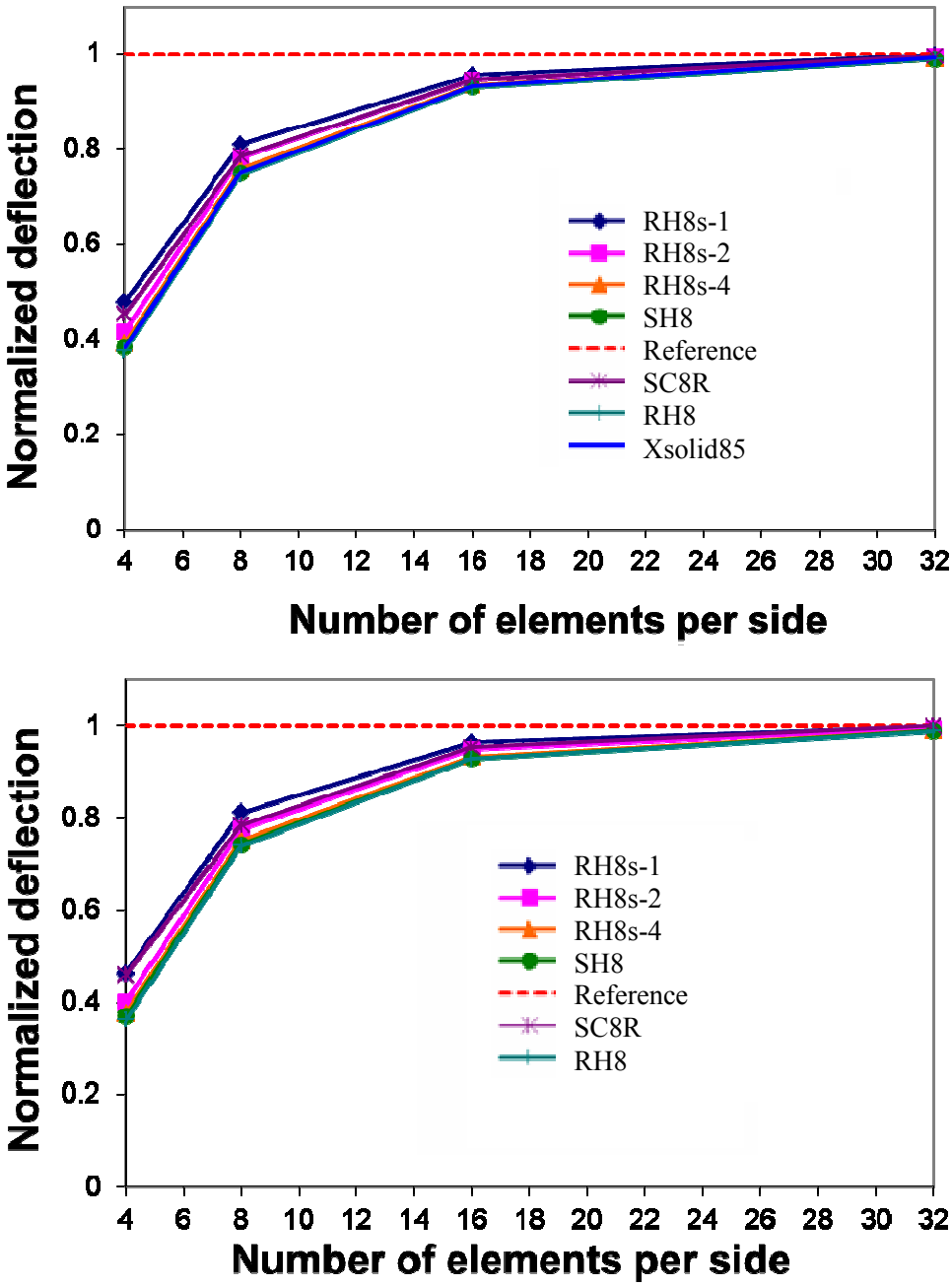

Figure 4.12: Pinched cylinder with end diaphragm problem normalized results

4.7.3 Scordelis-Lo roof problem

The Scordellis-Lo roof problem was first introduced by Scordelis & Lo (1964). Since then, many researchers used it as a standard benchmark problem to check membrane as well as bending shell elements performance. The geometry parameters of the simple curved structure illustrated in Figure 4.13(a) are a length L = 50, a radius R = 25 and a thickness t = 0.25. The used material has a Young's modulus E=4.32e8 and a Poisson's ratio $\nu = 0.0$. The end diaphragms placed at each extremity of the structure are taken into account using the boundary conditions $u_x = u_y = 0$. As for the pinched cylinder with end diaphragm problem, the symmetry of the model allows to consider only one quarter of the structure. The vertical displacement of point A is compared to the reference solution $U_y = -0.3024$. The proposed element capability is tested using a regular as well as an irregular mesh configuration as illustrated in Figure 4.13(b). Convergence results are then presented in Table 4.4 and in Figure 4.14.

The classical RH8 and the SH8 elements are the most accurate when the mesh is regular and offer a better convergence than the proposed RH8s-X elements. However, when an irregular mesh is used, the proposed RH8s-X elements converge faster than the other resultant elements. Moreover, RH8s-4 remains the most accurate resultant element emphasizing the ability of SFEM technique to deal with membrane and bending problem without any locking.

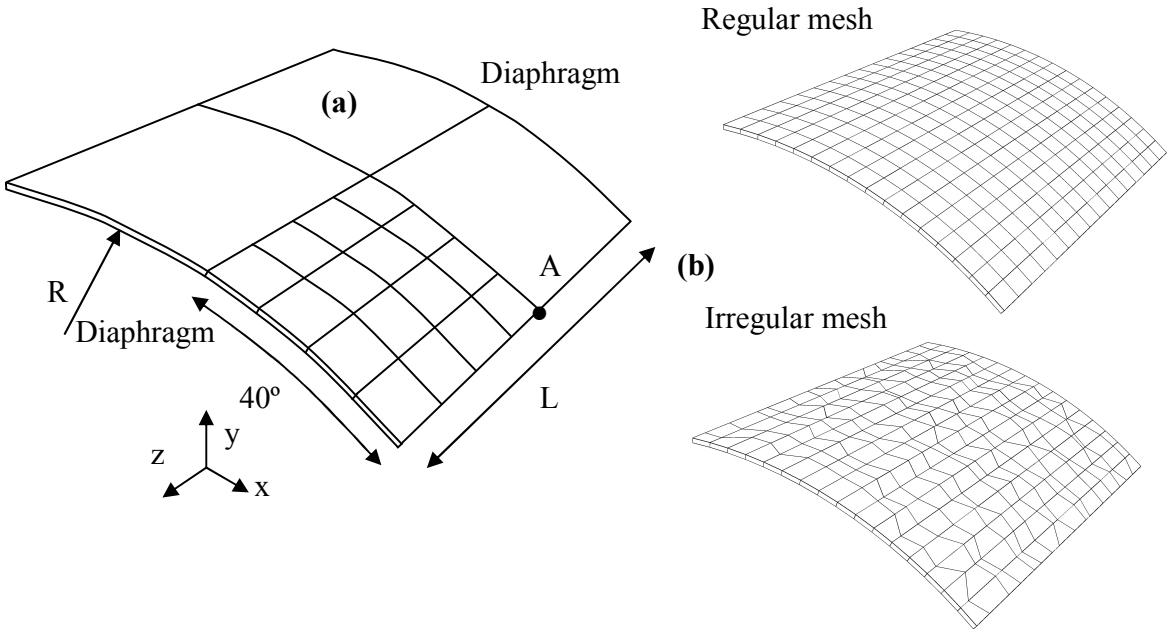

Figure 4.13: Scordelis-Lo roof problem

Table 4.4: The normalized results of Scordelis-Lo roof problem

Regular mesh						
Element number	SC8R	SH8	RH8	**RH8s-2**	**RH8s-2**	**RH8s-4**
4x4	1.206	1.035	1.031	**1.297**	**1.179**	**1.089**
8x8	1.041	1.019	1.018	**1.096**	**1.068**	**1.041**
16x16	1.010	1.009	1.009	**1.035**	**1.028**	**1.021**
32x32	1.000	1.000	1.000	**1.012**	**1.010**	**1.008**
Irregular mesh						
Element number	SC8R	SH8	RH8	**RH8s-1**	**RH8s-2**	**RH8s-4**
4x4	1.281	1.075	1.071	**1.382**	**1.245**	**1.135**
8x8	1.027	0.95	0.949	**1.086**	**1.005**	**0.973**
16x16	1.010	1.000	1.000	**1.036**	**1.022**	**1.013**
32x32	0.998	0.995	0.995	**1.010**	**1.007**	**1.004**

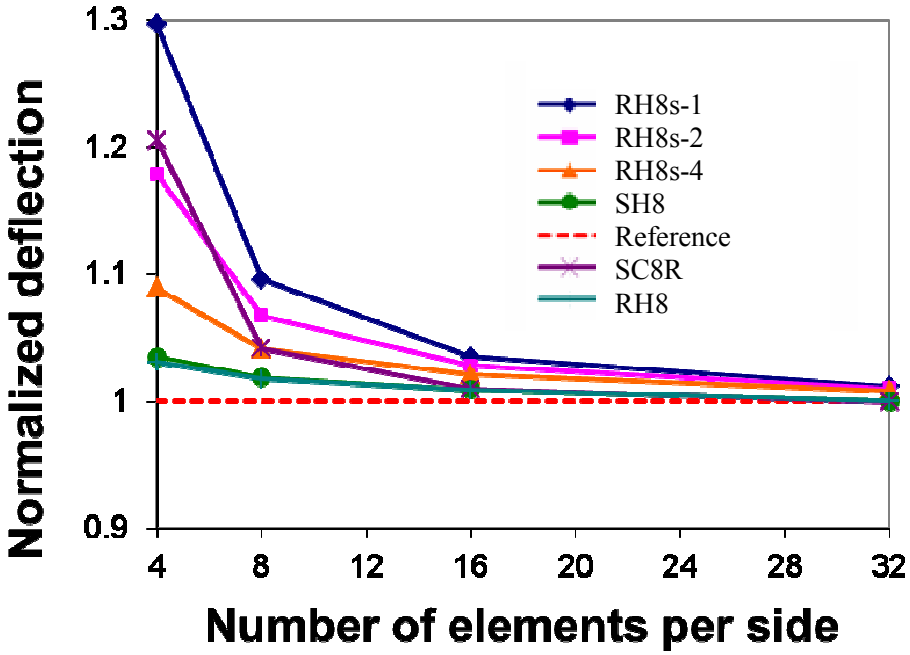

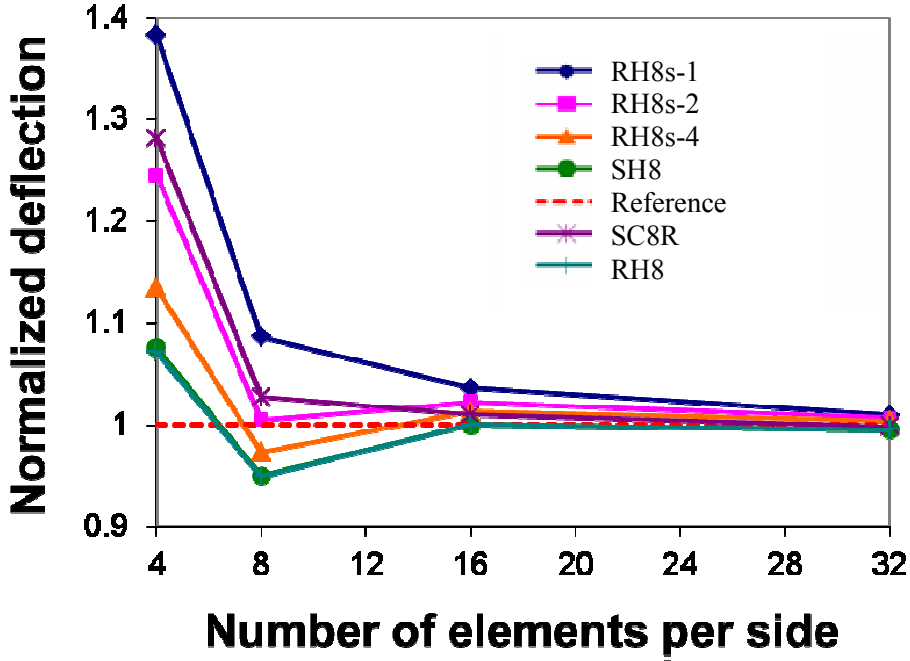

Figure 4.14: Scordelis-Lo roof problem normalized results

4.7.4 Pinched hemispherical with 18º hole problem

This problem was initially proposed to examine the element capability to deal with inextentional bending mode and rigid body movements. The double curvature geometry used in this problem is a severe test and a great way to estimate the jacobian transformation accuracy. A hemispherical with a hole of 18 º is subjected to two opposite concentrated loads Fx = 1 and Fy = -1 as presented in Figure 4.15. Its radius R = 10 and its thickness t = 0.04. The Young's modulus is $E = 6.825e7$ and the Poisson's ratio is $\nu = 0.3$. Due to the problem symmetry, only a quarter of the geometry was studied. The reference analytical point A displacement proposed in Macneal & Harder (1985) was 9.4e-2. Results for different mesh sizes are presented in Table 4.5 and in Figure 4.16.

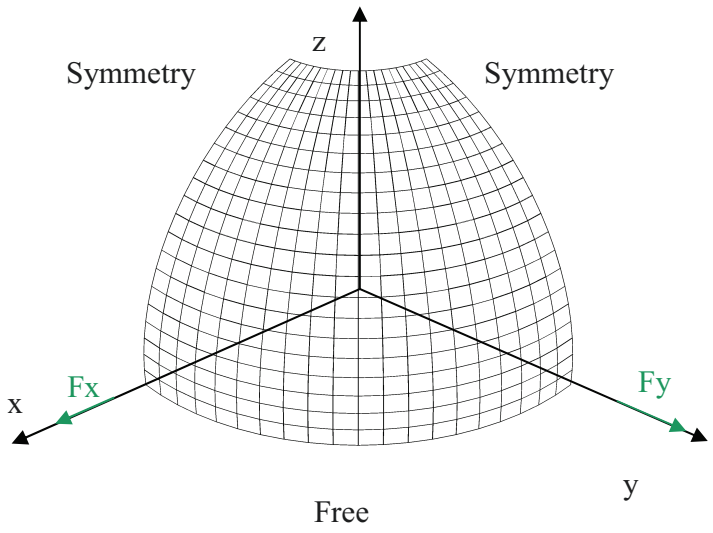

(a)

Figure 4.15: Pinched hemispherical with 18º hole problem

The RH8s-1 element remains more accurate than the other elements as well as the latest Schwarze & Reese (2009) element for thin mesh. However, the other RH8s-2 and RH8s-4 elements have a better convergence.

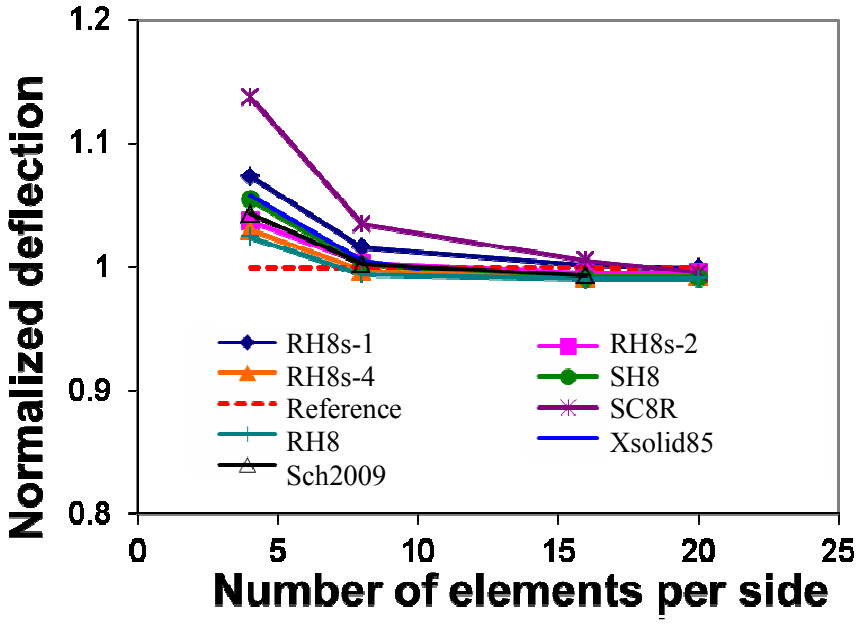

Figure 4.16: Pinched hemispherical with 18º hole problem normalized results

Table 4.5: The normalized results of pinched hemispherical problem

Element number	SC8R	Xsolid85	Sch2009	SH8	RH8	
4	1.138	1.058	1.043	1.055	1.024	
8	1.035	1.005	1.002	1.001	0.994	…
16	1.005	-	0.993	0.992	0.990	
20	0.995	-	-	0.992	0.991	

	RH8s-1	RH8s-2	RH8s-4
	1.073	**1.037**	**1.030**
…	**1.016**	**1.003**	**0.997**
	1.001	**0.996**	**0.992**
	0.999	**0.996**	**0.992**

4.8. Concluding remarks

A review of existing developments using the SFEM is proposed in the introduction of this chapter. The SFEM is already used in shell as well as in solid element formulations however, some issues are still opened. For example, Hung Nguyen-Xuan (2008) has emphasized the necessity to introduce in their solid element formulation based on the SFEM, a stabilization procedure to compensate for the induced rank deficiency and to increase its accuracy. However, this last point still needs some development. The present work has demonstrated that solid-shell elements can also successfully take advantage of this method through the resultant stress theory. The present eight-node resultant solid-shell element does not require any stabilization to remain stable as well and s accurate either for regular or distorted meshes. Following some recent contributions as in Nguyen-Thanh et al. (2008), a 3D variational formulation has been developed yielding in a set of resultant solid-shell elements with smoothed membrane and bending strains. In the proposed element the membrane and bending stiffness matrix integration is transferred to the boundary of cells defined on the mid-surface. No intrinsic shape function derivative and no transformation jacobian matrix inverse calculation are required which makes the element easier to implement than a classical resultant shell element. Moreover, only the normal vectors of four cell boundaries are required per cell to integrate the membrane and bending part of the proposed element. The corresponding theoretical aspects of this method are then presented. Using the ANS techniques the proposed element is free from trapezoidal as well as shear locking. An accurate calculation of the jacobian matrix allows the proposed element to represent very well plate as well as double curved structures. This element remains accurate even with highly distorted meshes and even provides the best accuracy among the tested resultant shell elements. Several 3D numerical benchmark problems have been tested revealing the efficiency of the SFEM when compared to the classical FEM method for membrane and bending problems. Only the linear elastic aspect is considered in this contribution. However, the authors believe that the SFEM could remain efficient in non-linear geometric context regarding the work initiated in Élie-Dit-Cosaque et al. (2011). In addition, investigations on the extension of the SFEM to the two other effects, i.e the transverse shear and through-the-thickness effects could be a good axis of development for future work.

Chapter 5. Improved non-linear eight-node solid – shell element: the case of SH8RSe element

The RH8s-X element presented in Chapter 4 has shown very encouraging results in linear implicit with regular and irregular meshes. However, some development is still necessary to improve its formulation especially for the non-linear terms. As one of the objectives of the present work is to develop a 3D solid shell element and to use it in the hydroforming context, the following investigations will focus on a more classical formulation that also requires some improvement. Various existing solid-shell elements, such as those presented in Chapter 2, could possibly be appropriate for the present study. The SHB8PS reduced integration solid-shell element, has successfully been tested in explicit in Abed-Meraim & Combescure (2002) and in implicit in Legay & Combescure (2003) and more recently in Abed-Meraim & Combescure (2009). This element appears to provide accurate results and is fairly time efficient. Regarding these results, it has been decided to develop a new improved reduced integration solid-shell element, the SH8RSe, which is able to read classical 3D constitutive laws similar to the element proposed by Schwarze & Reese (2011). Its formulation, based on the Hu-Washizu variational formulation, is developed in this chapter in terms of displacements. The present element has been implemented in implicit on the ABAQUS/Standard commercial software, using the ABAQUS/UEL implicit subroutine. The kinematics of the new element is developed based on the work of Abed-Meraim & Combescure (2009) since the terms that require stabilization appear in the displacements field (Source code freely accessible at www.code-aster.org). However, contrary to their element which uses a generalized plane stress constitutive law, the proposed element is based on a full classical 3D constitutive law. Its capabilities are then tested in various linear and non-linear classical benchmark problems to validate the proposed implementation.

5.1. Introduction

A variety of shell finite elements has been developed in order to accurately simulate non-linear behavior of shell like structures. The interest for developing these increasingly sophisticated elements has accelerated since the end of last century with the improvements in computer capabilities. It becomes more and more obvious that the use of such efficient element formulations helps in increasing competitiveness and in saving time and thus money. This is the reason why more and more engineering companies involved in structural analysis and qualification are willing to grasp the potential of these new opportunities in developing non-linear shell elements. Shell elements can be classified into three main types: classical plate and shell elements, degenerated shell elements, and solid-shell elements.

Classical plate and shell elements remain extensively used because they offer a good balance between time efficiency and accuracy, which is well appreciated. They use displacement and rotation degrees of freedoms and usually apply the plane stress assumption. This type of shell elements has been developed by researchers such as Betsch et al. (1996), Bischoff & Ramm (1997), Cardoso & Yoon (2005) and Klinkel et al. (2008).

Degenerated shell elements are four node shell elements obtained by degenerating a solid element to its mid-surface first introduced by Ahmad et al. (1970); but, in contrast with classical plate and shell elements, their variational formulations are defined in 3D. Many authors contributed to those degenerated shell element developments such as Zienkiewicz et al. (1971), Parisch (1978), Dvorkin & Bathe (1984), Belytschko et al. (1984), Bathe & Dvorkin (1985), Simo & Fox (1989), Simo & Rifai (1990) and César de Sá et al. (2002).

Solid-shell elements are the most recently developed shell elements. They combine the advantages of shell theory with the best features of geometry of 3D solid element. They can thus be used to mesh different types of 3D structures, mixing both thin and thick parts. Contact definition remains simplified, when compared with the classical plate and shell elements and degenerated shell ones, due to the presence of nodes on their volume boundary. Moreover, since only displacement degrees of freedoms are used, their kinematics is highly simplified by avoiding the introduction of complicated rotation

concepts. Hence overall, their numerical formulation and implementation becomes more simplified when compared to other types of shell elements relying on both the displacements and rotational degree of freedoms. Parisch (1995), Hauptmann & Schweizerhof (1998), Hauptmann et al. (2000) and Hauptmann et al. (2001) provide valuable contributions to the subject.

However, like other shell elements, solid-shell elements face several locking issues, which can occur because of defects inherent in the related mathematical formulation mostly based on Reissner-Mindlin theory. Transverse shear locking, volumetric locking, Poisson thickness locking, curvature or trapezoidal locking, and membrane locking, detailed in Chapter 2, are among the main locking phenomena. Much effort has been devoted to tackle the five aforementioned locking phenomena.

The assumed natural strain (ANS) method initially developed by Hughes & Tezduyar (1981), Macneal (1982) and Dvorkin & Bathe (1984) has been shown to be an efficient technique to tackle transverse shear locking. This technique consists in interpolating at each integration points the natural transverse shear strain calculated at the middle of the element mid-surface edges. Following the work of Alves de Sousa et al. (2003) and Alves de Sousa et al. (2005), Li et al. (2011) have eliminated transverse shear locking problems using six enhanced assumed strain (EAS) parameters. This technique, initially developed by Simo & Rifai (1990), consists in adding a field of internal variables in the strain field of an element, which creates additional modes of deformation. The proposed reduced integration explicit framework element was based on the Hu-Washizu variational principle to deal with non-linear problems. Prior research on the topic have emphasized the interest of using some enhanced strain parameters to increase the efficiency of the solid-shell element like in the work proposed by Wriggers et al. (1996) and of Alves de Sousa et al. (2003). Seven EAS variables were then used to get rid of the transverse shear locking and the thickness (or volumetric) locking was eliminated using the B-Bar approach as initially developed by Hughes (1980).

Simo & Rifai (1990) proposed the enhanced assumed strain (EAS) method to deal with volumetric locking. However, despite the fact that this provides a good accuracy, it has not been largely used because of the high amount of calculation time required and the relatively

limited computer performance at that time. In fact, adding internal variables in a 3D structure, simultaneously increases the stiffness matrix size and even local condensation consume large computer time if several EAS modes are used. Nevertheless, because of improvements in computer efficiency, researchers now tend to introduce the EAS method in the finite element formulations. Büchter et al. (1994) successfully used this EAS technique in an eight-node shell element in a full 3D integration context to avoid Poisson thickness locking in small as well as in large deformation problems. Miehe (1998) took a different approach and developed a solid type element wherein membrane locking was overcome using one enhanced parameter.

Similar to the shear locking treatment, Betsch et al. (1996) used ANS method to cure curvature locking. The natural thickness strain is calculated in four sampling points located at the corners of the element mid-surface and then interpolated at the integration points. Büchter et al. (1994) employed the EAS method with only one enhanced parameter to circumvent Poisson thickness locking for both linear and non-linear elements. Moreover, it remains very common to combine ANS and EAS method in a given element as illustrated by Kim et al. (2005) or more recently by Hannachi (2007).

Reduced integration, first introduced in Zienkiewicz et al. (1971) is also a numerical solution to limit or to suppress the locking phenomenon. The reduced integration method consists in using fewer integration points than used for a classical fully integrated element. However, this technique introduces zero energy modes, named “hourglass modes”, which require some stabilization as the one proposed by Hughes et al. (1978) and Flanagan & Belytschko (1981). Such stabilization consists in reintroducing artificially the part of stiffness eliminated due to reduced integration. In some recent work, Reese (2005) proposed a solid-shell element with reduced integration and hourglass stabilization. Moreover, three EAS parameters are used to circumvent thickness locking effect. This element is very efficient in dealing with membrane patch test because of the use of the stabilization vector γ originally introduced by Belytschko & Bindeman (1993). However, one element through-the-thickness remains insufficient in bending dominated problems. Besides, even if this element offers interesting properties to deal with thin structures, it does not remain efficient in case of very thin ones. Alves de Sousa et al. (2005) and Alves

de Sousa et al. (2006) have developed another non-linear reduced integration element named RESS with stabilization in linear conditions, not subject to shear or thickness locking phenomenon. This EAS element exhibits a low calculation time. Its stabilization was necessary to counteract the hourglass modes introduced by the reduce integration. Quak (2007) also contributed to the understanding of the RESS element theory. He underlines the fact that, in case of reduced integration, a standard evaluation of the internal stabilization forces is no longer relevant. Similar to the RESS element, one can cite in explicit the work of Abed-Meraim & Combescure (2002) or its adaptation to implicit codes by Legay & Combescure (2003). Their version of the SHB8PS element successfully passed a number of classical patch tests. The use of a modified 3D constitutive law provides to this element immunity to thickness locking. This holds even in case of thin structures, since its response in the normal direction remains independent of its in-plane reaction. However, it appears that its convergence is very slow for some other examples such as the pinched hemispherical. Furthermore, some persistent locking modes still exist due to the out of plane stiffness stabilization term $\mathbf{K}_{33}^{stab}$. The SHB8PS element has then been implemented in implicit in the freeware code ASTER initially developed by the french power supply company EDF. The code for this element and much documentation on the subject are now freely accessible at the following address: www.code-aster.org. A non-linear release of the SHB8PS element is proposed by Abed-Meraim & Combescure (2009). In their contribution, they have developed the variational principle in term of deformation field rate. One of the improvements consists in projecting the discrete gradient operator into some sub-spaces. This allows eliminating both the remaining membrane and transverse shear locking. Moreover, they have used the mean expression of the Hallquist parameters $\hat{\mathbf{b}}_i$ to increase the convergence rate in case of distorted elements, for the stabilized and the unstabilized part of the $\mathbf{B}$ matrix. However, this element uses a modified 3D constitutive law to simulate thin structures. More recently, Schwarze & Reese (2009), Nguyen (2009) and Schwarze & Reese (2011) have proposed a new solid-shell element with reduced integration for geometrically linear and non-linear problems. The ANS technique is used to circumvent both curvature thickness and transverse shear locking. These works have emphasized the fact that transverse shear locking still remains a crucial issue for reduced integration elements. The key point is that four sampling points are used for each transverse

shear terms, rather than two as commonly used for example in the work introduced by Cardoso et al. (2008).

The objective of this chapter is to present a non-linear reduced integration solid-shell element that can deal with thin structures with a classical 3D constitutive law. This new element is named the SH8RSe (**S**hell **h**exahedra **eight** nodes **r**educes integration and **s**tabilized with one **e**nhanced parameter). Doing so, the variational principle is developed in terms of displacement. In the present implicit formulation, a proper identification of the membrane / bending, the transverse shear and the transverse normal components of $\mathbf{B}$ matrix is performed to facilitate locking treatment. Only one enhanced parameter is used to deal with the transverse normal locking. Stabilization is necessary in order to tackle the hourglass modes induced by the reduced integration. The mean expressions of the Hallquist parameters $\hat{\mathbf{b}}_i$ are applied only for the stabilized part of the $\mathbf{B}$ matrix. The present element has successfully been tested in many classical benchmark problems even with highly distorted mesh.

This chapter is organized as follows: The geometric description of a classical eight-node solid element, as well as the calculation of transformation jacobian matrix $\mathbf{J}$ from the global cartesian coordinates system to the natural coordinates system, are presented in section 5.2. The non-linear Green-Lagrange strain tensor $\mathbf{E}$ used in the present formulation is then presented in section 5.3. Moreover, the expression of the SH8RSe element kinematics is documented by identifying the degree of freedoms which require stabilization due to the used reduced integration and in section 5.4.2, the stabilization process is discussed. The variational formulation is given in terms of displacements in section 5.4 and the concept of co-rotational coordinate system initially defined in Ted Belytschko & Bindeman (1993) is introduced for the simplification of the stabilization terms. The concept of a local cartesian coordinates system aligned with the natural coordinates system and its determination method are further discussed in section 5.7.1. Finally, stiffness matrix and internal forces expressions are detailed by bringing out stabilization terms. The present formulation of the SH8RSe element is then successfully validated through various classical linear as well as non-linear benchmark problems even with highly distorted meshes in section 5.9.

5.2. Geometric description of a solid-shell element

The present low order solid-shell element is developed by using the Reissner-Mindlin kinematics presented in section 2.2.1. Its geometry can be fully expressed using the coordinates of its eight nodes as for a classical solid element. In order to overcome the disadvantages of using rotational degrees of freedoms as in classical shell theory, pointed out in Chapter 4, the shell geometry is described through the use of the position vectors of a point located on the upper and on the lower surface respectively $\mathbf{X}_{q_0}^{0,U}$ and $\mathbf{X}_{q_0}^{0,L}$ as illustrated in Figure 5.1. The three configurations of the shell structure discussed in this work and illustrated in Figure 5.2, are: the undeformed configuration, the deformed configuration and the natural configuration. The related coordinates systems are, respectively a global cartesian coordinates system $\mathbf{X}(X,Y,Z)$, a local cartesian coordinates system $\mathbf{x}(x\ ,y\ ,z\ )$ and a convected coordinates system $\boldsymbol{\xi}(\xi^1,\xi^2,\xi^3)$ as detailed in Table 5.1.

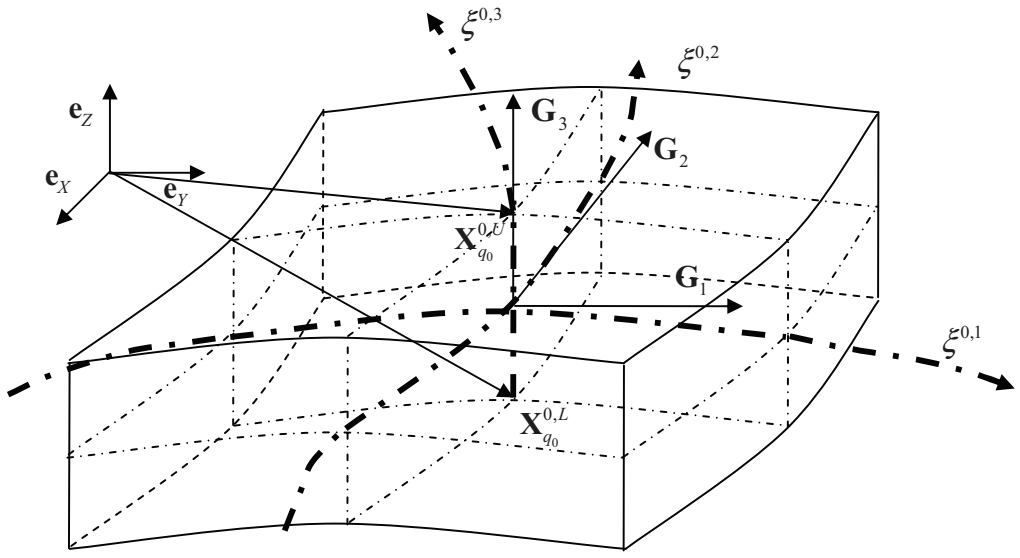

Figure 5.1: Solid-shell element parametrization, undeformed configuration

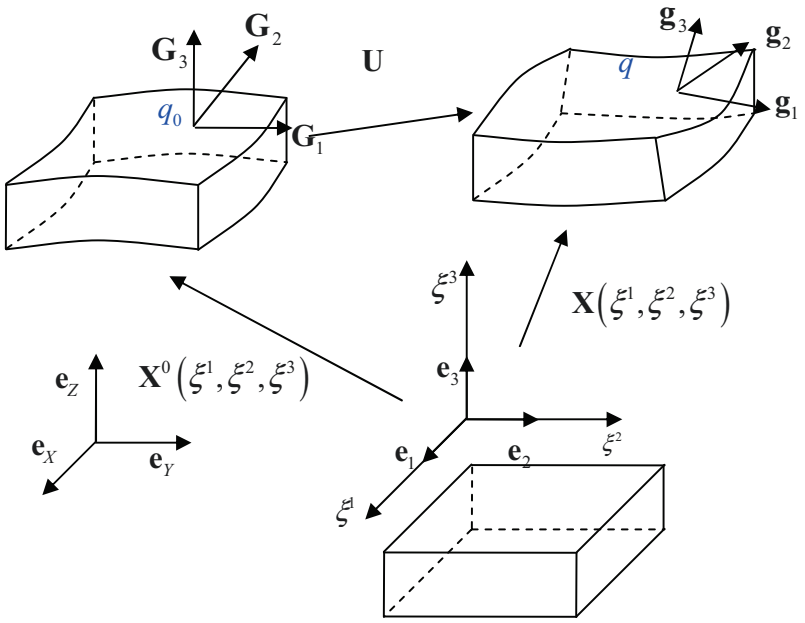

Figure 5.2: Solid-shell element configurations

Table 5.1: Coordinates systems definition		
Level	Base vectors	Coordinates
Global cartesian	$(\mathbf{e}_X, \mathbf{e}_Y, \mathbf{e}_Z)$	$\mathbf{X}^0(X^0, Y^0, Z^0)$ or $\mathbf{X}_i^0, \quad i=1,2,3$ undeformed configuration
		$\mathbf{X}(X, Y, Z)$ or $\mathbf{X}_i, \quad i=1,2,3$ deformed configuration
Natural	$(\mathbf{G}_1, \mathbf{G}_2, \mathbf{G}_3)$ $(\mathbf{g}_1, \mathbf{g}_2, \mathbf{g}_3)$	$\xi(\xi^1, \xi^2, \xi^3)$ or $\xi^i, \quad i=1,2,3$
Local cartesian	$(\mathbf{R}_x, \mathbf{R}_y, \mathbf{R}_z)$ $(\mathbf{r}_x, \mathbf{r}_y, \mathbf{r}_z)$	$\mathbf{x}^0(x^0, y^0, z^0)$ or $\mathbf{x}_i^0, \quad i=1,2,3$ undeformed configuration
		$\mathbf{x}(x, y, z)$ or $\mathbf{x}_i, \quad i=1,2,3$ deformed configuration

By considering ξ^3 as the thickness direction, the position vector of a point q_0 on the solid-shell structure is classically expressed such that:

$$\mathbf{X}_{q_0}^0\left(\xi^1,\xi^2,\xi^3\right)=\frac{(1+\xi^3)}{2}\times\mathbf{X}_{q_0}^{0,U}(\xi^1,\xi^2)+\frac{(1-\xi^3)}{2}\times\mathbf{X}_{q_0}^{0,L}(\xi^1,\xi^2) \qquad (5.1)$$
$$\left(-1\le\xi^1,\xi^2,\xi^3\le 1\right)$$

The covariant base vectors $\left(\mathbf{G}_1,\mathbf{G}_2,\mathbf{G}_3\right)$ in the undeformed configuration shown in Figure 5.1 are not necessarily orthonormal and takes the form:

$$\mathbf{G}_i=\frac{\partial\mathbf{X}^0}{\partial\xi^i},\quad i=1,2,3 \qquad (5.2)$$

and hence the contravariant (or reciprocal) base vectors $\left(\mathbf{G}^1,\mathbf{G}^2,\mathbf{G}^3\right)$, also not necessarily orthonormal, is determined as:

$$\mathbf{G}^i=\frac{\partial\xi^i}{\partial\mathbf{X}^0},\quad i=1,2,3 \qquad (5.3)$$

The covariant base vectors components can then be used to define a local cartesian base vectors $\mathbf{Q}_2=\left[\mathbf{R}_x\quad\mathbf{R}_y\quad\mathbf{R}_z\right]$ in a way that is similar to the approach proposed by Batoz & Dhatt (1992).

The unit normal vector $\mathbf{R}_z=\left\langle R_z^x\quad R_z^y\quad R_z^z\right\rangle$ to the in-plane tangent space is first calculated as:

$$\mathbf{R}_z=\frac{\mathbf{G}_1\wedge\mathbf{G}_2}{\left\|\mathbf{G}_1\wedge\mathbf{G}_2\right\|} \qquad (5.4)$$

Hence, the rotation matrix $\mathbf{Q}_2=\left[\mathbf{R}_x\quad\mathbf{R}_y\quad\mathbf{R}_z\right]$ which rotates a vector from the local cartesian coordinates system $\mathbf{x}^0\left(x^0,y^0,z^0\right)$ to the global cartesian coordinates system $\mathbf{X}^0\left(X^0,Y^0,Z^0\right)$ can be defined as Batoz & Dhatt (1992):

$$\mathbf{Q}_2 = \begin{bmatrix} R_z^z + \dfrac{1}{1+R_z^z} \times \left(R_z^y\right)^2 & -\dfrac{1}{1+R_z^z} \times R_z^x \times R_z^y & R_z^x \\ -\dfrac{1}{1+R_z^z} \times R_z^x \times R_z^y & R_z^z + \dfrac{1}{1+R_z^z} \times \left(R_z^x\right)^2 & R_z^y \\ -R_z^x & -R_z^y & R_z^z \end{bmatrix} \tag{5.5}$$

In the particular case where $\mathbf{R}_z = -\mathbf{e}_z$, $\mathbf{Q}_2$ takes the form:

$$\mathbf{Q}_2 = \begin{bmatrix} 1 & 0 & 0 \\ 0 & -1 & 0 \\ 0 & 0 & -1 \end{bmatrix} \tag{5.6}$$

Moreover in the case where $\mathbf{R}_z = \mathbf{e}_z$, $\mathbf{Q}_2$ is:

$$\mathbf{Q}_2 = \begin{bmatrix} 1 & 0 & 0 \\ 0 & 1 & 0 \\ 0 & 0 & 1 \end{bmatrix} = \mathbf{I} \tag{5.7}$$

where $\mathbf{I} = \begin{bmatrix} 1 & 0 & 0 \\ 0 & 1 & 0 \\ 0 & 0 & 1 \end{bmatrix}$ is the identity matrix.

The position vector $\mathbf{X}_{q_0}^0$ and the displacement vector $\mathbf{U}_q$ of an arbitrary point q expressed in the global cartesian coordinates system $\mathbf{X}^0\left(X^0, Y^0, Z^0\right)$ are transformed into the position vector $\mathbf{x}_{q_0}^0$ and the displacement vector $\mathbf{u}_q$ of the same point q expressed in the local cartesian coordinates system $\mathbf{x}^0\left(x^0, y^0, z^0\right)$ as:

$$\mathbf{x}_q = \mathbf{Q}_2^T \times \left(\mathbf{X}_q - \mathbf{X}_c\right) \tag{5.8}$$

$$\mathbf{u}_q = \mathbf{Q}_2^T \times \mathbf{U}_q \tag{5.9}$$

where $\mathbf{X}_c$ is the position vector of the origin of the local cartesian coordinate system in the global coordinates one.

In the current configuration the position vector is defined in term of the displacement field as:

$$\mathbf{x}\left(\mathbf{X},t\right)=\mathbf{X}+\mathbf{u}\left(\mathbf{X},t\right) \tag{5.10}$$

This becomes in term of shell parameterization or natural coordinates system:

$$\mathbf{x}\left(\xi\right)=\mathbf{X}\left(\xi\right)+\mathbf{u}\left(\xi\right)=X^{i}\left(\xi\right)\mathbf{e}_{i}+\mathbf{u}^{i}\left(\xi^{m}\right)\mathbf{e}_{i} \tag{5.11}$$

The covariant basic vectors in the form of spatial (deformed) description are:

$$\mathbf{g}_{(\alpha)}\left(\xi^{m}\right)=\frac{\partial\mathbf{x}\left(\xi^{m}\right)}{\partial\xi^{\alpha}}=G_{(\alpha)}\left(\xi^{m}\right)+\frac{\partial\mathbf{u}\left(\xi^{m}\right)}{\partial\xi^{\alpha}} \tag{5.12}$$

Hence the metric tensor component $g_{(ij)}$ in the deformed configuration can be expressed in terms of convected basic vector $G_{(i)}$ and the displacement vector $\mathbf{u}$ as follows:

$$\begin{aligned}\mathbf{g}_{(ij)}&=\mathbf{g}_{(i)}\times\mathbf{g}_{(j)}=\left(G_{(i)}+\frac{\partial\mathbf{u}}{\partial\xi^{i}}\right).\left(G_{(j)}+\frac{\partial\mathbf{u}}{\partial\xi^{j}}\right)\\&=G_{(ij)}+G_{(i)}\frac{\partial\mathbf{u}}{\partial\xi^{j}}+G_{(j)}\frac{\partial\mathbf{u}}{\partial\xi^{i}}+\frac{\partial\mathbf{u}}{\partial\xi^{i}}\frac{\partial\mathbf{u}}{\partial\xi^{j}}\end{aligned} \tag{5.13}$$

So the deformation gradient could be written as:

$$\mathrm{F}\left(\xi\right)=\frac{\partial\mathbf{x}\left(\xi\right)}{\partial\mathbf{X}\left(\xi\right)}=\frac{\partial\mathbf{x}\left(\xi\right)}{\partial\xi}\times\frac{\partial\xi}{\partial\mathbf{X}\left(\xi\right)}=\mathbf{g}_{(i)}\otimes\mathbf{G}^{(i)} \tag{5.14}$$

For the sake of simplify, the subscript $\left(\ \right)_q$ is omitted in the subsequent developments as well as the super script $\left(\ \right)^0$ used in reference to the undeformed configuration.

5.3. Deformation of a solid-shell element

Following Vu-Quoc & Tan (2003), the Green-Lagrange strain tensor components E_{ij}^{ξ}, can be defined in the natural coordinates system $\boldsymbol{\xi}\left(\xi^1,\xi^2,\xi^3\right)$ as:

$$E^c\left(\boldsymbol{\xi}\right)=\frac{1}{2}\times\left(\mathrm{F}\left(\boldsymbol{\xi}\right)^{\mathrm{T}}\mathrm{F}\left(\boldsymbol{\xi}\right)\text{-}\mathbf{I}\right)=\frac{1}{2}\times\left[\left(\frac{\partial\mathbf{x}\left(\boldsymbol{\xi}\right)}{\partial\mathbf{X}\left(\boldsymbol{\xi}\right)}\right)^{\mathrm{T}}\times\frac{\partial\mathbf{x}\left(\boldsymbol{\xi}\right)}{\partial\mathbf{X}\left(\boldsymbol{\xi}\right)}\text{-}\mathbf{I}\right]$$
$$=\frac{1}{2}\times\left[\left(\mathbf{g}_{(i)}\otimes\mathbf{G}^{(i)}\right)^{\mathrm{T}}\times\left(\mathbf{g}_j\otimes\mathbf{G}^j\right)\text{-}\mathbf{I}\right]=\frac{1}{2}\times\left[\left(\mathbf{G}^{(i)}\otimes\mathbf{g}_{(i)}\right)\times\left(\mathbf{g}_{(j)}\otimes\mathbf{G}^{(j)}\right)-\mathbf{G}_{(ij)}\times\left(\mathbf{G}^{(i)}\otimes\mathbf{G}^{(j)}\right)\right]$$
$$=\frac{1}{2}\times\left(g_{(ij)}-G_{(ij)}\right)\times\mathbf{G}^{(i)}\otimes\mathbf{G}^{(j)}=\frac{1}{2}\times E_{(ij)}\times\left(\mathbf{G}^{(i)}\otimes\mathbf{G}^{(j)}\right)$$

(5.15)

where

$$E_{ij}^{\xi}=\frac{1}{2}\left(\mathbf{G}_i\frac{\partial\mathbf{u}}{\xi^j}+\frac{\partial\mathbf{u}}{\xi^i}\mathbf{G}_j+\frac{\partial\mathbf{u}}{\xi^i}\frac{\partial\mathbf{u}}{\xi^j}\right),\quad i,j=1,2,3 \tag{5.16}$$

In detail form, the components of the Green-Lagrange natural strain tensor E_{ij}^{ξ} defined in equation (5.16) become:

$$E_{11}^{\xi}=\mathbf{G}_1\times\frac{\partial\mathbf{u}}{\partial\xi^1}+\frac{\partial\mathbf{u}}{\xi^1}\frac{\partial\mathbf{u}}{\xi^1}\qquad E_{22}^{\xi}=\mathbf{G}_2\times\frac{\partial\mathbf{u}}{\partial\xi^2}+\frac{\partial\mathbf{u}}{\xi^2}\frac{\partial\mathbf{u}}{\xi^2}\qquad E_{33}^{\xi}=\mathbf{G}_3\times\frac{\partial\mathbf{u}}{\partial\xi^3}+\frac{\partial\mathbf{u}}{\xi^3}\frac{\partial\mathbf{u}}{\xi^3}$$
$$\Gamma_{12}^{\xi}=\mathbf{G}_1\times\frac{\partial\mathbf{u}}{\partial\xi^2}+\mathbf{G}_2\times\frac{\partial\mathbf{u}}{\partial\xi^1}+\frac{\partial\mathbf{u}}{\xi^1}\frac{\partial\mathbf{u}}{\xi^2}$$
$$\Gamma_{23}^{\xi}=\mathbf{G}_2\times\frac{\partial\mathbf{u}}{\partial\xi^3}+\mathbf{G}_3\times\frac{\partial\mathbf{u}}{\partial\xi^2}+\frac{\partial\mathbf{u}}{\xi^2}\frac{\partial\mathbf{u}}{\xi^3} \tag{5.17}$$
$$\Gamma_{13}^{\xi}=\mathbf{G}_1\times\frac{\partial\mathbf{u}}{\partial\xi^3}+\mathbf{G}_3\times\frac{\partial\mathbf{u}}{\partial\xi^1}+\frac{\partial\mathbf{u}}{\xi^1}\frac{\partial\mathbf{u}}{\xi^3}$$

The Green-Lagrange strain tensor $\mathbf{E}$ can also be written with respect to the local cartesian base vectors as:

$$\mathbf{E}=E_{ij}\mathbf{R}_i\otimes\mathbf{R}_j,\quad i,j=1,2,3 \tag{5.18}$$

Then, when expressed in terms of the contravariant base vectors, the Green-Lagrange strain tensor $\mathbf{E}$ can also be written as:

$$\begin{aligned}\mathbf{E} &= E_{kl}^{\xi}\mathbf{G}^{k}\otimes\mathbf{G}^{l}\\ &= E_{kl}^{\xi}\frac{\partial\xi^{k}}{\partial x_{i}}\mathbf{R}_{i}\otimes\frac{\partial\xi^{l}}{\partial x_{j}}\mathbf{R}_{j}\\ &= E_{kl}^{\xi}\frac{\partial\xi^{k}}{\partial x_{i}}\frac{\partial\xi^{l}}{\partial x_{j}}\mathbf{R}_{i}\otimes\mathbf{R}_{j},\quad i,j,k,l=1,2,3\end{aligned} \tag{5.19}$$

Hence using equations (5.18) and (5.19) it is possible to set-up the relation that transforms the components of the Green-Lagrange natural strain tensor E_{kl}^{ξ} into the components of the Green-Lagrange strain tensor E_{ij} in the local cartesian coordinates system $\mathbf{x}\left(x\ ,y\ ,z\ \right)$ as:

$$E_{ij}=E_{kl}^{\xi}\frac{\partial\xi^{k}}{\partial x_{i}}\frac{\partial\xi^{l}}{\partial x_{j}},\quad i,j,k,l=1,2,3 \tag{5.20}$$

Following Kim et al. (2005), the admissible (or compatible) Green-Lagrange strain tensor $\mathbf{E}$ can be written in the local cartesian coordinates system $\mathbf{x}\left(x\ ,y\ ,z\ \right)$ as:

$$\mathbf{E}=\frac{1}{2}\left(\mathbf{F}^{T}\mathbf{F}-\mathbf{I}\right)=\frac{1}{2}\left\{\left(\nabla_{x}\mathbf{u}\right)+\left(\nabla_{x}\mathbf{u}\right)^{T}+\left(\nabla_{x}\mathbf{u}\right)^{T}\times\left(\nabla_{x}\mathbf{u}\right)\right\} \tag{5.21}$$

where

$$\mathbf{F}=\mathbf{I}+\nabla_{x}\mathbf{u} \tag{5.22}$$

with

$$\nabla_{x}\mathbf{u}=\begin{bmatrix}\dfrac{\partial u}{\partial x} & \dfrac{\partial u}{\partial y} & \dfrac{\partial u}{\partial z}\\ \dfrac{\partial v}{\partial x} & \dfrac{\partial v}{\partial y} & \dfrac{\partial v}{\partial z}\\ \dfrac{\partial w}{\partial x} & \dfrac{\partial w}{\partial y} & \dfrac{\partial w}{\partial z}\end{bmatrix},\qquad \mathbf{u}=\begin{Bmatrix}u\\ v\\ w\end{Bmatrix}=\begin{Bmatrix}u_{1}\\ u_{2}\\ u_{3}\end{Bmatrix} \tag{5.23}$$

Its components E_{ij} in the local cartesian coordinate system $\mathbf{x}\left(x\ ,y\ ,z\ \right)$ are then:

$$E_{ij}=\frac{1}{2}\left(\frac{\partial u_i}{\partial x_j}+\frac{\partial u_j}{\partial x_i}+\frac{\partial u_k}{\partial x_i}\times\frac{\partial u_k}{\partial x_j}\right),\quad i,j,k=1,2,3 \tag{5.24}$$

and can be detailed as follows:

$$\begin{aligned}
E_{xx}&=\frac{\partial u}{\partial x}+\frac{1}{2}\left[\left(\frac{\partial u}{\partial x}\right)^2+\left(\frac{\partial v}{\partial x}\right)^2+\left(\frac{\partial w}{\partial x}\right)^2\right]\\
E_{yy}&=\frac{\partial v}{\partial y}+\frac{1}{2}\left[\left(\frac{\partial u}{\partial y}\right)^2+\left(\frac{\partial v}{\partial y}\right)^2+\left(\frac{\partial w}{\partial y}\right)^2\right]\\
E_{zz}&=\frac{\partial w}{\partial z}+\frac{1}{2}\left[\left(\frac{\partial u}{\partial z}\right)^2+\left(\frac{\partial v}{\partial z}\right)^2+\left(\frac{\partial w}{\partial z}\right)^2\right]\\
\Gamma_{xy}&=\frac{\partial u}{\partial y}+\frac{\partial v}{\partial x}+\left[\frac{\partial u}{\partial x}\times\frac{\partial u}{\partial y}+\frac{\partial v}{\partial x}\times\frac{\partial v}{\partial y}+\frac{\partial w}{\partial x}\times\frac{\partial w}{\partial y}\right]\\
\Gamma_{yz}&=\frac{\partial v}{\partial z}+\frac{\partial w}{\partial y}+\left[\frac{\partial u}{\partial y}\times\frac{\partial u}{\partial z}+\frac{\partial v}{\partial y}\times\frac{\partial v}{\partial z}+\frac{\partial w}{\partial y}\times\frac{\partial w}{\partial z}\right]\\
\Gamma_{xz}&=\frac{\partial u}{\partial z}+\frac{\partial w}{\partial x}+\left[\frac{\partial u}{\partial x}\times\frac{\partial u}{\partial z}+\frac{\partial v}{\partial x}\times\frac{\partial v}{\partial z}+\frac{\partial w}{\partial x}\times\frac{\partial w}{\partial z}\right]
\end{aligned} \tag{5.25}$$

The relation that defines the transformation of the Green-Lagrange strain tensor components from the natural coordinates system to the local coordinates system is obtained by developing and reorganizing the terms of equation (5.20) yielding in:

$$\begin{Bmatrix}E_{xx}\\E_{yy}\\E_{zz}\\\Gamma_{xy}\\\Gamma_{yz}\\\Gamma_{xz}\end{Bmatrix}=\mathbf{T}^G\times\begin{Bmatrix}E_{11}\\E_{22}\\E_{33}\\\Gamma_{12}\\\Gamma_{23}\\\Gamma_{13}\end{Bmatrix} \tag{5.26}$$

where

$$\mathbf{T}^G = \begin{bmatrix} J_{11}^2 & J_{21}^2 & J_{31}^2 & J_{11}J_{21} & J_{21}J_{31} & J_{11}J_{31} \\ J_{12}^2 & J_{22}^2 & J_{32}^2 & J_{12}J_{22} & J_{22}J_{32} & J_{12}J_{32} \\ J_{13}^2 & J_{23}^2 & J_{33}^2 & J_{13}J_{23} & J_{23}J_{33} & J_{13}J_{33} \\ 2J_{11}J_{12} & 2J_{21}J_{22} & 2J_{31}J_{32} & J_{12}J_{21}+J_{11}J_{22} & J_{22}J_{31}+J_{21}J_{32} & J_{12}J_{31}+J_{11}J_{32} \\ 2J_{12}J_{13} & 2J_{22}J_{23} & 2J_{32}J_{33} & J_{23}J_{12}+J_{22}J_{13} & J_{23}J_{32}+J_{22}J_{33} & J_{13}J_{32}+J_{12}J_{33} \\ 2J_{11}J_{13} & 2J_{21}J_{23} & 2J_{31}J_{33} & J_{23}J_{11}+J_{21}J_{13} & J_{23}J_{31}+J_{21}J_{33} & J_{13}J_{31}+J_{11}J_{33} \end{bmatrix} \quad (5.27)$$

with $j_{ij}^G = \left(J_{ij}^G\right)^{-1} = \left(\mathbf{G}_i \times \mathbf{R}_j\right)^{-1}$ the inverse of the components of the matrix $\mathbf{J}^G$ such that $\mathbf{J}^G = \mathbf{G}_i \otimes \mathbf{R}_j$. In order to simplify the notation, the superscript $(\ )^G$ is deliberately omitted in the components of matrix $\mathbf{T}^G$ in equation (5.27) and in the following developments.

Regrouping equation (5.25) in matrix and vector form yields in:

$$\mathbf{E} = \begin{Bmatrix} E_{xx} \\ E_{yy} \\ E_{zz} \\ \Gamma_{xy} \\ \Gamma_{yz} \\ \Gamma_{xz} \end{Bmatrix} = \mathbf{B} \times \mathbf{u} \quad (5.28)$$

where $\mathbf{B} = \mathbf{B}^l + \mathbf{B}^{nl}$ is a sum of a linear and a non-linear part namely $\mathbf{B}^l$ and $\mathbf{B}^{nl}$ such that:

$$\mathbf{B}^{l} = \begin{bmatrix} \dfrac{\partial}{\partial x} & 0 & 0 \\ 0 & \dfrac{\partial}{\partial y} & 0 \\ 0 & 0 & \dfrac{\partial}{\partial z} \\ \dfrac{\partial}{\partial y} & \dfrac{\partial}{\partial x} & 0 \\ 0 & \dfrac{\partial}{\partial z} & \dfrac{\partial}{\partial y} \\ \dfrac{\partial}{\partial z} & 0 & \dfrac{\partial}{\partial x} \end{bmatrix} \tag{5.29}$$

and

$$\mathbf{B}^{nl}\left(\mathbf{u}\right) = \begin{bmatrix} \dfrac{1}{2}\overleftarrow{\times}\dfrac{\partial u}{\partial x}\overleftarrow{\times}\dfrac{\partial}{\partial x} & \dfrac{1}{2}\overleftarrow{\times}\dfrac{\partial v}{\partial x}\overleftarrow{\times}\dfrac{\partial}{\partial x} & \dfrac{1}{2}\overleftarrow{\times}\dfrac{\partial w}{\partial x}\overleftarrow{\times}\dfrac{\partial}{\partial x} \\ \dfrac{1}{2}\overleftarrow{\times}\dfrac{\partial u}{\partial y}\overleftarrow{\times}\dfrac{\partial}{\partial y} & \dfrac{1}{2}\overleftarrow{\times}\dfrac{\partial v}{\partial y}\overleftarrow{\times}\dfrac{\partial}{\partial y} & \dfrac{1}{2}\overleftarrow{\times}\dfrac{\partial w}{\partial y}\overleftarrow{\times}\dfrac{\partial}{\partial y} \\ \dfrac{1}{2}\overleftarrow{\times}\dfrac{\partial u}{\partial z}\overleftarrow{\times}\dfrac{\partial}{\partial z} & \dfrac{1}{2}\overleftarrow{\times}\dfrac{\partial v}{\partial z}\overleftarrow{\times}\dfrac{\partial}{\partial z} & \dfrac{1}{2}\overleftarrow{\times}\dfrac{\partial w}{\partial z}\overleftarrow{\times}\dfrac{\partial}{\partial z} \\ \dfrac{\partial u}{\partial y}\overleftarrow{\times}\dfrac{\partial}{\partial x}+\dfrac{\partial u}{\partial x}\overleftarrow{\times}\dfrac{\partial}{\partial y} & \dfrac{\partial v}{\partial y}\overleftarrow{\times}\dfrac{\partial}{\partial x}+\dfrac{\partial v}{\partial x}\overleftarrow{\times}\dfrac{\partial}{\partial y} & \dfrac{\partial w}{\partial y}\overleftarrow{\times}\dfrac{\partial}{\partial x}+\dfrac{\partial w}{\partial x}\overleftarrow{\times}\dfrac{\partial}{\partial y} \\ \dfrac{\partial u}{\partial z}\overleftarrow{\times}\dfrac{\partial}{\partial y}+\dfrac{\partial u}{\partial y}\overleftarrow{\times}\dfrac{\partial}{\partial z} & \dfrac{\partial v}{\partial z}\overleftarrow{\times}\dfrac{\partial}{\partial y}+\dfrac{\partial v}{\partial y}\overleftarrow{\times}\dfrac{\partial}{\partial z} & \dfrac{\partial w}{\partial z}\overleftarrow{\times}\dfrac{\partial}{\partial y}+\dfrac{\partial w}{\partial y}\overleftarrow{\times}\dfrac{\partial}{\partial z} \\ \dfrac{\partial u}{\partial z}\overleftarrow{\times}\dfrac{\partial}{\partial x}+\dfrac{\partial u}{\partial x}\overleftarrow{\times}\dfrac{\partial}{\partial z} & \dfrac{\partial v}{\partial z}\overleftarrow{\times}\dfrac{\partial}{\partial x}+\dfrac{\partial v}{\partial x}\overleftarrow{\times}\dfrac{\partial}{\partial z} & \dfrac{\partial w}{\partial z}\overleftarrow{\times}\dfrac{\partial}{\partial x}+\dfrac{\partial w}{\partial x}\overleftarrow{\times}\dfrac{\partial}{\partial z} \end{bmatrix} \tag{5.30}$$

In order to facilitate the treatments of the transverse shear locking and the trapezoidal effect, equation (5.28) can be put in a form that highlights the shell deformation modes by decomposing the Green-Lagrange strain tensors into membrane-bending, transverse shear and transverse normal as:

$$\mathbf{E} = \begin{Bmatrix} \mathbf{E}^{mb} \\ \boldsymbol{\Gamma} \\ E^{zz} \end{Bmatrix} \tag{5.31}$$

where the membrane and bending part $\mathbf{E}^{mb}$ of the Green-Lagrange strain tensor is:

$$\mathbf{E}^{mb} = \begin{Bmatrix} \dfrac{\partial u}{\partial x} + \dfrac{1}{2}\left[\left(\dfrac{\partial u}{\partial x}\right)^2 + \left(\dfrac{\partial v}{\partial x}\right)^2 + \left(\dfrac{\partial w}{\partial x}\right)^2\right] \\ \dfrac{\partial v}{\partial y} + \dfrac{1}{2}\left[\left(\dfrac{\partial u}{\partial y}\right)^2 + \left(\dfrac{\partial v}{\partial y}\right)^2 + \left(\dfrac{\partial w}{\partial y}\right)^2\right] \\ \dfrac{\partial u}{\partial y} + \dfrac{\partial v}{\partial x} + \left[\dfrac{\partial u}{\partial x}\times\dfrac{\partial u}{\partial y} + \dfrac{\partial v}{\partial x}\times\dfrac{\partial v}{\partial y} + \dfrac{\partial w}{\partial x}\times\dfrac{\partial w}{\partial y}\right] \end{Bmatrix} = \mathbf{B}^{mb} \times \mathbf{u} \tag{5.32}$$

with

$$\mathbf{B}^{mb} = \begin{bmatrix} \dfrac{\partial}{\partial x} + \dfrac{1}{2}\times\dfrac{\partial u}{\partial x}\times\dfrac{\partial}{\partial x} & \dfrac{1}{2}\times\dfrac{\partial v}{\partial x}\times\dfrac{\partial}{\partial x} & \dfrac{1}{2}\times\dfrac{\partial w}{\partial x}\times\dfrac{\partial}{\partial x} \\ \dfrac{1}{2}\times\dfrac{\partial u}{\partial y}\times\dfrac{\partial}{\partial y} & \dfrac{\partial}{\partial y} + \dfrac{1}{2}\times\dfrac{\partial v}{\partial y}\times\dfrac{\partial}{\partial y} & \dfrac{1}{2}\times\dfrac{\partial w}{\partial y}\times\dfrac{\partial}{\partial y} \\ \dfrac{\partial}{\partial y} + \dfrac{\partial u}{\partial y}\times\dfrac{\partial}{\partial x} + \dfrac{\partial u}{\partial x}\times\dfrac{\partial}{\partial y} & \dfrac{\partial}{\partial x} + \dfrac{\partial v}{\partial y}\times\dfrac{\partial}{\partial x} + \dfrac{\partial v}{\partial x}\times\dfrac{\partial}{\partial y} & \dfrac{\partial w}{\partial y}\times\dfrac{\partial}{\partial x} + \dfrac{\partial w}{\partial x}\times\dfrac{\partial}{\partial y} \end{bmatrix} \tag{5.33}$$

The transverse shear strain part $\mathbf{\Gamma} = \begin{Bmatrix} \Gamma_{yz} \\ \Gamma_{xz} \end{Bmatrix}$ of the Green-Lagrange strain tensor is:

$$\begin{Bmatrix} \Gamma_{yz} \\ \Gamma_{xz} \end{Bmatrix} = \begin{Bmatrix} \dfrac{\partial v}{\partial z} + \dfrac{\partial w}{\partial y} + \left[\dfrac{\partial u}{\partial y}\times\dfrac{\partial u}{\partial z} + \dfrac{\partial v}{\partial y}\times\dfrac{\partial v}{\partial z} + \dfrac{\partial w}{\partial y}\times\dfrac{\partial w}{\partial z}\right] \\ \dfrac{\partial u}{\partial z} + \dfrac{\partial w}{\partial x} + \left[\dfrac{\partial u}{\partial x}\times\dfrac{\partial u}{\partial z} + \dfrac{\partial v}{\partial x}\times\dfrac{\partial v}{\partial z} + \dfrac{\partial w}{\partial x}\times\dfrac{\partial w}{\partial z}\right] \end{Bmatrix} = \mathbf{B}^{\gamma} \times \mathbf{u} \tag{5.34}$$

with $\mathbf{B}^{\gamma}$ is:

$$\mathbf{B}^{\gamma} = \begin{bmatrix} \dfrac{\partial u}{\partial z}\times\dfrac{\partial}{\partial y} + \dfrac{\partial u}{\partial y}\times\dfrac{\partial}{\partial z} & \dfrac{\partial}{\partial z} + \dfrac{\partial v}{\partial z}\times\dfrac{\partial}{\partial y} + \dfrac{\partial v}{\partial y}\times\dfrac{\partial}{\partial z} & \dfrac{\partial}{\partial y} + \dfrac{\partial w}{\partial z}\times\dfrac{\partial}{\partial y} + \dfrac{\partial w}{\partial y}\times\dfrac{\partial}{\partial z} \\ \dfrac{\partial}{\partial z} + \dfrac{\partial u}{\partial z}\times\dfrac{\partial}{\partial x} + \dfrac{\partial u}{\partial x}\times\dfrac{\partial}{\partial z} & \dfrac{\partial v}{\partial z}\times\dfrac{\partial}{\partial x} + \dfrac{\partial v}{\partial x}\times\dfrac{\partial}{\partial z} & \dfrac{\partial}{\partial x} + \dfrac{\partial w}{\partial z}\times\dfrac{\partial}{\partial x} + \dfrac{\partial w}{\partial x}\times\dfrac{\partial}{\partial z} \end{bmatrix}$$

(5.35)

The transverse normal strain E_{zz} is:

$$E_{zz} = \frac{\partial w}{\partial z} + \frac{1}{2}\left[\left(\frac{\partial u}{\partial z}\right)^2 + \left(\frac{\partial v}{\partial z}\right)^2 + \left(\frac{\partial w}{\partial z}\right)^2\right] = \mathbf{B}^{zz} \times \mathbf{u} \tag{5.36}$$

with $\mathbf{B}^{zz}$ is:

$$\mathbf{B}^{zz} = \left[\frac{1}{2}\times\frac{\partial u}{\partial z}\times\frac{\partial}{\partial z} \quad \frac{1}{2}\times\frac{\partial v}{\partial z}\times\frac{\partial}{\partial z} \quad \frac{\partial}{\partial z} + \frac{1}{2}\times\frac{\partial w}{\partial z}\times\frac{\partial}{\partial z}\right] \tag{5.37}$$

5.4. Finite element interpolation for the SH8RSe element and hourglass modes

5.4.1 General description of the SH8RSe element derivative operators

Let's consider a standard eight node isoparametric element as presented in Figure 5.3. The positions $\mathbf{x}(x_1, x_2, x_3)$ and the displacements $\mathbf{u}(u_1, u_2, u_3)$ of an arbitrary point q within the element in the local cartesian coordinates system $\mathbf{x}(x, y, z)$, can be linearly interpolated as follows using the classical tri-linear shape functions N_I where the node number $I = 1, \ldots, 8$.

The arbitrary point q coordinates are:

$$x_i = x_{iI} \times N_I\left(\xi^1, \xi^2, \xi^3\right) = \sum_{I=1}^{8} x_{iI} \times N_I\left(\xi^1, \xi^2, \xi^3\right), \quad \left(i = 1, \ldots, 3 \text{ and } I = 1, \ldots, 8\right) \tag{5.38}$$

The arbitrary point q displacements field could be defined as:

$$u_i = u_{iI} \times N_I\left(\xi^1, \xi^2, \xi^3\right) = \sum_{I=1}^{8} u_{iI} \times N_I\left(\xi^1, \xi^2, \xi^3\right), \quad \left(i = 1, \ldots, 3 \text{ and } I = 1, \ldots, 8\right) \tag{5.39}$$

The expression of the tri-linear shape functions are written in the natural coordinates system $\xi\left(\xi^1, \xi^2, \xi^3\right)$ as:

$$N_I\left(\xi^1,\xi^2,\xi^3\right)=\frac{1}{8}\times\left(1+\xi_I^1\times\xi^1\right)\times\left(1+\xi_I^2\times\xi^2\right)\times\left(1+\xi_I^3\times\xi^3\right) \tag{5.40}$$

with $\xi_I^1,\xi_I^2,\xi_I^3\in\left[-1,1\right]$ are the vertices of the bi-unit cube and $I=1,\ldots,8$.

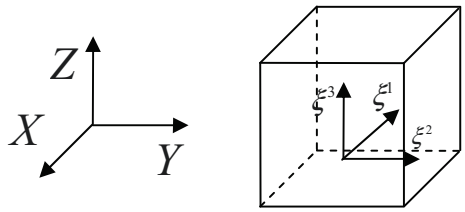

Figure 5.3: Standard eight – node geometry

In order to ease the stabilization process introduced to circumvent the hourglass modes caused by the reduced integration, it is more convenient to redefine the displacements field presented in equation (5.39) in a new basis system as proposed by Belytschko & Bindeman (1993) and which exploits the orthogonality properties of the hourglass modes. This new definition put emphasis on the terms that vanish due to the reduced integration process. The displacements field in the local cartesian coordinate system $\mathbf{x}\left(x,y,z\right)$ can thus be written as:

$$u_i=a_{0i}+a_{1i}\times x+a_{2i}\times y+a_{3i}\times z+c_{1i}\times h_1+c_{2i}\times h_2+c_{3i}\times h_3+c_{4i}\times h_4,\quad\left(i=1,\ldots,3\right) \tag{5.41}$$

where

$$h_1=\xi^2\times\xi^3,\ h_2=\xi^3\times\xi^1,\ h_3=\xi^1\times\xi^2,\ h_4=\xi^1\times\xi^2\times\xi^3 \tag{5.42}$$

are the hourglass functions. The displacements field expressed in equation (5.9) can be approximated in finite element form, $\mathbf{u}\approx\mathbf{u}^e$. For sake of simplicity the superscript $\left(\ \right)^e$ is omitted. Using equation (5.38) and (5.40), equation (5.41) is used to determine the displacements field at each node $\mathbf{u}_i\left(u_{i1},u_{i2},u_{i3},u_{i4},u_{i5},u_{i6},u_{i7},u_{i8}\right)$ as:

$$\mathbf{u}_i = a_{0i}\mathbf{s} + a_{1i}\mathbf{x}_1 + a_{2i}\mathbf{x}_2 + a_{3i}\mathbf{x}_3 + c_{1i}\mathbf{h}_1 + c_{2i}\mathbf{h}_2 + c_{3i}\mathbf{h}_3 + c_{4i}\mathbf{h}_4 \quad ,(i=1,\ldots,3) \tag{5.43}$$

with $\mathbf{x}_i = (x_{i1}, x_{i2}, x_{i3}, x_{i4}, x_{i5}, x_{i6}, x_{i7}, x_{i8}), (i=1,\ldots,3)$ being the nodal positions and

$$\begin{aligned}
\mathbf{s}^T &= (1,1,1,1,1,1,1,1) \\
\mathbf{h}_1^T &= (1,1,-1,-1,-1,-1,1,1) \\
\mathbf{h}_2^T &= (1,-1,-1,1,-1,1,1,-1) \\
\mathbf{h}_3^T &= (1,-1,1,-1,1,-1,1,-1) \\
\mathbf{h}_4^T &= (-1,1,-1,1,1,-1,1,-1)
\end{aligned} \tag{5.44}$$

The vectors $\mathbf{h}_1, \mathbf{h}_2, \mathbf{h}_3, \mathbf{h}_4$ are the degrees of freedom responsible for hourglass modes while implementing reduced integration. They are illustrated in Figure 5.4 taken from Belytschko & Bindeman (1993). As all integration points are located along ξ^3 axis, considered as the thickness direction, with their other coordinate components $\xi^1 = \xi^2 = 0$, they are not taken into account in the element integration. A stabilization technique based on the physical recovery of these lost parameters is then required.

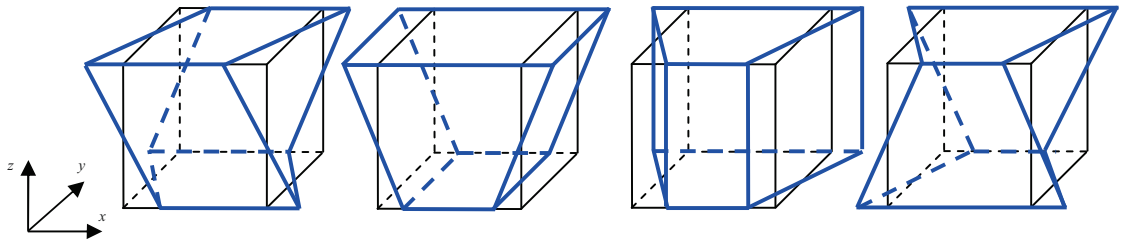

Figure 5.4: Classical hourglass modes in the x direction for a reduced integration hexahedron

As detailed in Puso (2000) and more recently in Abed-Meraim & Combescure (2009), the parameters used in equation (5.43) $a_{0i}, a_{1i}, a_{2i}, a_{3i}, c_{1i}, c_{2i}, c_{3i}, and\ c_{4i}$ appear while writing the classical shape functions in term of local cartesian coordinates $\mathbf{x}(x,y,z)$ instead of the natural coordinates $\xi(\xi^1,\xi^2,\xi^3)$. A brief demonstration aiming at determining the above parameters is presented below, following the same idea.

On the reference element, with the hourglass functions defined in equation (5.42), equation (5.40) can be expanded in terms of new orthogonal set of linearly independent base vectors:

$$\mathbf{s}, \mathbf{g}_{\xi} = \xi_I^1, \mathbf{g}_{\eta} = \xi_I^2, \mathbf{g}_{\zeta} = \xi_I^3, \mathbf{h}_1, \mathbf{h}_2, \mathbf{h}_3, \mathbf{h}_4 \tag{5.45}$$

that span the space $\Re^8$ so that the N_I can be decomposed additively into constant, linear, bilinear and trilinear terms and written as:

$$\mathbf{N}\left(\xi^1, \xi^2, \xi^3\right) = \frac{1}{8}\mathbf{s} + \frac{1}{8}\xi^1\mathbf{g}_{\xi} + \frac{1}{8}\xi^2\mathbf{g}_{\eta} + \frac{1}{8}\xi^3\mathbf{g}_{\zeta} + \frac{1}{8}\xi^1\xi^2\mathbf{h}_1 + \frac{1}{8}\xi^1\xi^3\mathbf{h}_2 + \frac{1}{8}\xi^2\xi^3\mathbf{h}_3 + \frac{1}{8}\xi^1\xi^2\xi^3\mathbf{h}_4 \tag{5.46}$$

with

$$\begin{aligned} \mathbf{g}_{\xi}^T &= (-1,1,1,-1,-1,1,1,-1) \\ \mathbf{g}_{\eta}^T &= (-1,-1,1,1,-1,-1,1,1) \\ \mathbf{g}_{\zeta}^T &= (-1,-1,-1,-1,1,1,1,1) \end{aligned} \tag{5.47}$$

According to Puso (2000), the shape function in equation (5.46) can also be written as:

$$\mathbf{N}\left(\xi^1, \xi^2, \xi^3\right) = \frac{1}{8} \times \left(\mathbf{s} + \sum_{i=1}^{3} \xi_I^i \xi^i + \sum_{\alpha=1}^{4} h_{\beta}\left(\xi^1, \xi^2, \xi^3\right) \times \mathbf{h}_{\beta} \right) \tag{5.48}$$
$$I = 1, \ldots, 8 \; and \; \beta = 1, \ldots, 4$$

A novel expression of the coordinates of an arbitrary point given by equation (5.38) is obtained by using the introduced base vector defined in equations (5.44) and (5.47) and can be written as:

$$\begin{aligned} x_i &= \left[\frac{1}{8}\mathbf{s} + \frac{1}{8}\xi\mathbf{g}_{\xi} + \frac{1}{8}\eta\mathbf{g}_{\eta} + \frac{1}{8}\zeta\mathbf{g}_{\zeta} + \frac{1}{8}\xi\eta\mathbf{h}_1 + \frac{1}{8}\xi\zeta\mathbf{h}_2 + \frac{1}{8}\eta\zeta\mathbf{h}_3 + \frac{1}{8}\xi\eta\zeta\mathbf{h}_4 \right] \times \{\mathbf{x}_i\} \\ &= \frac{1}{8} \times \left(\mathbf{s} + \xi_I^i \xi^i + \sum_{\beta=1}^{4} h_{\beta}\left(\xi^1, \xi^2, \xi^3\right) \times \mathbf{h}_{\beta} \right) \times \mathbf{x}_i \end{aligned} \tag{5.49}$$

with $\mathbf{x}_i = \left(x_{i1}, x_{i2}, x_{i3}, x_{i4}, x_{i5}, x_{i6}, x_{i7}, x_{i8}\right), \left(i = 1, \ldots, 3\right)$.

In the local cartesian coordinates $\mathbf{x}(x,y,z)$ and using equation (5.38), a new expression of matrix $\mathbf{J}$, whose inverse components are used in equation (5.27), can be written as:

$$\begin{aligned}\mathbf{J} &= \frac{\partial \mathbf{x}\left(\xi^1,\xi^2,\xi^3\right)}{\partial \boldsymbol{\xi}} = \frac{\partial \mathbf{N}\left(\xi^1,\xi^2,\xi^3\right)\times \mathbf{x}_i}{\partial \boldsymbol{\xi}} \\ &= \frac{1}{8}\times\frac{\partial\left(\mathbf{s}+\sum_{j=1}^{3}\xi_I^j\xi^i+\sum_{\beta=1}^{4}h_\beta\left(\xi^1,\xi^2,\xi^3\right)\times\mathbf{h}_\beta\right)}{\partial\boldsymbol{\xi}}\times\mathbf{x}_i, \qquad I=1,\ldots,8 \\ &= \frac{1}{8}\times\left[\underbrace{\frac{\partial(\mathbf{s})}{\partial\boldsymbol{\xi}}}_{0}+\sum_{j=1}^{3}\xi_I^j+\frac{\partial\left(\sum_{\beta=1}^{4}h_\beta\left(\xi^1,\xi^2,\xi^3\right)\times\mathbf{h}_\beta\right)}{\partial\boldsymbol{\xi}}\right]\times\mathbf{x}_i\end{aligned} \tag{5.50}$$

At the centroid of the element $\boldsymbol{\xi}(0,0,0)$, the hourglass functions are zero, i.e. $h_1=h_2=h_3=h_4=0$ and the matrix $\mathbf{J}$ evaluated at element centroid becomes $\mathbf{J}_0$ given by:

$$\begin{aligned}\left(\mathbf{J}_0\right)_{ij} &= \frac{1}{8}\times\sum_{j=1}^{3}\xi_I^j\times\mathbf{x}_i \\ &= \frac{1}{8}\times\xi_I^j\times\mathbf{x}_i \qquad , \quad I=1,\ldots,8\end{aligned} \tag{5.51}$$

Introducing equation (5.51) into equation (5.38) yields in:

$$\begin{aligned}x_j &= \frac{1}{8}\times\left(\mathbf{s}+\xi_I^i\xi^i+\sum_{\beta=1}^{4}h_\beta\left(\xi^1,\xi^2,\xi^3\right)\times\mathbf{h}_\beta\right)\times\mathbf{x}_j \\ &= \frac{1}{8}\times\left(\xi_I^i\times\mathbf{x}_j\right)\times\xi^i+\frac{1}{8}\times\left[\mathbf{s}+\sum_{\beta=1}^{4}h_\beta\left(\xi^1,\xi^2,\xi^3\right)\times\mathbf{h}_\beta\right]\times\mathbf{x}_j \qquad , \quad I=1,\ldots,8 \\ &= \left(\mathbf{J}_0\right)_{ij}\times\xi^i+\frac{1}{8}\times\left[\mathbf{s}+\sum_{\beta=1}^{4}h_\beta\left(\xi^1,\xi^2,\xi^3\right)\times\mathbf{h}_\beta\right]\times\mathbf{x}_j\end{aligned} \tag{5.52}$$

Separating the above in term of cartesian and natural coordinates gives:

$$
\begin{aligned}
x_j &= \left(\mathbf{J}_0\right)_{ij} \times \xi^i + \frac{1}{8} \times \left[\mathbf{s} + \sum_{\beta=1}^{4} h_\beta\left(\xi^1,\xi^2,\xi^3\right) \times \mathbf{h}_\beta \right] \times \mathbf{x}_j \\
\Rightarrow \xi^i &= \left(\mathbf{J}_0\right)_{ij}^{-1} \times \left[x_j - \frac{1}{8} \times \mathbf{x}_j \times \left(\mathbf{s} + \sum_{\beta=1}^{4} h_\beta\left(\xi^1,\xi^2,\xi^3\right) \times \mathbf{h}_\beta \right) \right]
\end{aligned}
\tag{5.53}
$$

ξ^i are then expressed in term of cartesian coordinates x_j as:

$$
\xi^i = \left(\mathbf{J}_0\right)_{ij}^{-1} \times \left(x_j - \frac{1}{8} \times \mathbf{s} \times \mathbf{x}_j - \frac{1}{8} \times \sum_{\beta=1}^{4} h_\beta\left(\xi^1,\xi^2,\xi^3\right) \times \mathbf{h}_\beta \times \mathbf{x}_j \right) \tag{5.54}
$$

By replacing the new expression of ξ^i into equation (5.48) and developing the obtained expressions gives:

$$
\begin{aligned}
\mathbf{N}\left(\xi^1,\xi^2,\xi^3\right) = \frac{1}{8} \times \Bigg[& \mathbf{s} + \sum_{i=1}^{3} \left(\mathbf{J}_0\right)_{ij}^{-1} \times \xi_I^i \times \Bigg(x_j - \frac{1}{8} \times \mathbf{s} \times \mathbf{x}_j - \dots \\
& \dots - \frac{1}{8} \times \sum_{\beta=1}^{4} h_\beta\left(\xi^1,\xi^2,\xi^3\right) \times \mathbf{h}_\beta \times \mathbf{x}_j \Bigg) + \sum_{\beta=1}^{4} h_\beta\left(\xi^1,\xi^2,\xi^3\right) \times \mathbf{h}_\beta \Bigg] \\
= \frac{1}{8} \times & \left(\mathbf{s} - \sum_{j=1}^{3} \mathbf{s} \times \mathbf{x}_j \times \mathbf{b}_j \times \right) + \mathbf{b}_j \times x_j + \dots \\
\dots + \frac{1}{8} \times & \sum_{\beta=1}^{4} h_\beta\left(\xi^1,\xi^2,\xi^3\right) \times \left[\mathbf{h}_\beta - \sum_{\beta=1}^{3} \mathbf{h}_\beta \times \mathbf{x}_j \times \mathbf{b}_j \right]
\end{aligned}
\tag{5.55}
$$

where $I = 1,\dots,8$ refers to the node number and where

$$
\mathbf{b}_j = \frac{1}{8} \times \sum_{i=1}^{3} \left(\mathbf{J}_0\right)_{ij}^{-1} \times \xi_I^i = \left. \frac{\partial \mathbf{N}}{\partial x_j} \right|_{\xi^1=0,\xi^2=0,\xi^3=\xi_k^3} \tag{5.56}
$$

is the cartesian derivative of shape function at element centroid.

The new expression of the shape function initially defined in equation (5.40) is then:

$$
\mathbf{N}\left(\xi^1,\xi^2,\xi^3\right) = \mathbf{b}_0 + \mathbf{b}_j \times x_j + \frac{1}{8} \times \sum_{\beta=1}^{4} h_\beta\left(\xi^1,\xi^2,\xi^3\right) \times \boldsymbol{\gamma}_\beta \tag{5.57}
$$

where

$$\mathbf{b}_0 = \frac{1}{8} \times \left(\mathbf{s} - \sum_{j=1}^{3} \mathbf{s} \times \mathbf{x}_j \times \mathbf{b}_j \right) \tag{5.58}$$

$$\boldsymbol{\gamma}_\beta = \frac{1}{8} \times \left[\mathbf{h}_\beta - \sum_{j=1}^{3} \left(\mathbf{h}_\beta^T \times \mathbf{x}_j \right) \times \mathbf{b}_j \right] \tag{5.59}$$

At this step of the demonstration, it remains possible to interpolate the displacements field $\mathbf{u}_I$ at nodes in order to determine the displacements field $\mathbf{u}$ at integration points as detailed in equation (5.39). This is achieved by replacing the expression of the shape function expressed in equation (5.40) by the new expression calculated in equation (5.57). Developing this new expression and identifying terms with those of equation (5.43) then allow determining the parameters $a_{0i}, a_{1i}, a_{2i}, a_{3i}, c_{1i}, c_{2i}, c_{3i}, and\, c_{4i}$ defined in equation (5.43) as follows:

$$\begin{aligned} \mathbf{u} &= \left(\mathbf{b}_0 + \mathbf{b}_j \times x_j + \frac{1}{8} \times \sum_{\beta=1}^{4} h_\beta \left(\xi^1, \xi^2, \xi^3 \right) \times \boldsymbol{\gamma}_\beta \right) \times \mathbf{u}_i \\ &= \mathbf{b}_0 \times \mathbf{u}_i + \mathbf{b}_j \times x_j \times \mathbf{u}_i + \frac{1}{8} \times \sum_{\beta=1}^{4} h_\beta \left(\xi^1, \xi^2, \xi^3 \right) \times \boldsymbol{\gamma}_\beta \times \mathbf{u}_i \\ &= \underbrace{\mathbf{b}_0 \times \mathbf{u}_i}_{a_{0i}} + \underbrace{\mathbf{b}_j \mathbf{u}_i}_{a_{ji}} \times x_j + \underbrace{\boldsymbol{\gamma}_\beta \times \mathbf{u}_i}_{c_{ji}} \times \frac{1}{8} \times \sum_{\beta=1}^{4} h_\beta \left(\xi^1, \xi^2, \xi^3 \right) \\ &\left(i \; and \; j = 1, \ldots, 3 \right) and \left(\beta = 1, \ldots, 4 \right) \end{aligned} \tag{5.60}$$

where $\mathbf{u}_i = \left(u_{i1}, u_{i2}, u_{i3}, u_{i4}, u_{i5}, u_{i6}, u_{i7}, u_{i8} \right)$ and

$$\begin{aligned} a_{0i} &= \mathbf{b}_{0i} \times \mathbf{u}_i \\ a_{ji} &= \mathbf{b}_j^T \times \mathbf{u}_i \left(i \; and \; j = 1, \ldots, 3 \right) and \left(\beta = 1, \ldots, 4 \right) \\ c_{\beta i} &= \gamma_\beta^T \times \mathbf{u}_i \end{aligned} \tag{5.61}$$

Using the displacements field that emphasizes the hourglass modes expressed in equation (5.43) or in equation (5.60), the displacement gradient with respect to x_j can be written as:

$$u_{i,j} = \left(\mathbf{b}_j^T + \sum_{\alpha=1}^{4} \mathbf{h}_{\alpha,j} \times \boldsymbol{\gamma}^T{}_\alpha \right) \times \mathbf{u}_i = \left(\mathbf{b}_j^T + \mathbf{h}_{\alpha,j} \times \boldsymbol{\gamma}^T{}_\alpha \right) \times \mathbf{u}_i \tag{5.62}$$

So the element Green-Lagrange strain tensor given by:

$$E_{ij}^{e} = \frac{1}{2}\left(u_{i,j} + u_{j,i} + u_{k,i}u_{k,j}\right), \quad i,j,k = 1,2,3 \tag{5.63}$$

can be rewritten, by introducing the strain operator decomposed into the linear and non linear contribution as:

$$\mathbf{E}^{e} = \left[\mathbf{B}^{l} + \mathbf{B}^{nl}\left(\mathbf{u}\right)\right]\times\mathbf{u} \tag{5.64}$$

The strain operators becomes, upon introduction of displacement gradient written in term of Halquist vectors $\mathbf{b}_i$ and hourglass terms:

$$\mathbf{B}^{l} = \begin{bmatrix} \mathbf{b}_1^T + \mathbf{h}_{\beta,1}\times\boldsymbol{\gamma}_\beta^T & \mathbf{0} & \mathbf{0} \\ \mathbf{0} & \mathbf{b}_2^T + \mathbf{h}_{\beta,2}\times\boldsymbol{\gamma}_\beta^T & \mathbf{0} \\ \mathbf{0} & \mathbf{0} & \mathbf{b}_3^T + \mathbf{h}_{\beta,3}\times\boldsymbol{\gamma}_\beta^T \\ \mathbf{b}_2^T + \mathbf{h}_{\beta,2}\times\boldsymbol{\gamma}_\beta^T & \mathbf{b}_1^T + \mathbf{h}_{\beta,1}\times\boldsymbol{\gamma}_\beta^T & \mathbf{0} \\ \mathbf{0} & \mathbf{b}_3^T + \mathbf{h}_{\beta,3}\times\boldsymbol{\gamma}_\beta^T & \mathbf{b}_2^T + \mathbf{h}_{\beta,2}\times\boldsymbol{\gamma}_\beta^T \\ \mathbf{b}_3^T + \mathbf{h}_{\beta,3}\times\boldsymbol{\gamma}_\beta^T & \mathbf{0} & \mathbf{b}_1^T + \mathbf{h}_{\beta,1}\times\boldsymbol{\gamma}_\beta^T \end{bmatrix} \tag{5.65}$$

$$\mathbf{B}^{nl} = \begin{bmatrix} \frac{1}{2}\times\mathbf{b}_1^T\times\mathbf{b}_1 & \frac{1}{2}\times\mathbf{b}_1^T\times\mathbf{b}_1 & \frac{1}{2}\times\mathbf{b}_1^T\times\mathbf{b}_1 \\ \frac{1}{2}\times\mathbf{b}_2^T\times\mathbf{b}_2 & \frac{1}{2}\times\mathbf{b}_2^T\times\mathbf{b}_2 & \frac{1}{2}\times\mathbf{b}_2^T\times\mathbf{b}_2 \\ \frac{1}{2}\times\mathbf{b}_3^T\times\mathbf{b}_3 & \frac{1}{2}\times\mathbf{b}_3^T\times\mathbf{b}_3 & \frac{1}{2}\times\mathbf{b}_3^T\times\mathbf{b}_3 \\ \mathbf{b}_2^T\times\mathbf{b}_1 + \mathbf{b}_1^T\times\mathbf{b}_2 & \mathbf{b}_2^T\times\mathbf{b}_1 + \mathbf{b}_1^T\times\mathbf{b}_2 & \mathbf{b}_2^T\times\mathbf{b}_1 + \mathbf{b}_1^T\times\mathbf{b}_2 \\ \mathbf{b}_3^T\times\mathbf{b}_2 + \mathbf{b}_2^T\times\mathbf{b}_3 & \mathbf{b}_3^T\times\mathbf{b}_2 + \mathbf{b}_2^T\times\mathbf{b}_3 & \mathbf{b}_3^T\times\mathbf{b}_2 + \mathbf{b}_2^T\times\mathbf{b}_3 \\ \mathbf{b}_3^T\times\mathbf{b}_1 + \mathbf{b}_1^T\times\mathbf{b}_3 & \mathbf{b}_3^T\times\mathbf{b}_1 + \mathbf{b}_1^T\times\mathbf{b}_3 & \mathbf{b}_3^T\times\mathbf{b}_1 + \mathbf{b}_1^T\times\mathbf{b}_3 \end{bmatrix} \tag{5.66}$$

The superscript $\left(\ \right)^{e}$ is deliberately omitted in the above equations to simplify the notation.

It is interesting to note that all non-linear stabilization terms vanish due to the orthogonality properties of $\boldsymbol{\gamma}_\beta$ $\left(\beta = 1,\ldots,4\right)$ detailed in Abed-Meraim & Combescure (2002) and remember in equations (5.67):

$$\begin{aligned} \gamma_\beta^T \times \mathbf{x}_j &= 0 \\ \gamma_{\beta_1}^T \times \mathbf{h}_{\beta_2} &= \delta_{\beta_1\beta_2} \end{aligned} \tag{5.67}$$

5.4.2 Hourglass stabilization of the SH8RSe element

First of all, the non-linear terms of the strain matrix operator $\mathbf{B}^{nl}$ are not considered in matrix $\mathbf{B}$, in order to alleviate notations. However, these terms need to be considered while dealing with large strain problems. Equation (5.65) then reduces to:

$$\mathbf{B} = \begin{bmatrix} \mathbf{b}_1^T + \mathbf{h}_{\beta,1} \times \gamma_\beta^T & \mathbf{0} & \mathbf{0} \\ \mathbf{0} & \mathbf{b}_2^T + \mathbf{h}_{\beta,2} \times \gamma_\beta^T & \mathbf{0} \\ \mathbf{0} & \mathbf{0} & \mathbf{b}_3^T + \mathbf{h}_{\beta,3} \times \gamma_\beta^T \\ \mathbf{b}_2^T + \mathbf{h}_{\beta,2} \times \gamma_\beta^T & \mathbf{b}_1^T + \mathbf{h}_{\beta,1} \times \gamma_\beta^T & \mathbf{0} \\ \mathbf{0} & \mathbf{b}_3^T + \mathbf{h}_{\beta,3} \times \gamma_\beta^T & \mathbf{b}_2^T + \mathbf{h}_{\beta,2} \times \gamma_\beta^T \\ \mathbf{b}_3^T + \mathbf{h}_{\beta,3} \times \gamma_\beta^T & \mathbf{0} & \mathbf{b}_1^T + \mathbf{h}_{\beta,1} \times \gamma_\beta^T \end{bmatrix} \tag{5.68}$$

As mentioned in the previous section, the SH8RSe element integration points are aligned on the thickness direction as pointed up in Figure 5.5. Their positions in the natural coordinates system $\left(\xi^1, \xi^2, \xi^3\right)$ are defined as $\left(0, 0, \xi^3_{n_{ip}}\right)$ where n_{ip} refers to the number of used integration points.

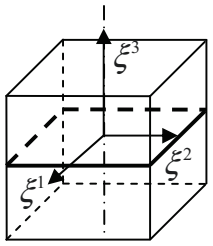

Figure 5.5: Standard eight – node geometry

A set of five integration point coordinates is proposed in Table 5.2 (See Abed-Meraim & Combescure (2009))**.**

n_{ip}	ξ^1	ξ^2	ξ^3	w
1	0	0	−0.906179845938664	0.236926885056189
2	0	0	−0.538469310105683	0.478628670499366
3	0	0	0	0.568888888888889
4	0	0	0.538469310105683	0.478628670499366
5	0	0	0.906179845938664	0.236926885056189

Table 5.2: Five integration points position and weight

However, using these integration points in the element integration process makes the derivative terms $h_{\beta,i}, \left(\beta = 3,4 \; and \; i = 1,\ldots,3\right)$ in matrix $\mathbf{B}$ of equation (5.68) equal to zero. Hence, the matrix $\mathbf{B}$ takes the reduced form:

$$\mathbf{B}_{\xi=\xi_{n_{ip}}} = \mathbf{B}_{12} = \begin{bmatrix} \mathbf{b}_1^T + \sum_{\beta=1}^{2} \mathbf{h}_{\beta,1} \times \boldsymbol{\gamma}_\beta^T & \mathbf{0} & \mathbf{0} \\ \mathbf{0} & \mathbf{b}_2^T + \sum_{\beta=1}^{2} \mathbf{h}_{\beta,2} \times \boldsymbol{\gamma}_\beta^T & \mathbf{0} \\ \mathbf{0} & \mathbf{0} & \mathbf{b}_3^T + \sum_{\beta=1}^{2} \mathbf{h}_{\beta,3} \times \boldsymbol{\gamma}_\beta^T \\ \mathbf{b}_2^T + \sum_{\beta=1}^{2} \mathbf{h}_{\beta,2} \times \boldsymbol{\gamma}_\beta^T & \mathbf{b}_1^T + \sum_{\beta=1}^{2} \mathbf{h}_{\beta,1} \times \boldsymbol{\gamma}_\beta^T & \mathbf{0} \\ \mathbf{0} & \mathbf{b}_3^T + \sum_{\beta=1}^{2} \mathbf{h}_{\beta,3} \times \boldsymbol{\gamma}_\beta^T & \mathbf{b}_2^T + \sum_{\beta=1}^{2} \mathbf{h}_{\beta,2} \times \boldsymbol{\gamma}_\beta^T \\ \mathbf{b}_3^T + \sum_{\beta=1}^{2} \mathbf{h}_{\beta,3} \times \boldsymbol{\gamma}_\beta^T & \mathbf{0} & \mathbf{b}_1^T + \sum_{\beta=1}^{2} \mathbf{h}_{\beta,1} \times \boldsymbol{\gamma}_\beta^T \end{bmatrix} \tag{5.69}$$

However, this reduction is responsible for a rank deficiency in the stiffness matrix that needs to be fixed with a stabilization process. Among the pioneers of the method, Flanagan & Belytschko (1981) developed a stabilization method for a four nodes element. Many extensions of this method have then been developed by Belytschko & Bindeman (1991) for four node elements and by Belytschko & Bindeman (1993) for eight node elements. Some other researchers proposed some valuable works for element stabilization such as Reese et al. (1999), Cardoso et al. (2002) and more recently Schwarze & Reese (2009).

The method initially proposed in Belytschko & Bindeman (1993) and further detailed in Abed-Meraim & Combescure (2009) is applied in the present work. As they mentioned, the

six hourglass modes (h_3 and h_4 for the three degrees of freedom), illustrated in Figure 5.4 inspired by Belytschko & Bindeman (1993), that need to be fixed have been found by solving at each integration points the following equation:

$$\mathbf{B}\left(\xi^3_{n_{ip}}\right)\times\mathbf{u}=\mathbf{0} \tag{5.70}$$

Equation (5.70) helps then to determine the stabilization section $\mathbf{B}_{34}$ of matrix $\mathbf{B}$ that vanishes with the reduced integration. Equation (5.68) can be decomposed into a sum of an unstabilized and a stabilized part, respectively represented by $\mathbf{B}_{12}$ and $\mathbf{B}_{34}$ such that:

$$\mathbf{B}=\mathbf{B}_{12}+\mathbf{B}_{34} \tag{5.71}$$

where the stabilization part $\mathbf{B}_{34}$ is:

$$\mathbf{B}_{34}=\begin{bmatrix} \sum_{\beta=3}^{4} h_{\beta,1}\times\gamma_\beta^T & \mathbf{0} & \mathbf{0} \\ \mathbf{0} & \sum_{\beta=3}^{4} h_{\beta,2}\times\gamma_\beta^T & \mathbf{0} \\ \mathbf{0} & \mathbf{0} & h_{4,3}\times\gamma_4^T \\ \sum_{\beta=3}^{4} h_{\beta,2}\times\gamma_\beta^T & \sum_{\beta=3}^{4} h_{\beta,1}\times\gamma_\beta^T & \mathbf{0} \\ \mathbf{0} & h_{4,3}\times\gamma_4^T & \sum_{\beta=3}^{4} h_{\beta,2}\times\gamma_\beta^T \\ h_{4,3}\times\gamma_4^T & \mathbf{0} & \sum_{\beta=3}^{4} h_{\beta,1}\times\gamma_\beta^T \end{bmatrix} \tag{5.72}$$

For convergence problem it has been found useful to replace the Hallquist form of the $\mathbf{b}_i$ vectors (See Hallquist (1983)), in the previous equation (5.56) by their averaged values $\hat{\mathbf{b}}_i$ used by Flanagan & Belytschko (1981):

$$\hat{\mathbf{b}}_i=\frac{1}{V}\int_V \mathbf{N}_{,i}\left(\xi,\eta,\zeta\right)dV,\quad i=1,2,3 \tag{5.73}$$

where $V \approx V^e$ is the element volume.

As a consequence, γ_β of equation (5.59) becomes:

$$\hat{\gamma}_\beta = \frac{1}{8} \times \left[\mathbf{h}_\beta - \sum_{j=1}^{3} \left(\mathbf{h}_\beta^T \times \mathbf{X}_j \right) \times \hat{\mathbf{b}}_j \right] \tag{5.74}$$

The strain matrix operator $\mathbf{B}$ will thus be replaced by a modified strain matrix operator $\hat{\mathbf{B}}$ obtained by substituting the Hallquist parameters $\mathbf{b}_i$ with their corresponding averaged values $\hat{\mathbf{b}}_i$ on the element.

It is important to note that in the present work development, equations (5.73) and (5.74) are used only for the stabilized part of the strain matrix operator $\mathbf{B}$. Consequently, replacing $\mathbf{b}_i$ by $\hat{\mathbf{b}}_i$ and γ_β by $\hat{\gamma}_\beta$ in equation (5.72) the strain matrix operator $\mathbf{B}$ is transformed into the following $\hat{\mathbf{B}}$ matrix:

$$\hat{\mathbf{B}} = \mathbf{B}_{12} + \hat{\mathbf{B}}_{34} \tag{5.75}$$

where

$$\hat{\mathbf{B}}_{34} = \begin{bmatrix} \sum_{\beta=3}^{4} h_{\beta,1} \times \hat{\gamma}_\beta^T & \mathbf{0} & \mathbf{0} \\ \mathbf{0} & \sum_{\beta=3}^{4} h_{\beta,2} \times \hat{\gamma}_\beta^T & \mathbf{0} \\ \mathbf{0} & \mathbf{0} & h_{4,3} \times \hat{\gamma}_4^T \\ \sum_{\beta=3}^{4} h_{\beta,2} \times \hat{\gamma}_\beta^T & \sum_{\beta=3}^{4} h_{\beta,1} \times \hat{\gamma}_\beta^T & \mathbf{0} \\ \mathbf{0} & h_{4,3} \times \hat{\gamma}_4^T & \sum_{\beta=3}^{4} h_{\beta,2} \times \hat{\gamma}_\beta^T \\ h_{4,3} \times \hat{\gamma}_4^T & \mathbf{0} & \sum_{\beta=3}^{4} h_{\beta,1} \times \hat{\gamma}_\beta^T \end{bmatrix} \tag{5.76}$$

5.4.3 Description of the SH8RSe element unstabilized derivative operators

In order to achieve a locking-free finite element, the ANS and the EAS concepts are implemented at the level of the covariant strain components. Afterwards by means of equation (5.26), the latter are transformed into the cartesian basis. The finite element approximation of the membrane and bending strain field, defined in equation (5.32) is:

$$\mathbf{E}^{mb} = \mathbf{T}^{mb} \times \mathbf{E}^{mb,\xi} \tag{5.77}$$

where the natural membrane and bending strain $\mathbf{E}^{mb,\xi}$ in matrix form is obtained by developing equation (5.17) as:

$$\begin{aligned} \mathbf{E}^{mb,\xi} &= \sum_{I=1}^{8} \left(\mathbf{B}_{12}^{mb} \right)_I . \mathbf{u}_i \\ &= \sum_{I=1}^{8} \left[\left(\mathbf{B}_{12}^{l,mb} \right)_I + \left(\mathbf{B}_{12}^{nl,mb} \right)_I \right] . \mathbf{u}_i, \quad i = 1,2,3 \end{aligned} \tag{5.78}$$

and where $\left(\mathbf{B}_{12}^{mb} \right)_I = \left(\mathbf{B}_{12}^{l,mb} \right)_I + \left(\mathbf{B}_{12}^{nl,mb} \right)_I$ represent the membrane and bending strain operator with:

$$\left(\mathbf{B}_{12}^{l,mb} \right)_I = \begin{bmatrix} \mathbf{G}_1^T \times \dfrac{\partial N_I}{\partial \xi^1} & 0 \\ 0 & \mathbf{G}_2^T \times \dfrac{\partial N_I}{\partial \xi^2} \\ \mathbf{G}_2^T \times \dfrac{\partial N_I}{\partial \xi^1} & \mathbf{G}_1^T \times \dfrac{\partial N_I}{\partial \xi^2} \end{bmatrix}, \qquad (I = 1, \ldots, 8) \tag{5.79}$$

and

$$\left(\mathbf{B}_{12}^{nl,mb}\right)_I(\mathbf{u}) = \begin{bmatrix} \frac{1}{2}\times\frac{\partial u_1}{\partial \xi^1}\times\frac{\partial N_I}{\partial \xi^1} & \frac{1}{2}\times\frac{\partial u_2}{\partial \xi^1}\times\frac{\partial N_I}{\partial \xi^1} & \frac{1}{2}\times\frac{\partial u_3}{\partial \xi^1}\times\frac{\partial N_I}{\partial \xi^1} \\ \frac{1}{2}\times\frac{\partial u_1}{\partial \xi^2}\times\frac{\partial N_I}{\partial \xi^2} & \frac{1}{2}\times\frac{\partial u_2}{\partial \xi^2}\times\frac{\partial N_I}{\partial \xi^2} & \frac{1}{2}\times\frac{\partial u_3}{\partial \xi^2}\times\frac{\partial N_I}{\partial \xi^2} \\ \frac{\partial u_1}{\partial \xi^1}\times\frac{\partial N_I}{\partial \xi^2}+\frac{\partial u_1}{\partial \xi^2}\times\frac{\partial N_I}{\partial \xi^1} & \frac{\partial u_2}{\partial \xi^1}\times\frac{\partial N_I}{\partial \xi^2}+\frac{\partial u_2}{\partial \xi^2}\times\frac{\partial N_I}{\partial \xi^1} & \frac{\partial u_3}{\partial \xi^1}\times\frac{\partial N_I}{\partial \xi^2}+\frac{\partial u_3}{\partial \xi^2}\times\frac{\partial N_I}{\partial \xi^1} \end{bmatrix} \quad (5.80)$$

, $\quad (I = 1,\ldots,8)$

In equation (5.77), the matrix and $\mathbf{T}^{mb}$ is extracted from equation (5.27) as follows:

$$\mathbf{T}^{mb} = \begin{bmatrix} J_{11}^2 & J_{21}^2 & J_{11}J_{21} \\ J_{12}^2 & J_{22}^2 & J_{12}J_{22} \\ 2J_{11}J_{12} & 2J_{21}J_{22} & J_{12}J_{21}+J_{11}J_{22} \end{bmatrix} \quad (5.81)$$

The finite element approximation of the natural transverse shear strain, defined in equation (5.34), expressed in the element mid-surface $\xi^3 = 0$ is written as:

$$\mathbf{\Gamma} = \mathbf{T}^{\gamma}_{\xi^3=0}\times\mathbf{\Gamma}^{\xi} \quad (5.82)$$

where the natural transverse shear strain $\mathbf{\Gamma}^{\xi}$ in matrix form is obtained by developing equation (5.17) as:

$$\mathbf{\Gamma}^{\xi} = \begin{Bmatrix} \Gamma_{23}^{\xi} \\ \Gamma_{13}^{\xi} \end{Bmatrix} = \sum_{I=1}^{8}\left(\mathbf{B}_{12}^{\Gamma,0}\right)_I\times\mathbf{u}_i, \quad i = 1,2,3 \quad (5.83)$$

and where $\left(\mathbf{B}_{12}^{\Gamma,0}\right)_I = \left(\mathbf{B}_{12}^{l,\Gamma,0}\right)_I + \left(\mathbf{B}_{12}^{nl,\Gamma,0}\right)_I$ is the transverse shear strain operator expressed in the element mid-surface $\xi^3 = 0$, with:

$$\left(\mathbf{B}_{12}^{l,\Gamma,0}\right)_I = \begin{bmatrix} \mathbf{0} & \mathbf{G}_3 \times \dfrac{\partial N_I}{\partial \xi^2} & \mathbf{G}_2 \times \dfrac{\partial N_I}{\partial \xi^3} \\ \mathbf{G}_3 \times \dfrac{\partial N_I}{\partial \xi^1} & \mathbf{0} & \mathbf{G}_1 \times \dfrac{\partial N_I}{\partial \xi^3} \end{bmatrix}, \qquad (I = 1,\ldots,8) \tag{5.84}$$

and

$$\left(\mathbf{B}_{12}^{nl,\Gamma,0}\right)_I = \frac{1}{2} \times \begin{bmatrix} \dfrac{\partial u_1}{\partial \xi^2} \times \dfrac{\partial N_I}{\partial \xi^3} + \dfrac{\partial u_1}{\partial \xi^3} \times \dfrac{\partial N_I}{\partial \xi^2} & \dfrac{\partial u_2}{\partial \xi^2} \times \dfrac{\partial N_I}{\partial \xi^3} + \dfrac{\partial u_2}{\partial \xi^3} \times \dfrac{\partial N_I}{\partial \xi^2} & \dfrac{\partial u_3}{\partial \xi^2} \times \dfrac{\partial N_I}{\partial \xi^3} + \dfrac{\partial u_3}{\partial \xi^3} \times \dfrac{\partial N_I}{\partial \xi^2} \\ \dfrac{\partial u_1}{\partial \xi^1} \times \dfrac{\partial N_I}{\partial \xi^3} + \dfrac{\partial u_1}{\partial \xi^3} \times \dfrac{\partial N_I}{\partial \xi^1} & \dfrac{\partial u_2}{\partial \xi^1} \times \dfrac{\partial N_I}{\partial \xi^3} + \dfrac{\partial u_2}{\partial \xi^3} \times \dfrac{\partial N_I}{\partial \xi^1} & \dfrac{\partial u_3}{\partial \xi^1} \times \dfrac{\partial N_I}{\partial \xi^3} + \dfrac{\partial u_3}{\partial \xi^3} \times \dfrac{\partial N_I}{\partial \xi^1} \end{bmatrix}, \qquad (I = 1,\ldots,8) \tag{5.85}$$

The matrix and $\mathbf{T}^{\gamma}_{\xi^3=0}$ is extracted from equation (5.27) as follows:

$$\mathbf{T}^{\gamma}_{\xi^3=0} = \begin{bmatrix} j_{22} j_{33} & j_{12} j_{33} \\ j_{21} j_{33} & j_{11} j_{33} \end{bmatrix} \tag{5.86}$$

The finite element approximation of the element transverse normal strain, defined in equation (5.36) and expressed in the element mid-surface $\xi^3 = 0$ is:

$$E_{zz} = j_{33}^2 \times E_{33}^{\xi} \tag{5.87}$$

where the natural transverse normal strain $\mathbf{E}_{33}^{\xi}$ in matrix form is obtained by developing equation (5.17) as:

$$E_{33}^{\xi} = \sum_{I=1}^{8} \left(\mathbf{B}_{12}^{\zeta\zeta,0}\right)_I \times \mathbf{u}_i, \quad i = 1,2,3 \tag{5.88}$$

and where $\left(\mathbf{B}_{12}^{\zeta\zeta,0}\right)_I = \left(\mathbf{B}_{12}^{l,\zeta\zeta,0}\right)_I + \left(\mathbf{B}_{12}^{nl,\zeta\zeta,0}\right)_I$ is the transverse normal strain operator evaluated in the element mid-surface $\xi^3 = 0$, with:

$$\left(\mathbf{B}_{12}^{l,\zeta\zeta,0}\right)_I = \frac{1}{2}\times\left[0 \quad 0 \quad \mathbf{G}_3\times\frac{\partial N_I}{\partial\xi^3}\right], \qquad \left(I=1,\ldots,8\right) \tag{5.89}$$

and

$$\left(\mathbf{B}_{12}^{nl,\zeta\zeta,0}\right)_I = \left[\frac{1}{2}\times\frac{\partial u_1}{\partial\xi^3}\times\frac{\partial N_I}{\partial\xi^3} \quad \frac{1}{2}\times\frac{\partial u_2}{\partial\xi^3}\times\frac{\partial N_I}{\partial\xi^3} \quad \frac{1}{2}\times\frac{\partial u_3}{\partial\xi^3}\times\frac{\partial N_I}{\partial\xi^3}\right], \qquad \left(I=1,\ldots,8\right) \tag{5.90}$$

5.4.4 Transverse shear locking treatment

The Assumed Natural Strain (ANS) method, developed by Hughes & Tezduyar (1981), has been successfully used by several authors in order to reduce the transverse shear locking effects. In the fully integrated eight-node elements, two sampling points per transverse shear components, located at the middle of the mid-surface edges, are used to evaluate the natural shear strains Γ_{13}^{ξ} and Γ_{23}^{ξ}. However, as initially revealed by Cardoso et al. (2008), using only two sampling points per transverse shear components for reduced integration elements does not provide enough accuracy to the element. Their proposed method consists in interpolating the natural shear strains from four sampling points as illustrated Figure 5.6. Then following this approach, Schwarze & Reese (2009) and Schwarze & Reese (2011) successfully extended the ANS concept to the two remaining element planes $\left(\xi^2,\xi^3\right)$ and $\left(\xi^3,\xi^1\right)$, providing significantly more accuracy since the constant through the thickness transverse shear assumption is omitted. The sampling points for Γ_{13}^{ξ} calculation are (A_1,A_2,A_3,A_4) and those to determine Γ_{23}^{ξ} are (B_1,B_2,B_3,B_4).

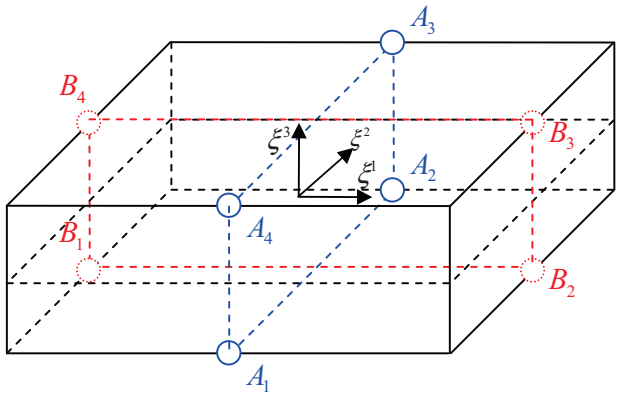

Figure 5.6: Eight-node shell element, 3D-ANS method for transverse shear locking

The new $\Gamma_{13}^{\xi,ANS}$ and $\Gamma_{23}^{\xi,ANS}$ obtained by using this 3D-ANS method are then calculated from natural shear strains evaluated at three orthogonal element mid-plane as follows (Schwarze & Reese (2009)):

$$\begin{aligned}\Gamma_{23}^{\xi,ANS} &= \frac{1}{4}\times\left(1-\xi^1\right)\times\left(1-\xi^3\right)\times\Gamma_{23}^{\xi,B_1} + \frac{1}{4}\times\left(1+\xi^1\right)\times\left(1-\xi^3\right)\times\Gamma_{23}^{\xi,B_2} \\ &+ \frac{1}{4}\times\left(1+\xi^1\right)\times\left(1+\xi^3\right)\times\Gamma_{23}^{\xi,B_3} + \frac{1}{4}\times\left(1-\xi^1\right)\times\left(1+\xi^3\right)\times\Gamma_{23}^{\xi,B_4}\end{aligned} \tag{5.91}$$

where

$$\Gamma_{23}^{\xi,B_1} = \Gamma_{23}^{\xi}\Big|_{\xi^1=-1,\xi^2=0,\xi^3=-1} \tag{5.92}$$

$$\Gamma_{23}^{\xi,B_2} = \Gamma_{23}^{\xi}\Big|_{\xi^1=1,\xi^2=0,\xi^3=-1} \tag{5.93}$$

$$\Gamma_{23}^{\xi,B_3} = \Gamma_{23}^{\xi}\Big|_{\xi^1=1,\xi^2=0,\xi^3=1} \tag{5.94}$$

$$\Gamma_{23}^{\xi,B_4} = \Gamma_{23}^{\xi}\Big|_{\xi^1=-1,\xi^2=0,\xi^3=1} \tag{5.95}$$

and similarly,

$$\begin{aligned}\Gamma_{13}^{\xi,ANS} &= \frac{1}{4}\times\left(1-\xi^2\right)\times\left(1-\xi^3\right)\times\Gamma_{13}^{\xi,A_1} + \frac{1}{4}\times\left(1+\xi^2\right)\times\left(1-\xi^3\right)\times\Gamma_{13}^{\xi,A_2} \\ &+ \frac{1}{4}\times\left(1+\xi^2\right)\times\left(1+\xi^3\right)\times\Gamma_{13}^{\xi,A_3} + \frac{1}{4}\times\left(1-\xi^2\right)\times\left(1+\xi^3\right)\times\Gamma_{13}^{\xi,A_4}\end{aligned} \tag{5.96}$$

where

$$\Gamma_{13}^{\xi,A_1} = \Gamma_{13}^{\xi}\Big|_{\xi^1=0,\,\xi^2=-1,\,\xi^3=-1} \qquad (5.97) \qquad \Gamma_{13}^{\xi,A_2} = \Gamma_{13}^{\xi}\Big|_{\xi^1=0,\,\xi^2=1,\,\xi^3=-1} \qquad (5.98)$$

$$\Gamma_{13}^{\xi,A_3} = \Gamma_{13}^{\xi}\Big|_{\xi^1=0,\,\xi^2=1,\,\xi^3=1} \qquad (5.99) \qquad \Gamma_{13}^{\xi,A_4} = \Gamma_{13\,\xi^1=0,\,\xi^2=-1,\,\xi^3=1}^{\xi} \qquad (5.100)$$

The ANS transverse shear components calculated in equations (5.91) and (5.96) are then used to replace the natural transverse shear defined in equation (5.82) and then transformed in the local cartesian frame as:

$$\boldsymbol{\Gamma}^{ANS} = \mathbf{T}^{\gamma}_{\xi^3=0} \times \boldsymbol{\Gamma}^{\xi,ANS} \qquad (5.101)$$

where

$$\boldsymbol{\Gamma}^{\xi,ANS} = \begin{Bmatrix} \Gamma_{23}^{\xi,ANS} \\ \Gamma_{13}^{\xi,ANS} \end{Bmatrix} = \sum_{I=1}^{8} \left(\mathbf{B}_{12}^{\Gamma,\,ANS}\right)_I \times \mathbf{u}_i, \quad i = 1,2,3 \qquad (5.102)$$

with

$$\left(\mathbf{B}_{12}^{\Gamma,\,ANS}\right)_I = \begin{Bmatrix} \left(\mathbf{B}_{12}^{\Gamma 23,\,ANS}\right)_I \\ \left(\mathbf{B}_{12}^{\Gamma 13,\,ANS}\right)_I \end{Bmatrix} \qquad (5.103)$$

in which

$$\begin{aligned}
\left(\mathbf{B}_{12}^{\Gamma 23,\,ANS}\right)_I &= \frac{1}{4}\times\left(1-\xi^1\right)\times\left(1-\xi^3\right)\times\left(\mathbf{B}_{12}^{\Gamma 23,\,B_1}\right)_I + \frac{1}{4}\times\left(1+\xi^1\right)\times\left(1-\xi^3\right)\times\left(\mathbf{B}_{12}^{\Gamma 23,\,B_2}\right)_I \\
&\quad + \frac{1}{4}\times\left(1+\xi^1\right)\times\left(1+\xi^3\right)\times\left(\mathbf{B}_{12}^{\Gamma 23,\,B_3}\right)_I + \frac{1}{4}\times\left(1-\xi^1\right)\times\left(1+\xi^3\right)\times\left(\mathbf{B}_{12}^{\Gamma 23,\,B_4}\right)_I \\
\left(\mathbf{B}_{12}^{\Gamma 13,\,ANS}\right)_I &= \frac{1}{4}\times\left(1-\xi^2\right)\times\left(1-\xi^3\right)\times\left(\mathbf{B}_{12}^{\Gamma 13,\,A_1}\right)_I + \frac{1}{4}\times\left(1+\xi^2\right)\times\left(1-\xi^3\right)\times\left(\mathbf{B}_{12}^{\Gamma 13,\,A_2}\right)_I \\
&\quad + \frac{1}{4}\times\left(1+\xi^2\right)\times\left(1+\xi^3\right)\times\left(\mathbf{B}_{12}^{\Gamma 13,\,A_3}\right)_I + \frac{1}{4}\times\left(1-\xi^2\right)\times\left(1+\xi^3\right)\times\left(\mathbf{B}_{12}^{\Gamma 13,\,A_4}\right)_I
\end{aligned} \qquad (5.104)$$

5.4.5 *Trapezoidal effect and thickness locking treatments*

Trapezoidal effect treatment

The ANS method can also be used in order to significantly reduce the trapezoidal effects. The natural thickness strain E_{33}^{ξ} is calculated at four sampling points located at the corners of the element mid-surface (C,D,E,F) as illustrated in Figure 5.7. The natural normal through-thickness strain E_{33}^{ξ}, which is constant in the standard H8 element, is replaced by $E_{33}^{\xi,ANS}$ obtained by bi-linearly interpolating the natural strain evaluated at points (C,D,E,F).

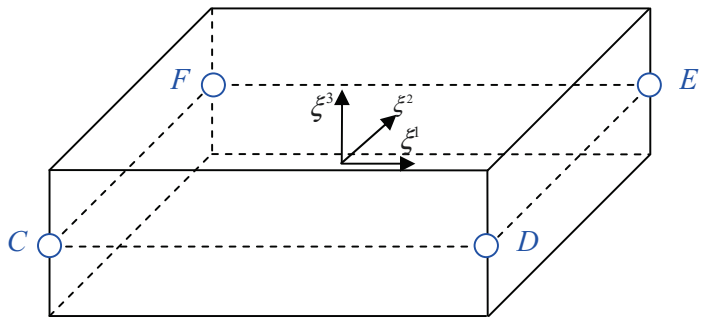

Figure 5.7: Eight-node shell element, ANS method for transverse shear locking

$$E_{33}^{\xi,ANS} = \frac{1}{4}\times(1-\xi^1)\times(1-\xi^2)\times E_{33}^{\xi,C} + \frac{1}{4}\times(1+\xi^1)\times(1-\xi^2)\times E_{33}^{\xi,D} + \frac{1}{4}\times(1+\xi^1)\times(1+\xi^2)\times E_{33}^{\xi,E} + \frac{1}{4}\times(1-\xi^1)\times(1+\xi^2)\times E_{33}^{\xi,F} \tag{5.105}$$

where

$$E_{33}^{\xi,C} = E_{33}^{\xi}\Big|_{\xi^1=-1,\xi^2=-1} \quad (5.106) \qquad E_{33}^{\xi,D} = E_{33}^{\xi}\Big|_{\xi^1=1,\xi^2=-1} \quad (5.107)$$

$$E_{33}^{\xi,E} = E_{33}^{\xi}\Big|_{\xi^1=1,\xi^2=1} \quad (5.108) \qquad E_{33}^{\xi,F} = E_{33}^{\xi}\Big|_{\xi^1=-1,\xi^2=1} \quad (5.109)$$

Introducing the ANS components calculated in equation (5.105) into the natural normal transverse strain defined in equation (5.87) leads to:

$$E_{zz}^{ANS} = j_{33}^{2} \times E_{33}^{\xi,ANS} \tag{5.110}$$

where

$$E_{33}^{\xi,ANS} = \sum_{I=1}^{8} \left(\mathbf{B}_{12}^{\zeta\zeta,ANS} \right)_I \times \mathbf{u}_i, \quad i = 1,2,3 \tag{5.111}$$

with

$$\begin{aligned} \left(\mathbf{B}_{12}^{\zeta\zeta,ANS} \right)_I = & \frac{1}{4} \times \left(1-\xi^1\right) \times \left(1-\xi^2\right) \times \left(\mathbf{B}_{12}^{\zeta\zeta,C} \right)_I + \frac{1}{4} \times \left(1+\xi^1\right) \times \left(1-\xi^2\right) \times \left(\mathbf{B}_{12}^{\zeta\zeta,D} \right)_I \\ & + \frac{1}{4} \times \left(1+\xi^1\right) \times \left(1+\xi^2\right) \times \left(\mathbf{B}_{12}^{\zeta\zeta,E} \right)_I + \frac{1}{4} \times \left(1-\xi^1\right) \times \left(1+\xi^2\right) \times \left(\mathbf{B}_{12}^{\zeta\zeta,F} \right)_I \end{aligned} \tag{5.112}$$

In the current section we defined the assumed transverse normal strain $E_{33}^{\xi,ANS}$ independent of ζ. Hence, to overcome the locking effects (volumetric locking and Poisson thickness locking), we construct $E_{33}^{\xi} = \mathbf{G}_3 \times \frac{\partial \mathbf{u}}{\partial \xi^3} + \frac{\partial \mathbf{u}}{\xi^3} \frac{\partial \mathbf{u}}{\xi^3}$ as varying linearly in ζ. This can be done by introducing a single enhanced mode as will be explained in the next section.

5.5. Virtual work principle: mixed variational formulation

5.5.1 EAS Variational formulation

The enhanced assumed strain finite element formulation was first proposed by Simo & Rifai (1990) and in an improved version in Simo et al. (1993). The EAS concept is introduced to eliminate the Poisson thickness locking and the volumetric locking. Similarly, the SH8RSe element is based on the Hu-Washizu non-linear three-field variational principle. An appropriate combination of the ANS technique with the enhanced assumed strain method yields a formulation that is free of locking. The formulation of the proposed element could be introduced as follows:

$$W\left(\mathbf{u},\mathbf{E},\mathbf{S}\right)=\int_V \mathbf{E}:\mathbf{S}\,dV+\int_V \bar{\mathbf{S}}:\left[\frac{1}{2}\left(\mathbf{F}^T\mathbf{F}-\mathbf{I}\right)-\mathbf{E}\right]dV-\mathbf{u}^T\times\mathbf{f}_{ext}=0 \qquad (5.113)$$

where $\mathbf{u}$ is the displacements field, $\mathbf{S}$ the second Piola-Kirchhoff stress tensor, $\bar{\mathbf{S}}$ the assumed stress, $\mathbf{f}_{ext}$ the exterior forces and V the domain volume.

In the EAS method, the Green-Lagrange strain tensor $\mathbf{E}$ is enriched with the contribution of enhanced parameters such that:

$$\mathbf{E}^{\text{mod}}=\frac{1}{2}\left(\mathbf{F}^T\mathbf{F}-\mathbf{I}\right)+\mathbf{E}^{\alpha} \qquad (5.114)$$

in which $\mathbf{E}^{\alpha}$ is the enhanced assumed strain field.

Replacing the Green-Lagrange strain tensor $\mathbf{E}$ in equation (5.113) by the modified Green-Lagrange strain tensor $\mathbf{E}^{\text{mod}}$ leads to the new three-field variational formulation:

$$W\left(\mathbf{u},\mathbf{E}^{\text{mod}},\mathbf{S}^{\text{mod}}\right)=\int_V \mathbf{E}^{\text{mod}}:\mathbf{S}^{\text{mod}}\,dV-\int_V \bar{\mathbf{S}}:\mathbf{E}^{\alpha}\,dV-\mathbf{u}^T\times\mathbf{f}_{ext}=0 \qquad (5.115)$$

Following standard practice in EAS method, the enhanced assumed strain field $\mathbf{E}^{\alpha}$ and the assumed stress $\bar{\mathbf{S}}$ have to be chosen so as to satisfy the following orthogonality condition:

$$\int_V \bar{\mathbf{S}}:\mathbf{E}^{\alpha}\,dV=0 \qquad (5.116)$$

Moreover, $\mathbf{S}^{\text{mod}}$ is the modified second Piola-Kirchhoff stress verifying the constitutive relation:

$$\mathbf{S}^{\text{mod}} = \mathbf{H} \times \mathbf{E}^{\text{mod}} \tag{5.117}$$

If the temperature remains constant and if the model is purely elastic, the hyperelastic Saint Venant 3D constitutive law could be used. It can be expressed as:

$$\begin{aligned} \mathbf{S} &= 2 \times \mu \times \mathbf{E} + \lambda \times trace\left(\mathbf{E}\right) \times \mathbf{I} \\ &= \mathbf{H} \times \mathbf{E} \end{aligned} \tag{5.118}$$

where $\mathbf{H}$ is a classical 3D elastic constitutive matrix defined below as:

$$\mathbf{H} = \begin{bmatrix} \lambda+2\mu & \lambda & \lambda & 0 & 0 & 0 \\ \lambda & \lambda+2\mu & \lambda & 0 & 0 & 0 \\ \lambda & \lambda & \lambda+2\mu & 0 & 0 & 0 \\ 0 & 0 & 0 & \mu & 0 & 0 \\ 0 & 0 & 0 & 0 & \mu & 0 \\ 0 & 0 & 0 & 0 & 0 & \mu \end{bmatrix} \tag{5.119}$$

with the Lamé's coefficients given by $\lambda = \dfrac{E.\nu}{\left(1+\nu\right) \times \left(1-2 \times \nu\right)}$ and $\mu = \dfrac{E}{2.\left(1+\nu\right)}$ with E the Young's modulus and ν the Poisson's ratio.

This classical 3D elastic constitutive law $\mathbf{H}$ can also be separated in membrane and bending, transverse shear and thickness modes respectively $\mathbf{H}^{mb}$, $\mathbf{H}^{\Gamma}$ and H^{zz} such as:

$$\mathbf{H}^{mb} = \begin{bmatrix} \lambda+2\mu & \lambda & \lambda \\ \lambda & \lambda+2\mu & \lambda \\ \lambda & \lambda & \mu \end{bmatrix} \tag{5.120}$$

$$\mathbf{H}^{\Gamma} = \begin{bmatrix} \mu & 0 \\ 0 & \mu \end{bmatrix} \tag{5.121}$$

$$H^{zz} = \lambda + 2\mu \tag{5.122}$$

Following Simo & Hughes (1986), equation (5.115) is then simplified in:

$$W\left(\mathbf{u},\mathbf{E}^{\text{mod}},\mathbf{S}^{\text{mod}}\right)=\int_V \mathbf{E}^{\text{mod}}:\mathbf{S}^{\text{mod}}\ dV-\mathbf{u}^T\times\mathbf{f}_{ext}=0 \tag{5.123}$$

The first variation of equation (5.123) with respect to $\mathbf{u}$ and with respect to the enhanced parameter α takes the form:

$$\begin{aligned}\delta W\left(\mathbf{u},\mathbf{E}^{\text{mod}},\mathbf{S}^{\text{mod}}\right)&=\int_V \delta\mathbf{E}^{\text{mod}}:\mathbf{S}^{\text{mod}}\ dV-\delta\mathbf{u}^T\times\mathbf{f}_{ext}\\&=\delta\pi_{\text{int}}+\delta\pi_{ext}\end{aligned} \tag{5.124}$$

where the first variation of the internal work δW_{int} is:

$$\delta W_{\text{int}}=\int_V \delta\mathbf{E}^{\text{mod}}:\mathbf{S}^{\text{mod}}\ dV \tag{5.125}$$

and the first variation of the external work δW_{ext} is:

$$\delta W_{ext}=-\delta\mathbf{u}^T\times\mathbf{f}_{ext} \tag{5.126}$$

In the present formulation, only one enhanced parameter α is used in order to provide a linear variation to the transverse normal strain component $\mathbf{E}_{33}$. At the element level, the variation of the modified Green-Lagrange strain tensor $\delta\mathbf{E}^{\text{mod}}$ can be expressed, by using equations (5.65), (5.66) and (5.131), as a sum of compatible differential operators $\mathbf{B}^l$ and $\mathbf{B}^{nl}\left(\mathbf{u}_i\right)$, applied to the displacement variation at each node $\delta\mathbf{u}_i$ and incompatible operator, $\mathbf{B}^\alpha$, applied to the enhancing parameter variation $\delta\alpha$:

$$\begin{aligned}\delta\mathbf{E}^{\text{mod}}\left(\mathbf{u}_i,\alpha\right)&=\delta\mathbf{E}^l\left(\mathbf{u}_i\right)+\delta\mathbf{E}^{nl}\left(\mathbf{u}_i\right)+\delta\mathbf{E}^\alpha\\&=\left[\mathbf{B}^l+\mathbf{B}^{nl}\left(\mathbf{u}_i\right)\right]\times\delta\mathbf{u}_i+\mathbf{B}^\alpha\times\delta\alpha\\&\left(i=1,\ldots,3\right)\end{aligned} \tag{5.127}$$

Introducing equation (5.127) into equation (5.125) gives another expression of the internal virtual work principle:

$$\begin{aligned}\delta W_{\text{int}}^{e} &= \int_{V^e} \delta \mathbf{E}^{\text{mod}} : \mathbf{S}^{\text{mod}}\, dV^e \\ &= \delta \mathbf{u}_i^T \cdot \int_{V^e} \left[\mathbf{B}^l + \mathbf{B}^{nl}\left(\mathbf{u}_i\right) \right]^T \cdot \mathbf{S}^{\text{mod}}\, dV^e + \delta \alpha^T \cdot \int_{V^e} \left(\mathbf{B}^{\alpha}\right)^T \cdot \mathbf{S}^{\text{mod}}\, dV^e \\ &= \delta \mathbf{u}_i^T \cdot \mathbf{f}_{\text{int}}^{e} + \delta \alpha^T \cdot \mathbf{f}_{\alpha}^{e}, \quad i = 1,2,3\end{aligned} \tag{5.128}$$

where the internal forces $\mathbf{f}_{\text{int}}^{e}$ and the enhanced forces $\mathbf{f}_{\alpha}^{e}$ are given by:

$$\begin{aligned}\mathbf{f}_{\text{int}}^{e} &= \int_{V^e} \left[\mathbf{B}^l + \mathbf{B}^{nl}\left(\mathbf{u}_i\right) \right]^T \cdot \mathbf{S}^{\text{mod}}\, dV^e \\ &= \int_{-1}^{1}\int_{-1}^{1}\int_{-1}^{1} \left[\mathbf{B}^l + \mathbf{B}^{nl}\left(\mathbf{u}_i\right) \right]^T \cdot \mathbf{S}^{\text{mod}} \cdot \left|\mathbf{J}\right| d\xi^1 d\xi^2 d\xi^3\end{aligned} \tag{5.129}$$

$$\begin{aligned}\mathbf{f}_{\alpha}^{e} &= \int_{V^e} \left(\mathbf{B}^{\alpha}\right)^T \cdot \mathbf{S}^{\text{mod}}\, dV^e \\ &= \int_{-1}^{1}\int_{-1}^{1}\int_{-1}^{1} \left(\mathbf{B}^{\alpha}\right)^T \cdot \mathbf{S}^{\text{mod}} \cdot \left|\mathbf{J}\right| d\xi^1 d\xi^2 d\xi^3\end{aligned} \tag{5.130}$$

where, following the work of Simo & Rifai (1990), $\mathbf{B}^{\alpha}$ takes the form:

$$\mathbf{B}^{\alpha} = \frac{\left|\mathbf{J}_0\right|}{\left|\mathbf{J}_{\xi^3}\right|} \cdot J_{33}^2 \cdot \begin{bmatrix} 0 & 0 & 0 \\ 0 & 0 & 0 \\ 0 & 0 & \xi^3 \\ 0 & 0 & 0 \\ 0 & 0 & 0 \\ 0 & 0 & 0 \end{bmatrix} \tag{5.131}$$

$\left|\mathbf{J}_0\right|$ and $\left|\mathbf{J}_{\xi^3}\right|$ used in equation (5.131) are respectively the determinants of the transformation matrix at the center of the element and at a given integration point out of the element mid-plane respectively. A reason to do this, is that the enhanced strain field $\mathbf{E}_{kl}^{\alpha}$ is defined in the natural coordinates system $\xi\left(\xi^1,\xi^2,\xi^3\right)$. Hence, it is necessary to transform $\mathbf{E}_{kl}^{\alpha}$ into $\mathbf{E}_{ij}^{\alpha}$ expressed in the local cartesian coordinates system $\mathbf{x}\left(x\ ,y\ ,z\ \right)$. By defining

the enhanced parameter in the mid-plane of the element and by using the transformation equation (5.20) one then obtain:

$$\begin{aligned} & E_{kl}^{\alpha} \times \left|\mathbf{J}_0\right| = \left|\mathbf{J}_{\xi^3}\right| \times \mathbf{J}_{ki0} \times E_{ij}^{\alpha} \times \mathbf{J}_{lj0} = \left|\mathbf{J}_{\xi^3}\right| \times \mathbf{T}_0 \times E_{ij}^{\alpha} \\ & \Rightarrow E_{kl}^{\alpha} \times \left|\mathbf{J}_0\right| = \left|\mathbf{J}_{\xi^3}\right| \times \mathbf{T}_0 \times E_{ij}^{\alpha} \\ & \Rightarrow E_{ij}^{\alpha} = \frac{\left|\mathbf{J}_0\right|}{\left|\mathbf{J}_{\xi^3}\right|} \times \mathbf{T}_0^{-T} \times E_{kl}^{\alpha} \end{aligned} \tag{5.132}$$

where $\mathbf{T}_0$ and $\mathbf{J}_0$ are respectively the expression of $\mathbf{T}$ defined in (5.27) and $\mathbf{J}$ evaluated at $\xi^3 = 0$ in the mid-plane of the element.

5.5.2 Linearization of the EAS variational weak form

The present section is the basis of non-linear finite element method. Indeed, the consistent linearization of the internal virtual work allows defining the equilibrium equations linearly with respect to an increment of the solution of the problem, Δu. A non-linear finite element problem could then be solved incrementally with only linear equations. Another important point is that this also characterizes the material stability while calculating the system stiffness matrix.

The linearization of the weak form of the internal work δW_{int} is performed using the Gâteaux derivative as presented in Simo & Hughes (1998). This derivative is defined as:

$$\Delta f\left(u\right) = \lim_{\varphi \to 0} \frac{f\left(u + \varphi \times \Delta u\right) - f\left(\varphi \times \Delta u\right)}{\varphi} = \frac{d}{d\varphi} f\left(u + \varphi \times \Delta u\right)\Big|_{\varphi=0} \tag{5.133}$$

where Δu is a displacement increment.

The Gâteaux derivative of the internal work first variation introduced in equation (5.125) is:

$$\begin{aligned} \Delta \delta W_{\text{int}} &= \Delta \int_V \left(\delta \mathbf{E}^{\text{mod}}\right)^T \times \mathbf{S}^{\text{mod}} \, dV \\ &= \int_V \left(\Delta \delta \mathbf{E}^{\text{mod}}\right)^T \times \mathbf{S}^{\text{mod}} \, dV + \int_V \left(\delta \mathbf{E}^{\text{mod}}\right)^T \times \Delta \mathbf{S}^{\text{mod}} \, dV \end{aligned} \tag{5.134}$$

Taking advantage of the symmetry of the second Piola-Kirchhoff stress tensor $\mathbf{S}$, the finite element approximation of equation (5.134) can be written as:

$$\begin{aligned}\Delta\delta W^e_{\text{int}} &= \Delta\delta W^e_{\text{int}} \times\Delta\mathbf{u}_I + \Delta\delta W^e_{\text{int}} \times\Delta\alpha \\ &= \delta\mathbf{u}_i^T \times\Delta_{\mathbf{u}_i}\mathbf{f}^e_{\text{int}} \times\Delta\mathbf{u}_i + \delta\mathbf{u}_i^T \times\Delta_{\alpha}\mathbf{f}^e_{\text{int}} \times\Delta\mathbf{u}_i + \delta\alpha^T \times\Delta_{\mathbf{u}_i}\mathbf{f}^e_{\alpha} \times\Delta\alpha + \delta\alpha^T \times\Delta_{\alpha}\mathbf{f}^e_{\alpha} \times\Delta\mathbf{u}_i \\ &= \left(\delta\mathbf{u}_i^T \times\mathbf{k}^e_{uu} + \delta\alpha^T \times\mathbf{k}^e_{\alpha u}\right)\times\Delta\mathbf{u}_i + \left(\delta\mathbf{u}_i^T \times\mathbf{k}^e_{u\alpha} + \delta\alpha^T \times\mathbf{k}^e_{\alpha\alpha}\right)\times\Delta\alpha\end{aligned} \tag{5.135}$$

where the stiffness matrix components are:

$$\begin{aligned}\mathbf{k}^e_{uu} &= \Delta_{\mathbf{u}_i}\mathbf{f}^e_{\text{int}} \\ &= \frac{\partial\mathbf{f}^e_{\text{int}}}{\partial\Delta\mathbf{u}_i} \\ &= \mathbf{k}^e_S + \mathbf{k}^e_{mat}\end{aligned} \tag{5.136}$$

with

$$\begin{aligned}\mathbf{k}^e_S &= \int_{V^e}\mathbf{B}^{0T} \times\hat{\mathbf{S}}^{\text{mod}}_{\xi} \times\mathbf{B}^0 \; dV^e \\ &= \int_{-1}^{1}\int_{-1}^{1}\int_{-1}^{1}\mathbf{B}^{0T} \times\hat{\mathbf{S}}^{\text{mod}}_{\xi} \times\mathbf{B}^0 \times|\mathbf{J}|\, d\xi^1 d\xi^2 d\xi^3\end{aligned} \tag{5.137}$$

and

$$\begin{aligned}\mathbf{k}^e_{mat} &= \int_{V^e}\left[\mathbf{B}^l + \mathbf{B}^{nl}\left(\mathbf{u}_i\right)\right]^T \times\mathbf{H} \times\left[\mathbf{B}^l + \mathbf{B}^{nl}\left(\mathbf{u}_i\right)\right] dV^e \\ &= \int_{-1}^{1}\int_{-1}^{1}\int_{-1}^{1}\left[\mathbf{B}^l + \mathbf{B}^{nl}\left(\mathbf{u}_i\right)\right]^T \times\mathbf{H} \times\left[\mathbf{B}^l + \mathbf{B}^{nl}\left(\mathbf{u}_i\right)\right] \times|\mathbf{J}|\, d\xi^1 d\xi^2 d\xi^3\end{aligned} \tag{5.138}$$

in which

$$\hat{\mathbf{S}}_{\xi}^{\mathrm{mod}} = \begin{bmatrix} S_{11}^{\mathrm{mod}} & S_{12}^{\mathrm{mod}} & S_{13}^{\mathrm{mod}} & & & & & & \\ S_{21}^{\mathrm{mod}} & S_{22}^{\mathrm{mod}} & S_{23}^{\mathrm{mod}} & & & & & (0) & \\ S_{31}^{\mathrm{mod}} & S_{32}^{\mathrm{mod}} & S_{33}^{\mathrm{mod}} & & & & & & \\ & & & S_{11}^{\mathrm{mod}} & S_{12}^{\mathrm{mod}} & S_{13}^{\mathrm{mod}} & & & \\ & & & S_{21}^{\mathrm{mod}} & S_{22}^{\mathrm{mod}} & S_{23}^{\mathrm{mod}} & & & \\ & & & S_{31}^{\mathrm{mod}} & S_{32}^{\mathrm{mod}} & S_{33}^{\mathrm{mod}} & & & \\ & & & & & & S_{11}^{\mathrm{mod}} & S_{12}^{\mathrm{mod}} & S_{13}^{\mathrm{mod}} \\ & (0) & & & & & S_{21}^{\mathrm{mod}} & S_{22}^{\mathrm{mod}} & S_{23}^{\mathrm{mod}} \\ & & & & & & S_{31}^{\mathrm{mod}} & S_{32}^{\mathrm{mod}} & S_{33}^{\mathrm{mod}} \end{bmatrix} \tag{5.139}$$

and

$$\mathbf{B}^{0} = \begin{bmatrix} \mathbf{G}_1 \times \dfrac{\partial N_I}{\partial \xi^1} & & (\mathbf{0}) \\ \mathbf{G}_2 \times \dfrac{\partial N_I}{\partial \xi^2} & & \\ \mathbf{G}_3 \times \dfrac{\partial N_I}{\partial \xi^3} & & \\ & \mathbf{G}_1 \times \dfrac{\partial N_I}{\partial \xi^1} & \\ & \mathbf{G}_2 \times \dfrac{\partial N_I}{\partial \xi^2} & \\ & \mathbf{G}_3 \times \dfrac{\partial N_I}{\partial \xi^3} & \\ & & \mathbf{G}_1 \times \dfrac{\partial N_I}{\partial \xi^1} \\ & & \mathbf{G}_2 \times \dfrac{\partial N_I}{\partial \xi^2} \\ (\mathbf{0}) & & \mathbf{G}_3 \times \dfrac{\partial N_I}{\partial \xi^3} \end{bmatrix}, \qquad (I = 1, \ldots, 8) \tag{5.140}$$

$$
\begin{aligned}
\mathbf{k}_{\alpha u}^{e} &= \Delta_{\alpha}\mathbf{f}_{\text{int}}^{e} \\
&= \frac{\partial \mathbf{f}_{\text{int}}^{e}}{\partial \Delta\alpha} \\
&= \int_{V^e} \left(\mathbf{B}^{\alpha}\right)^{T} \times \mathbf{H} \times \left[\mathbf{B}^{l} + \mathbf{B}^{nl}\left(\mathbf{u}_i\right)\right] dV^{e} \\
&= \int_{-1}^{1}\int_{-1}^{1}\int_{-1}^{1} \left(\mathbf{B}^{\alpha}\right)^{T} \times \mathbf{H} \times \left[\mathbf{B}^{l} + \mathbf{B}^{nl}\left(\mathbf{u}_i\right)\right] \times \left|\mathbf{J}\right| d\xi^{1} d\xi^{2} d\xi^{3}
\end{aligned}
\tag{5.141}
$$

$$
\begin{aligned}
\mathbf{k}_{u\alpha}^{e} &= \Delta_{u}\mathbf{f}_{\alpha}^{e} \\
&= \frac{\partial \mathbf{f}_{\alpha}^{e}}{\partial \Delta u} \\
&= \int_{V^e} \left[\mathbf{B}^{l} + \mathbf{B}^{nl}\left(\mathbf{u}_i\right)\right]^{T} \times \mathbf{H} \times \mathbf{B}^{\alpha}\, dV^{e} \\
&= \int_{-1}^{1}\int_{-1}^{1}\int_{-1}^{1} \left[\mathbf{B}^{l} + \mathbf{B}^{nl}\left(\mathbf{u}_i\right)\right]^{T} \times \mathbf{H} \times \mathbf{B}^{\alpha} \times \left|\mathbf{J}\right| d\xi^{1} d\xi^{2} d\xi^{3}
\end{aligned}
\tag{5.142}
$$

$$
\begin{aligned}
\mathbf{k}_{\alpha\alpha}^{e} &= \Delta_{\alpha}\mathbf{f}_{\alpha}^{e} \\
&= \frac{\partial \mathbf{f}_{\alpha}^{e}}{\partial \Delta\alpha} \\
&= \int_{V^e} \left(\mathbf{B}^{\alpha}\right)^{T} \times \mathbf{H} \times \mathbf{B}^{\alpha}\, dV^{e} \\
&= \int_{-1}^{1}\int_{-1}^{1}\int_{-1}^{1} \left(\mathbf{B}^{\alpha}\right)^{T} \times \mathbf{H} \times \mathbf{B}^{\alpha} \times \left|\mathbf{J}\right| d\xi^{1} d\xi^{2} d\xi^{3}
\end{aligned}
\tag{5.143}
$$

Similarly, the Gâteaux derivative of the first variation of the external forces work expressed in equation (5.126) is obtained by:

$$
\Delta\delta W_{ext}^{e} = -\Delta\delta\mathbf{u}_i^{T} \times \mathbf{f}_{ext}^{e} \tag{5.144}
$$

Considering the Gâteaux derivative of the whole work yields the following discrete linearized system:

$$
\begin{bmatrix} \mathbf{k}_{uu}^{e} & \mathbf{k}_{u\alpha}^{e} \\ \mathbf{k}_{\alpha u}^{e} & \mathbf{k}_{\alpha\alpha}^{e} \end{bmatrix} \times \begin{Bmatrix} \Delta\mathbf{u} \\ \Delta\alpha \end{Bmatrix} = \begin{Bmatrix} f_{ext}^{e} - f_{\text{int}}^{e} \\ -f_{\alpha}^{e} \end{Bmatrix} \tag{5.145}
$$

The treatment of the enhanced parameter is then further discussed in a following section.

Introducing the additive decomposition (5.75) into equation (5.138) leads to:

$$\begin{aligned}\hat{\mathbf{k}}_{mat}^{e} &= \int_{V^e} \left(\mathbf{B}_{12} + \hat{\mathbf{B}}_{34}\right)^T \times \mathbf{H} \times \left(\mathbf{B}_{12} + \hat{\mathbf{B}}_{34}\right) dV^e \\ &= \int_{V^e} \mathbf{B}_{12}^T \times \mathbf{H} \times \mathbf{B}_{12}\ dV^e + \int_{V^e} \mathbf{B}_{12}^T \times \mathbf{H} \times \hat{\mathbf{B}}_{34}\ dV^e + \cdots \\ &\cdots + \int_{V^e} \hat{\mathbf{B}}_{34}^T \times \mathbf{H} \times \mathbf{B}_{12}\ dV^e + \int_{V^e} \hat{\mathbf{B}}_{34}^T \times \mathbf{H} \times \hat{\mathbf{B}}_{34}\ dV^e\end{aligned} \tag{5.146}$$

The product between stabilized and unstabilized strain matrix operator terms is equal to zero, taking into consideration the previously mentioned orthogonality properties. This yields in a simplified form, the material part of the stiffness matrix $\hat{\mathbf{k}}_{mat}^{e}$:

$$\hat{\mathbf{k}}_{mat}^{e} = \mathbf{k}_{mat}^{e} + \hat{\mathbf{k}}_{stab}^{e} \tag{5.147}$$

where the standard material part of the stiffness matrix $\mathbf{k}_{mat}^{e}$ which does not vanish at point $\left(0,0,\xi^3\right)$ and the stabilization part of the stiffness matrix $\hat{\mathbf{k}}_{stab}^{e}$ are:

$$\mathbf{k}_{mat}^{e} = \int_{V^e} \mathbf{B}_{12}^T \times \mathbf{H} \times \mathbf{B}_{12}\ dV^e \tag{5.148}$$

$$\hat{\mathbf{k}}_{stab}^{e} = \int_{V^e} \hat{\mathbf{B}}_{34}^T \times \mathbf{H} \times \hat{\mathbf{B}}_{34}\ dV^e \tag{5.149}$$

Separating the element material stiffness matrix $\mathbf{k}_{mat}^{e}$ into the various contributions according to the Green-Lagrange strain tensor decomposition into shell deformation modes and taking advantage of the treatments of transverse shear locking and trapezoidal effect discussed in sections 5.4.4 and 5.4.5 one can then write:

$$\mathbf{k}_{mat}^{e} = \mathbf{k}_{mat}^{e,mb} + \mathbf{k}_{mat}^{e,\Gamma} + \mathbf{k}_{mat}^{e,zz} \tag{5.150}$$

where the membrane and bending material stiffness matrix $\mathbf{k}_{mat}^{e,mb}$ is given by:

$$\mathbf{k}_{mat}^{e,mb} = \sum_{I=1}^{8} \left(\mathbf{B}_{12}^{mb}\right)_I^T \times \mathbf{H}^{mb} \times \left(\mathbf{B}_{12}^{mb}\right)_I \left|\mathbf{J}\right| \tag{5.151}$$

the transverse shear material stiffness matrix $\mathbf{k}_{mat}^{e,\Gamma,ANS}$ is given by:

$$\mathbf{k}_{mat}^{e,\Gamma,ANS} = \sum_{I=1}^{8} \left(\mathbf{B}_{12}^{\Gamma,ANS} \right)_I^T \times \mathbf{H}^{\Gamma} \times \left(\mathbf{B}_{12}^{\Gamma,ANS} \right)_I \left| \mathbf{J} \right| \tag{5.152}$$

and the transverse normal material stiffness matrix component $\mathbf{k}_{mat}^{e,zz,ANS}$ is given by:

$$\mathbf{k}_{mat}^{e,zz,ANS} = \sum_{I=1}^{8} \left(\mathbf{B}_{12}^{\zeta\zeta,ANS} \right)_I^T \times H^{zz} \times \left(\mathbf{B}_{12}^{\zeta\zeta,ANS} \right)_I \left| \mathbf{J} \right| \tag{5.153}$$

$\mathbf{H}^{mb}$, $\mathbf{H}^{\Gamma}$ and H^{zz} are constitutive matrices defined in equations (5.120) , (5.121) and (5.122).

The Green-Lagrange strain tensor $\mathbf{E}^{ANS}$ whose transverse shear and transverse normal strain components are both calculated with the ANS method can also be decomposed as:

$$\mathbf{E}^{ANS} = \begin{Bmatrix} \mathbf{E}^{mb} \\ \mathbf{\Gamma}^{ANS} \\ E_{zz}^{ANS} \end{Bmatrix} \tag{5.154}$$

This induces an assumed stress field $\hat{\mathbf{S}}_{\xi}^{\text{mod},ANS}$ and consequently a new geometric stiffness matrix $\mathbf{k}_S^{e,ANS}$ given by:

$$\mathbf{k}_S^{e,ANS} = \sum_{I=1}^{8} \left(\mathbf{B}_I^0 \right)^T \times \hat{\mathbf{S}}_{\xi}^{\text{mod},ANS} \times \mathbf{B}_I^0 \left| \mathbf{J} \right| \tag{5.155}$$

The assumed element standard stiffness matrix free of transverse shear locking as well as trapezoidal effect $\mathbf{k}_{uu}^{e,ANS}$ is obtained by introducing equation (5.152) and (5.153) into equation (5.136) thus yielding:

$$\mathbf{k}_{uu}^{e,ANS} = \mathbf{k}_S^{e,ANS} + \mathbf{k}_{mat}^{e,ANS} \tag{5.156}$$

5.6. EAS method application

5.6.1 Thickness locking treatment

The EAS technique presented in Simo & Rifai (1990) is used in the present element to reduce the thickness locking. This consists in adding in the normal deformation field only one internal variable $\Delta\alpha$. In the present formulation, $\Delta\alpha = \xi^3$ transforms the assumed normal strain $E^{zz,ANS}$, constant in the thickness direction, into $E^{zz,ANS,\mathrm{mod}}$ which is a modified normal strain linear in the thickness direction. As this internal variable $\Delta\alpha$ is artificial, its local static condensation remains necessary before assembling the element matrices. The static condensation presented below is an efficient method employed to eliminate the enhanced variable $\Delta\alpha$ at element level.

By expliciting the two equations involved equation (5.145), this gives:

$$\mathbf{k}_{uu}^{e,ANS} \times \Delta\mathbf{u}_i + \mathbf{k}_{u\alpha}^{e,ANS} \times \Delta\alpha = f_{ext}^{e} - f_{\mathrm{int}}^{e,ANS} \tag{5.157}$$

$$\mathbf{k}_{\alpha u}^{e,ANS} \times \Delta\mathbf{u}_i + \mathbf{k}_{\alpha\alpha}^{e} \times \Delta\alpha = -f_{\alpha}^{e} \tag{5.158}$$

Rearranging equation (5.158), the enhanced variable increment $\Delta\alpha$ can thus be solved for and one obtains:

$$\Delta\alpha = -\frac{1}{k_{\alpha\alpha}^{e}} \times \left(f_{\alpha}^{e} + \mathbf{k}_{\alpha u}^{e,ANS} \times \Delta\mathbf{u}_i \right) \tag{5.159}$$

Introducing equation (5.159) into equation (5.157) gives:

$$\begin{aligned} &\mathbf{k}_{uu}^{e,ANS} \times \Delta\mathbf{u}_i + \mathbf{k}_{u\alpha}^{e,ANS} \times \left(-\frac{1}{k_{\alpha\alpha}^{e}} \times \left(f_{\alpha}^{e} + \mathbf{k}_{\alpha u}^{e,ANS} \times \Delta\mathbf{u}_i \right) \right) = f_{ext}^{e} - f_{\mathrm{int}}^{e} \\ \Rightarrow &\left[\mathbf{k}_{uu}^{e,ANS} - \mathbf{k}_{u\alpha}^{e,ANS} \times \left(\frac{1}{k_{\alpha\alpha}^{e}} \times \mathbf{k}_{\alpha u}^{e,ANS} \right) \right] \times \Delta\mathbf{u}_i = f_{ext}^{e} - f_{\mathrm{int}}^{e} + \frac{1}{k_{\alpha\alpha}^{e}} \times \mathbf{k}_{u\alpha}^{e,ANS} \times f_{\alpha}^{e} \end{aligned} \tag{5.160}$$

The standard stiffness matrix free of transverse shear and thickness locking as well as trapezoidal effect $\mathbf{k}^{e,\mathrm{mod},ANS}$ then takes the form:

$$\mathbf{k}_{uu}^{e,\mathrm{mod},ANS} = \mathbf{k}_{uu}^{e,ANS} - \mathbf{k}_{u\alpha}^{e,ANS} \times \left(\frac{1}{k_{\alpha\alpha}^{e}} \times \mathbf{k}_{\alpha u}^{e,ANS} \right) \tag{5.161}$$

5.6.2 Static condensation

The static condensation detailed from equation (5.157) to equation (5.161) is performed iteratively at the element level. The Newton-Raphson iterative resolution scheme remains a classical method to solve this problem. The applied classical algorithm is illustrated in Figure 5.8.

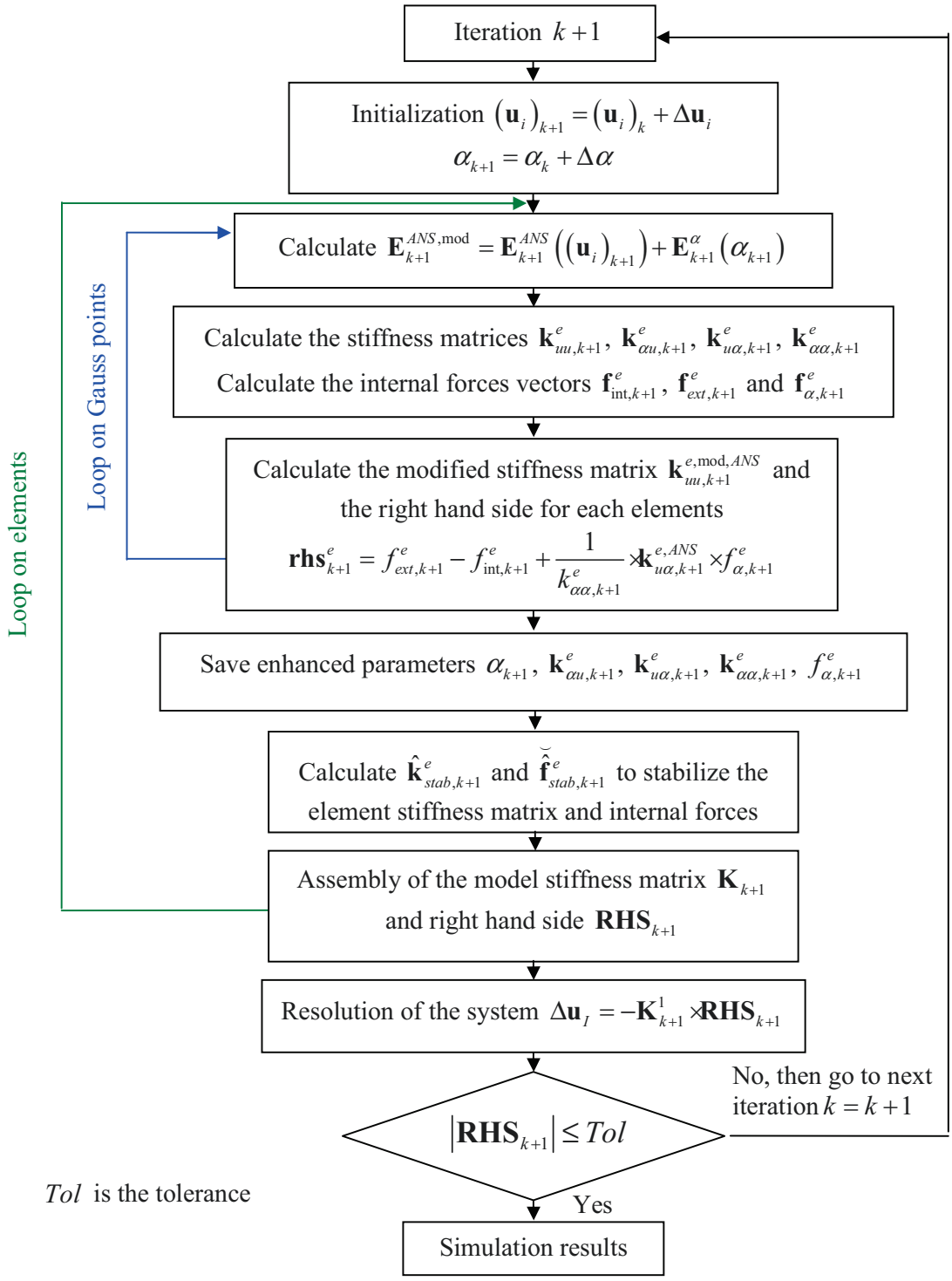

Figure 5.8: Classical static condensation algorithm for an elastic constitutive law

5.7. Stabilization

5.7.1 Coordinates systems definition for stabilization

As previously mentioned, some terms of the stiffness matrix and of the internal force vector vanish due to the reduced integration scheme at the element mid-surface. Some stabilization parameters, presented in this section, are then required to avoid hourglass modes. Unlike the standard terms, these last parameters are calculated in an appropriate local cartesian coordinates system, called the co-rotational system, that takes advantage of the orthogonality properties of the hourglass modes. This technique was first initiated in Belytschko & Bindeman (1993) and then detailed in Abed-Meraim & Combescure (2009). Using the last reference, the so called local orthogonal co-rotational coordinates system is redefined below as well as its properties useful to stabilize their element.

Rotation matrix for stabilization part, $\mathbf{Q}^{stab}$

The rotation matrix $\mathbf{Q}^{stab}$ that transforms the stabilization parameters from the local cartesian coordinates system to the global cartesian coordinates system can be defined as presented below.

Let the in-plane natural base vector $\mathbf{g}^{stab}$ with components $\mathbf{g}_{1i}^{stab}$, $\mathbf{g}_{2i}^{stab}$ and $\mathbf{g}_{3i}^{stab}$ used for the stabilization procedure be calculated as follows:

$$\mathbf{g}_{1i}^{stab} = \mathbf{\Lambda}_1^T \times \mathbf{x}_i \tag{5.162}$$

$$\mathbf{g}_{2i}^{stab} = \mathbf{\Lambda}_2^T \times \mathbf{x}_i \tag{5.163}$$

$$\mathbf{g}_{3i}^{stab} = \mathbf{\Lambda}_3^T \times \mathbf{x}_i \tag{5.164}$$

where $i = 1,\ldots,3$ refers to the vector components and where, in the previous equations, $\mathbf{\Lambda}_1^T$, $\mathbf{\Lambda}_2^T$ and $\mathbf{\Lambda}_3^T$ represent the element nodal coordinates in the natural parametric reference space and defined as follow:

$$\begin{aligned}\boldsymbol{\Lambda}_1^T &= \left(-1,1,1,-1,-1,1,1,-1\right)\\ \boldsymbol{\Lambda}_2^T &= \left(-1,-1,1,1,-1,-1,1,1\right)\\ \boldsymbol{\Lambda}_3^T &= \left(-1,-1,-1,-1,1,1,1,1\right)\end{aligned} \tag{5.165}$$

Then the transformation matrix $\mathbf{Q}^{stab}$ between the global and the local cartesian coordinates system can be defined by:

$$\mathbf{Q}^{stab} = \left[\mathbf{r}_{1i}^{stab} \quad \mathbf{r}_{2i}^{stab} \quad \mathbf{r}_{3i}^{stab}\right] \tag{5.166}$$

where $\mathbf{r}_{1i}^{stab} = \dfrac{\mathbf{g}_{1i}^{stab}}{\left\|\mathbf{g}_{1i}^{stab}\right\|}$, $\mathbf{r}_{2i}^{stab} = \dfrac{\mathbf{g}_{2ci}^{stab}}{\left\|\mathbf{g}_{2ci}^{stab}\right\|}$ and $\mathbf{r}_{3i}^{stab} = \dfrac{\mathbf{g}_{3ci}^{stab}}{\left\|\mathbf{g}_{3ci}^{stab}\right\|}$ are its components.

with

$$\mathbf{g}_{2ci}^{stab} = \mathbf{g}_{2i}^{stab} + \mathbf{g}_{ci}^{stab} \tag{5.167}$$

in which $\mathbf{g}_{ci}^{stab}$ is a correction term added to $\mathbf{g}_{2i}^{stab}$ in order to create a new vector $\mathbf{g}_{2ci}^{stab}$ normal to $\mathbf{g}_{1i}^{stab}$ and defined as:

$$\mathbf{g}_{ci}^{stab} = -\frac{\left(\mathbf{g}_{1i}^{stab}\right)^T \times \mathbf{g}_{2i}^{stab}}{\left(\mathbf{g}_{1i}^{stab}\right)^T \times \mathbf{g}_{1i}^{stab}} \times \mathbf{g}_{1i}^{stab} \tag{5.168}$$

and the normal vector $\mathbf{g}_{3i}^{stab}$ is calculated by cross product as:

$$\mathbf{g}_{3i}^{stab} = \mathbf{g}_{1i}^{stab} \times \mathbf{g}_{2ci}^{stab} \tag{5.169}$$

The co-rotational coordinate system $\breve{\mathbf{x}}\left(\breve{x},\breve{y},\breve{z}\right)$ is embedded in the element and rotates with it and is chosen to be aligned with the referential natural coordinates system $\boldsymbol{\xi}\left(\xi^1,\xi^2,\xi^3\right)$. Rewriting equation (5.38) in co-rotational system and exploiting the orthogonality properties as in equation (5.43) leads to:

$$\breve{x}_i = \frac{1}{8} \times \left(\mathbf{s}^T + \xi^1 \times \mathbf{\Lambda}_1^T + \xi^2 \times \mathbf{\Lambda}_2^T + \xi^3 \times \mathbf{\Lambda}_3^T + h_1 \times \mathbf{h}_1^T + h_2 \times \mathbf{h}_2^T + h_3 \times \mathbf{h}_3^T + h_4 \times \mathbf{h}_4^T \right) \times \breve{\mathbf{x}}_i \quad (5.170)$$

where $i = 1, \ldots, 3$ and $\breve{\mathbf{x}}_i = \left(\breve{x}_1, \breve{y}_1, \breve{z}_1, \ldots, \breve{x}_8, \breve{y}_8, \breve{z}_8 \right)$ are the node positions in the orthogonal co-rotational coordinate system $\breve{\mathbf{x}}\left(\breve{x}, \breve{y}, \breve{z} \right)$.

Proceeding similarly as in equation (5.50), we can evaluate the relationship between the two coordinates.

Since the orthogonal co-rotational system $\breve{\mathbf{x}}\left(\breve{x}, \breve{y}, \breve{z} \right)$ is aligned with the referential natural coordinates system $\boldsymbol{\xi}\left(\xi^1, \xi^2, \xi^3 \right)$, it follows that $\frac{\partial \breve{x}_i}{\partial \xi_j} = \frac{\partial \xi_j}{\partial \breve{x}_i} = 0 \quad if \quad i \neq j$ and the relationship between the two coordinates , represented by matrix $\breve{\mathbf{J}}$

$$\breve{\mathbf{J}}_{ij} = \frac{\partial \breve{x}_i}{\partial \xi^j} = \frac{1}{8} \times \left(\mathbf{\Lambda}_j^T + h_{\beta, \xi^j} \times \mathbf{h}_\beta^T \right) \times \breve{\mathbf{x}}_i \quad (5.171)$$

becomes, when evaluated at the center of the element $\xi^1 = \xi^2 = \xi^3 = 0$ where $h_1 = h_2 = h_3 = h_4 = 0$:

$$\begin{aligned} \breve{\mathbf{J}}_{\xi^1 = \xi^2 = \xi^3 = 0} = \breve{\mathbf{J}}_0 &= \frac{1}{8} \times \mathbf{\Lambda}_j^T \times \breve{\mathbf{x}}_i \\ &= \frac{1}{8} \times \begin{bmatrix} \mathbf{\Lambda}_1^T \times \breve{\mathbf{x}}_1 & \mathbf{\Lambda}_2^T \times \breve{\mathbf{x}}_1 & \mathbf{\Lambda}_3^T \times \breve{\mathbf{x}}_1 \\ \mathbf{\Lambda}_1^T \times \breve{\mathbf{x}}_2 & \mathbf{\Lambda}_2^T \times \breve{\mathbf{x}}_2 & \mathbf{\Lambda}_3^T \times \breve{\mathbf{x}}_2 \\ \mathbf{\Lambda}_1^T \times \breve{\mathbf{x}}_3 & \mathbf{\Lambda}_2^T \times \breve{\mathbf{x}}_3 & \mathbf{\Lambda}_3^T \times \breve{\mathbf{x}}_3 \end{bmatrix} \end{aligned} \quad (5.172)$$

Due to the orthogonality properties detailed in Abed-Meraim & Combescure (2009) the determinant of matrix $\breve{\mathbf{J}}_0$ is:

$$\left| \breve{\mathbf{J}}_0 \right| = \frac{\mathbf{\Lambda}_1^T \times \breve{\mathbf{x}}_1}{8} \times \frac{\mathbf{\Lambda}_2^T \times \breve{\mathbf{x}}_2}{8} \times \frac{\mathbf{\Lambda}_3^T \times \breve{\mathbf{x}}_3}{8} \quad (5.173)$$

5.7.2 Stabilization stiffness matrix

It remains possible to simplify $\mathbf{k}_{stab}$ expression into $\breve{\mathbf{k}}_{stab}$ expression by projecting the terms related to the stabilization in the co-rotational coordinates system $\breve{\mathbf{x}}\left(\breve{x},\breve{y},\breve{z}\right)$, defined in section 5.7.1. This system of coordinates is only rotated as compared to the global coordinates system but its axes are defined aligned with those of the natural coordinates system. Using this last property, the product of standard and stabilization partial derivatives matrices, $\mathbf{B}_{12}$ and $\mathbf{B}_{34}$ remains equal to zero. Equation (5.149) can then be estimated using only the last integral. Moreover, a simplification of matrix $\hat{\mathbf{B}}_{34}$ in $\breve{\hat{\mathbf{B}}}_{34}$ can be formulated while using this co-rotational coordinates system $\breve{\mathbf{x}}\left(\breve{x},\breve{y},\breve{z}\right)$, as:

$$\breve{\hat{\mathbf{B}}}_{34}=\begin{bmatrix}\sum_{\beta=3}^{4}h_{\beta,x}\times\hat{\gamma}_{\beta}^{T} & \mathbf{0} & \mathbf{0}\\ \mathbf{0} & \sum_{\beta=3}^{4}h_{\beta,y}\times\hat{\gamma}_{\beta}^{T} & \mathbf{0}\\ \mathbf{0} & \mathbf{0} & h_{3,z}\times\hat{\gamma}_{3}^{T}\\ \mathbf{0} & \mathbf{0} & \mathbf{0}\\ \mathbf{0} & \mathbf{0} & \mathbf{0}\\ \mathbf{0} & \mathbf{0} & h_{4,x}\times\hat{\gamma}_{4}^{T}\end{bmatrix} \tag{5.174}$$

Using equation (5.174) in equation (5.149) and taking advantage of the properties of the orthogonal co-rotational coordinates system $\breve{\mathbf{x}}\left(\breve{x},\breve{y},\breve{z}\right)$ properties, it is possible to determine the new stabilization part of the stiffness matrix:

$$\breve{\hat{\mathbf{k}}}_{stab}^{e}=\sum_{I=1}^{8}\left(\breve{\hat{\mathbf{B}}}_{34}\right)_{I}^{T}\times\mathbf{H}'\times\left(\breve{\hat{\mathbf{B}}}_{34}\right)_{I}\left|\breve{\mathbf{J}}\right| \tag{5.175}$$

The chosen constitutive law $\mathbf{H}'$ is a modified 3D law based on the generalized plane stress theory. It prevents some coupling between membrane, bending and shear strain modes and the thickness mode, reducing the risk of locking in the stabilization stiffness matrix. It takes the form:

$$\mathbf{H}' = \begin{bmatrix} \bar{\lambda}+2\mu & \bar{\lambda} & 0 & 0 & 0 & 0 \\ \bar{\lambda} & \bar{\lambda}+2\mu & 0 & 0 & 0 & 0 \\ 0 & 0 & E & 0 & 0 & 0 \\ 0 & 0 & 0 & \mu & 0 & 0 \\ 0 & 0 & 0 & 0 & \mu & 0 \\ 0 & 0 & 0 & 0 & 0 & \mu \end{bmatrix} \tag{5.176}$$

where the Lamé's coefficients are $\bar{\lambda} = \frac{E.\nu}{\left(1-\nu^2\right)}$ and $\mu = \frac{E}{2.\left(1+\nu\right)}$.

As detailed in Abed-Meraim & Combescure (2002), the following equations can be set in the co-rotational coordinates system $\breve{\mathbf{x}}\left(\breve{x},\breve{y},\breve{z}\right)$:

$$\int_{V^e} h_{i,j} dV^e = 0$$

$$\begin{aligned} H_{ii} &= \int_{V^e} \left(h_{i,j}\right)^2 dV^e = \int_{V^e} \left(h_{k,i}\right)^2 dV^e = \int_{V^e} \left(h_{4,i}\right)^2 dV^e \\ &= \frac{1}{3} \times \frac{\left(\boldsymbol{\Lambda}_j^T \times \breve{\mathbf{x}}_j\right) \times \left(\boldsymbol{\Lambda}_k^T \times \breve{\mathbf{x}}_k\right)}{\left(\boldsymbol{\Lambda}_i^T \times \breve{\mathbf{x}}_i\right)} \end{aligned} \tag{5.177}$$

$$H_{ij} = \int_{V^e} h_{i,j} \times h_{j,i} dV^e = \frac{1}{3} \times \boldsymbol{\Lambda}_k^T \times \breve{\mathbf{x}}_k$$

Moreover, some parameters of $\breve{\hat{\mathbf{B}}}_{34}$ have orthogonally properties that help to simplify $\breve{\hat{\mathbf{k}}}_{stab}$, namely:

$$\begin{aligned} \gamma_{\beta_1}^T \times h_{\beta_2} &= \delta_{\beta_1\beta_2} \\ h_{\beta_2}^T \times h_{\beta_1} &= 8 \times \delta_{\beta_1\beta_2} \end{aligned} \tag{5.178}$$

Developing equation (5.175) yields in:

$$\breve{\hat{\mathbf{k}}}_{stab} = \begin{bmatrix} \breve{\hat{\mathbf{k}}}_{stab,11} & \mathbf{0} & \mathbf{0} \\ \mathbf{0} & \breve{\hat{\mathbf{k}}}_{stab,22} & \mathbf{0} \\ \mathbf{0} & \mathbf{0} & \breve{\hat{\mathbf{k}}}_{stab,33} \end{bmatrix} \tag{5.179}$$

where $\breve{\hat{\mathbf{k}}}_{stab,ii}$ are 8×8 matrices such that (See Appendix C):

$$\begin{aligned} \breve{\hat{\mathbf{k}}}_{stab,11} &= \left(\overline{\lambda} + 2\times\mu\right)\times H'_{11}\times\left[\hat{\gamma}_3\times\hat{\gamma}_3^T + \frac{1}{3}\times\hat{\gamma}_4\times\hat{\gamma}_4^T\right] \\ \breve{\hat{\mathbf{k}}}_{stab,22} &= \left(\overline{\lambda} + 2\times\mu\right)\times H'_{22}\times\left[\hat{\gamma}_3\times\hat{\gamma}_3^T + \frac{1}{3}\times\hat{\gamma}_4\times\hat{\gamma}_4^T\right] \\ \breve{\hat{\mathbf{k}}}_{stab,33} &= \mu\times H'_{11}\times\frac{1}{3}\times\hat{\gamma}_4\times\hat{\gamma}_4^T \end{aligned} \tag{5.180}$$

The present adopted stiffness stabilization remains efficient enough for thin structures.

5.8. Internal forces vector calculation

The internal force vector calculation depends on the element strain operator matrix $\mathbf{B}$ as well as on the stresses vector and takes the form:

$$\mathbf{f}_{\text{int}}^e = \int_{V^e} \mathbf{B}^T.\mathbf{S}dV^e \tag{5.181}$$

Introducing equation (5.75) and the simplified form of $\mathbf{B}_{34}$ illustrated by equation (5.174) in equation (5.181) helps to express $\mathbf{f}_{\text{int}}^e$ as a sum of an unstabilized term $\mathbf{f}_{12}$ and a stabilization term $\mathbf{f}_{stab}$:

$$\begin{aligned} \breve{\hat{\mathbf{f}}}_{\text{int}}^e &= \int_{V^e}\left(\mathbf{B}_{12} + \breve{\hat{\mathbf{B}}}_{34}\right)^T.\left(\mathbf{S}_{12} + \breve{\hat{\mathbf{S}}}_{34}\right)dV^e \\ &= \mathbf{f}_{12}^e + \breve{\hat{\mathbf{f}}}_{stab}^e \end{aligned} \tag{5.182}$$

where

$$\mathbf{f}_{12}^{e} = \sum_{I=1}^{8} \left(\mathbf{B}_{12}\right)_{I}^{T} .\mathbf{S}_{12} \left|\mathbf{J}\right| \tag{5.183}$$

$$\breve{\hat{\mathbf{f}}}_{stab}^{e} = \sum_{I=1}^{8} \left(\breve{\hat{\mathbf{B}}}_{34}\right)_{I}^{T} .\breve{\hat{\mathbf{S}}}_{34} \left|\breve{\mathbf{J}}\right| \tag{5.184}$$

The simplified form of the stabilized stress tensor $\breve{\hat{\mathbf{S}}}_{34}$ is explicitly calculated as detailed below:

$$\begin{aligned} \breve{\hat{\mathbf{S}}}_{34} &= \mathbf{H}' \times \breve{\hat{\mathbf{B}}}_{34} \times \begin{Bmatrix} u_{I1} \\ u_{I2} \\ u_{I3} \end{Bmatrix} \\ &= \begin{Bmatrix} h_{3,x} \times q_{13} + h_{4,x} \times q_{14} \\ h_{3,y} \times q_{23} + h_{4,y} \times q_{24} \\ h_{3,z} \times q_{33} \\ 0 \\ 0 \\ h_{4,x} \times q_{34} \end{Bmatrix} \end{aligned} \tag{5.185}$$

where $\mathbf{u}_{Ii}, \quad i = 1,2,3 \; and \; I = 1,\ldots,8$ is the displacements field for the three degrees of freedom and $q_{i\beta}, \quad i = 1,2,3 \; and \; \beta = 3,4$ are the generalized strains defined as:

$$q_{i\beta} = \hat{\gamma}_{\beta}^{T} \times u_{Ii}, \quad i = 1,2,3 \; ; I = 1,\ldots,8 \; and \; \beta = 3,4 \tag{5.186}$$

From equation (5.184) and (5.185) it is easy to get (See Appendix C):

$$\begin{aligned}\breve{\hat{\mathbf{f}}}^{e}_{stab} &= \sum_{\beta=3}^{4} Q_{i\beta} \times \breve{\hat{\gamma}}_{\beta}, \quad i = 1,2,3 \\ &= \begin{Bmatrix} \left(\bar{\lambda} + 2\times\mu\right)\times H'_{11} \times \left(q_{13} + \frac{1}{3}\times q_{14}\right) \\ \left(\bar{\lambda} + 2\times\mu\right)\times H'_{22} \times \left(q_{23} + \frac{1}{3}\times q_{24}\right) \\ \left(\bar{\lambda} + 2\times\mu\right)\times H'_{11} \times \frac{1}{3}\times q_{34} \end{Bmatrix}\end{aligned} \tag{5.187}$$

5.9. Benchmark problems

In this section, the proposed SH8RSe element using a classical 3D constitutive law is compared with other well known eight - node solid-shell elements. In order to check its potential on a common basis, some popular benchmark analytical results like those proposed in Macneal & Harder (1985) are taken as references. In section 5.9.1, the element accuracy is estimated for classical linear elastic geometric problems. Then in section 5.9.2, the element evaluation is extended to classical problems in elastic non-linear problems. One has to note that an implicit version of the SH8RSe element is considered in these two sections.

The solid-shell elements compared in this section are named as follows:

SH8 – eight-node element with ANS and EAS equivalent to the SCH8 element from Hannachi (2007).

SC8R – eight-node element with reduced integration and plane stress assumption Abaqus user's manual, ver 6.8, (2007).

Xsolid85 – resultant eight-node element with ANS and plane stress assumption Kim et al. (2005).

Abed2009 - Abed-Meraim & Combescure (2009): solid-shell element SHB8PS with reduced integration.

Sch2009 - Schwarze & Reese (2009): reduced integration eight – node solid-shell element with ANS and EAS.

SHB8PS – Implementation of the SHB8PS element done in the course of this work, similar as the Abed2009 element, with a modified 3D constitutive law.

SH8RSe – Present ANS and EAS solid-shell element with reduced integration.

All linear results are normalized compared to the analytical reference solutions.

5.9.1 Evaluation of SH8RSe element for classical linear implicit benchmark problems

Pinched cylinder with end diaphragm problem

Figure 5.9(a) shows a pinched cylinder with an end diaphragm which sets all displacement to zero in the XZ plane. A concentrated vertical force F is applied at point A which helps testing the capability of the present element to deal with inextensional bending modes and complex membrane states. This cylinder has a length $L = 600$, a radius $R = 25$ and a thickness $t = 0.25$. Its material properties are a Young's modulus $E = 3e^6$ and a Poisson's ratio $\nu = 0.3$. The symmetry of the model allows considering only a quarter of the problem. The reference vertical displacement of point A is $U_y = 1.8248\, e^{-5}$. Results for different mesh sizes are presented in Figure 5.10 and Table 5.3 for regular mesh and Figure 5.11 and table Table 5.4 for irregular mesh. Irregular meshes, like in Figure 5.9(b), are determined using a technique in the same idea of the one proposed by Nguyen-Thanh et al. (2008). The SH8RSe element shows the best results compared to the other tested elements and remains accurate even in case of very irregular mesh.

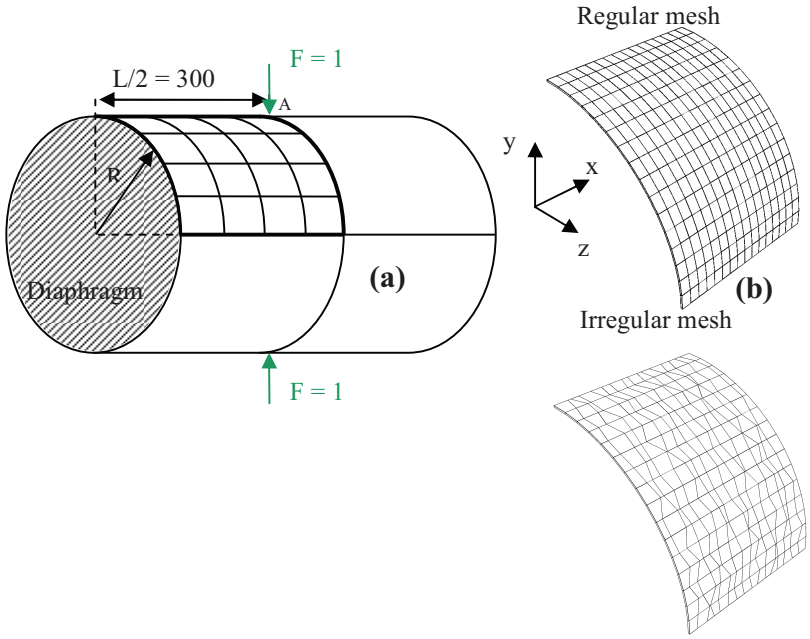

Figure 5.9: Pinched cylinder with end diaphragm problem

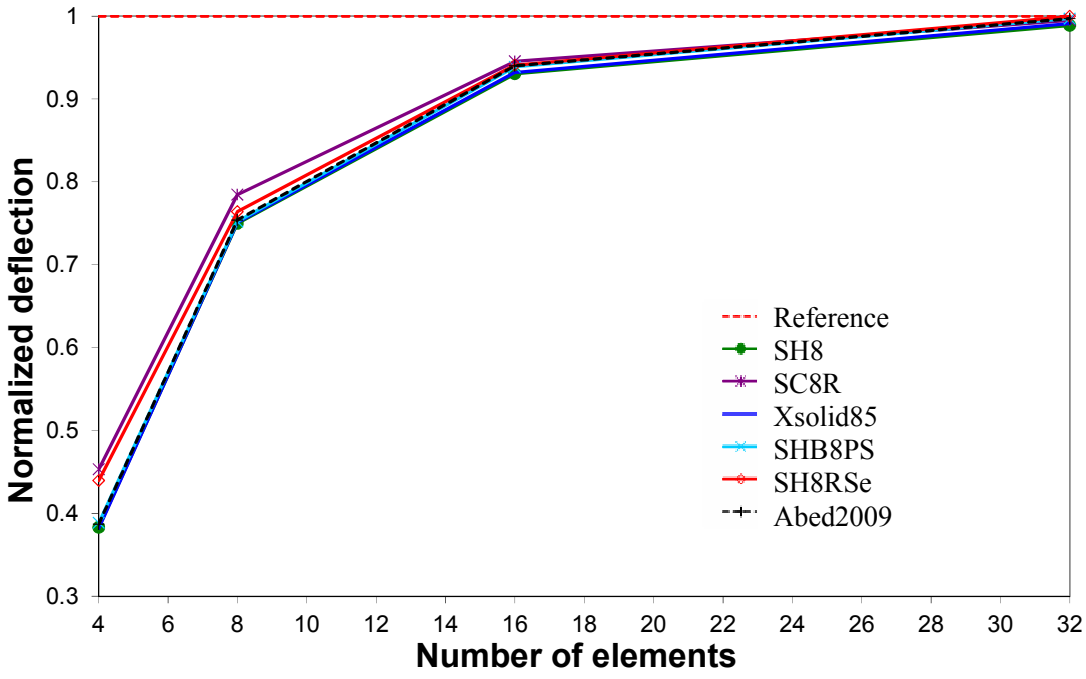

Figure 5.10: Graph, pinched cylinder with end diaphragm problem, regular mesh

Element number	SC8R	Xsolid85	Abed2009	SH8	SHB8PS	**SH8RSe**
4	0.4532	0.382	0.387	0.3830	0.3886	**0.4397**
8	0.7845	0.751	0.754	0.7499	0.7520	**0.7640**
16	0.9454	0.932	0.94	0.9304	0.9387	**0.9410**
32	0.9949	0.991	0.997	0.9888	0.997	**0.9997**

Table 5.3: Pinched cylinder with end diaphragm problem, regular mesh results

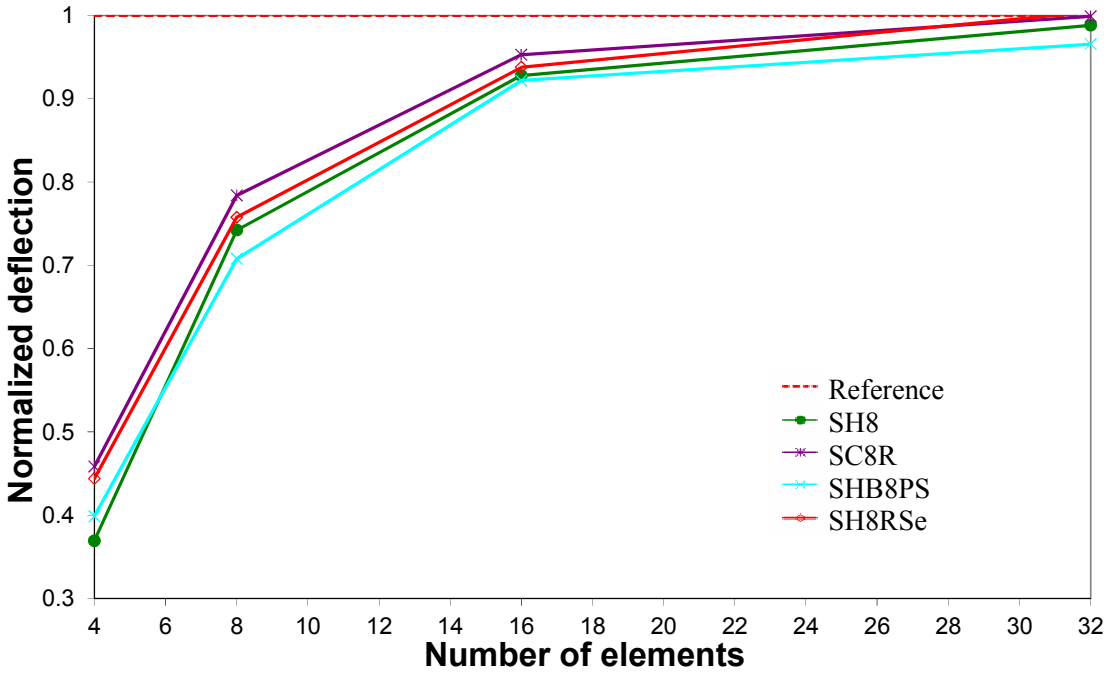

Figure 5.11: Graph, pinched cylinder with end diaphragm problem, irregular mesh

Element number	SC8R	SH8	SHB8PS	**SH8RSe**
4	0.4584	0.3693	0.3986	**0.4439**
8	0.7838	0.7422	0.7078	**0.7577**
16	0.9528	0.9278	0.9217	**0.9378**
32	0.9989	0.9882	0.9656	**1.0041**

Table 5.4: Pinched cylinder with end diaphragm problem, irregular mesh results

Twisted beam problem

This example evaluates the response of an element in case of severe distortion of the geometry. A twisted beam clamped at one end was loaded in two different ways: one in-plane and one out-of-plane concentrated loads, respectively F_1 and F_2 were applied as presented in Figure 5.12. The geometry parameters are defined by a length of $L = 12$, a width of $W = 1.1$ and a twist of 90º. Two thicknesses are tested: $t = 0.32$ and $t = 0.05$. The Young's modulus is $\mathrm{E} = 29\mathrm{e}^{6}$ and the Poisson's ratio is $\nu = 0.22$. The observed parameter is the displacement of the beam loaded extremity. The jacobian transformation accuracy can then be checked for the present element. The reference solution vertical displacement for F_1 is $5.424\mathrm{e}^{-3}$ with $t = 0.32$ and 1.387 with $t = 0.05$. The reference solution lateral displacement for F_2 is $1.754\mathrm{e}^{-3}$ with $t = 0.32$ and 0.343 with $t = 0.05$ Macneal & Harder (1985). For $t = 0.32$, the displacement of point A is presented in Figure 5.13 and Table 5.5 for twisted beam loaded with F_1 and in Figure 5.14 and Table 5.6 for twisted beam loaded with F_2 for different mesh sizes. For $t = 0.05$, the displacement of point A is presented in Figure 5.15 and Table 5.7 for twisted beam loaded with F_1 and in Figure 5.16 and Table 5.8 for twisted beam loaded with F_2 for different mesh sizes.

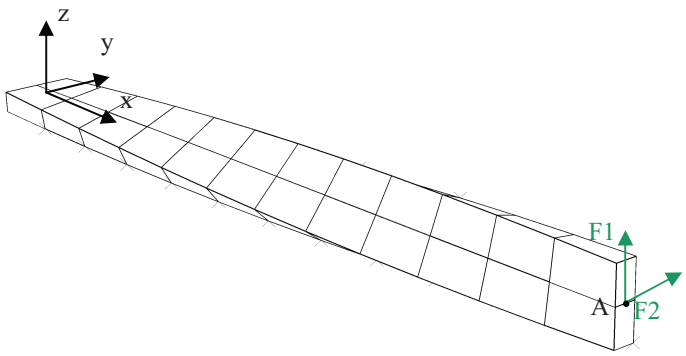

Figure 5.12: Twisted beam problem

The studied reduced integration elements have a rapid convergence regarding the reference result. The proposed SH8RSe element remains the most accurate when the geometry with $t = 0.32$ is loaded with F_1. At the contrary, the SHB8PS element is more accurate while

loaded with F_2 using the same geometry. The accuracy of the SH8RSe element stays high with a thinner structure, $t = 0.05$.

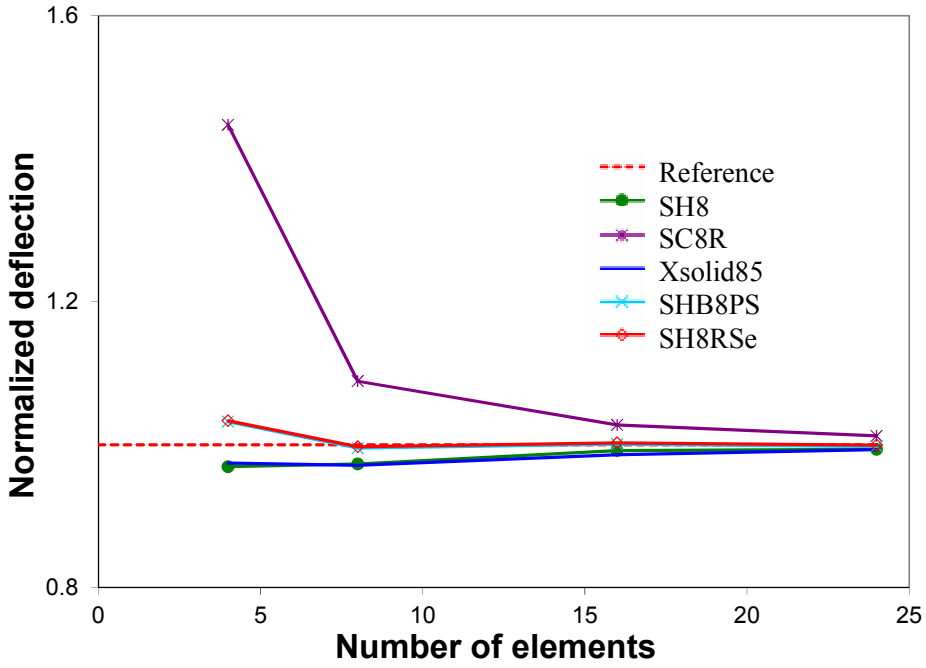

Figure 5.13: Graph, twisted beam t=0.32 problem, F_1 load

Element number	SC8R	SH8	Xsolid85	SHB8PS	**SH8RSe**
4	1.447	0.969	0.974	1.032	**1.033**
8	1.089	0.973	0.971	0.995	**0.997**
16	1.028	0.992	0.986	1.001	**1.002**
24	1.012	0.993	0.993	0.998	**0.999**

Table 5.5: Twisted beam t=0.32 problem, F_1 load results

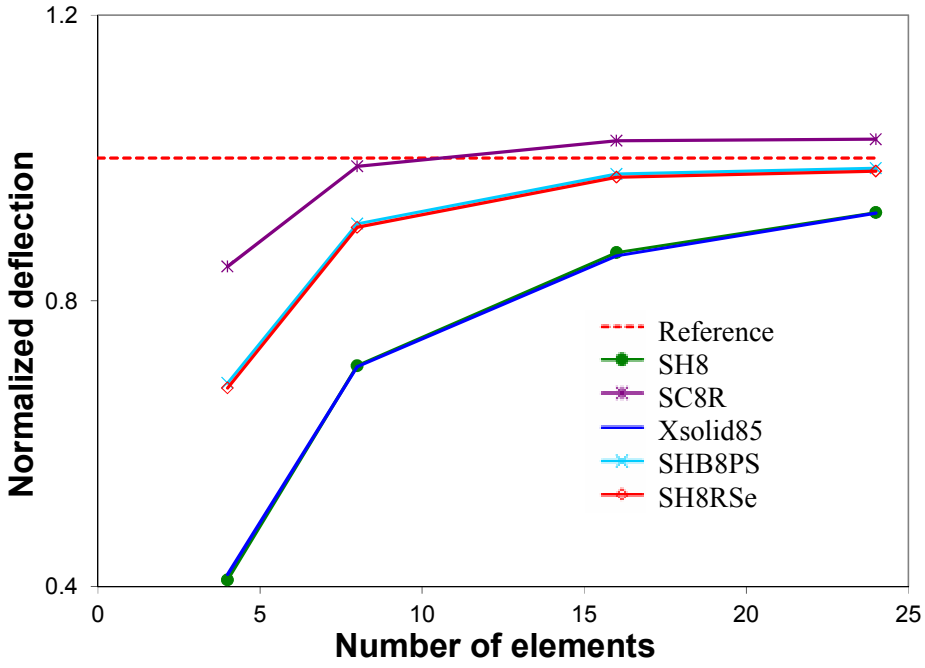

Figure 5.14: Graph, twisted beam t=0.32 problem, F_2 load

Element number	SC8R	SH8	Xsolid85	SHB8PS	**SH8RSe**
4	0.848	0.409	0.417	0.685	**0.678**
8	0.988	0.709	0.708	0.908	**0.903**
16	1.024	0.868	0.863	0.977	**0.973**
24	1.026	0.923	0.923	0.986	**0.982**

Table 5.6: Twisted beam t=0.32 problem, F_2 load results

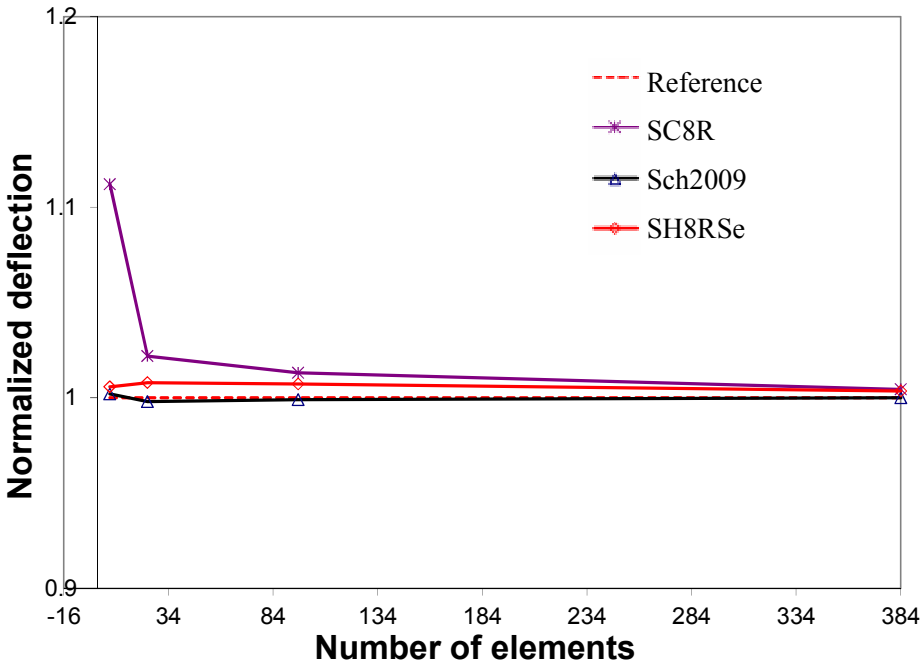

Figure 5.15: Graph, twisted beam t=0.05 problem, F_1 load

Element number	SC8R	Sch2009	**SH8RSe**
4	1.112	1.002	**1.006**
8	1.022	0.998	**1.008**
16	1.013	0.999	**1.007**
24	1.004	1	**1.004**

Table 5.7: Twisted beam t=0.05 problem, F_1 load results

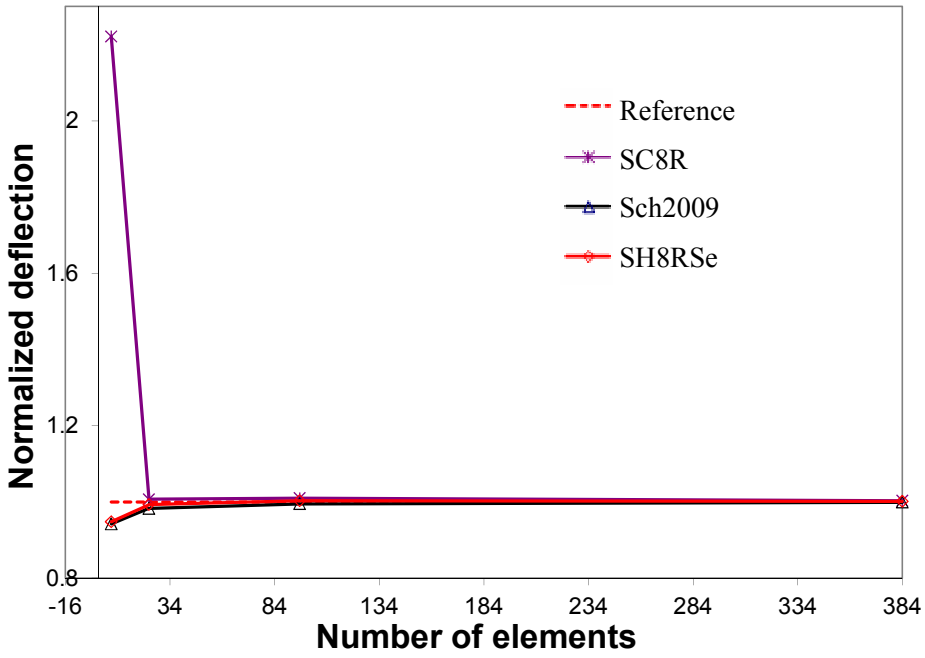

Figure 5.16: Graph, twisted beam t=0.05 problem, F_2 load

Element number	SC8R	Sch2009	**SH8RSe**
4	2.221	0.942	**0.948**
8	1.007	0.983	**0.993**
16	1.010	0.995	**1.003**
24	1.003	0.999	**1.001**

Table 5.8: Twisted beam t=0.05 problem, F_2 load results

Pinched hemispherical with and without 18º hole problem

The pinched hemispherical problem initially suggested by Macneal & Harder (1985) remains popular in the literature to estimate an element capability to deal with inextentional bending mode and rigid body movements. Moreover, due to the double curvature geometry, this benchmark problem helps to verify the ability of an element to reproduce acceptable results even with distorted mesh. Figure 5.17 shows that two concentrated and opposite forces $F_x = 1$ and $F_y = -1$ are applied to the geometry. The studied geometry has a radius $R = 10$ and a thickness $t = 0.04$ and the symmetry of the model allows considering only a quarter of the problem. Two configurations are presented here: one hemispherical with a 18º hole along z axis and one without hole, illustrated respectively in Figure 5.17 (a) and Figure 5.17 (b). This last configuration appears to be more severe since the elements appear to be more distorted than with a hole. The related material properties are a Young's modulus $E = 6.8225e^7$ and a Poisson's ratio $\nu = 0.3$. Macneal & Harder (1985) give the analytical displacement of point A along x axis for the case with a 18º hole U_y=9.4e^{-2} and for the case without hole U_y=9.24e^{-2}. Results for different mesh sizes are presented in Figure 5.18 and Table 5.9 for configuration with 18º hole and Figure 5.19 and Table 5.10 without hole.

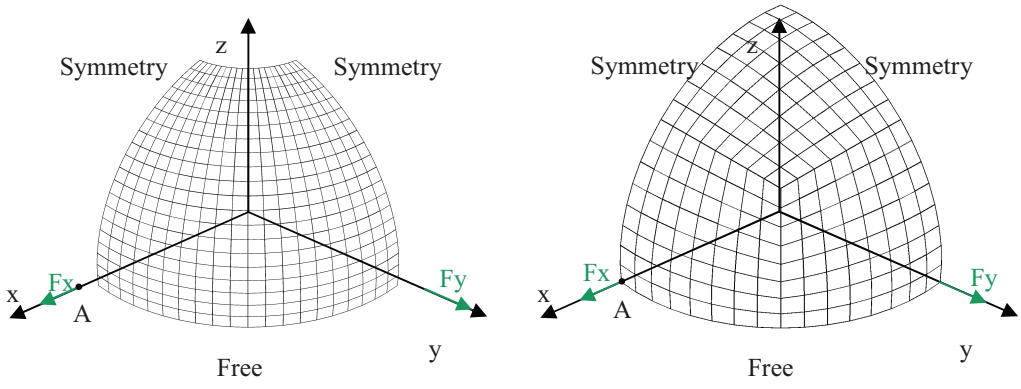

Figure 5.17: Pinched hemispherical with 18º hole (a) and without hole (b) problem

In the configuration with a 18º hole, the present SH8RSe element proposes more accurate results than the other reduced integration 3D Sch2009 element but less accurate than those

obtained with the SHB8PS element. With the geometry without hole, the proposed element gives the exact solution.

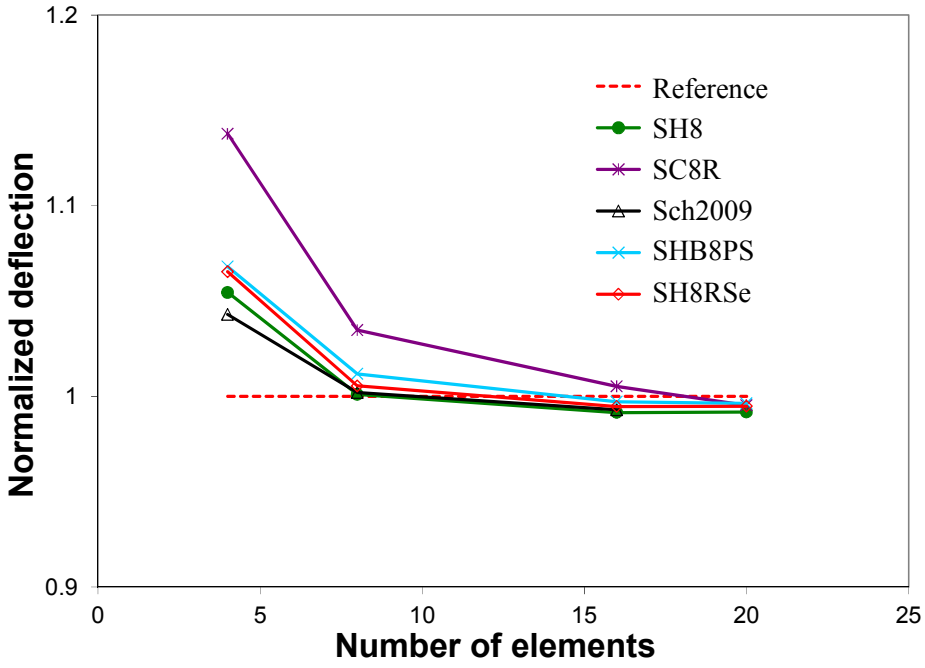

Figure 5.18: Graph, pinched hemispherical with 18º hole problem

Element number	SC8R	SH8	Sch2009	SHB8PS	**SH8RSe**
4	1.1378	1.0545	1.043	1.0681	**1.0654**
8	1.0347	1.0011	1.002	1.0118	**1.0055**
16	1.0052	0.9915	0.993	0.9971	**0.9947**
24	0.9954	0.9918	0.994	0.9963	**0.9948**

Table 5.9: Pinched hemispherical with 18º hole problem

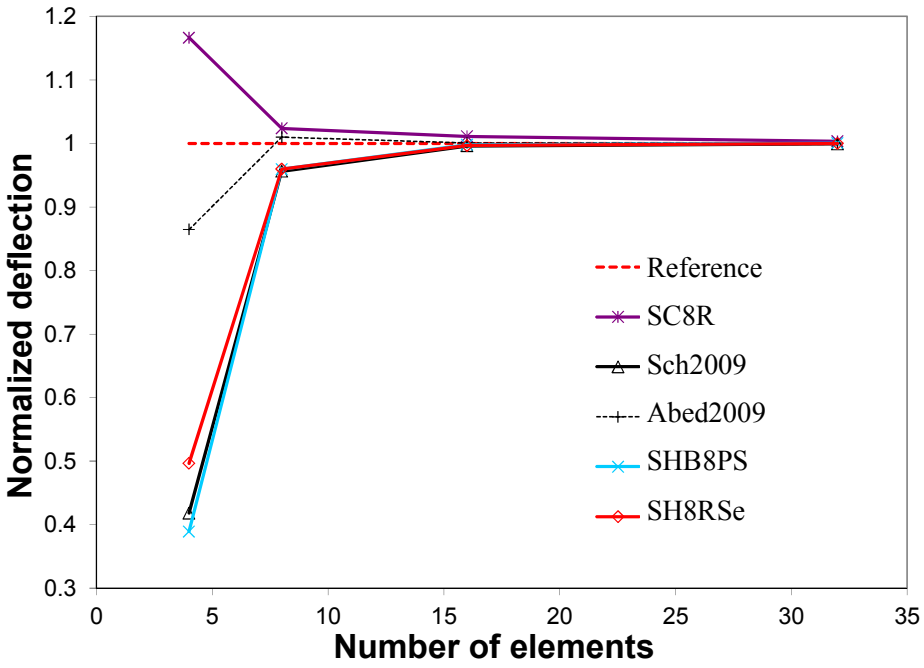

Figure 5.19: Graph, pinched hemispherical without hole problem

Element number	SC8R	Abed2009	Sch2009	SHB8PS	**SH8RSe**
4	1.1662	0.8645	0.418	0.3891	**0.4963**
8	1.0238	1.0098	0.956	0.9593	**0.9595**
16	1.0112	1.0008	0.996	0.9979	**0.9966**
20	1.0033	1.0006	0.999	1.0005	**1.000**

Table 5.10: Pinched hemispherical without hole problem

5.9.2 Evaluation of SH8RSe element for classical non-linear geometric implicit benchmark problems

Slit annular plate subjected to lifting line force

This benchmark problem proposed by Wriggers & Gruttmann (1993) and later used by other authors as Brank et al. (1995), Barut et al. (1997), Sansour & Bocko (1998), Sansour & Kollmann (2000), Hong et al. (2001), Sze et al. (2002), Abed-Meraim & Combescure (2009) is efficient in proving an element ability to deal with large deformation and large rotation problems. A circular flat ring is cut between points A and B as presented in Figure 5.20. One of the two cutting sides remains clamped and the other one is subjected to a linear upwards force $P_{\max} = 0.8\left(\mathit{force/length}\right)$. The employed mesh is the same 8×64 mesh with only one element through the thickness as in Abed-Meraim & Combescure (2009). The geometry parameters are defined by an internal radius $R_i = 6$, an external radius of $R_e = 10$ and a thickness of $t = 0.03$. The Young's modulus is $E = 21\text{e}^6$ and the Poisson's ratio is $\nu = 0.0$. Results presented in Figure 5.21 illustrate the good agreement of results obtained with the SH8RSe element compared with the reference.

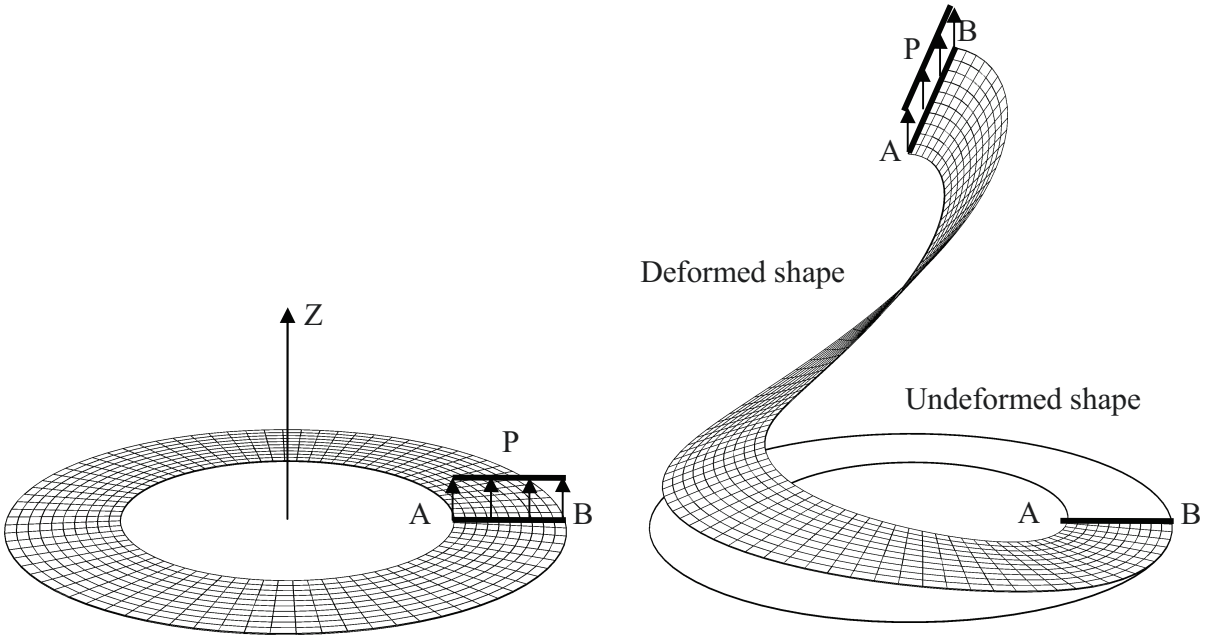

Figure 5.20: Slit annular plate subjected to lifting line force

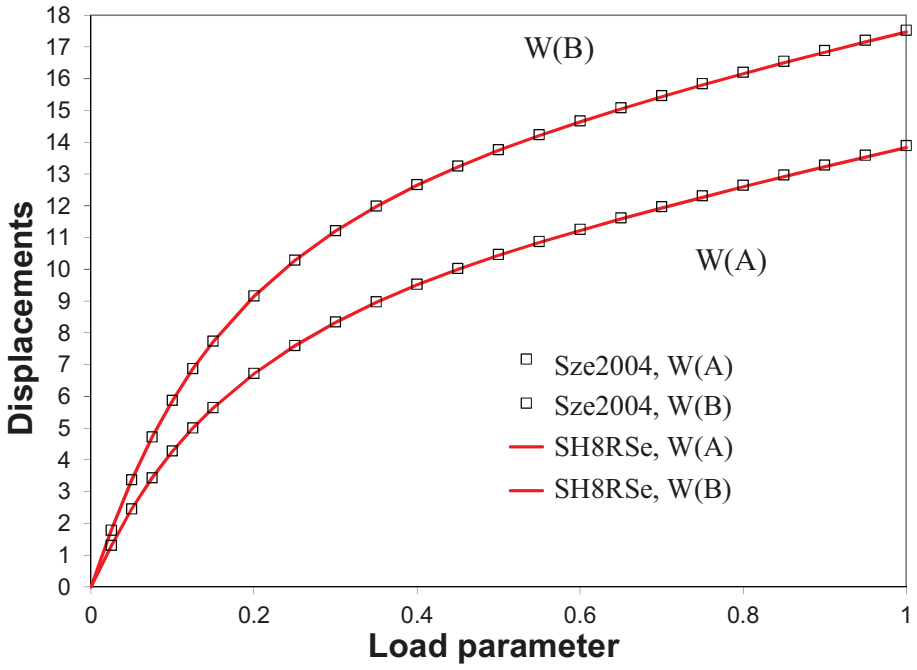

Figure 5.21: Graph, slit annular plate subjected to lifting line force

Twisted beam under out-of-plane loading

The twisted beam bench mark problem became a reference in the literature to test new element performances. One of its main characteristics remains in the initial warping of the elements used to mesh the beam. In term of geometrical properties, the angle between the two beam ends is 90º. The beam length, thickness and width are respectively $\mathrm{L}=12$, $\mathrm{t}=0.032$ and $\mathrm{W}=1.1$ (see Figure 5.22). The Young's modulus is $\mathrm{E}=29\mathrm{e}^{6}$ and the Poisson's ratio is $\nu=0.22$. A lateral force is progressively applied with a maximum value $P_{\max}=40$ at point A. Abed-Meraim & Combescure (2009) observed that their implementation of the SHB8PS element gives results in good agreement with the non-linear results presented in Smolenski (1998) taken as a reference. Then the proposed SH8RSe element results are compared with the element of Abed-Meraim & Combescure (2009) using the same 24×4 mesh with one element through the thickness.

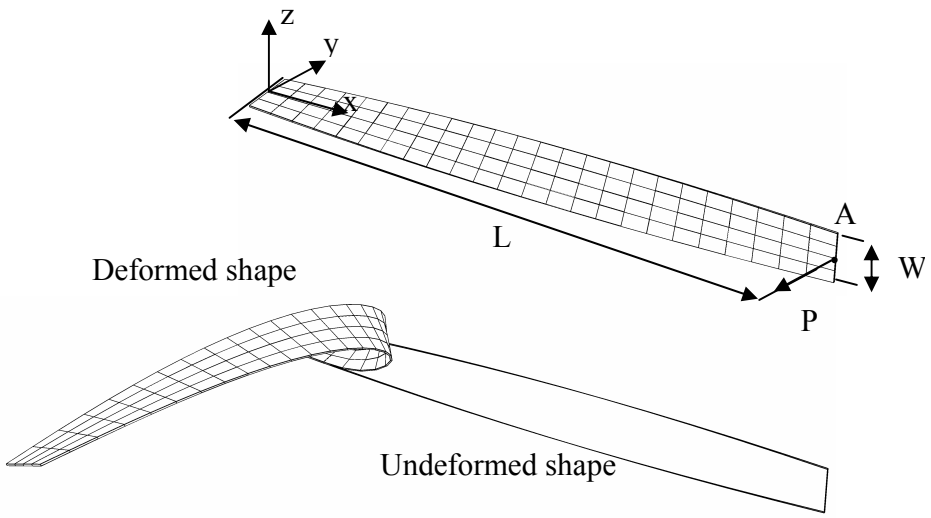

Figure 5.22: Thin twisted beam under out of plane loading

Figure 5.23 plots the displacements of point A in the three directions with the Abed2009 element and with the SH8RSe element. It clearly appears that the proposed element performance remains in good agreement with the reference.

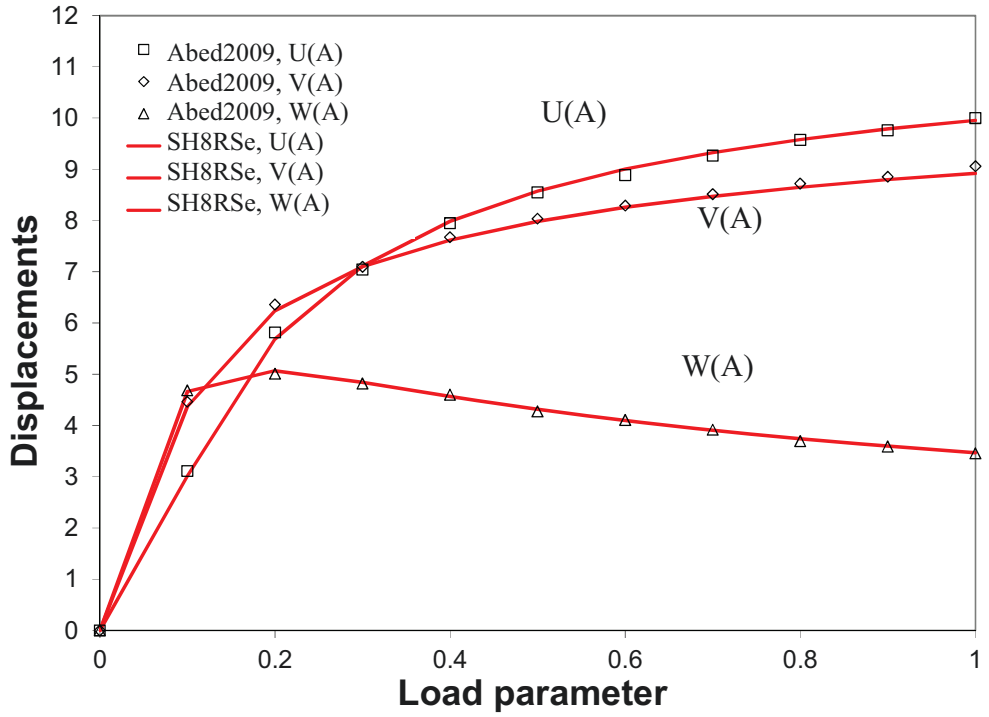

Figure 5.23: Graph, thin twisted beam under out of plane loading

Pinched hemispherical with a hole

This double curvature benchmark problem has the same geometry and elastic material properties as for the linear case already presented in section 5.9.1. However, in this section the capabilities of the element are tested for large displacements and large rotations. A hemispherical with a hole of 18 º is subject to two opposite concentrated loads $F_x = 100$ and $F_y = -100$ as presented in Figure 5.24. Its radius and thickness are respectively $R = 10$ and $t = 0.04$. In term of geometry, the Young's modulus is $E = 6.825e^7$ and the Poisson's ratio is $\nu = 0.3$. Due to the problem symmetry, only a quarter of the geometry was studied. Among those who used this problem are Simo et al. (1990), Domissy (1997), Sze et al. (2004), Kim et al. (2005), Hannachi (2007) and Schwarze & Reese (2011). The good convergence of the present element has been compared with the reference solution Simo et al. (1990) and Sansour & Kollmann (2000) with 20×20 mesh.

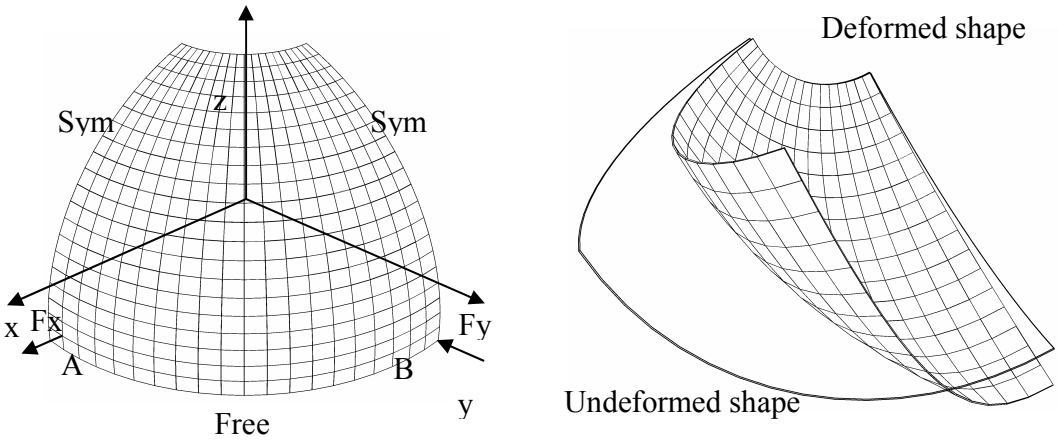

Figure 5.24: Pinched hemispherical with a hole

The SH8RSe element remains very accurate according to reference results as shown in Figure 5.25 without any locking.

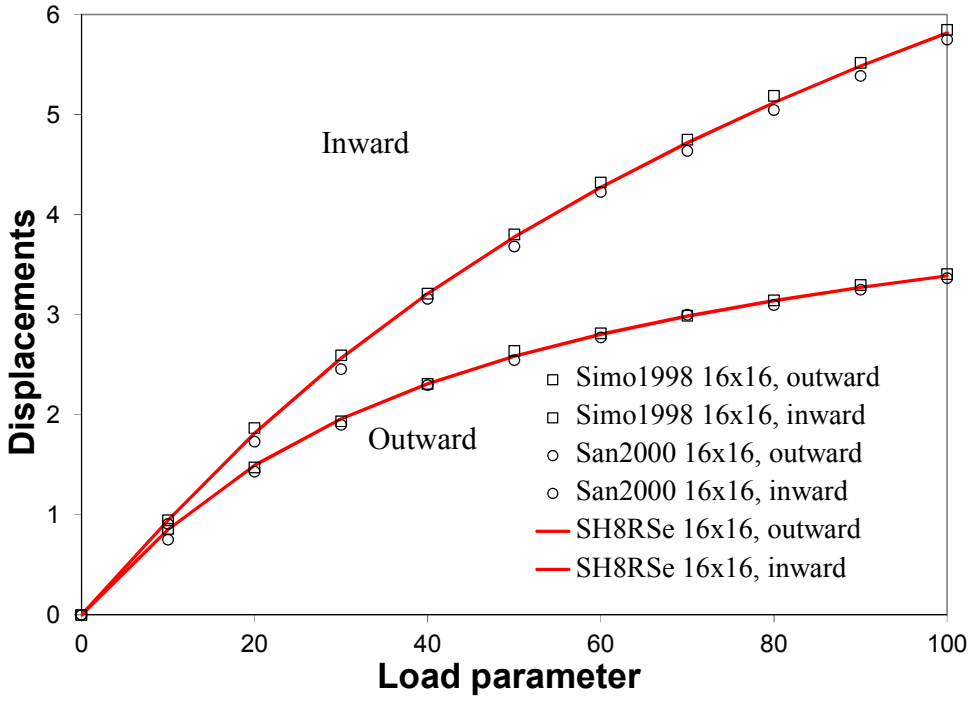

Figure 5.25: Graph, pinched hemispherical with a hole

Pinched clamped cylinder

A cylinder fully clamped on one side is subjected to two opposite concentrated forces to the other side with a maximum value of $P_{\max} = 1600$. Its length is $L = 3.048$, radius $R = 1.016$ and thickness $t = 0.03$ as detailed in Figure 5.26. The elastic properties of the problem are a Young's modulus $\mathrm{E} = 2.0685\mathrm{e}^{7}$ and a Poisson's ratio $\nu = 0.3$. Due to the model symmetry, only a quarter of the problem was considered. This problem has already been used by Brank et al. (1995), Alves de Sousa et al. (2006). The vertical displacement of point A reference solution of Brank et al. (1995) is used for comparison and a similar 16×16 mesh is adopted for the cylinder meshing.

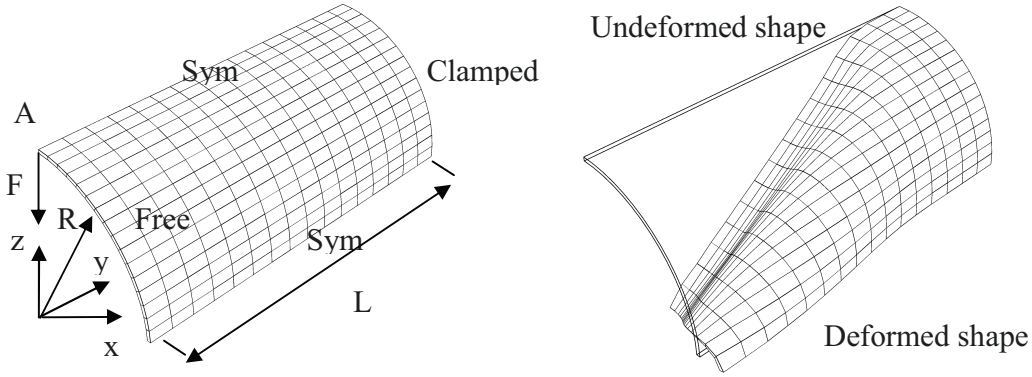

Figure 5.26: Pinched clamped cylinder

Figure 5.27 then illustrates the good performance of the SH8RSe element.

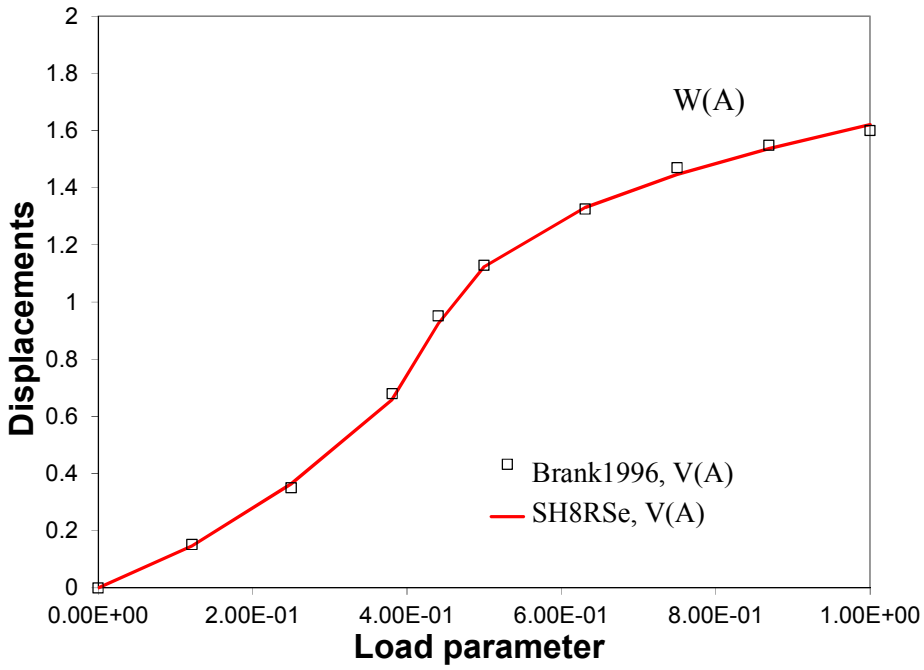

Figure 5.27: Graph, pinched clamped cylinder

5.10. Concluding remarks

The recently developed SH8RSe element implicit formulation presented in this work has been successfully updated to be able to read all classical 3D constitutive laws and performed well for non-linear applications. All development and programming have been performed in ABAQUS/standard using the ABAQUS/UEL interface. The present element takes advantage of reduced integration in terms of time efficiency. In this reduced integration element, only one integration point is used per integration plane. Moreover, five integration points are used in the thickness direction in order to have information through the thickness. This last property allows for the element to be accurate even in cases of bending problems with only one layer of elements. A consequence of this reduced integration is the loss of stability due to some parameter disappearance. As a matter of fact, a stabilization method remains necessary to recover the lost stability. The variational mixed formulation helps identifying the strain field components which facilitates locking problem treatment. The present element then remains locking free even while dealing with thin structures. The ANS method is used to reduce the transverse shear locking as well as the trapezoidal effect. Moreover, the EAS method used with only one enhanced parameter helps reducing thickness locking. The SH8RSe element exhibits attractive properties compared with existing elements which confirms the observations declared by the first developers of this type of element. In order to complement this study, Chapter 6 goes further by presenting the explicit formulation of the SH8RSe element and its combination with a classical 3D constitutive law. This combination is then used in the tube hydroforming context and the capabilities of the new element combined with a classical 3D constitutive law are evaluated and compared with those of other existing one.

Chapter 6. Application of improved SH8RSe solid-shell element in tube hydroforming

Chapter 6 presents the SH8RSe element capabilities when combined with a 3D hyperelastoplastic behavior law in the tube hydroforming context. In order to achieve this, a polar decomposition of the deformation gradient $\mathbf{F}$ and the separation of the SH8RSe kinematics from its constitutive parts have been necessary in its implementation. The pressure definition in the internal forces is also proposed. The ABAQUS/VUEL explicit module of ABAQUS/Explicit is used for these developments. Hence, the present work can take advantage of the explicit contact definition implemented in ABAQUS/Explicit. The chosen 3D hyperelastoplastic constitutive law developed by Matei (2011) is briefly described in Appendix D of this thesis as well as its incorporation in the resolution scheme of the current element. The SH8RSe solid-shell element is then tested in two typical forming conditions encountered in the tube hydroforming context namely tube bending and tube hydroforming of a conical die. The use of only one enhanced parameter allows the SH8RSe element to use a non modified 3D constitutive law without any thickness locking occurrence.

6.1. Introduction

Since the beginning of last century, many forming processes have been developed and used in order to fabricate more and more complex parts. Tube hydroforming (THF) process, which today is mainly exploited in the automotive industry, has continuously been studied and employed in other sectors such as the aerospace because of its very interesting capabilities in line with industrial needs. Some advantages of the THF method are:

- Possibility to form a complex part without any welding stage, bolt devices or machining, in only one stage;
- In some cases, improvements of material properties of a part providing strain hardening in working areas (part consolidation);
- High tolerance standard.

A typical THF process can be described as follows: i) A straight tube - or with another arbitrary shape - is positioned between dies; ii) The dies are closed, thus crushing the tube in the same time, depending on its initial shape; iii) Thanks to an appropriate sealing, the pressure level increases inside the tube, and simultaneously an end feeding is provided at the tube extremities so as to achieve a loading path necessary to hydroform a final part tailored to specific requirements; (iv) Then pressure inside the tube decreases and the dies are opened to free the hydroformed part. The final shape of the newly hydroformed part is reached after springback. Step (iii) above is the most critical one since many defects could occur, making the hydroformed parts unusable. Among the most common defects, one can mention wrinkling or buckling when end feeding is too high compared to the internal pressure and bursting if the end feeding is too low when compared to the internal pressure, Aydemir et al. (2005).

However, the THF process has some persistent drawbacks that need to be properly addressed. These include:

- Difficulty to determine an acceptable loading path;
- Expensive initial investments;

- Requirement to study the THF process and materials carefully for each application.

For these reasons, the finite element method (FEM) is particularly interesting, especially while dealing with expensive aerospace materials, because it allows avoiding the trial and error method generally used to determine an acceptable loading path. In addition, this method gives a rapid and accurate overview of the tooling required to hydroform a given part, thus saving development time and material. However, the finite element results highly depend on the type of elements used for a given simulation. In the THF process simulation solid elements using a 3D constitutive law are interesting for their ability to capture some thickness variations. Their exterior nodes also allow explicit contact definition. However in order to obtain accurate results, at least three linear solid elements are necessary in the thickness direction as noted in Élie-Dit-Cosaque et al. (2009) but at the cost of increased computation time. For this reason, many researchers use other lower dimension finite elements such as the axisymmetric 2D elements in the Deform 2D software used in Koç & Altan (2002) and Lang et al. (2004) or the four nodes Belytschko Tsay shell elements as in Ray & Mac Donald (2005) with plane stress assumption. However, if this last type of element remains time efficient, it does not give accurate through the thickness information due to plane stress hypothesis.

Many researchers then paid attention to the well know solid-shell element type which has the advantages of having eight exterior nodes allowing explicit contact definition as well as shell ability to deal efficiently with thin structures with a 3D constitutive law. Moreover, this element type remains very time efficient compared with solid elements, since only one elements layer in the thickness direction usually remains sufficient. Parisch (1995) was among the first to work on the subject. However, solid-shell elements exhibit locking problems inherent to their formulation, like transverse shear locking, volumetric locking, Poisson thickness locking, curvature or trapezoidal locking, in plane shear locking and membrane locking. Since then, many developments have been made in order to circumvent these locking problems. Simo & Rifai (1990) initially proposed the enhanced assumed strain (EAS) method to deal with volumetric locking. The key concept of this method consists in the enrichment of internal variables with enhanced parameters. This technique was then developed to handle other locking problems, like Poisson thickness locking in

Büchter et al. (1994), membrane locking in Miehe (1998), transverse shear locking in Alves de Sousa et al. (2003), Alves de Sousa et al. (2005) and Li et al. (2011). Initially introduced by Hughes & Tezduyar (1981), MacNeal (1982) and Dvorkin & Bathe (1984), the ANS method was used to overcome transverse shear locking. The basis of the concept is that the natural transverse shear strains are calculated in four sampling points located at the center of the element mid-surface edges. Transverse shear strains are then interpolated at the integration points. Another solution to avoid locking problem is the reduced integration concept first introduced in Zienkiewicz et al. (1971). The element integration is then performed with fewer integration points than for a standard solid element. However, this last point is responsible for hourglass occurrence which needs to be stabilized as in Hughes et al. (1978) and Flanagan & Belytschko (1981). Among the most recent contribution, various authors can be cited as Reese (2005), Reese (2007), Alves de Sousa et al. (2005) and Alves de Sousa et al. (2006) who combined reduced integration with EAS , Legay & Combescure (2003), Abed-Meraim & Combescure (2002) and Abed-Meraim & Combescure (2009), who developed the SHB8PS element using only reduced integration, Cardoso et al. (2008), Schwarze & Reese (2009) and Schwarze & Reese (2011) who combined ANS and EAS methods. The SHB8PS element initially developed in explicit in EUROPLEXUS code and now commercialized by SAMTEC Company was used in impact study context. It has then been extended in implicit and introduced in CodeAster. The explicit Abed-Meraim & Combescure (2002) or the implicit Abed-Meraim & Combescure (2009) versions of the SHB8PS element were prone to be efficient and accurate compared to existing equivalent element.

Willing to support the forming industry, some researchers have verified the ability of newly developed solid-shell elements in the forming context. Parente et al. (2006) proposed an EAS based solid-shell element in which the transverse shear locking and the volumetric locking are dealt with by introducing a selected set of enhanced parameters. The implicit version of their element has shown results in good agreement with experimental data in sheet metal forming simulations such as the S-rail forming or the cylindrical cup drawing. Only two integration points have been used in the thickness direction. However, they highlighted the limitations of the adopted $2\times2\times2$ integration scheme while dealing with simulation involving curvature or bending link in springback. In these cases, further

integration points should be used in the thickness direction. Alves de Sousa et al. (2007) successfully tested their reduced enhanced solid-shell (RESS) element combined with a full 3D non-linear constitutive law in sheet metal forming context which induce large elastoplastic strains. The good accuracy of their element was proven using only one element layer in the thickness direction. This last point is possible thanks to the option to increase the number of integration points in the thickness direction of the RESS element. This contrasts with the common technique in sheet metal forming simulation using classical solid elements, which instead, increases the number of element layers. Cardoso et al. (2008) improved the RESS element. This new element, named M-RESS, combines a modified version of the ANS method which increases the transverse shear accuracy with the EAS method using only one enhanced parameter to deal with thickness locking. This new upgrade's benefit has been demonstrated in a deep-drawing simulation. Sena et al. (2011) further extended the application range of the RESS element in the incremental sheet metal forming named single point incremental forming (SPIF). Once again, their proposed element provided results at least comparable with those of the solid elements existing in the commercial code ABAQUS regarding experimental data, but with better time efficiency. They also emphasized the positive influence of enhanced parameter employment on the result accuracy of reduced integration elements. Schwarze & Reese (2011) validated their element accuracy in one sheet metal forming simulation including large deformations and plasticity. They then demonstrated the advantage of using such elements in sheet metal forming context and its ability to simulate springback. Li et al. (2011), Li et al. (2011) have successfully evaluated their explicit reduced integration EAS solid-shell element in several sheet metal forming processes like the S-rail forming or the U-channel forming. Among these simulations characteristics are large deformation, material plasticity and contact management. Their element has the ability to use 3D elastoplastic behavior laws thanks to enhanced parameters which tackled some related locking problems. A good accordance with experimental data has been observed. The implicit version of the SHB8PS reduced integration element has also been successfully tested in the same forming context has demonstrated in Salahouelhadj et al. (2011) and Salahouelhadj et al. (2012) using an elastoplastic modified 3D behavior law. In the same idea, Xu et al. (2012) has also proposed a solid-shell element in which the thickness locking is tackled by using a

modified 3D constitutive law. Their element based on a dynamic explicit as well as implicit algorithm has been tested in sheet metal forming context. For example, the good accuracy of this element has been proven simulating an automobile axle housing forming as well as the subsequent springback. This element results have shown good accordance with experimental data. As a conclusion, solid-shell elements are performing well within the sheet metal forming process involving geometric as well as material non-linearities. Introducing solid-shell elements in THF process simulations could be of great support to the aerospace industry. In the present work, the SH8RSe element has been introduced in the explicit finite element code ABAQUS/Explicit with the ABAQUS/VUEL user subroutine combined with a 3D hyper elastoplastic constitutive law. This chapter is outlined as follows: sections 6.2 and 6.3 remind the geometric and kinematics description of the SH8RSe element. The virtual work principle for a dynamic explicit formulation is then presented in section 6.4. In section 6.5, the stabilization procedure in case of plasticity is given. The constitutive law and its combination with the present element are detailed in sections 6.6 and 6.7. Two numerical examples of typical problems encountered in THF context are then presented in section 6.8.

6.2. SH8RSe geometric description

As already described in Chapter 5, the SH8RSe element is an eight-node solid-shell element illustrated in Figure 5.3. The following coordinate systems are necessary to define the element kinematics: a global cartesian coordinates system $\mathbf{X}(X,Y,Z)$, a local cartesian coordinates system $\mathbf{x}(x,y,z)$ inspired by the work of Batoz & Dhatt (1992) and a natural coordinates system $\boldsymbol{\xi}(\xi^1,\xi^2,\xi^3)$ as defined in Table 5.1.

An arbitrary point q within the element in the local cartesian coordinates system $\mathbf{x}(x,y,z)$ can be linearly interpolated using the classical tri-linear shape functions N_I where the node numbers are $I=1,\ldots,8$.

Considering again the development proposed in section 5.4.1, the arbitrary point q coordinates in the local cartesian coordinates system $\mathbf{x}(x,y,z)$, are:

$$x_i = x_{iI} \times N_I\left(\xi^1,\xi^2,\xi^3\right) = \sum_{I=1}^{8} x_{iI} \times N_I\left(\xi^1,\xi^2,\xi^3\right), \quad \left(i=1,\ldots,3 \text{ and } I=1,\ldots,8\right) \quad (6.1)$$

and its displacements field components (u_1,u_2,u_3) are:

$$u_i = u_{iI} \times N_I\left(\xi^1,\xi^2,\xi^3\right) = \sum_{I=1}^{8} u_{iI} \times N_I\left(\xi^1,\xi^2,\xi^3\right), \quad \left(i=1,\ldots,3 \text{ and } I=1,\ldots,8\right) \quad (6.2)$$

The tri-linear shape functions written in the natural coordinates system $\boldsymbol{\xi}\left(\xi^1,\xi^2,\xi^3\right)$ are :

$$N_I\left(\xi^1,\xi^2,\xi^3\right) = \frac{1}{8} \times \left(1+\xi_I^1 \times \xi^1\right) \times \left(1+\xi_I^2 \times \xi^2\right) \times \left(1+\xi_I^3 \times \xi^3\right) \quad (6.3)$$

with $\xi_I^1,\xi_I^2,\xi_I^3 \in [-1,1]$ and $I=1,\ldots,8$.

6.3. SH8RSe deformation description

The compatible part of the Green-Lagrange strain tensor $\mathbf{E}$ is:

$$\mathbf{E} = \frac{1}{2}\left(\mathbf{F}^T\mathbf{F}-\mathbf{I}\right) = \frac{1}{2}\left\{\left(\nabla_x\mathbf{u}\right)+\left(\nabla_x\mathbf{u}\right)^T+\left(\nabla_x\mathbf{u}\right)^T \times \left(\nabla_x\mathbf{u}\right)\right\} \quad (6.4)$$

in which the deformation gradient tensor $\mathbf{F}$ expression is:

$$\mathbf{F} = \mathbf{I} + \nabla_x\mathbf{u} \quad (6.5)$$

$$\mathbf{I} = \begin{bmatrix} 1 & 0 & 0 \\ 0 & 1 & 0 \\ 0 & 0 & 1 \end{bmatrix} \quad (6.6)$$

and

$$\nabla_x\mathbf{u} = \begin{bmatrix} \frac{\partial u}{\partial x} & \frac{\partial u}{\partial y} & \frac{\partial u}{\partial z} \\ \frac{\partial v}{\partial x} & \frac{\partial v}{\partial y} & \frac{\partial v}{\partial z} \\ \frac{\partial w}{\partial x} & \frac{\partial w}{\partial y} & \frac{\partial w}{\partial z} \end{bmatrix}, \qquad \mathbf{u} = \begin{Bmatrix} u \\ v \\ w \end{Bmatrix} = \begin{Bmatrix} u_1 \\ u_2 \\ u_3 \end{Bmatrix} \quad (6.7)$$

It is possible to transform the Green-Lagrange strain tensor expressed from the natural coordinates system $\boldsymbol{\xi}\left(\xi^1,\xi^2,\xi^3\right)$ to the local cartesian coordinates system $\mathbf{x}\left(x\ ,y\ ,z\ \right)$ by using the transformation matrix $\mathbf{T}$ as in equation (5.26):

$$\begin{Bmatrix} E_{xx} \\ E_{yy} \\ E_{zz} \\ \Gamma_{xy} \\ \Gamma_{yz} \\ \Gamma_{xz} \end{Bmatrix} = \mathbf{T} \times \begin{Bmatrix} E_{11} \\ E_{22} \\ E_{33} \\ \Gamma_{12} \\ \Gamma_{23} \\ \Gamma_{13} \end{Bmatrix} \tag{6.8}$$

where

$$\mathbf{T} = \begin{bmatrix} J_{11}^2 & J_{21}^2 & J_{31}^2 & J_{11}J_{21} & J_{21}J_{31} & J_{11}J_{31} \\ J_{12}^2 & J_{22}^2 & J_{32}^2 & J_{12}J_{22} & J_{22}J_{32} & J_{12}J_{32} \\ J_{13}^2 & J_{23}^2 & J_{33}^2 & J_{13}J_{23} & J_{23}J_{33} & J_{13}J_{33} \\ 2J_{11}J_{12} & 2J_{21}J_{22} & 2J_{31}J_{32} & J_{12}J_{21}+J_{11}J_{22} & J_{22}J_{31}+J_{21}J_{32} & J_{12}J_{31}+J_{11}J_{32} \\ 2J_{12}J_{13} & 2J_{22}J_{23} & 2J_{32}J_{33} & J_{23}J_{12}+J_{22}J_{13} & J_{23}J_{32}+J_{22}J_{33} & J_{13}J_{32}+J_{12}J_{33} \\ 2J_{11}J_{13} & 2J_{21}J_{23} & 2J_{31}J_{33} & J_{23}J_{11}+J_{21}J_{13} & J_{23}J_{31}+J_{21}J_{33} & J_{13}J_{31}+J_{11}J_{33} \end{bmatrix} \tag{6.9}$$

with $j_{ij} = \left(J_{ij}\right)^{-1} = \left(\mathbf{G}_i \times \mathbf{R}_j\right)^{-1}$ the inverse of the components of the matrix $\mathbf{J}$ such that $\mathbf{J} = \mathbf{G}_i \otimes \mathbf{R}_j$.

6.4. Virtual work principle: mixed variational formulation

The variational formulation based on the assumed strain method can be described by the Hu-Washizu three- field variational principle as proposed by Simo & Hughes (1986).The non-linear three fields Hu-Washizu variational principle for dynamic problems takes the form:

$$W\left(\mathbf{u},\mathbf{E},\mathbf{S}\right) = \int_V \mathbf{u}^T \times \rho \times \ddot{\mathbf{u}}\, dV + \int_V \mathbf{E} : \mathbf{S}\, dV + \int_V \bar{\mathbf{S}} : \left[\frac{1}{2}\left(\mathbf{F}^T\mathbf{F} - \mathbf{1}\right) - \mathbf{E}\right] dV - \mathbf{u}^T \times \mathbf{f}_{ext} = 0 \tag{6.10}$$

where the displacements field $\mathbf{u}$, the Green-Lagrange strain tensor $\mathbf{E}$ and the second Piola-Kirchhoff stress tensor $\mathbf{S}$ are three independent variables, $\bar{\mathbf{S}}$ is the assumed stress field, $\mathbf{f}_{ext}$ are the exterior forces, ρ is the density and V is the domain volume.

Introducing in the above equation the contribution of the enhanced parameters yields in a modified Green-Lagrange strain field $\mathbf{E}^{\text{mod}}$ such as:

$$\mathbf{E}^{\text{mod}} = \frac{1}{2}\left(\mathbf{F}^T\mathbf{F} - \mathbf{I}\right) + \mathbf{E}^{\alpha} \tag{6.11}$$

Moreover, it is possible to define a subspace where the assumed stress field $\bar{\mathbf{S}}$ is orthogonal to the enhanced assumed strain field $\mathbf{E}^{\alpha}$ which yields in:

$$\int_V \bar{\mathbf{S}} : \mathbf{E}^{\alpha}\, dV = 0 \tag{6.12}$$

Reducing equation (6.10) into the modified three fields Hu-Washizu variational principle results in:

$$W\left(\mathbf{u}, \mathbf{E}^{\text{mod}}, \mathbf{S}^{\text{mod}}\right) = \int_V \mathbf{u}^T \times \rho \times \ddot{\mathbf{u}}\, dV + \int_V \mathbf{E}^{\text{mod}} : \mathbf{S}^{\text{mod}}\, dV - \mathbf{u}^T \times \mathbf{f}_{ext} = 0 \tag{6.13}$$

The weak form of equation (6.13) is determined by calculating its first variation as:

$$\begin{aligned} \delta W\left(\mathbf{u}, \mathbf{E}^{\text{mod}}, \mathbf{S}^{\text{mod}}\right) &= \int_V \delta\mathbf{u}^T \times \rho \times \ddot{\mathbf{u}}\, dV + \int_V \delta\mathbf{E}^{\text{mod}} : \mathbf{S}^{\text{mod}}\, dV - \delta\mathbf{u}^T \times \mathbf{f}_{ext} \\ &= \int_V \delta\mathbf{u}^T \times \rho \times \ddot{\mathbf{u}}\, dV + \delta W_{\text{int}} + \delta W_{ext} \end{aligned} \tag{6.14}$$

At element level, the finite element approximation of equation (6.14) thus leads after discretization to:

$$\mathbf{M}^e \times \ddot{\mathbf{u}}_i \times \delta\mathbf{u}_i = \mathbf{f}^e_{ext} \times \delta\mathbf{u}_i - \mathbf{f}^e_{\text{int}} \times \delta\mathbf{u}_i \tag{6.15}$$

where $\mathbf{u}_i\left(u_{i1}, u_{i2}, u_{i3}, u_{i4}, u_{i5}, u_{i6}, u_{i7}, u_{i8}\right)$ is the displacements field at each node. The element mass matrix $\mathbf{M}^e$ is chosen diagonal to improve computer efficiency. Indeed, an estimate of the mass matrix $\mathbf{M}^e$, which is a 24×24 matrix, is required while dealing with dynamic

explicit problems. One eight of the element mass is set on the mass matrix diagonal as follows:

$$\mathbf{M}^e = \frac{1}{8} \times M^e \times \begin{bmatrix} \mathbf{I}_{8\times 8} & \mathbf{0} & \mathbf{0} \\ \mathbf{0} & \mathbf{I}_{8\times 8} & \mathbf{0} \\ \mathbf{0} & \mathbf{0} & \mathbf{I}_{8\times 8} \end{bmatrix} \tag{6.16}$$

where $\mathbf{I}_{8\times 8}$ is the 8×8 identity matrix and M^e is the element mass calculated as:

$$M^e = \int_{V^e} \rho^e \, dV^e \tag{6.17}$$

Considering the nodal displacements vector variation $\delta \mathbf{u}_i$, the internal virtual work defines in equation (6.14) is obtained as:

$$\begin{aligned} \delta W_{\text{int}}^e &= \int_{V^e} \delta \mathbf{E}^{\text{mod}} : \mathbf{S}^{\text{mod}} \, dV^e \\ &= \delta \mathbf{u}_i^T \times \mathbf{f}_{\text{int}}^e + \delta \alpha^T \times \mathbf{f}_\alpha^e \end{aligned} \tag{6.18}$$

where the internal forces $\mathbf{f}_{\text{int}}^e$ are:

$$\mathbf{f}_{\text{int}}^e = \int_{-1}^{1}\int_{-1}^{1}\int_{-1}^{1} \left[\mathbf{B}^l + \mathbf{B}^{nl}\left(\mathbf{u}_i\right) \right]^T \times \mathbf{S}^{\text{mod}} \times \left|\mathbf{J}\right| d\xi^1 d\xi^2 d\xi^3 \tag{6.19}$$

with the differential operators $\mathbf{B}^l$, $\mathbf{B}^{nl}\left(\mathbf{u}_i\right)$ calculated as in Chapter 5.

The modified Green-Lagrange strain field $\mathbf{E}^{\text{mod}}$ is further improved to handle the transverse shear locking and the trapezoidal effect using the ANS method, as detailed in Chapter 5, to give the modified Green-Lagrange ANS strain field $\mathbf{E}^{ANS,\text{mod}}$. Then, the modified stress field $\mathbf{S}^{\text{mod}}$ is calculated with the hyperelastoplastic constitutive law developed by Matei (2011) and more detailed in a next section.

The enhanced internal forces $\mathbf{f}_\alpha^e$ are then expressed as:

$$\mathbf{f}_\alpha^e = \int_{-1}^{1}\int_{-1}^{1}\int_{-1}^{1} \left(\mathbf{B}^\alpha\right)^T \times \mathbf{S}^{\text{mod}} \times \left|\mathbf{J}\right| d\xi^1 d\xi^2 d\xi^3 \tag{6.20}$$

with the enhanced differential operators $\mathbf{B}^{\alpha}$ defined similarly as in Simo & Rifai (1990):

$$\mathbf{B}^{\alpha} = \frac{\left|\mathbf{J}_0\right|}{\left|\mathbf{J}_{\xi^3}\right|} \times J_{33}^2 \times \begin{bmatrix} 0 & 0 & 0 \\ 0 & 0 & 0 \\ 0 & 0 & \xi^3 \\ 0 & 0 & 0 \\ 0 & 0 & 0 \\ 0 & 0 & 0 \end{bmatrix} \tag{6.21}$$

In order to consider the SH8RSe element in the THF context, the pressure follower forces need to be added in the external forces evaluation to give:

$$\mathbf{f}_{ext} = \int_S P.\mathbf{n}.\mathbf{u} dS \tag{6.22}$$

where P is the applied pressure intensity and $\mathbf{n}$ is the normal to the surface on which the pressure is applied..

At the element level, equation (6.22) becomes:

$$\mathbf{f}_{ext}^{e} = \int_{-1}^{1}\int_{-1}^{1} P.\mathbf{n}^{e}.\mathbf{u}_i dS^{e} \times \left|\mathbf{J}\right| d\xi^1 d\xi^2 \tag{6.23}$$

6.5. SH8RSe stabilization

6.5.1 Stabilized strain field

The integration points of the present element are aligned in the thickness direction as illustrated in Figure 6.1. Their positions in the natural coordinates system $\boldsymbol{\xi}\left(\xi^1, \xi^2, \xi^3\right)$ are then articulated as follows $\left(0, 0, \xi^3_{n_{ip}}\right)$ where n_{ip} refers to the number of used integration points. This last characteristic has the consequence to set to zero all degree of freedoms involving ξ^1 and ξ^2 directions hence inducing hourglass modes. It is thus possible to identify the terms of the formulation that require stabilization using the displacements field description detailed in Abed-Meraim & Combescure (2009) and recalled in Chapter 5.

The related gradient operator then appears as a summation of an unstabilized as well as stabilized term. The compatible part of the Green-Lagrange strain tensor $\mathbf{E}$ can take the form of:

$$\mathbf{E}(\mathbf{u}) = (\mathbf{B}_{12} + \mathbf{B}_{34}) \times \mathbf{u} \tag{6.24}$$

where the gradient operators $\mathbf{B}_{12}$ and $\mathbf{B}_{34}$ describe respectively the unstabilized and the stabilized parts of the gradient operator matrix $\mathbf{B}$.

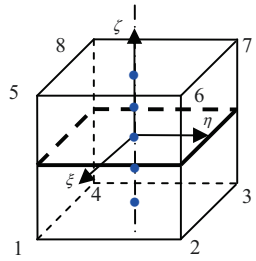

Figure 6.1: Integration through the thickness alignment

Moreover as indicated in Chapter 5 and in the spirit of Belytschko & Bindeman (1993) work, the modified stabilized gradient operator $\hat{\mathbf{B}}_{34}$ based on averaged terms was introduced instead of the standard stabilized gradient operator $\mathbf{B}_{34}$, in order to improve convergence properties of the formulation. This modified stabilized gradient operator $\hat{\mathbf{B}}_{34}$ is calculated using the Hallquist parameters to give:

$$\hat{\mathbf{B}} = \mathbf{B}_{12} + \hat{\mathbf{B}}_{34} \tag{6.25}$$

Moreover, a simplified modified stabilized gradient operator $\breve{\hat{\mathbf{B}}}_{34}$ can be obtained by projecting the terms related to the stabilization in a local orthogonal co-rotational coordinates system that takes advantage of the orthogonality properties of the hourglass modes.

The equation (6.25) then becomes:

$$\breve{\hat{\mathbf{B}}} = \mathbf{B}_{12} + \breve{\hat{\mathbf{B}}}_{34} \tag{6.26}$$

6.5.2 Stabilized internal forces

The constitutive law $\mathbf{H}'$ used to calculate the stabilization terms is a modified 3D law. This law tends to avoid thickness locking in the stabilized terms by decoupling the in-plane and the out-of-plane stress components. As described in equation (5.176), it takes the form:

$$\mathbf{H}' = \begin{bmatrix} \bar{\lambda}+2\mu & \bar{\lambda} & 0 & 0 & 0 & 0 \\ \bar{\lambda} & \bar{\lambda}+2\mu & 0 & 0 & 0 & 0 \\ 0 & 0 & E & 0 & 0 & 0 \\ 0 & 0 & 0 & \mu & 0 & 0 \\ 0 & 0 & 0 & 0 & \mu & 0 \\ 0 & 0 & 0 & 0 & 0 & \mu \end{bmatrix} \tag{6.27}$$

where the Lamé's coefficients are $\bar{\lambda} = \dfrac{E.\nu}{\left(1-\nu^2\right)}$ and $\mu = \dfrac{E}{2.\left(1+\nu\right)}$ with E the Young's modulus and ν the Poisson's ratio.

If some plastification occurs, the Young's modulus is replaced by a tangent modulus $E_{\tan g}$ as in F. Abed-Meraim & Combescure (2002) which takes the form:

$$E_{\tan g} = E \times \sqrt{\left(\frac{\bar{h}}{E+\bar{h}} \right)} \tag{6.28}$$

where the mean hardening modulus $\bar{h}$ for five integration points is given by:

$$\bar{h} = \frac{1}{5} \times \sum_{ip=1}^{5} \left(\frac{\partial \mathbf{S}_H}{\partial \mathbf{E}_{plas}} \right)_{ip} \tag{6.29}$$

and

$$\sqrt{\left(\frac{\overline{h}}{E+\overline{h}}\right)} \leq \frac{1}{1000} \tag{6.30}$$

$\mathbf{E}_{plas}$ is the plastic strain and $\mathbf{S}_H$ is the material hardening at each integration point has explicitly shown in section 6.6. This method appears to be a simple as well as an efficient method to consider plasticity in the stabilized part of the internal forces $\left(\mathbf{f}_{stab}\right)_{\text{int}}$ determination. Moreover, using a mean hardening modulus $\overline{h}$ smoothes the actual material state over the thickness direction. This avoids having to many changes between integration points, especially in cases where plastification occurs in some points and not in others.

As a consequence of equation (6.26), the internal forces can be decomposed into a standard $\mathbf{f}_{12}$ and a stabilized $\breve{\hat{\mathbf{f}}}_{stab}$ parts as:

$$\begin{aligned} \mathbf{f}_{\text{int}}^{e} &= \int_{V^e} \left(\mathbf{B}_{12}\right)^T . \mathbf{S}_{12} dV^e + \int_{V^e} \left(\breve{\hat{\mathbf{B}}}_{34}\right)^T . \breve{\hat{\mathbf{S}}}_{34} dV^e \\ &= \mathbf{f}_{12} + \breve{\hat{\mathbf{f}}}_{stab} \end{aligned} \tag{6.31}$$

The stabilized part of internal forces $\breve{\hat{\mathbf{f}}}_{stab}$ are calculated out of the integration points loop in the same idea as in Abed-Meraim & Combescure (2002). The stabilization strain tensor $\breve{\hat{\mathbf{E}}}_{34}$ induced by the modified stabilized gradient operator $\breve{\hat{\mathbf{B}}}_{34}$ is calculated first:

$$\breve{\hat{\mathbf{E}}}_{34} = \breve{\hat{\mathbf{B}}}_{34} \times \mathbf{u}_i, \quad i = 1,2,3 \tag{6.32}$$

Then, the related stabilization stress tensor $\breve{\hat{\mathbf{S}}}_{34}$ is determined as:

$$\breve{\hat{\mathbf{S}}}_{34} = \mathbf{H}' \times \breve{\hat{\mathbf{E}}}_{34} \tag{6.33}$$

6.6. Hyperelastoplastic behavior law and damage strategy description

In the forming process simulation, it is necessary to have robust constitutive laws in order to have accurate results. Many constitutive laws considering plasticity have then been developed since the middle of last century. Recently, various contributions like Alves de Sousa et al. (2007), Li et al. (2011) and Salahouelhadj et al. (2012) combined the latest solid-shell finite elements developments with accurate elastoplastic constitutive laws to simulate sheet metal forming. However, phenomena involved in sheet metal forming and described by constitutive laws such as material flow, stresses and strains fields are different than those encountered in THF process. The new 3D hyperelastoplastic constitutive law developed by Matei (2011) and based on the work of Simo & Hughes (1998) appears to consider many of the THF particularities and has been proven to provide very accurate results in this context. A brief description of this law is proposed in Appendix D. Combining this last full 3D behavior law with the SH8RSe element would help the hydroforming industry to take advantage of the newest developments in finite element analysis.

6.7. Implementation in ABAQUS/explicit: ABAQUS/VUEL module and ABAQUS/VUMAT module like subroutine combination for stress update

ABAQUS/VUMAT utility routine allows using various type of constitutive law. In Salahouelhadj et al. (2012), they used an ABAQUS/UMAT type routine to implement a hypoelastoplastic constitutive law with non-linear Voce and Swift models and a linear isotropic hardening. In this work, the SH8RSe element described above is combined with a hyperelastoplastic user material subroutine like the program developed by Matei (2011). The element is implemented in ABAQUS/VUEL subroutine, which is an ABAQUS subroutine dedicated to element development using an explicit integration algorithm. As a consequence, it is possible to take advantage of the ABAQUS non-linear contact algorithm modules very useful in forming simulations context.

6.7.1 Polar decomposition

The deformation gradient tensor $\mathbf{F}$ defined in equation (6.5) is not a good measurement of the strain field, since it includes some rigid body rotations. The polar decomposition of the deformation gradient tensor $\mathbf{F}$ is then a solution to separate pure rotations from pure strains. This then allows defining other strain measurements like the right Cauchy Green strain tensor $\mathbf{C}$ discussed above which keeps out any rotations.

Theorem

The non singular deformation gradient tensor $\mathbf{F}$ can take the form of a product between a rotation tensor $\mathbf{R}$ and a right or left stretch tensor namely $\mathbf{U}$ or left $\mathbf{V}$ as in:

$$\mathbf{F} = \mathbf{R} \times \mathbf{U} = \mathbf{V} \times \mathbf{R} \tag{6.34}$$

where the rotation tensor $\mathbf{R}$ is defined orthogonal and the stretch tensors $\mathbf{U}$ and $\mathbf{V}$ describe the deformation level and are defined as symmetric and positive.

This property takes all its interest to keep the Green Lagrange strain tensor $\mathbf{E}$ independent of the observer (objectivity property of the Green Lagrange strain tensor $\mathbf{E}$), since it remains possible to project it in a co-rotational coordinate system which follows the system deformation.

Polar decomposition description

Let us define the parameters $\left(\lambda_{(1)}, \lambda_{(2)}, \lambda_{(3)}\right)$, the stretch tensor $\mathbf{U}$ eigenvalues which correspond to the extension in principal directions in relation with the deformation and $\left(\mathbf{N}_{(1)}, \mathbf{N}_{(2)}, \mathbf{N}_{(3)}\right)$ the corresponding eigenvectors.

The right Cauchy Green strain tensor $\mathbf{C}$ then takes the following form:

$$\begin{aligned}\mathbf{C} &= \mathbf{F}^T \times \mathbf{F} \\ &= \mathbf{U}^2 \\ &= \mathbf{P}^T \times \begin{bmatrix} \lambda_{(1)}^2 & 0 & 0 \\ 0 & \lambda_{(2)}^2 & 0 \\ 0 & 0 & \lambda_{(3)}^2 \end{bmatrix} \times \mathbf{P} \\ &= \sum_{i=1}^{3} \lambda_{(i)}^2 \times \mathbf{N}_{(i)} \otimes \mathbf{N}_{(i)}\end{aligned} \tag{6.35}$$

where $\mathbf{P}$ is the orthogonal eigenvector matrix defined as:

$$\mathbf{P} = \begin{bmatrix} \mathbf{N}_{(1)} & \mathbf{N}_{(2)} & \mathbf{N}_{(3)} \end{bmatrix} \tag{6.36}$$

and $\left(\lambda_{(1)}^2, \lambda_{(2)}^2, \lambda_{(3)}^2\right)$ are the right Cauchy Green strain tensor eigenvalues calculated solving the polynomial equation:

$$\begin{aligned}\det(\mathbf{C} - \lambda^2 \times \mathbf{I}) &= \mathbf{0} \\ &= \left(\lambda^2\right)^3 - \mathbf{I}_1 \times \left(\lambda^2\right)^2 + \mathbf{I}_2 \times \left(\lambda^2\right) - \mathbf{I}_3\end{aligned} \tag{6.37}$$

In the previous equation (6.37), $\left(\mathbf{I}_1, \mathbf{I}_2, \mathbf{I}_3\right)$ are right Cauchy Green strain tensor invariants defined as:

$$\mathbf{I}_1 = trace\left(\mathbf{C}\right) \tag{6.38}$$

$$\mathbf{I}_2 = \frac{1}{2} \times \left[\mathbf{I}_1^2 - trace\left(\mathbf{C}\right)\right] \tag{6.39}$$

$$\mathbf{I}_3 = \det\left(\mathbf{C}\right) \tag{6.40}$$

and $\mathbf{I}$ is the 3×3 identity matrix:

$$\mathbf{I} = \begin{bmatrix} 1 & 0 & 0 \\ 0 & 1 & 0 \\ 0 & 0 & 1 \end{bmatrix} \tag{6.41}$$

The right Cauchy Green strain tensor eigenvectors $\left(\mathbf{N}_{(1)}, \mathbf{N}_{(2)}, \mathbf{N}_{(3)}\right)$ are determined by solving the following equation:

$$\left(\mathbf{C} - \left(\lambda^2\right) \times \mathbf{I}\right) \times \mathbf{N}_{(i)} \tag{6.42}$$

Using equation (6.35), the stretch tensor $\mathbf{U}$ is:

$$\mathbf{U} = \mathbf{P}^T \times \begin{bmatrix} \lambda_{(1)} & 0 & 0 \\ 0 & \lambda_{(2)} & 0 \\ 0 & 0 & \lambda_{(3)} \end{bmatrix} \times \mathbf{P} \tag{6.43}$$

and the rotation tensor $\mathbf{R}$ is then calculated with equation (6.34).

Modified stretch tensor calculation

One of the scopes of the hyperelastoplastic constitutive law presented in Matei (2011) is its development in a spatial frame free of rigid body rotations. In order to combine in ABAQUS/VUEL user subroutine the hyperelastoplastic constitutive law from Matei (2011), a polar decomposition is used to articulate the SH8RSe transformation gradient tensor $\mathbf{F}^{ANS,\text{mod}}$ into the product of a rotation tensor $\mathbf{R}$ with a stretch tensor $\mathbf{U}^{ANS,\text{mod}}$ as:

$$\mathbf{F}^{ANS,\text{mod}} = \mathbf{R} \times \mathbf{U}^{ANS,\text{mod}} \tag{6.44}$$

Starting from the element formulation described in section 6.4, it remains necessary to determine the quantities used in equation (6.44) in order to achieve the combination. Following the methodology presented in Hauptmann et al. (2000), the rotation tensor $\mathbf{R}$ is first determined using the unmodified transformation gradient tensor $\mathbf{F}$ of the element:

$$\mathbf{F} = \mathbf{R} \times \mathbf{U} \Rightarrow \mathbf{R} = \mathbf{F} \times \mathbf{U}^{-1} \tag{6.45}$$

Besides, using equation (6.45), the compatible part of the Green-Lagrange strain tensor $\mathbf{E}$ can yield in an equation depending only on the stretch tensor $\mathbf{U}$ as:

$$\begin{aligned}\mathbf{E} &= \frac{1}{2}\times\left[\mathbf{F}^T\times\mathbf{F}-\mathbf{I}\right]\\ &= \frac{1}{2}\times\left[\left(\mathbf{R}\times\mathbf{U}\right)^T\times\mathbf{R}\times\mathbf{U}-\mathbf{I}\right]=\frac{1}{2}\times\left[\mathbf{U}^T\times\mathbf{R}^T\times\mathbf{R}\times\mathbf{U}-\mathbf{I}\right]\\ &= \frac{1}{2}\times\left[\mathbf{U}^T\times\mathbf{U}-\mathbf{I}\right]=\frac{1}{2}\times\left[\mathbf{U}^2-\mathbf{I}\right]\end{aligned} \tag{6.46}$$

Similarly, considering a Green Lagrange strain field $\mathbf{E}^{ANS,\mathrm{mod}}$ which includes the ANS and the EAS improvements in gives:

$$\begin{aligned}&\mathbf{E}^{ANS,\mathrm{mod}} = \frac{1}{2}\times\left[\left(\mathbf{U}^{ANS,\mathrm{mod}}\right)^2-\mathbf{I}\right]\\ &\Rightarrow \mathbf{U}^{ANS,\mathrm{mod}} = \sqrt{2\times\mathbf{E}^{ANS,\mathrm{mod}}+\mathbf{I}}\end{aligned} \tag{6.47}$$

where the following condition is verified:

$$\left|2\times\mathbf{E}^{ANS,\mathrm{mod}}\right|\langle\mathbf{I} \tag{6.48}$$

The square function of equation (6.47) can then be developed using a Taylor series to give:

$$\begin{aligned}\mathbf{U}^{ANS,\mathrm{mod}} &\approx \mathbf{I}+\frac{1}{2}\times\left(2\times\mathbf{E}^{ANS,\mathrm{mod}}\right)-\frac{1}{8}\times\left(2\times\mathbf{E}^{ANS,\mathrm{mod}}\right)^2+\cdots\\ &\cdots+\frac{1}{16}\times\left(2\times\mathbf{E}^{ANS,\mathrm{mod}}\right)^3-\frac{5}{128}\times\left(2\times\mathbf{E}^{ANS,\mathrm{mod}}\right)^4\\ &\approx \mathbf{I}+\mathbf{E}^{ANS,\mathrm{mod}}-\frac{1}{2}\times\left(\mathbf{E}^{ANS,\mathrm{mod}}\right)^2+\frac{1}{2}\times\left(\mathbf{E}^{ANS,\mathrm{mod}}\right)^3-\frac{5}{8}\times\left(\mathbf{E}^{ANS,\mathrm{mod}}\right)^4\end{aligned} \tag{6.49}$$

A non negligible drawback of this method is the increased computational time due to the two polar decompositions. However, this method is easy to implement and allows an accurate evaluation of the present element kinematics that is to be fed to the material constitutive law integration module.

6.7.2 Description of SH8RSe element and hyperelastoplastic constitutive law combination description

Considering two consecutive configurations n and $n+1$, respectively at time increment t and $t+1$, the SH8RSe element then needs to supply to the constitutive law the following kinematics parameters: i) $\left(\mathbf{F}^{ANS,\text{mod}}\right)_t$ and $\left(\mathbf{F}^{ANS,\text{mod}}\right)_{t+1}$ the modified deformation gradient tensors at time step t respectively at time step $t+1$; ii) $\left(\mathbf{U}^{ANS,\text{mod}}\right)_t$ and $\left(\mathbf{U}^{ANS,\text{mod}}\right)_{t+1}$ the modified stretch tensors at time step t respectively at time step $t+1$ calculated via a polar decomposition of the deformation gradient as illustrated in equation (6.44). The ABAQUS/VUMAT module like subroutine then updates the modified second Piola-Kirchhoff stress tensor $\left(\mathbf{S}^{ANS,\text{mod}}\right)_{t+1}$ and returns this result to the element. The algorithm used for coupling the element with a hyperelastoplastic constitutive law is illustrated in Figure 6.2, Figure 6.3 and Figure 6.4.

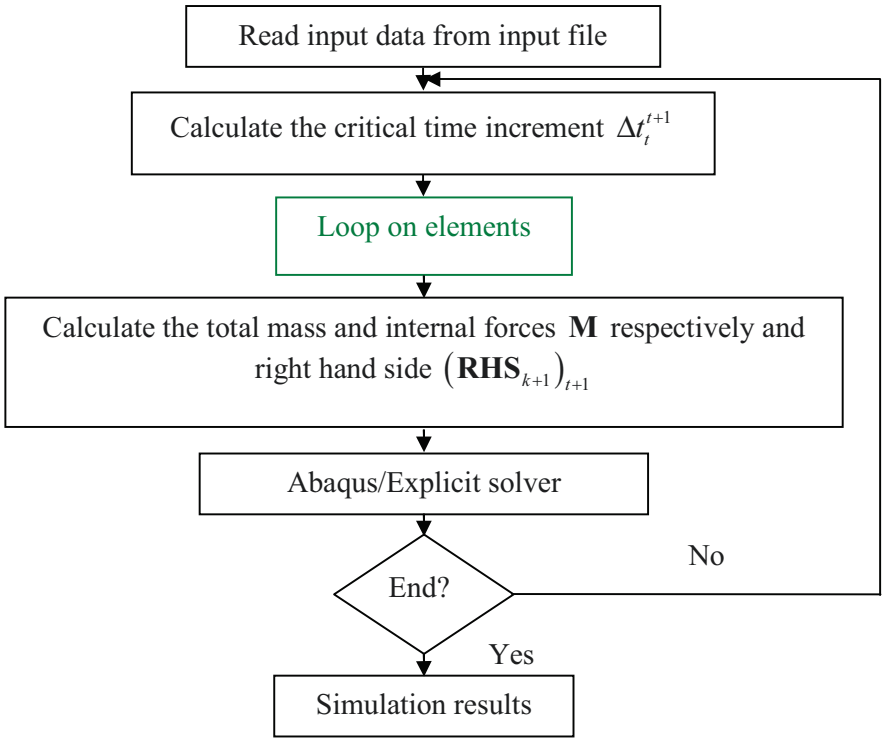

Figure 6.2: SH8RSe explicit element combined with a hyperelastoplastic constitutive law, general algorithm

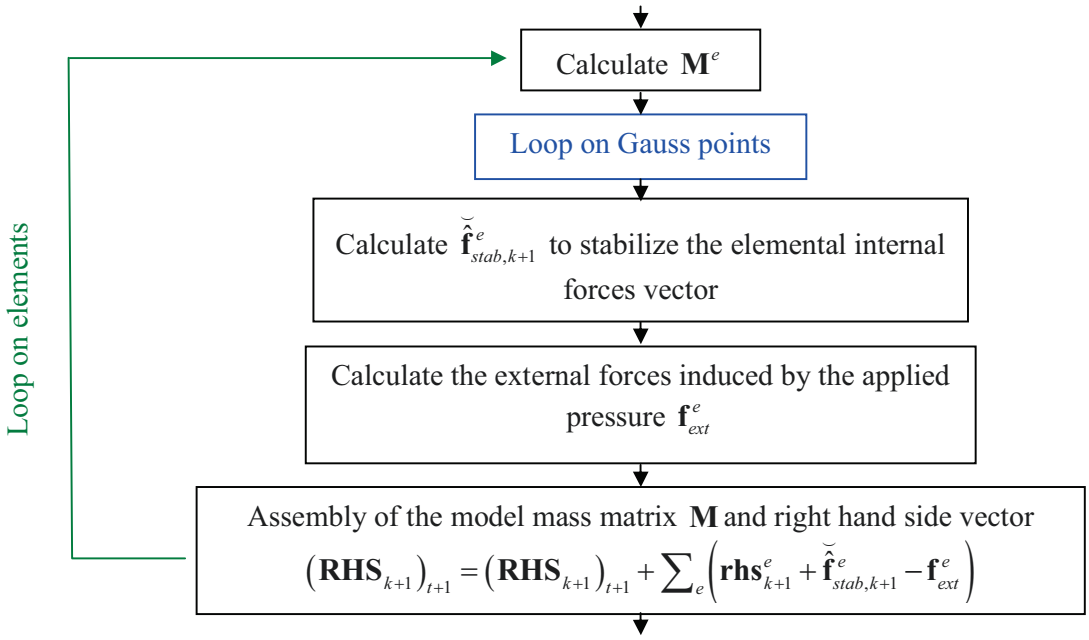

Figure 6.3: SH8RSe explicit element combined with a hyperelastoplastic constitutive law, loop on elements

The enhanced parameter is eliminated using a modified local static condensation similarly to the work detailed in Simo et al. (1993). The modified enhanced variable $\Delta\alpha_2$ is then:

$$\Delta\alpha_2 = -\frac{1}{k^e_{\alpha\alpha}} \times f^e_\alpha \tag{6.50}$$

where $\mathbf{f}^e_\alpha$ are the enhanced forces defined in equation (5.130).

The algorithm of this iterative method is further detailed in Figure 6.4.

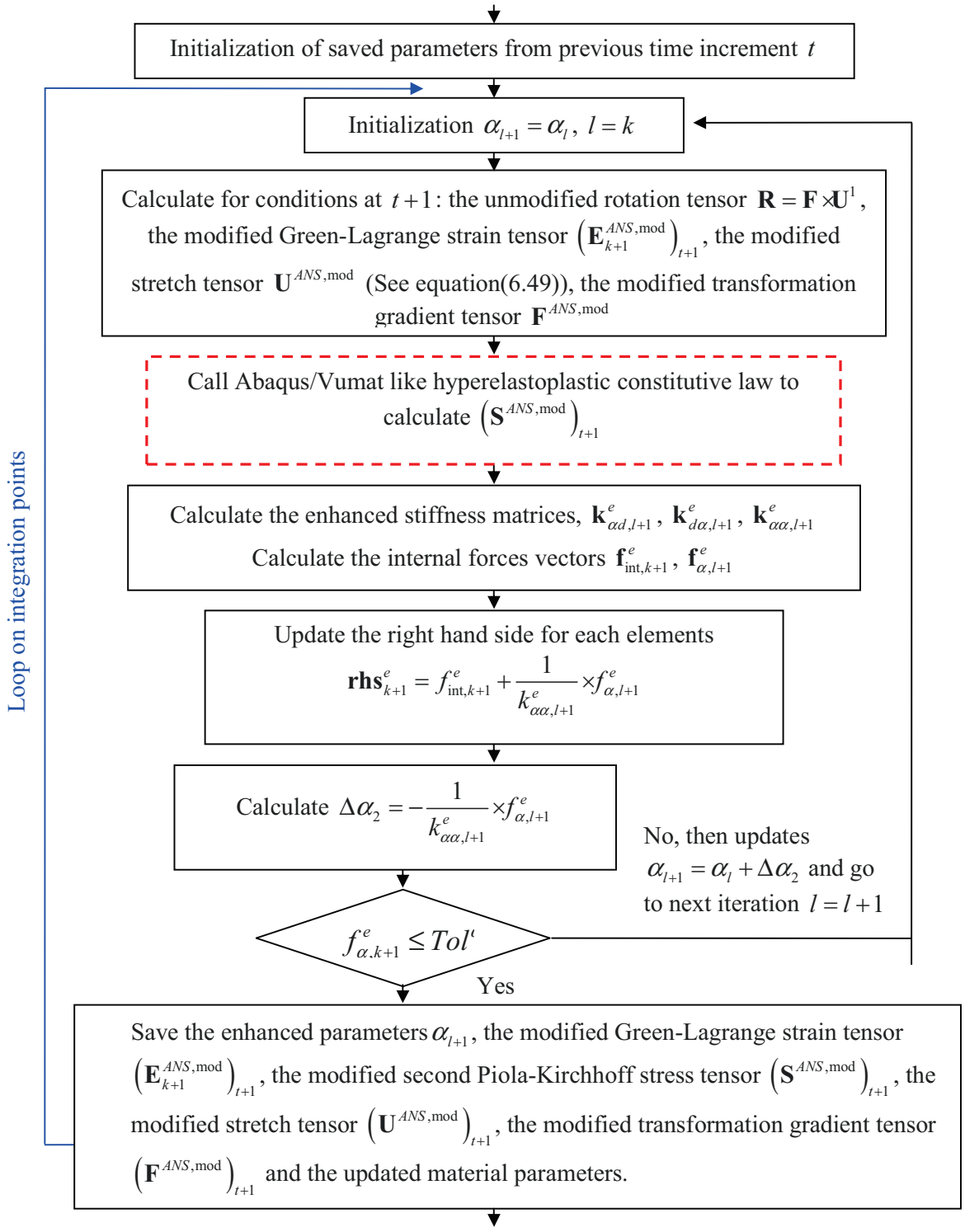

Figure 6.4: SH8RSe explicit element combined with a hyperelastoplastic constitutive law, loop on integration points

6.8. Numerical examples

The explicit formulation of the SH8RSe element implemented in ABAQUS/Explicit combined with the ABAQUS/VUEL module is evaluated in this section in different situations. The present element coupled with a hyperelastoplastic constitutive law is tested in typical forming conditions encountered in THF process, including geometric as well as material non-linearities and contact. The obtained results with only one layer of SH8RSe in the thickness direction are compared with those obtained using three layers of C3D8R or C3D8I ABAQUS/Explicit elements. The use of these elements with several layers in industrial applications usually helps to observe an acceptable through the thickness deformation when compared to experiments. In some cases, some experimental data are also taken as a reference.

The tested elements in the present work are named as follows:

SH8RSe – eight-node solid-shell element with reduced integration using 3D constitutive law. Five integrations points are used in the thickness direction.

C3D8R – eight-node solid element with reduced integration using three 3D law. One integration point is used in the thickness direction. Abaqus user's manual, ver 6.8, (2007).

C3D8I – eight-node solid element with incompatible modes using 3D constitutive law. This element has eight integrations points and two integration points are used in the thickness direction. Abaqus user's manual, ver 6.8, (2007).

6.8.1 Bending problem

In order to facilitate the positioning of the tube between THF dies, it is sometimes necessary to use a preforming operation before the hydroforming process. Tube bending is one of the most popular preforming processes in the THF industry. However, tube bending has some effects on the tube geometry such as wrinkling in compressed areas and thinning in stretched areas as discussed in Li et al. (2007). The present bending problem is then used to check the ability of the present SH8RSe element to deal with these previously mentioned effects. The bending type used in this contribution is a translational bending process as

already discussed in Élie-Dit-Cosaque et al. (2009a). In the model description illustrated in Figure 6.5, an initial straight tube is positioned between two wing dies and a ram die. Then the ram die translates in the forward direction with a magnitude $u = 105.41\,mm$ to force the tube against the two wing dies. The two wing dies then rotate around their axes keeping contact with the tube through an applied force $F = 100\,N$. The tube has an external diameter $\theta = 76.2$ mm, a thickness $t = 3.175$ mm and a length $L = 1\,m$ as illustrated in Figure 6.6a. The employed material is the same aluminum alloy AA6061-O used in Matei (2011) with a density $\rho = 2680\ Kg/m^3$, a Young's modulus $E = 68300\ Mpa$, a Poisson's ratio $\nu = 0.3$ and a yield stress σ_y=35.1848 Mpa. This material is assumed to follow a hyperelastoplastic constitutive law from Simo & Hughes (1998). The wing dies which use the elastic properties of the stainless steel alloy SS321, with a density $\rho = 8027\ Kg/m^3$, a Young's modulus $E = 184.5\ GPa$ and a Poisson's ratio $\nu = 0.3$ are meshed with ABAQUS C3D8R elements. The ram die is supposed to be rigid and is meshed with four-node R3D4 elements as shown in Figure 6.6b. The tangential friction coefficient is 0.2.

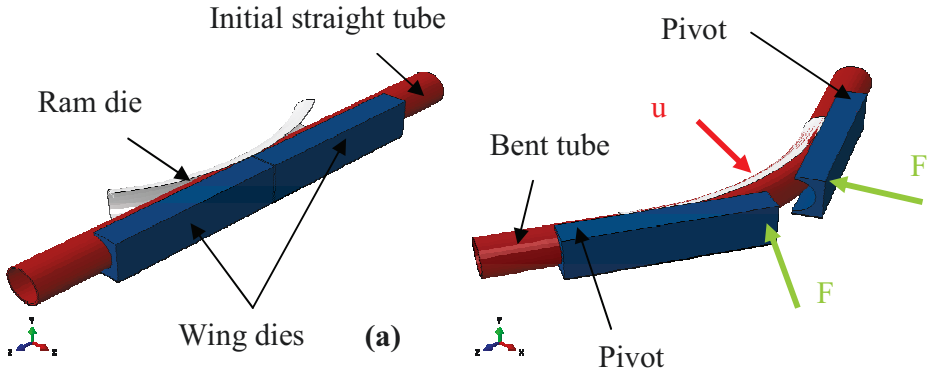

Figure 6.5: Tube bending model description

In this problem, five integration points are used with the present SH8RSe element. Figure 6.7 shows the deformed geometry of the tube after bending using one layer of the proposed element. According to the convergence study of a similar problem presented in Table 3.3, three elements layers in the thickness direction remain sufficient to provide a good accuracy. In the present models using C3D8R and C3D8I elements, three element layers are also used in the thickness direction.

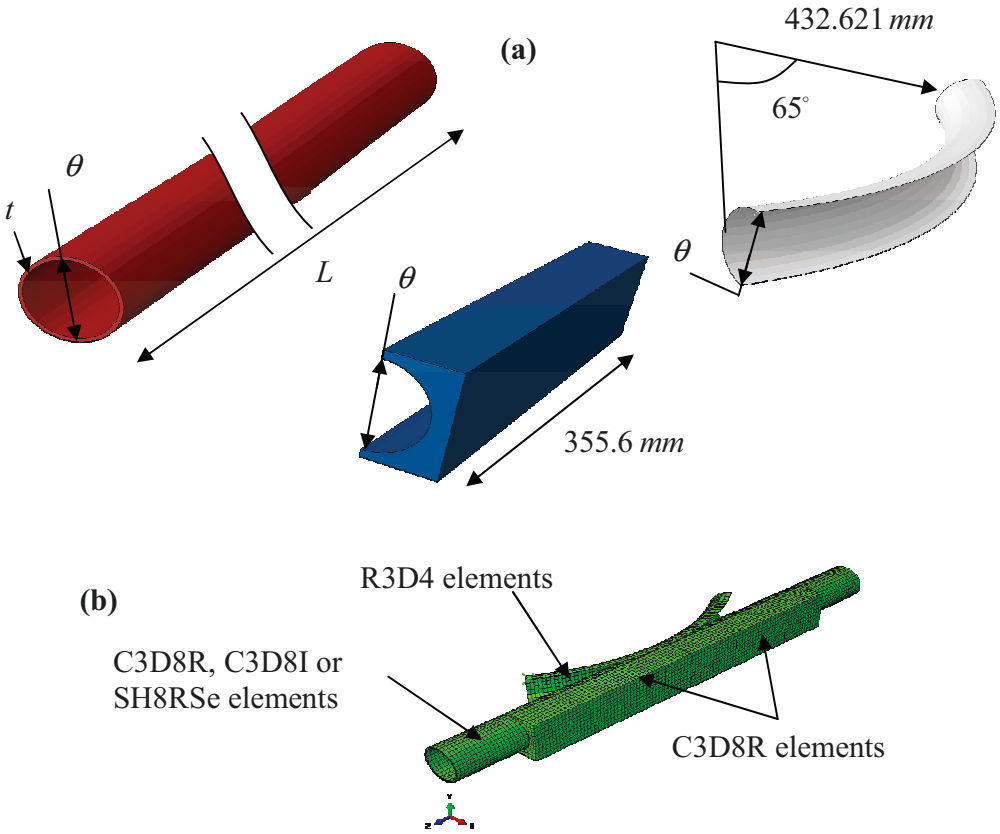

Figure 6.6: Tube bending model geometry (a) and mesh (b)

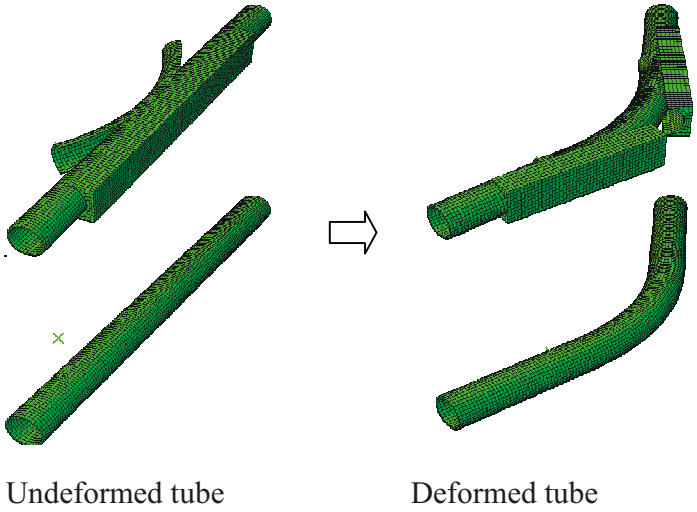

Figure 6.7: Tube bending result, deformed geometry

The thickness distribution along the tube after bending is presented in Figure 6.8.

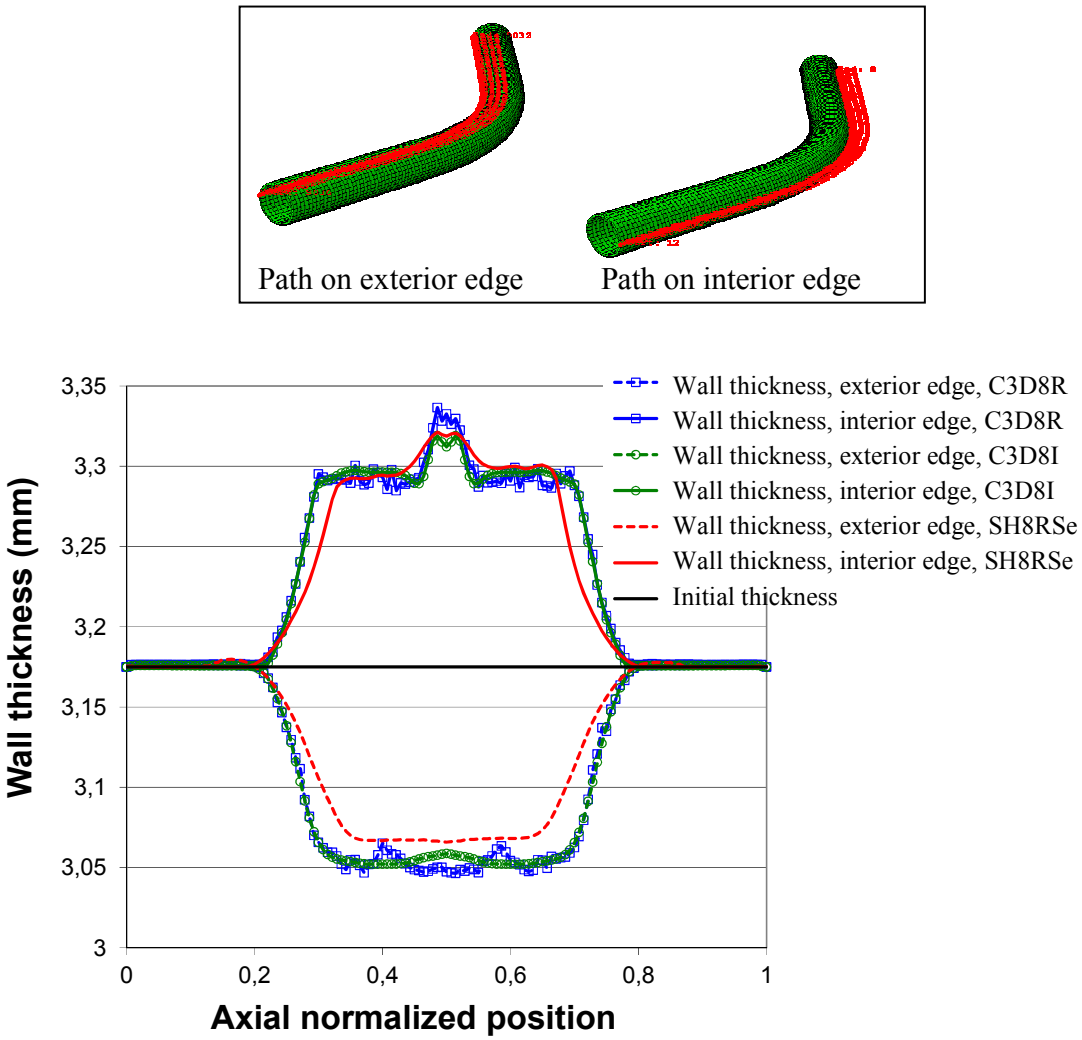

Figure 6.8: Tube bending result, thickness variation along path

The classical thickening at the interior edge as well as the classical thinning at the exterior edge can be observed for all results. As presented in Table 6.1, the present element with one layer through the thickness gives results similar to those obtained with the C3D8R or the C3D8I elements with three elements in the thickness direction, with a difference of 0.3%. However, if the present element is able to capture the thickness distribution trends, however along edges it seems to be stiffer than the other tested elements. A possible reason

to this could be the choice of the maximum limit of the coefficient $\sqrt{\left(\frac{\bar{\bar{h}}}{E+\bar{\bar{h}}}\right)}$ introduced in equation (6.30) which has been set to $\frac{7}{10}$ instead of $\frac{1}{1000}$ in order to avoid oscillation while measuring the thickness of the tube.

(mm)	3 C3D8R element	3 C3D8I elements	1 SH8RSe element
Thickness max	3.337	3.319	3.321
Thickness min	3.046	3.052	3.066

Table 6.1: Tube bending result, thickness extremum values

6.8.2 Conical shape THF problem

The THF process is a forming process which results into the combination of two main parameters namely axial feeding and internal pressure. An inappropriate combination of these parameters could generate a loading path out of the admissible process window and could possibly cause defects such as wrinkling, buckling, bursting and necking. Jansson et al. (2007a) studied various procedures to estimate acceptable hydroforming parameters to form defect free tube in a conical shape. The objective of this section is to evaluate the performance of the present SH8RSe element explicit formulation in a typical conical shape THF process simulation while including axial end feeding, high pressure increase, contact management and plasticity. The tube has a mean diameter of $47.625\,mm$, a thickness of $3.175\,mm$ and a length of $266.7\,mm$. The geometry is illustrated in Figure 6.9.

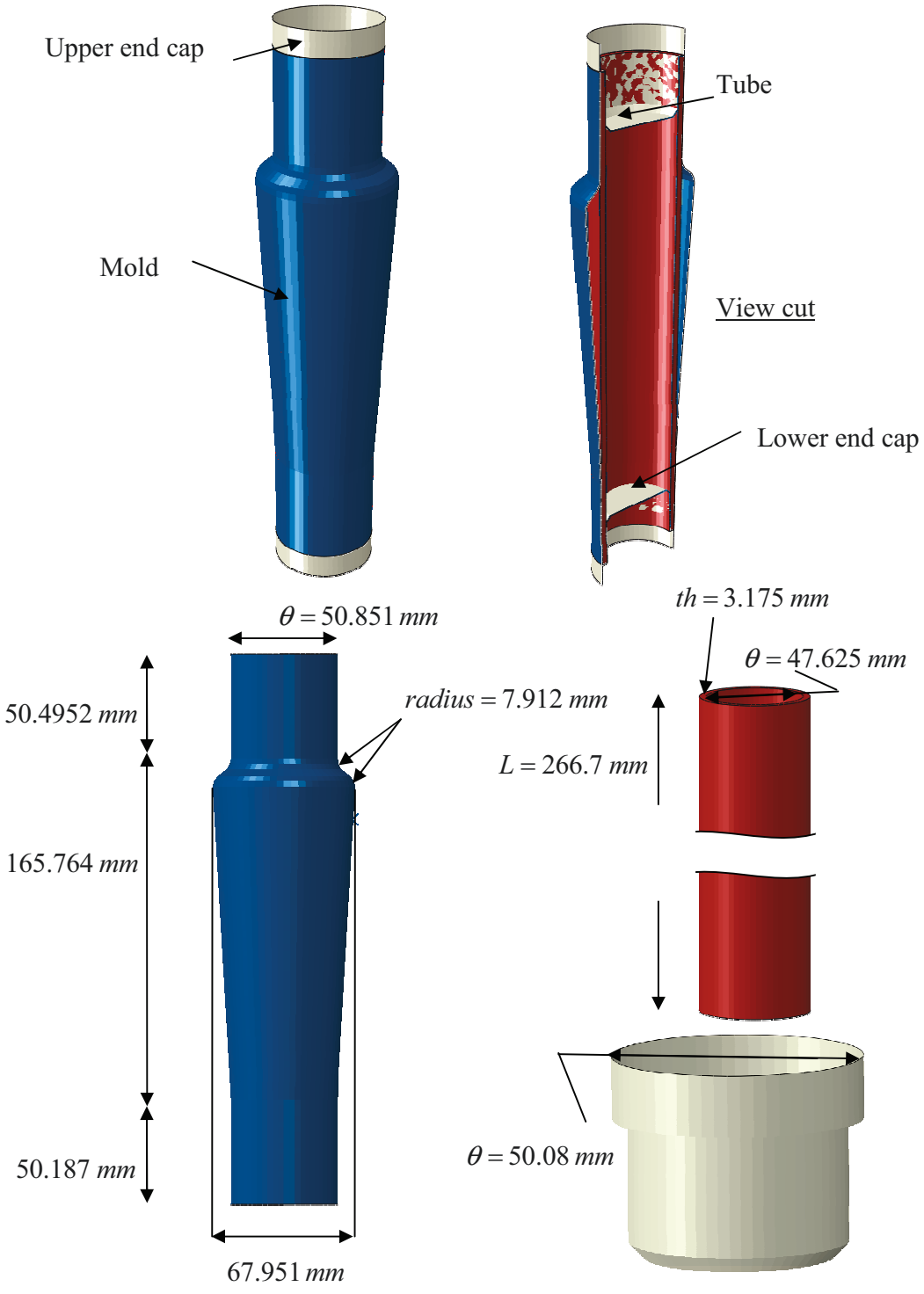

Figure 6.9: Conical shape THF model geometry

The lower tube extremity moves up following the lower end cap displacement with a maximum value of $u = 23\,mm$ and in the same time, the upper tube extremity moves down following the upper end cap displacement with a maximum value of $u = 3.48\,mm$. An internal pressure is applied with a maximum value of $P = 36.2\,Mpa$. The end caps displacements, as well as the applied pressure increase, follow the amplitude illustrated in Figure 6.10. After forming, the pressure inside the tube is then decreased and the end caps removed allowing the springback process to take place.

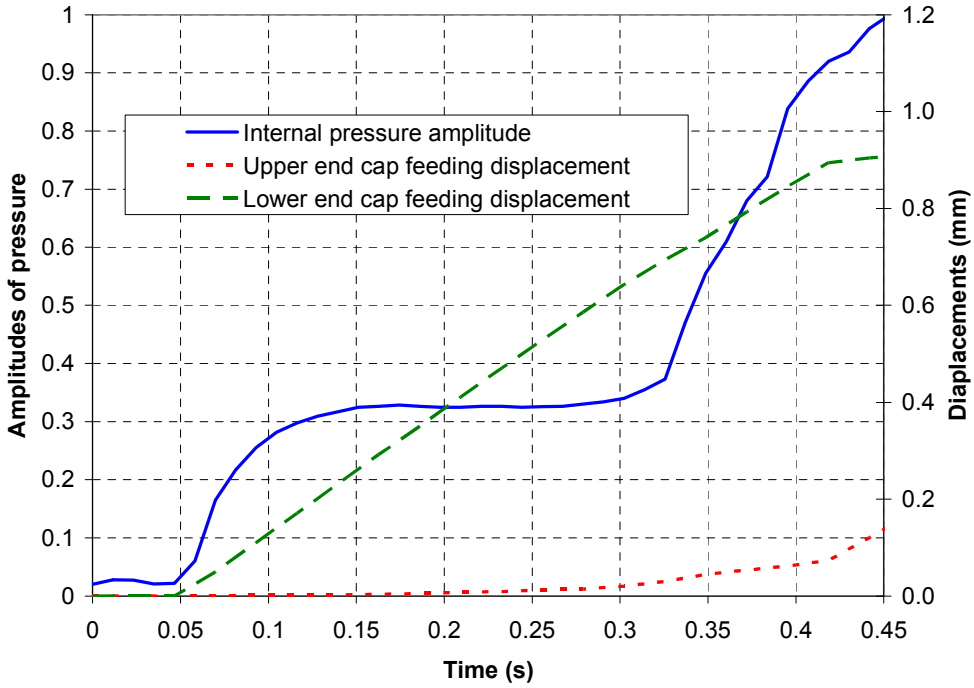

Figure 6.10: Conical shape THF loading path

The tangential friction coefficient is considered constant in the tube dies and equal to 0.04 (The use of a dry lubricant is assumed). The tube mesh has 72 circumferential elements and 127 longitudinal elements as shown in Figure 6.11.

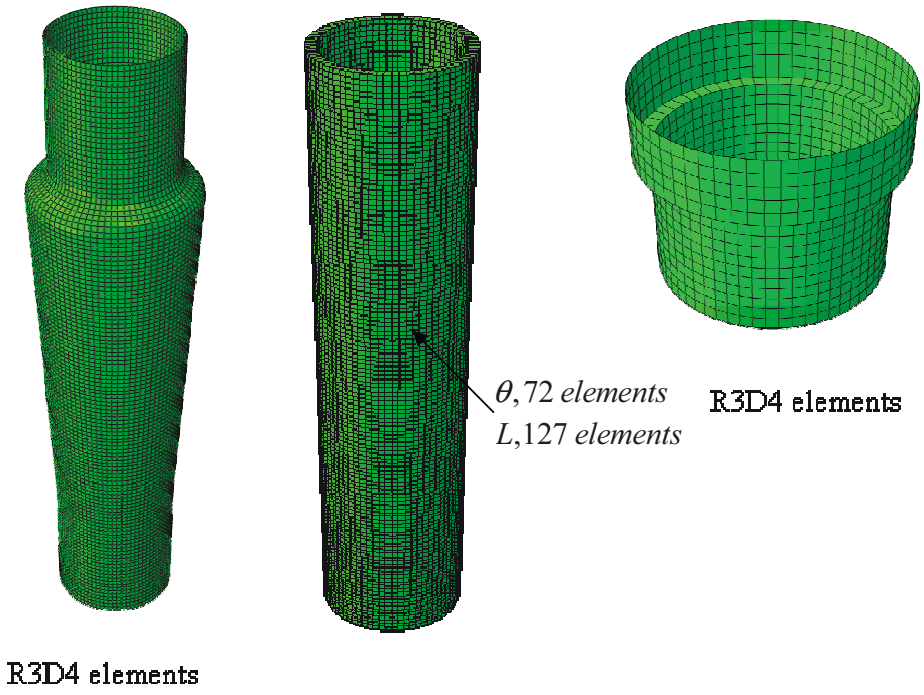

Figure 6.11: Conical shape THF model mesh

Figure 6.12 presents the thickness variation along the hydroformed part using models meshed with one, two and three C3D8R elements layers in the thickness direction. Three elements layers then appear to provide acceptable accuracy. For this reason, the run models with the C3D8R and the C3D8I elements use three elements layers in the thickness direction. However, only one layer of elements is used for the model run with the present element. The mold and the end caps are considered rigid and meshed with ABAQUS R3D4 rigid elements.

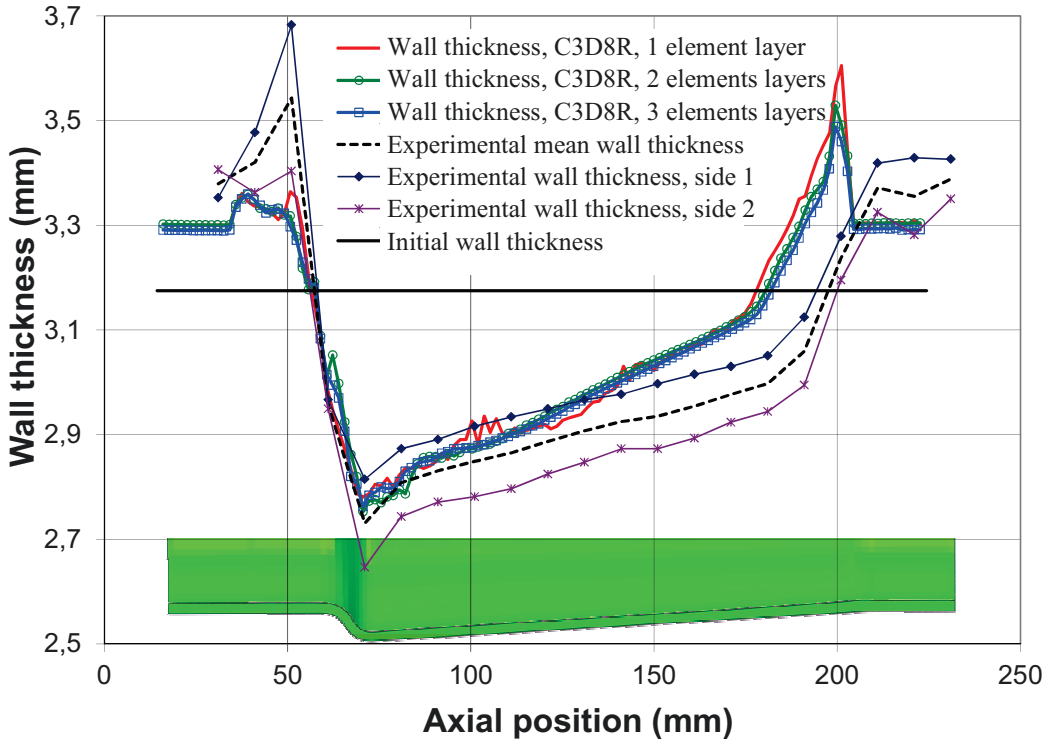

Figure 6.12: Conical shape THF, convergence study

The tube is made of aluminum alloy AA6061-O and a hyperelastoplastic non-linear Voce hardening model is used in the simulations. Used material properties are: density $\rho = 2680\ Kg/m^3$, Young's modulus $E = 68300\ Mpa$, Poisson's ratio $\nu = 0.3$ and yield stress σ_y=35.1848 Mpa . The numerical results are then compared with data obtained from the experimental set-up of Professor Michel Guillot of Laval University shown in Figure 6.13.

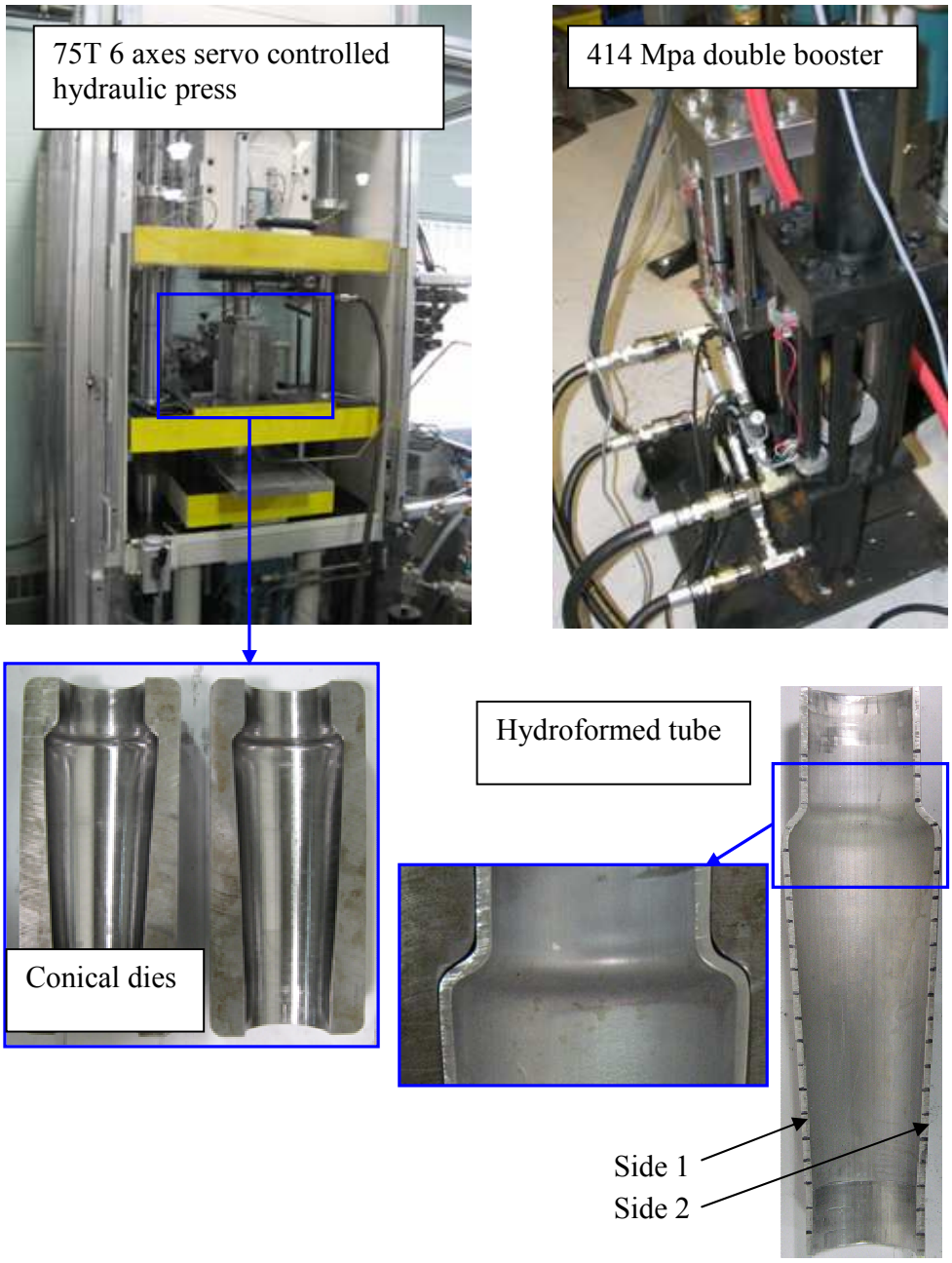

Figure 6.13: Experimental set-up, Élie-Dit-Cosaque et al. (2009)

The results obtained with three layers of C3D8R or C3D8I elements are similar to those obtained with on layer of SH8RSe element in the thickness direction as presented in Figure 6.14. Moreover, the loading path presented in Figure 6.10 allows the tube filling entirely the internal shape of the dies without any defect. The wall thickness has been measured

experimentally at both sides of the tube cut. These values have then been averaged yielding in the experimental wall thickness mean value presented in Figure 6.14 and in Table 6.2. In the sliding area, the thickness variation from the simulations is different compared with the thickness variation obtained experimentally. This is probably due to the choice of a constant friction coefficient inside the dies. Nevertheless, the thickness variation from the simulations is of the same order of magnitude as the thickness variation obtained experimentally in the bent shape. The lowest wall thickness of the tube is shown in Table 6.2.

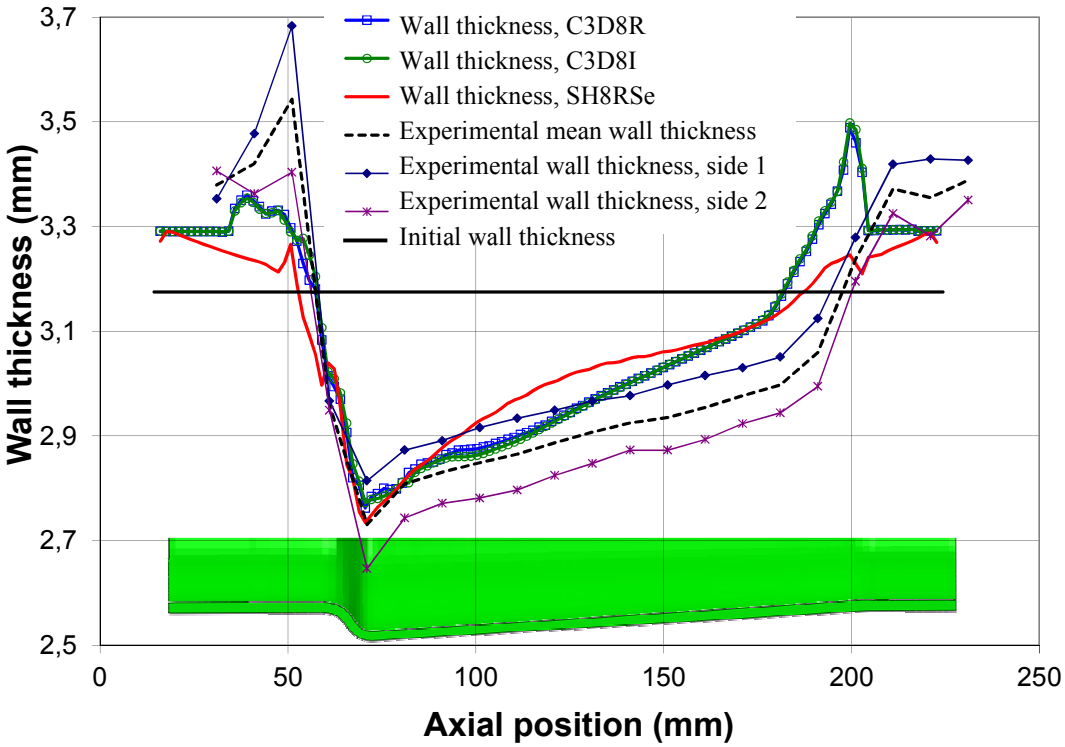

Figure 6.14: Conical shape THF wall thickness variation along path

(mm)	Experimental data mean value	3 C3D8R elements	3 C3D8I elements	1 SH8RSe element
Thickness min	2.7305	2.762	2.772	2.734

Table 6.2: Conical shape THF lowest wall thickness

This last example shows the relative performance of the present element used in a typical THF process simulation. It is able to simulate the physics of the model with only one layer of elements in the thickness direction. However, as in the previous example, the maximum limit of the coefficient $\sqrt{\left(\frac{\bar{h}}{E+\bar{h}}\right)}$ introduced in equation (6.30) has been set to $\frac{7}{10}$ in order to avoid the occurrence of hourglass modes especially in the axial feeding areas.

6.9. Concluding remarks

The benefits of using the 3D hexahedral elements in sheet metal forming context has been recently emphasized by different research contributions as presented in the introduction to this chapter. The present contribution aims at increasing the knowledge on this kind of element, to develop an eight node reduced integration solid-shell element compatible with all the 3D constitutive law and to confirm its efficiency in the tube hydroforming context. In the present work, the reduced integration SH8RSe element has been implemented in the explicit code ABAQUS/Explicit. This element has been improved so as to be able to deal with all classical 3D constitutive laws without locking issues. One of these improvements consists in using an enhanced parameter to avoid thickness locking. This enhanced parameter is then eliminated by a modified local static condensation. An improved version on the ANS theory is also used to avoid the transverse shear locking, as well as the classical four interpolation points ANS method to avoid trapezoidal effects. An appropriate decomposition of the element kinematics is then necessary to deal with all deformation modes individually. Moreover, the present element is able to provide various 3D kinematics parameters, such as the deformation gradient tensor $\mathbf{F}$ and the stretch tensor $\mathbf{U}$. This allows easily any combination of this element with a large variety of 3D constitutive laws beyond the single framework of the forming process. The 3D hyperelastoplastic constitutive law developed by Matei (2011) has been integrated within the SH8RSe element using a ABAQUS/VUMAT like subroutine in order to take advantage of its good representativeness of material behavior in the tube hydroforming process. This combination has then been successfully tested in forming situation generally encountered in the tube hydroforming context. In addition, the choice of the coefficient, presented in equation (6.30), that considers plasticity in the stabilization forces depends on the type of problem studied. More investigations should be performed on this coefficient given its influence on the results. This could be the topic of further studies.

Chapter 7. Conclusion and future work

This section summarizes the various contributions presented in the previous chapters and proposes some guidelines with regard to conducting hydroforming simulations in the aerospace domain. The goal of this contribution is to provide a solution to a real industrial concern in term of virtual product development. The end result is the development of a new design and methodology using the tube hydroforming process which is an unknown fabrication process for the field of helicopter skid landing gear.

Investigations were focused on determining an efficient solid-shell element suitable for tube hydroforming simulations. As part of this effort, the new SFEM has been investigated for use in THF simulation. This has led to the development of a resultant solid-shell element formulation successfully tested in various linear benchmark problems. However, at this stage of its development, this element is not ready to be tested in the THF context. Hence an alternative development was directed toward improvement of more classical formulation and this resulted in a novel SH8RSe element that has then been successfully created and tested in THF context. Some recommendations are then proposed for future developments in tube hydroforming as well as in solid-shell element development.

7.1. Thesis retrospective

In Chapter 1 and Chapter 2, the proposed literature review deals with two principal topics. The first one gives an overview of the tube hydroforming process. A description of the process is then presented emphasizing the crucial importance of the use of an appropriate pressure / end-feeding combination in order to be able to hydroform a part without defects. Friction between the tube and the dies is also a parameter of primary importance since it influences the final part geometry and possible defects occurrence. Due to its various advantages such as its ability to reduce the number of experimental set-ups, its ability to rapidly create numerical prototypes and its capacity to give a rapid numerical overview of a new tube hydroforming process, the finite element method is increasingly employed in that field. It also appears that some commercial softwares are dedicated to hydroforming process like HydroFORM. However, if this type of software gives accurate results in their specific area, they can hardly be used in other area like in impact analysis. Some other more

general commercial softwares like ABAQUS or Ls-Dyna are then used in the literature to simulate the tube hydroforming process. This last type of software appears to be well appreciated due to its versatility, since it could be used in the tube hydroforming process as well as in impact analysis for example. The proposed literature review highlighted some crucial aspects that still require improvements. One of them is the development of a more accurate constitutive law validated by an appropriate material characterization. Another one is the necessity to develop an efficient methodology which considers material history in a multi-steps fabrication process guaranteeing accurate material properties while simulating the final part in its in-service conditions. One more aspect is the development and the validation of more accurate and flexible non-linear finite elements formulation.

Chapter 3 provides an answer to the necessity of developing an improved methodology for multi-steps fabrication process using ABAQUS/Explicit. A skid landing gear cross tube has been first redesigned in order to be hydroformable. Then it has been numerically fabricated from a straight tube in aluminum alloy 7075 in W condition in different steps with the following sequence: i) first bending in explicit; ii) springback in implicit after first bending; iii) second bending in explicit; iv) springback after second bending in implicit; v) Crushing + tube hydroforming in explicit. It is noteworthy that the springback effect has not been considered after the tube hydroforming step. The hydroformed part has then been numerically aged from W to T73 condition to complete the fabrication process. Afterwards, the final hydroformed cross tube has been assembled in the skid landing gear replacing the standard forward cross tube. This new assembly has then successfully been tested in hard landing explicit simulations revealing the good performance of the new design as well as the efficiency of the proposed methodology.

The SFEM, which is a combination between the mesh free and the classical finite element methods, has been identified in the literature as a simple to implement method providing insensitiveness to mesh distortion. As an element having these last characteristics could be well appreciated in hydroforming process, some investigations on the subject have been proposed in Chapter 4. These investigations have resulted in the development of a new 3D linear resultant eight-node solid-shell element using the SFEM to calculate the membrane and bending deformation modes. This new element has shown in some classical linear

benchmark problems better accuracy compared with existing equivalent elements and this regarding analytical results.

The work done in Chapter 5 has been performed using the ABAQUS 3D C3D8R reduced integration element exhibiting one integration point. Three layers of this element have been necessary to have information in the thickness direction. This last issue has also been observed in the literature as this leads to increased computational effort that reduces the simulation time efficiency. The present thesis has then been partially proposed in order to develop and apply the new non-linear 3D SH8RSe solid-shell element in the hydroforming context in order to take advantages of its performance in term of time efficiency and accuracy. Chapter 5 presents the formulation behind this element as well as its stabilization procedure following the work of Abed-Meraim & Combescure (2009). The current formulation has been implemented in ABAQUS/Standard using the ABAQUS/UEL subroutine and validated through various implicit linear as well as non-linear benchmark problems.

The SH8RSe element is then combined with a hyperelastoplastic constitutive law implemented by Matei (2011), a co-rotational coordinates system is introduced for hourglass stabilization procedures. The kinematics of the proposed element has been implemented so as to allow such a combination as presented in Chapter 6. A polar decomposition has also been necessary in order to adapt the element kinematics to classical 3D constitutive laws. This new combination has then been tested in the tube hydroforming context, involving contact definition, high internal pressure loads as well as large strains with plasticity. In addition, some of the obtained results have been successfully compared with experimental data.

7.2. Recommendations for future work

The presented work gives some relevant answers to the different issues emphasized in the establishment of the initial objectives. Nevertheless, while some issues were addressed in a satisfactory manner some however still require further developments.

The methodology presented in Chapter 3 has been applied for an aluminum alloy in the hydroforming process. Other forming process simulations, which require different

fabrication sequences that force the material in the plastic regime, could take advantage of the developed methodology. Moreover, a more detailed study of the springback prediction in complex hydroformed shapes using an implicit hyperelastoplastic law is still required. The idea behind this is to include, in the design definition, the geometry changes that could occur from the hydroformed part shape to its shape after springback. Besides, the tube hydroforming process offers many advantages developed in the literature review that could help the industry to develop new improved designs for existing structural components. Other more efficient shapes of the hydroformable cross tube which consider important issue of its aerodynamics performance, could be considered in some future developments. The resultant solid-shell element with SFEM, the RH8s-X element, has been developed and presented in linear context in Chapter 4 for an eight-node element without resorting to stabilization. The related theory could then be extended for non-linear applications in the same idea as in the preliminary version proposed in Élie-Dit-Cosaque et al. (2011). Subsequently, the introduction of SFEM in the SH8RSe element for the in plane integration could be considered. The variational formulation, as well as the appropriate kinematics proper organization of the newly developed SH8RSe element presented in Chapter 5 and in Chapter 6, have allowed the coupling with a classical 3D constitutive law. The application of this improved element in other applications that could take advantage of the 3D formulation of the SH8RSe as FLD diagram simulations, simulation of springback or hard landing study could help, in future studies, to further emphasize the interest of using this type of element. In addition, the choice of the coefficient that considers plasticity in the stabilization forces depends on the type of problem studied. More investigations should be performed of this coefficient given its influence on the results. Moreover, an extension of this work in the context of composite materials could be considered. This would extend the validation range of the SH8RSe element with 3D oriented materials.

Bibliography

Abaqus user's manual, ver 6.8, 2007. *Abaqus user's manual*, Dassault Systèmes, Simulia.

Abaqus user's manual, ver 6.9, 2007. *Abaqus user's manual*, Dassault Systèmes, Simulia.

Abed-Meraim, F. & Combescure, A., 2002. SHB8PS--a new adaptative, assumed-strain continuum mechanics shell element for impact analysis. *Computers & Structures*, 80(9–10), p.791–803.

Abed-Meraim, F. & Combescure, A., 2009. An improved assumed strain solid-shell element formulation with physical stabilization for geometric non-linear applications and elastic-plastic stability analysis. *International Journal for Numerical Methods in Engineering*, 80(13), p.1640–1686.

Abrantes, J.P., Szabo-Ponce, A. & Batalha, G.F., 2005. Experimental and numerical simulation of tube hydroforming (THF). *Journal of Materials Processing Technology*, 164–165(-), p.1140–1147.

Ahmad, S., Irons, B.M. & Zienkiewicz, O., 1970. Analysis of thick and thin shell structures by curved finite elements. *International Journal for Numerical Methods in Engineering*, 2, p.419–451.

Ahmetoglu, M. & Altan, T., 2000. Tube hydroforming: state-of-the-art and future trends. *Journal of Materials Processing Technology*, 98(1), p.25–33.

Alves de Sousa, R.J., Natal Jorge, R.M., Fontes Valente, R.A. & César De Sá, J.M.A, 2003. A new volumetric and shear locking-free 3D enhanced strain element. *Engineering Computations*, 20(7), p.896–925.

Alves de Sousa, R.J., Cardoso, R.P.R, Fontes Valente, R.A., Yoon, J-W., Grácio, J.J. & Natal Jorge, R.M., 2005. A new one-point quadrature enhanced assumed strain (EAS) solid-shell element with multiple integration points along thickness: Part I - geometrically linear applications. *International Journal for Numerical Methods in Engineering*, 62(7), p.952–977.

Alves de Sousa, R.J., Cardoso, R.P.R, Fontes Valente, R.A., Yoon, J-W., Grácio, J.J. & Natal Jorge, R.M., 2006. A new one-point quadrature enhanced assumed strain (EAS) solid-shell element with multiple integration points along thickness - part II: nonlinear applications. *International Journal for Numerical Methods in Engineering*, 67(2), p.160–188.

Alves de Sousa, R.J., Yoon, J.W., Cardoso, R.P.R., Fontes Valente, R.A. & Grácio, J.J., 2007. On the use of a reduced enhanced solid-shell (RESS) element for sheet forming simulations. *International Journal of Plasticity*, 23(3), p.490–515.

Andelfinger, U. & Ramm, E., 1993. EAS-elements for two-dimensional, three-dimensional, plate and shell structures and their equivalence to HR-elements. *International Journal for Numerical Methods in Engineering*, 36(8), p.1311–1337.

Arrieux, R., 1995. Determination and use of the forming limit stress diagrams in sheet metal forming. *Journal of Materials Processing Technology*, 53(1–2), p.47–56.

Aydemir, A., De Vree, J.H.P., Brekelmans, W.A.M., Geers, M.G.D., Sillekens, W.H. & Werkhoven, R.J., 2005. An adaptive simulation approach designed for tube hydroforming processes. *Journal of Materials Processing Technology*, 159(3), p.303–310.

Barlat, F., Brem, J.C., Yoon, J.W., Chung, K., Dick, R.E., Lege, D.J., Pourboghrat, F., Choi, S.-H. & Chu, E., 2003. Plane stress yield function for aluminum alloy sheets—part 1: theory. *International Journal of Plasticity*, 19(9), p.1297–1319.

Barlat, F. & Lian, K., 1989. Plastic behavior and stretchability of sheet metals. Part I: A yield function for orthotropic sheets under plane stress conditions. *International Journal of Plasticity*, 5(1), p.51–66.

Barut, A., Madenci, E. & Tessler, A., 1997. Nonlinear analysis of laminates through a mindlin-type shear deformable shallow shell element. *Computer Methods in Applied Mechanics and Engineering*, 143(1–2), p.155–173.

Bathe, K.J. & Bolourchi, S., 1980. A geometric and material nonlinear plate and shell element. *Computers & Structures*, 11(1–2), p.23–48.

Bathe, K.J., 1982. *Finite element procedures in engineering analysis*, New Jersey: Prentice-Hall.

Bathe, K.J., Dvorkin, E. & Ho, L.W., 1983. Our discrete-Kirchhoff and isoparametric shell elements for nonlinear analysis—An assessment. *Computers & Structures*, 16(1–4), p.89–98.

Bathe, K.J. & Dvorkin, E.N., 1985. A four-node plate bending element based on Mindlin/Reissner plate theory and a mixed interpolation. *International Journal for Numerical Methods in Engineering*, 21(2), p.367–383.

Bathe, K.J., Iosilevich, A. & Chapelle, D., 2000. An evaluation of the MITC shell elements. *Computers & Structures*, 75(1), p.1–30.

Batoz, J.-L. & Dhatt, G., 1992. *Modélisation des structures par éléments finis: coques* Les Presses de l'Université Laval.

Belytschko, T. & Bindeman, L.P., 1991. Assumed strain stabilization of the 4-node quadrilateral with 1-point quadrature for nonlinear problems. *Computer Methods in Applied Mechanics and Engineering*, 88(3), p.311–340.

Belytschko, T. & Bindeman, L.P., 1993. Assumed strain stabilization of the eight node hexahedral element. *Computer Methods in Applied Mechanics and Engineering*, 105(2), p.225–260.

Belytschko, T., Lin, J.I. & Chen-Shyh, T., 1984. Explicit algorithms for the nonlinear dynamics of shells. *Computer Methods in Applied Mechanics and Engineering*, 42(2), p.225–251.

Betsch, P., Gruttmann, F. & Stein, E., 1996. A 4-node finite shell element for the implementation of general hyperelastic 3D-elasticity at finite strains. *Computer Methods in Applied Mechanics and Engineering*, 130(1–2), p.57–79.

Bianchi, C., Cozzolino, C., Rossiello, F., Sordelli, E. & Usuelli, M., 2001. Fatigue analysis on a helicopter skid landing gear. In 16th European MDI User Conference 2001. Berchtesgaden, Germany.

Bischoff, M. & Ramm, E., 1997. Shear deformable shell elements for large strains and rotations. *International Journal for Numerical Methods in Engineering*, 40(23), p.4427–4449.

Blanchet-Létourneau, J., 2010. *Développement de concepts et de méthodes de fabrication par hydroformage d'une traverse d'Hélicoptère en aluminium*. Master. Québec City, CA: Laval University.

Bordas, S.P.A. Rabczuk, T., Hung, N-X, Nguyen, V. P., Natarajan, S., Bog, T., Quan, D. M. & Hiep, N. V., 2010. Strain smoothing in FEM and XFEM. *Computers & Structures*, 88(23–24), p.1419–1443.

Bordas, S.P.A. & Natarajan, S., 2009. On the approximation in the smoothed finite element method (SFEM). *International Journal for Numerical Methods in Engineering*, 81(5), p.660–670.

Brank, B., Damjanić, F.B. & Perić, D., 1995. On implementation of a nonlinear four node shell finite element for thin multilayered elastic shells. *Computational Mechanics*, 16(5), p.341–359.

Brank, B., Korelc, J. & Ibrahimbegović, A., 2002. Nonlinear shell problem formulation accounting for through-the-thickness stretching and its finite element implementation. *Computers & Structures*, 80(9–10), p.699–717.

Brendel, B. & Ramm, E., 1980. Linear and nonlinear stability analysis of cylindrical shells. *Computers & Structures*, 12(4), p.549–558.

Bucalem, M.L. & Bathe, K.-J., 1993. Higher-order MITC general shell elements. *International Journal for Numerical Methods in Engineering*, 36(21), p.3729–3754.

Büchter, N., Ramm, E. & Roehl, D., 1994. Three-dimensional extension of non-linear shell formulation based on the enhanced assumed strain concept. *International Journal for Numerical Methods in Engineering*, 37(15), p.2551–2568.

Cardoso, R.P.R., Yoon, J-W., Grácio, J. J., Barlat, F. & César de Sá , J. M.A., 2002. Development of a one point quadrature shell element for nonlinear applications with contact and anisotropy. *Computer Methods in Applied Mechanics and Engineering*, 191(45), p.5177–5206.

Cardoso, R.P.R., Yoon, J-W., Mahardika, M., Choudhry, S., Alves de Sousa, R. J. & Fontes Valente R. A., 2008. Enhanced assumed strain (EAS) and assumed natural strain (ANS) methods for one point quadrature solid shell elements. *International Journal for Numerical Methods in Engineering*, 75(2), p.156–187.

Cardoso, R.P.R. & Yoon, J.W., 2005. One point quadrature shell element with through-thickness stretch. *Computer Methods in Applied Mechanics and Engineering*, 194(9–11), p.1161–1199.

César de Sá, J.M.A., Natal Jorge, R.M., Fontes Valente, R.A. & Almeida Areias, P.M., 2002. Development of shear locking-free shell elements using an enhanced assumed strain formulation. *International Journal for Numerical Methods in Engineering*, 53(7), p.1721–1750.

Chandra, S. & Prathap, G., 1989. A field-consistent formulation for the eight-noded solid finite element. *Computers & Structures*, 33(2), p.345–355.

Chapelle, D., Oliveira, D.L. & Bucalem, M.L., 2003. MITC elements for a classical shell model. *Computers & Structures*, 81(8–11), p.523–533.

Chen, J.-S. C.-T. Wu, S. Yoon & Y.You¶, 2001. A stabilized conforming nodal integration for Galerkin mesh-free methods. *International Journal for Numerical Methods in Engineering*, 50(2), p.435–466.

Cheng-Ho, T., Sparks, C.E., Sareen, A.K., Smith, M.R. & Johnson, J., 2003. Efficient helicopter skid landing gear dynamic drop simulation using Ls-Dyna.

Cook, R.D., Malkus, R.D., Plesha, M.E. & Witt, R.L., 2001. *Concepts and Applications of Finite Element Analysis, 4th Edition* 4^{e} éd., Wiley.

Coret, M. & Combescure, A., 2002. A mesomodel for the numerical simulation of the multiphasic behavior of materials under anisothermal loading (application to two low-carbon steels). *International Journal of Mechanical Sciences*, 44(9), p.1947–1963.

Cui, X. Liu, G., Li, G.Y., Zhao, X., Nguyen, T.T. & Sun, G.Y., 2008. A Smoothed Finite Element Method (SFEM) for Linear and Geometrically Nonlinear Analysis of Plates and Shells. *Computer Modeling in Engineering and Sciences*, 28(2), p.109–125.

Dai, K.Y. & Liu, G.R., 2007a. Free and forced vibration analysis using the smoothed finite element method (SFEM). *Journal of Sound and Vibration*, 301(3–5), p.803–820.

Dai, K.Y. & Liu, G.R., 2007b. Smoothed Finite Element Method, *CE006, http://hdl.handle.net/1721.1/35825*.

Dai, K.Y., Liu, G.R. & Nguyen, T.T., 2007. An n-sided polygonal smoothed finite element method (nSFEM) for solid mechanics. *Finite Elements in Analysis and Design*, 43(11–12), p.847–860.

Dohmann, F. & Hartl, C., 1997. Tube hydroforming—research and practical application. *Journal of Materials Processing Technology*, 71(1), p.174–186.

Domissy, E. & Batoz, J.-L., 1997. *Formulation et évaluation d'éléments finis volumiques modifiés pour l'analyse linéaire et non linéaire des coques*. France: Université de technologie de Compiègne, UTC.

Duarte Filho, L.A. & Awruch, A.M., 2004. Geometrically nonlinear static and dynamic analysis of shells and plates using the eight-node hexahedral element with one-point quadrature. *Finite Elements in Analysis and Design*, 40(11), p.1297–1315.

Dutton, T., Ireghu, S., Sturt, R., Kellicut, A., Cowell, B. & Kavikondala, K., 1999. The effect of forming on the crashworthiness of vehicles with hydroformed frame siderails. *SAE 1999-01-3208*.

Dvorkin, E.N. & Bathe, K.-J., 1984. A continuum mechanics based four-node shell element for general non-linear analysis. *Engineering Computations*, 1(1), p.77–88.

Élie-Dit-Cosaque, X., Blanchet-Létourneau, J., Lévesque, J. & Gakwaya, A., 2008. *Landing gear drop test simulation and new hydroformable cross tube optimization*, Québec City, CA: Laval University.

Élie-Dit-Cosaque, X., Gakwaya, A., Guillot, M., Lévesque, J. & Blanchet-Létourneau, J., 2009. Loading path optimization for tube hydroforming of aerospace components. *The encyclopaedia of research on aluminium in Québec - 2009 (Aluminium Research Center - REGAL)*.

Élie-Dit-Cosaque, X., Gakwaya, A., Lévesque, J. & Guillot, M., 2011. Smoothed finite element method for the resultant eight-node solid shell element analysis. In Simulia Customer Conference. Barcelona: Simulia.

Élie-Dit-Cosaque, X., Gakwaya, A. & Lévesque, J., 2009a. Design and drop test simulation of a helicopter skid landing gear with Abaqus/CAE. In 2009 SIMULIA Customer Conference. London, UK.

Élie-Dit-Cosaque, X., Gakwaya, A. & Lévesque, J., 2009b. *Drop test implementation and element development*, Québec City, CA: Laval University.

Fann, K.-J. & Hsiao, P.-Y., 2003. Optimization of loading conditions for tube hydroforming. *Journal of Materials Processing Technology*, 140(1-3), p.520–524.

FAR, 1965. Part 27, Airworthiness standards: normal category rotorcraft.

Flanagan, D.P. & Belytschko, T., 1981. A uniform strain hexahedron and quadrilateral with orthogonal hourglass control. *International Journal for Numerical Methods in Engineering*, 17(5), p.679–706.

Fontes Valente, R.A., Alves de Sousa, R.J. & Natal Jorge, R.M., 2004. An enhanced strain 3D element for large deformation elastoplastic thin-shell applications. *Computational Mechanics*, 34(1), p.38–52.

Goodwin, G.M., 1968. Application of Strain Analysis to Sheet Metal Forming Problems in the Press Shop. , SAE Technical Paper (680093).

Grantab, R., 2006. *Interaction Between Forming and Crashworthiness of Advanced High Strength Steel S-Rails*. Canada.

Green, D.E., 2008. Forming analysis for tubular hydroformed parts. In *Hydroforming for Advanced Manufacturing*. CRC Press, p. 93–120.

Grolleau, V., Galpin, B., Penin, A. & Rio, G., 2008. Modelling the effect of forming history in impact simulations: evaluation of the effect of thickness change and strain hardening based on experiments. *International Journal of Crashworthiness*, 13(4), p.363–373.

Hallquist, J., 1983. *Theoretical manual for DYNA3D*, Livermore,CA: Lawrence Livermore Laboratory.

Hannachi, M., 2007. *Formulation d'éléments finis volumiques adaptés à l'analyse, linéaire et non linéaire, et à l'optimisation de coques isotropes et composites*. France: Université de technologie de Compiègne, UTC.

Hauptmann, R., Doll, S., Harnau, M. & Schweizerhof, K., 2001. `Solid-shell' elements with linear and quadratic shape functions at large deformations with nearly incompressible materials. *Computers & Structures*, 79(18), p.1671–1685.

Hauptmann, R. & Schweizerhof, K., 1998. A systematic development of 'solid shell' element formulations for linear and non-linear analyses employing only displacement degrees of freedom. *International Journal for Numerical Methods in Engineering*, 42(1), p.49–69.

Hauptmann, R., Schweizerhof, K. & Doll, S., 2000. Extension of the 'solid shell' concept for application to large elastic and large elastoplastic deformations. *International Journal for Numerical Methods in Engineering*, 49(9), p.1121–1141.

Hill, R., 1991. A theoretical perspective on in-plane forming of sheet metal. *Journal of the Mechanics and Physics of Solids*, 39(2), p.295–307.

Hill, R., 1990. Constitutive modeling of orthotropic plasticity in sheet metals. *Journal of the Mechanics and Physics of Solids*, 38(3), p.405–417.

Hill, R., 1950. *The Mathematical theory of plasticity*, Oxford: the Clarendon press.

Hodge, P.G., 1970. *Continuum mechanics: an introductory text for engineers*, McGraw-Hill.

Hong, W.I., Kim, J.H. & Lee, S.W., 2001. An assumed strain triangular curved solid shell element formulation for analysis of plates and shells undergoing finite rotations. *International Journal for Numerical Methods in Engineering*, 52(7), p.747–761.

Hosford, W.F., 1972. A Generalized Isotropic Yield Criterion. *Journal of Applied Mechanics*, 39(2), p.607–609.

Howard, J., Thiagarajan, R., Smith, M.R& Sareen, A.K., 2002. Stiffness decoupled skid landing gear.

Hughes, T. J. R. & Tezduyar, T.E., 1981. Finite Elements Based Upon Mindlin Plate Theory With Particular Reference to the Four-Node Bilinear Isoparametric Element. *Journal of Applied Mechanics*, 48(3), p.587–596.

Hughes, T. J. R., 1980. Generalization of selective integration procedures to anisotropic and nonlinear media. *International Journal for Numerical Methods in Engineering*, 15(9), p.1413–1418.

Hughes, T. J. R. & Liu, W.K., 1981. Nonlinear finite element analysis of shells: Part I. three-dimensional shells. *Computer Methods in Applied Mechanics and Engineering*, 26(3), p.331–362.

Hughes, T. J.R., Cohen, M. & Haroun, M., 1978. Reduced and selective integration techniques in the finite element analysis of plates. *Nuclear Engineering and Design*, 46(1), p.203–222.

Hwang, Y.-M. & Altan, T., 2002. FE simulations of the crushing of circular tubes into triangular cross-sections. *Journal of Materials Processing Technology*, 125-126(-), p.833–838.

Hwang, Y.-M. & Altan, T., 2003. Finite element analysis of tube hydroforming processes in a rectangular die. *Finite Elem. Anal. Des.*, 39(11), p.1071–1082.

Imaninejad, M., Subhash, G. & Loukus, A., 2004. Influence of end-conditions during tube hydroforming of aluminum extrusions. *International Journal of Mechanical Sciences*, 46(8), p.1195–1212.

Jansson, M., Nilsson, L. & Simonsson, K., 2005. On constitutive modeling of aluminum alloys for tube hydroforming applications. *International Journal of Plasticity*, 21(5), p.1041–1058.

Jansson, M., Nilsson, L. & Simonsson, K., 2007a. On process parameter estimation for the tube hydroforming process. *Journal of Materials Processing Technology*, 190(1–3), p.1–11.

Jansson, M., Nilsson, L. & Simonsson, K., 2007b. The use of biaxial test data in the validation of constitutive descriptions for tube hydroforming applications. *Journal of Materials Processing Technology*, 184(1–3), p.69–76.

Kang, S.-J., Kim, H.-K. & Kang, B.-S., 2005. Tube size effect on hydroforming formability. *Journal of Materials Processing Technology*, 160(1), p.24–33.

Keeler, S.P., 1961. *Plastic Instability and Fracture in Sheets Stretched Over Rigid Punches*, MIT.

Kim, D.-N. & Bathe, K.J., 2008. A 4-node 3D-shell element to model shell surface tractions and incompressible behavior. *Computers & Structures*, 86(21–22), p.2027–2041.

Kim, H., Hong, Su., Hong, Se. & Huh, H., 2003. The evaluation of crashworthiness of vehicles with forming effect. In 4th European Ls-Dyna Users Conference. Germany.

Kim J., Lei L.-P. & Kang B.-S., 2003. Preform design in hydroforming of automobile lower arm by FEM. *Journal of Materials Processing Technology*, 138(1), p.58–62.

Kim, K.D., Liu, G.Z. & Han, S.C., 2005. A resultant 8-node solid-shell element for geometrically nonlinear analysis. *Computational Mechanics*, 35(5), p.315–331.

Klinkel, S., Gruttmann, F. & Wagner, W., 2008. A mixed shell formulation accounting for thickness strains and finite strain 3d material models. *International Journal for Numerical Methods in Engineering*, 74(6), p.945–970.

Klinkel, S., Gruttmann, F. & Wagner, W., 2006. A robust non-linear solid shell element based on a mixed variational formulation. *Computer Methods in Applied Mechanics and Engineering*, 195(1–3), p.179–201.

Koç, M. éd., 2008. *Hydroforming for Advanced Manufacturing*, CRC Press.

Koç, M. & Altan, T., 2001. An overall review of the tube hydroforming (THF) technology. *Journal of Materials Processing Technology*, 108(3), p.384–393.

Koç, M. & Altan, T., 2002. Application of two dimensional (2D) FEA for the tube hydroforming process. *International Journal of Machine Tools and Manufacture*, 42(11), p.1285–1295.

Korkolis, Y.P. & Kyriakides, S., 2008. Inflation and burst of anisotropic aluminum tubes for hydroforming applications. *International Journal of Plasticity*, 24(3), p.509–543.

Kuwabara, T., Ishiki, M., Kuroda, M. & Takahashi, S., 2003. Yield locus and work hardening behavior of a thin-walled steel tube subjected to combined tension-internal pressure. *Journal de physique IV*, 105, p.347–354.

Lang, L., Yuanb, S., Wangb, X., Wangb, Z.R., Fub, Z., Danckerta, J. & Nielsena, K.B., 2004. A study on numerical simulation of hydroforming of aluminum alloy tube. *Journal of Materials Processing Technology*, 146(3), p.377–388.

Lee, H., Tyne, C.J.V. & Field, D., 2005. Finite element bending analysis of oval tubes using rotary draw bender for hydroforming applications. *Journal of Materials Processing Technology*, 168(2), p.327–335.

Lee, S.H., Han, C.-S. & Oh, S.-I., 2001. Comparative crash simulations incorporating the results of sheet forming analyses. *Engineering computations*, 18(5–6), p.744–758.

Legay, A. & Combescure, A., 2003. Elastoplastic stability analysis of shells using the physically stabilized finite element SHB8PS. *International Journal for Numerical Methods in Engineering*, 57(9), p.1299–1322.

Lemaître, J. & Chaboche, J.-L., 2001. *Mécanique des matériaux solides* 2th edition., Dunod.

Lemosse, D., 2000. *Eléments finis isoparamétriques tridimensionnels pour l'étude des structures minces*. France: INSA - Rouen.

Li, H., Yang, H., Zhan, M. & Gu, R.J., 2007. The interactive effects of wrinkling and other defects in thin-walled tube NC bending process. *Journal of Materials Processing Technology*, 187–188, p.502–507.

Li, L., Li, D. & Peng, Y., 2011. The simulation of sheet metal forming processes via integrating solid-shell element with explicit finite element method. *Engineering with Computers*, 27(3), p.273–284.

Li, L.M., Peng, Y.H. & Li, D.Y., 2011. A stabilized underintegrated enhanced assumed strain solid-shell element for geometrically nonlinear plate/shell analysis. *Finite Elements in Analysis and Design*, 47(5), p.511–518.

Liu, G.R., Nguyen-Thoi, T., Nguyen-Xuan, H. & Lam, K.Y., 2009. A node-based smoothed finite element method (NS-FEM) for upper bound solutions to solid mechanics problems. *Computers & Structures*, 87(1–2), p.14–26.

Liu, G.R., Nguyen, T.T., Dai, K.Y. & Lam, K.Y., 2007. Theoretical aspects of the smoothed finite element method (SFEM). *International Journal for Numerical Methods in Engineering*, 71(8), p.902–930.

Liu, G.R., Dai, K.Y. & Nguyen, T.T., 2007. A Smoothed Finite Element Method for Mechanics Problems. *Computational Mechanics*, 39(6), p.859–877.

Liu, S.J., Wang, H. & Zhang, H., 2010. Smoothed finite elements large deformation analysis. *International Journal of Computational Methods*, 7(3), p.513–524.

Liu, W.K., Guo, Y., Tang, S. & Belytschko, T., 1998. A multiple-quadrature eight-node hexahedral finite element for large deformation elastoplastic analysis. *Computer Methods in Applied Mechanics and Engineering*, 154(1–2), p.69–132.

Lu, H., Ito, K., Kazama, K. & Namura, S., 2006. Development of a new quadratic shell element considering the normal stress in the thickness direction for simulating sheet metal forming. *Journal of Materials Processing Technology*, 171(3), p.341–347.

Luege, M. & Luccioni, B.M., 2008. Numerical simulation of the lubricant performance in tube hydroforming. *Journal of Materials Processing Technology*, 198(1–3), p.372–380.

Lundqvist, J., 2004. *Numerical simulation of tube hydroforming: adaptive loading paths*. Licentiate thesis. Lulea University of Technology.

Macneal, R.H., 1978. A simple quadrilateral shell element. *Computers & Structures*, 8(2), p.175–183.

Macneal, R.H., 1982. Derivation of element stiffness matrices by assumed strain distributions. *Nuclear Engineering and Design*, 70(1), p.3–12.

Macneal, R.H. & Harder, R.L., 1985. A proposed standard set of problems to test finite element accuracy. *Finite Elements in Analysis and Design*, 1(1), p.3–20.

Malkus, D.S. & Hughes, T.J.R., 1978. Mixed finite element methods — Reduced and selective integration techniques: A unification of concepts. *Computer Methods in Applied Mechanics and Engineering*, 15(1), p.63–81.

Matei, M., 2011. *Développement d'outils intégrés pour la fabrication virtuelle de produits en aluminium et en acier par hydroformage de tubes pour l'industrie aéronautique*. Québec City, CA: Université Laval.

Miehe, C., 1998. A theoretical and computational model for isotropic elastoplastic stress analysis in shells at large strains. *Computer Methods in Applied Mechanics and Engineering*, 155(3–4), p.193–233.

Militello, C. & Felippa, C.A., 1990a. A variational justification of the assumed natural strain formulation of finite elements—I. Variational principles. *Computers & Structures*, 34(3), p.431–438.

Militello, C. & Felippa, C.A., 1990b. A variational justification of the assumed natural strain formulation of finite elements—II. The C0 four-node plate element. *Computers & Structures*, 34(3), p.439–444.

Ngaile, G., Jaeger, S. & Altan, T., 2004a. Lubrication in tube hydroforming (THF). Part II. Performance evaluation of lubricants using LDH test and pear-shaped tube expansion test. *Journal of materials processing technology*, 146(1), p.116–123.

Ngaile, G., Jaeger, S. & Altan, T., 2004b. Lubrication in tube hydroforming (THF): Part I. Lubrication mechanisms and development of model tests to evaluate lubricants and die coatings in the transition and expansion zones. *Journal of Materials Processing Technology*, 146(1), p.108–115.

Nguyen, N.H., 2009. *Development of solid-shell elements for large deformation simulation and springback prediction*. Belgium: Université de Liège.

Nguyen-Thanh, N., Rabczuk, T., Nguyenxuan, H. & Bordas, S., 2008. A smoothed finite element method for shell analysis. *Computer Methods in Applied Mechanics and Engineering*, p.165–177.

Nguyen-Thanh, T., Liu, G.R., Dai, K.Y. & Lam, K.Y., 2007. Selective Smoothed Finite Element Method. *Tsinghua Science & Technology*, 12(5), p.497–508.

Nguyen-Thoi, T., Liu, G.R. & Nguyen-Xuan, H., 2011. An n-sided polygonal edge-based smoothed finite element method (nES-FEM) for solid mechanics. *International Journal for Numerical Methods in Biomedical Engineering*, 27(9), p.1446–1472.

Nguyen-Xuan, H, Rabczuk, T., Bordas, S. & Debongnie, J., 2008. A smoothed finite element method for plate analysis. *Computer Methods in Applied Mechanics and Engineering*, 197(13–16), p.1184–1203.

Nguyen-Xuan, H., 2008. *A strain smoothing method in finite elements for structural analysis*. Belgium: Université de Liège.

Nguyen-Xuan, H., Bordas, S. & Nguyen-Dang, H., 2008. Smooth finite element methods: Convergence, accuracy and properties. *International Journal for Numerical Methods in Engineering*, 74(2), p.175–208.

Normani, F.V., 2004. *Analytical Modeling of Tube Bending with Hydroforming*. University of Waterloo, Canada.

Oliveira, D.A., Worswick, M.J., Khodayari, G. & Gholipour, J., 2007. Effect of Bending Variables on the Characteristics of EN-AW5018 Tubes for Subsequent Hydroforming. *Canadian Metallurgical Quarterly*, 46(2), p.145–153.

Oliveira, D. A., Worswick, M.J., Grantab, R., Williams, B.W. & Mayer, R., 2006. Effect of forming process variables on the crashworthiness of aluminum alloy tubes. *International Journal of Impact Engineering*, 32(5), p.826–846.

Parente, M.P.L., Fontes Valente, R.A., Natal Jorge, R.M., Cardoso, R.P.R. & Alves de Sousa, R.J., 2006. Sheet metal forming simulation using EAS solid-shell finite elements. *Finite Elem. Anal. Des.*, 42(13), p.1137–1149.

Parisch, H., 1995. A continuum-based shell theory for non-linear applications. *International Journal for Numerical Methods in Engineering*, 38(11), p.1855–1883.

Parisch, H., 1979. A critical survey of the 9-node degenerated shell element with special emphasis on thin shell application and reduced integration. *Computer Methods in Applied Mechanics and Engineering*, 20(3), p.323–350.

Parisch, H., 1978. Geometrical nonlinear analysis of shells. *Computer Methods in Applied Mechanics and Engineering*, 14(2), p.159–178.

Puso, M. A & Solberg, J., 2006. A stabilized nodally integrated tetrahedral. *International Journal for Numerical Methods in Engineering*, 67(6), p.841–867.

Puso, M.A., 2000. A highly efficient enhanced assumed strain physically stabilized hexahedral element. *International Journal for Numerical Methods in Engineering*, 49(8), p.1029–1064.

Quak, W., 2007. *A solid-shell element for use in sheet deformation processes and the EAS method*. University of Twente.

Rashid, M.M. & Sadri, A., 2012. The partitioned element method in computational solid mechanics. *Computer Methods in Applied Mechanics and Engineering*, 237–240(–), p.152–165.

Ray, P. & Mac Donald, B.J., 2004. Determination of the optimal load path for tube hydroforming processes using a fuzzy load control algorithm and finite element analysis. *Finite Elements in Analysis and Design*, 41(2), p.173–192.

Ray, P. & Mac Donald, B.J., 2005. Experimental study and finite element analysis of simple X- and T-branch tube hydroforming processes. *International Journal of Mechanical Sciences*, 47(10), p.1498–1518.

Reese, S., Küssner, M. & Reddy, B.D., 1999. A new stabilization technique for finite elements in non-linear elasticity. *International Journal for Numerical Methods in Engineering*, 44(11), p.1617–1652.

Reese, S., 2007. A large deformation solid - shell concept based on reduced integration with hourglass stabilization. *International Journal for Numerical Methods in Engineering*, 69(8), p.1671–1716.

Reese, S., 2005. On a physically stabilized one point finite element formulation for three-dimensional finite elasto-plasticity. *Computer Methods in Applied Mechanics and Engineering*, 194(45–47), p.4685–4715.

Salahouelhadj, A., Abed-Meraim, F., Chalal, H. & Balan, T., 2011. On the implementation of the continuum shell finite element SHB8PS and application to sheet forming simulation. In The 14th International ESAFORM Conference on Material Forming. p. 1203–1208.

Salahouelhadj, A., Abed-Meraim, F., Chalal, H. & Balan, T., 2012. Application of the continuum shell finite element SHB8PS to sheet forming simulation using an extended large strain anisotropic elastic–plastic formulation. *Archive of Applied Mechanics*, p.1–22.

Sansour, C. & Bocko, J., 1998. On hybrid stress, hybrid strain and enhanced strain finite element formulations for a geometrically exact shell theory with drilling degrees of freedom. *International Journal for Numerical Methods in Engineering*, 43(1), p.175–192.

Sansour, C. & Kollmann, F.G., 2000. Families of 4-node and 9-node finite elements for a finite deformation shell theory. An assesment of hybrid stress, hybrid strain and enhanced strain elements. *Computational Mechanics*, 24(6), p.435–447.

Schwarze, M. & Reese, S., 2009. A reduced integration solid-shell finite element based on the EAS and the ANS concept-Geometrically linear problems. *International Journal for Numerical Methods in Engineering*, 80(10), p.1322–1355.

Schwarze, M. & Reese, S., 2011. A reduced integration solid-shell finite element based on the EAS and the ANS concept-Large deformation problems. *International Journal for Numerical Methods in Engineering*, 85(3), p.289–329.

Scordelis, A.C. & Lo, K.S., 1964. Computer Analysis of Cylindrical Shells. *Journal of American Concrete Institute*, 69, p.539–559.

Sena, J.I.V., Alves de Sousa, R.J. & Fontes Valente, R.A., 2011. On the use of EAS solid-shell formulations in the numerical simulation of incremental forming processes. *Engineering Computations*, 28(3), p.287–313.

Shrotri, K., 2008. *Composite skid landing gear design investigation*. USA: School of Aerospace Engineering, Georgia Institute of Technology.

Simha, C.H.M., Gholipour, J., Bardelcik, A. & Worswick, M.J., 2005. Application of an Extended Stress Based Flow Limit Curve to Predict Necking in Tubular Hydroforming. In Proceedings of Numisheet. Detroit, USA, p. 15–19.

Simo, J.C. & Rifai, M.S., 1990. A class of mixed assumed strain methods and the method of incompatible modes. , 29, p.1595–1638.

Simo, J.C. & Armero, F., 1992. Geometrically non-linear enhanced strain mixed methods and the method of incompatible modes. *International Journal for Numerical Methods in Engineering*, 33(7), p.1413–1449.

Simo, J.C., Armero, F. & Taylor, R.L., 1993. Improved versions of assumed enhanced strain tri-linear elements for 3D finite deformation problems. *Computer Methods in Applied Mechanics and Engineering*, 110(3–4), p.359–386.

Simo, J.C. & Fox, D.D., 1989. On a stress resultant geometrically exact shell model. Part I: Formulation and optimal parametrization. *Computer Methods in Applied Mechanics and Engineering*, 72(3), p.267–304.

Simo, J.C., Fox, D.D. & Rifai, M.S., 1990. On a stress resultant geometrically exact shell model. Part III: Computational aspects of the nonlinear theory. *Computer Methods in Applied Mechanics and Engineering*, 79(1), p.21–70.

Simo, J.C. & Hughes, T.J.R., 1998. *Computational Inelasticity*, Springer.

Simo, J.C. & Hughes, T.J.R., 1986. On the Variational Foundations of Assumed Strain Methods. *Journal of Applied Mechanics*, 53(1), p.51–54.

Simo, J.C., Rifai, M.S. & Fox, D.D., 1990. On a stress resultant geometrically exact shell model. Part IV: Variable thickness shells with through-the-thickness stretching. *Computer Methods in Applied Mechanics and Engineering*, 81(1), p.91–126.

Smolenski, W.M. 1998. Statically and kinematically exact nonlinear theory of rods and its numerical verification. *Computer Methods in Applied Mechanics and Engineering*, 178(1–2), p.89–113.

De Souza Neto, E.A., Perić, D., Huang, G. C, Owen, D. R. J, 1995. Remarks on the stability of enhanced strain elements in finite elasticity and elastoplasticity. *Communications in Numerical Methods in Engineering*, 11, p.951–961.

Stoughton, T.B., 2000. A general forming limit criterion for sheet metal forming. *International Journal of Mechanical Sciences*, (42), p.1–27.

Stoughton, T. B., and Zhu, X., 2004, "Review of Theoretical Models of the Strain-Based FLD and Their Relevance to the Stress-Based FLD," *Int. J. Plast*., 20(8–9), p. 1463–1486.

Strano, M., Jirathearanat, S. & Altan, T., 2001. Adaptive FEM Simulation for Tube Hydroforming: a Geometry-Based Approach for Wrinkle Detection. *CIRP Annals - Manufacturing Technology*, 50(1), p.185–190.

Sze, K.Y., Chan, W.K. & Pian, T.H.H., 2002. An eight-node hybrid-stress solid-shell element for geometric non-linear analysis of elastic shells. *International Journal for Numerical Methods in Engineering*, 55(7), p.853–878.

Sze, K.Y., Liu, X.H. & Lo, S.H., 2004. Popular benchmark problems for geometric nonlinear analysis of shells. *Finite Elements in Analysis and Design*, 40(11), p.1551–1569.

Sze, K.Y. & Yao, L., 2000. A hybrid-stress ANS solid-shell element and its generalization for smart structure modelling - part I: solid-shell element formulation. *International Journal for Numerical Methods in Engineering*, 48, p.545–564.

Taylor, R.L., Beresford, P.J. & Wilson, E.L., 1976. A non-conforming element for stress analysis. *International Journal for Numerical Methods in Engineering*, 10(6), p.1211–1219.

Timoshenko, S. & Woinowsky-Krieger, S., 1959. *Theory of Plates and Shells,* 2e éd., Mcgraw-Hill College.

Totten, G.E. & MacKenzie, D.S., 2003. *Handbook of Aluminum: Vol. 1: Physical Metallurgy and Processes*, United States of America.

Trana, K., 2002. Finite element simulation of the tube hydroforming process—bending, preforming and hydroforming. *Journal of Materials Processing Technology*, 127(3), p.401–408.

Vollertsen, F. & Plancak, M., 2002. On possibilities for the determination of the coefficient of friction in hydroforming of tubes. *Journal of Materials Processing Technology*, 125–126(–), p.412–420.

Vu-Quoc, L. & Tan, X.G., 2003. Optimal solid shells for non-linear analyses of multilayer composites. I. Statics. *Computer Methods in Applied Mechanics and Engineering*, 192(9–10), p.975–1016.

Williams, B.W., Oliveira, D.A., Simha, C.H.M., Worswick, M.J. & Mayer, R., 2007. Crashworthiness of straight section hydroformed aluminium tubes. *International Journal of Impact Engineering*, 34(8), p.1451–1464.

Wilson, E.L. & Ibrahimbegovic, A., 1990. Use of incompatible displacement modes for the calculation of element stiffnesses or stresses. *Finite Elements in Analysis and Design*, 7(3), p.229–241.

Wriggers, P., Eberlein, R. & Reese, S., 1996. A comparison of three-dimensional continuum and shell elements for finite plasticity. *International Journal of Solids and Structures*, 33(20–22), p.3309–3326.

Wriggers, P. & Gruttmann, F., 1993. Thin shells with finite rotations formulated in biot stresses: Theory and finite element formulation. *International Journal for Numerical Methods in Engineering*, 36(12), p.2049–2071.

Xu, H.J., Liu, Y.Q. & Zhong, W., 2012. Three-dimensional finite element simulation of medium thick plate metal forming and springback. *Finite Elem. Anal. Des.*, 51, p.49–58.

Yoon, J.-W., Barlat, F., Dick, R.E., Chung, K. & Kang, T.J., 2004. Plane stress yield function for aluminum alloy sheets—part II: FE formulation and its implementation. *International Journal of Plasticity*, 20(3), p.495–522.

Zhan, M., Yang, H., Huang, L. & Gu, R., 2006. Springback analysis of numerical control bending of thin-walled tube using numerical-analytic method. *Journal of Materials Processing Technology*, 177(1–3), p.197–201.

Zhan, M. & Huang, L., 2006. A numerical-analytic method for quickly predicting springback of numerical control bending of thin-walled tube. *Mater. Sci. Technol*, 22(5).

Zienkiewicz, O.C., Taylor, R.L. & Too, J.M., 1971. Reduced integration technique in general analysis of plates and shells. *International Journal for Numerical Methods in Engineering*, 3(2), p.275–290.

Appendix A: Federal Aviation Regulation (FAR) Part 27.725 FAR (1965)

The limit drop test must be conducted as follows:

(a) The drop height must be:

(1) 13 inches from the lowest point of the landing gear to the ground; or

(2) Any lesser height, not less than eight inches, resulting in a drop contact velocity equal to the greatest probable sinking speed likely to occur at ground contact in normal power-off landings.

(b) If considered, the rotor lift specified in § 27.473(a) must be introduced into the drop test by appropriate energy absorbing devices or by the use of an effective mass.

(c) Each landing gear unit must be tested in the attitude simulating the landing condition that is most critical from the standpoint of the energy to be absorbed by it.

(d) When an effective mass is used in showing compliance with paragraph (b) of this section, the following formula may be used instead of more rational computations:

$$W_e = W \times \frac{h + (1 - L).d}{h + d} \tag{8.1}$$

$$n = \left(n_j \times \frac{W_e}{W} + L \right) \tag{8.2}$$

where:

We=the effective weight to be used in the drop test (lbs.).

W= WM for main gear units (lbs.), equal to the static reaction on the particular unit with the rotorcraft in the most critical attitude. A rational method may be used in computing a main gear static reaction, taking into consideration the moment arm between the main wheel reaction and the rotorcraft center of gravity.

W= WN for nose gear units (lbs.), equal to the vertical component of the static reaction that would exist at the nose wheel, assuming that the mass of the rotorcraft acts at the center of gravity and exerts a force of 1.0 g downward and 0.25 g forward.

W= WT for tail wheel units (lbs.), equal to whichever of the following is critical:

(1) The static weight on the tail wheel with the rotorcraft resting on all wheels; or

(2) The vertical component of the ground reaction that would occur at the tail wheel, assuming that the mass of the rotorcraft acts at the center of gravity and exerts a force of 1 g downward with the rotorcraft in the maximum nose-up attitude considered in the nose-up landing conditions.

h = specified free drop height (inches).

L = ratio of assumed rotor lift to the rotorcraft weight.

n = limit inertia load factor.

nj = the load factor developed, during impact, on the mass used in the drop test (i.e., the acceleration dv/dt in g 's recorded in the drop test plus 1.0).

Appendix B: Stiffness matrix transformation from local to global coordinates

The expression of the final smoothed stiffness matrix is based on the following local degrees of freedom:

$$\breve{\mathbf{u}}_i\left(\xi^1,\xi^2,\xi^3\right)=\left\langle \overline{u}_i \quad \overline{v}_i \quad \overline{w}_i \quad \Delta u_i \quad \Delta v_i \quad \Delta w_i \right\rangle^T \quad , i=1,\cdots,4 \tag{9.1}$$

It is then necessary to project it in the local cartesian coordinates system $\mathbf{x}\left(x\ ,y\ ,z\ \right)$ based on the initial global degrees of freedom shown in equation (9.2) to make the assembly with other elements in a fixed frame:

$$u_i=\left\langle u_i^L \quad v_i^L \quad w_i^L \quad u_i^U \quad v_i^U \quad w_i^U \right\rangle_{,i=1,4} \tag{9.2}$$

In the above, the upper indices "U" and "L" refer respectively to the nodes of the upper surface and the nodes of the lower surface of the eight-node element. As presented by Kim et al. (2005), the relation between degrees of freedom in equations (9.1) and (9.2) is:

$$\begin{Bmatrix} \overline{u}_i \\ \overline{v}_i \\ \overline{w}_i \\ \Delta u_i \\ \Delta v_i \\ \Delta w_i \end{Bmatrix} = \frac{1}{2}\times \begin{bmatrix} 1 & 0 & 0 & 1 & 0 & 0 \\ 0 & 1 & 0 & 0 & 1 & 0 \\ 0 & 0 & 1 & 0 & 0 & 1 \\ 1 & 0 & 0 & -1 & 0 & 0 \\ 0 & 1 & 0 & 0 & -1 & 0 \\ 0 & 0 & 1 & 0 & 0 & -1 \end{bmatrix} \times \begin{Bmatrix} u_i^U \\ v_i^U \\ w_i^U \\ u_i^L \\ v_i^L \\ w_i^L \end{Bmatrix}$$

$$= \mathbf{A}_1 \times \begin{Bmatrix} u_i^U \\ v_i^U \\ w_i^U \\ u_i^L \\ v_i^L \\ w_i^L \end{Bmatrix} \tag{9.3}$$

because

$$\overline{u}_i = \frac{1}{2}\times\left(u_i^U + u_i^L\right) \qquad \overline{v}_i = \frac{1}{2}\times\left(v_i^U + v_i^L\right) \qquad \overline{w}_i = \frac{1}{2}\times\left(w_i^U + w_i^L\right)$$
$$\Delta u_i = \frac{1}{2}\times\left(u_i^U - u_i^L\right) \quad \Delta v_i = \frac{1}{2}\times\left(v_i^U - v_i^L\right) \quad \Delta w_i = \frac{1}{2}\times\left(w_i^U - w_i^L\right)$$
(9.4)

Coupling the previous equation with $\mathbf{Q}_1$, the degrees of freedom can then be transformed from the local cartesian coordinates system $\mathbf{x}\left(x\ ,y\ ,z\ \right)$ as:

$$\begin{Bmatrix} \overline{u}_i \\ \overline{v}_i \\ \overline{w}_i \\ \Delta u_i \\ \Delta v_i \\ \Delta w_i \end{Bmatrix} = \mathbf{A}_1 \times \begin{bmatrix} \mathbf{Q}_1^T & 0 \\ 0 & \mathbf{Q}_1^T \end{bmatrix} \times \begin{Bmatrix} U_i^U \\ V_i^U \\ W_i^U \\ U_i^L \\ V_i^L \\ W_i^L \end{Bmatrix}$$

$$= \mathbf{A}_2 \times \begin{Bmatrix} U_i^U \\ V_i^U \\ W_i^U \\ U_i^L \\ V_i^L \\ W_i^L \end{Bmatrix} \tag{9.5}$$

Equation (4.102) becomes in the global cartesian coordinates system $\mathbf{X}\left(X\ ,Y\ ,Z\ \right)$:

$$\tilde{\mathbf{K}}^{ANS} = \mathbf{A}_2^T \times \tilde{\mathbf{k}}^{ANS} \times \mathbf{A}_2 \tag{9.6}$$

Appendix C: Stiffness matrix and internal forces stabilization terms calculations

The classical form of partial derivative stabilization matrix is:

$$\mathbf{B}_{34} = \begin{bmatrix} \sum_{\beta=3}^{4} h_{\beta,x} \times \gamma_\beta^T & \mathbf{0} & \mathbf{0} \\ \mathbf{0} & \sum_{\beta=3}^{4} h_{\beta,y} \times \gamma_\beta^T & \mathbf{0} \\ \mathbf{0} & \mathbf{0} & \sum_{\beta=3}^{4} h_{\beta,z} \times \gamma_\beta^T \\ \sum_{\beta=3}^{4} h_{\beta,y} \times \gamma_\beta^T & \sum_{\beta=3}^{4} h_{\beta,x} \times \gamma_\beta^T & \mathbf{0} \\ \mathbf{0} & \sum_{\beta=3}^{4} h_{\beta,z} \times \gamma_\beta^T & \sum_{\beta=3}^{4} h_{\beta,y} \times \gamma_\beta^T \\ \sum_{\beta=3}^{4} h_{\beta,z} \times \gamma_\beta^T & \mathbf{0} & \sum_{\beta=3}^{4} h_{\beta,x} \times \gamma_\beta^T \end{bmatrix} \tag{10.1}$$

The stabilization stiffness matrix is given by:

$$\mathbf{K}_{stab} = \breve{\hat{\mathbf{K}}}_{stab} = \int_{V^e} \mathbf{B}_{34}^T \times \mathbf{H}' \times \mathbf{B}_{34} dV^e \tag{10.2}$$

The full form of stabilization matrix is then:

$$\mathbf{K}_{stab} = \begin{bmatrix} \mathbf{K}_{stab,11} & \mathbf{K}_{stab,12} & \mathbf{K}_{stab,13} \\ \mathbf{K}_{stab,21} & \mathbf{K}_{stab,22} & \mathbf{K}_{stab,23} \\ \mathbf{K}_{stab,31} & \mathbf{K}_{stab,32} & \mathbf{K}_{stab,33} \end{bmatrix} \tag{10.3}$$

where

$$\begin{aligned} \mathbf{K}_{stab,11} = \int_{V^e} \Bigg[& (\lambda + 2\times\mu) \times \left(\sum_{\beta=3}^{4} h_{\beta,x} \times \gamma_\beta^T \right) \times \left(\sum_{\beta=3}^{4} h_{\beta,x} \times \gamma_\beta^T \right) + \cdots \\ & \cdots + \mu \times \left(\sum_{\beta=3}^{4} h_{\beta,y} \times \gamma_\beta^T \right) \times \left(\sum_{\beta=3}^{4} h_{\beta,y} \times \gamma_\beta^T \right) + \mu \times \left(\sum_{\beta=3}^{4} h_{\beta,z} \times \gamma_\beta^T \right) \times \left(\sum_{\beta=3}^{4} h_{\beta,z} \times \gamma_\beta^T \right) \Bigg] dV^e \end{aligned} \tag{10.4}$$

$$\begin{aligned}\mathbf{K}_{stab,22} = \int_{V^e} \Bigg[& \mu \times \left(\sum_{\beta=3}^{4} h_{\beta,x} \times \gamma_\beta^T \right) \times \left(\sum_{\beta=3}^{4} h_{\beta,x} \times \gamma_\beta^T \right) + \cdots \\ & \cdots + (\lambda + 2 \times \mu) \times \left(\sum_{\beta=3}^{4} h_{\beta,y} \times \gamma_\beta^T \right) \times \left(\sum_{\beta=3}^{4} h_{\beta,y} \times \gamma_\beta^T \right) + \cdots \\ & \cdots + \mu \times \left(\sum_{\beta=3}^{4} h_{\beta,z} \times \gamma_\beta^T \right) \times \left(\sum_{\beta=3}^{4} h_{\beta,z} \times \gamma_\beta^T \right) \Bigg] dV^e \end{aligned} \tag{10.5}$$

$$\begin{aligned}\mathbf{K}_{stab,33} = \int_{V^e} \Bigg[& \mu \times \left(\sum_{\beta=3}^{4} h_{\beta,x} \times \gamma_\beta^T \right) \times \left(\sum_{\beta=3}^{4} h_{\beta,x} \times \gamma_\beta^T \right) + \cdots \\ & \cdots + \mu \times \left(\sum_{\beta=3}^{4} h_{\beta,y} \times \gamma_\beta^T \right) \times \left(\sum_{\beta=3}^{4} h_{\beta,y} \times \gamma_\beta^T \right) + \cdots \\ & \cdots + (\lambda + 2 \times \mu) \times \left(\sum_{\beta=3}^{4} h_{\beta,z} \times \gamma_\beta^T \right) \times \left(\sum_{\beta=3}^{4} h_{\beta,z} \times \gamma_\beta^T \right) \Bigg] dV^e \end{aligned} \tag{10.6}$$

$$\begin{aligned}\mathbf{K}_{stab,12} = \mathbf{K}_{stab,21} = \int_{V^e} \Bigg[& \lambda \times \left(\sum_{\beta=3}^{4} h_{\beta,x} \times \gamma_\beta^T \right) \times \left(\sum_{\beta=3}^{4} h_{\beta,y} \times \gamma_\beta^T \right) + \cdots \\ & \cdots + \mu \times \left(\sum_{\beta=3}^{4} h_{\beta,x} \times \gamma_\beta^T \right) \times \left(\sum_{\beta=3}^{4} h_{\beta,y} \times \gamma_\beta^T \right) \Bigg] dV^e \end{aligned} \tag{10.7}$$

$$\mathbf{K}_{stab,13} = \mathbf{K}_{stab,31} = \int_{V^e} \mu \times \left(\sum_{\beta=3}^{4} h_{\beta,x} \times \gamma_\beta^T \right) \times \left(\sum_{\beta=3}^{4} h_{\beta,z} \times \gamma_\beta^T \right) dV^e \tag{10.8}$$

$$\mathbf{K}_{stab,23} = \mathbf{K}_{stab,32} = \int_{V^e} \mu \times \left(\sum_{\beta=3}^{4} h_{\beta,y} \times \gamma_\beta^T \right) \times \left(\sum_{\beta=3}^{4} h_{\beta,z} \times \gamma_\beta^T \right) dV^e \tag{10.9}$$

The stabilization internal forces vector is given by:

$$\begin{aligned}\mathbf{f}_{stab} &= \int_{V^e} \left(\mathbf{B}_{34} \right)^T \times \mathbf{S}_{34} dV^e \\ &= \int_{V^e} \left(\mathbf{B}_{34} \right)^T \times \mathbf{H}' \times \mathbf{E}_{34} dV^e \end{aligned} \tag{10.10}$$

Thus, the un-simplified stabilization stress tensor $\mathbf{S}_{34}$ which reduced expression is presented in equation (5.185) takes the form:

$$\mathbf{S}_{34} = \mathbf{H}' \times \mathbf{E}_{34} = \mathbf{H}' \times \mathbf{B}_{34} \times \begin{Bmatrix} u_1 \\ u_2 \\ u_3 \end{Bmatrix}$$
$$= \begin{Bmatrix} (\mathbf{S}_{34})_{11} \\ (\mathbf{S}_{34})_{22} \\ (\mathbf{S}_{34})_{33} \\ (\mathbf{S}_{34})_{12} \\ (\mathbf{S}_{34})_{23} \\ (\mathbf{S}_{34})_{13} \end{Bmatrix} = \begin{Bmatrix} h_{3,x} \times q_{13} + h_{4,x} \times q_{14} \\ h_{3,y} \times q_{23} + h_{4,y} \times q_{24} \\ h_{3,z} \times q_{33} + h_{4,z} \times q_{34} \\ h_{3,y} \times q_{13} + h_{4,y} \times q_{14} + h_{3,x} \times q_{23} + h_{4,x} \times q_{24} \\ h_{3,z} \times q_{23} + h_{4,z} \times q_{24} + h_{3,y} \times q_{33} + h_{4,y} \times q_{34} \\ h_{3,z} \times q_{13} + h_{4,z} \times q_{14} + h_{3,x} \times q_{33} + h_{4,x} \times q_{34} \end{Bmatrix} \tag{10.11}$$

Equation (10.10) thus becomes:

$$\mathbf{f}_{stab} = \begin{Bmatrix} (\mathbf{f}_{stab})_1 \\ (\mathbf{f}_{stab})_2 \\ (\mathbf{f}_{stab})_3 \end{Bmatrix} \tag{10.12}$$

with

$$(\mathbf{f}_{stab})_1 = \left(\sum_{\beta=3}^{4} h_{\beta,x} \times \gamma_\beta^T \right) \times \left[(\lambda + 2 \times \mu) \times (\mathbf{S}_{34})_{11} + \lambda \times (\mathbf{S}_{34})_{22} \right] + \cdots$$
$$\cdots + \left(\sum_{\beta=3}^{4} h_{\beta,y} \times \gamma_\beta^T \right) \times \mu \times (\mathbf{S}_{34})_{12} + \left(\sum_{\beta=3}^{4} h_{\beta,z} \times \gamma_\beta^T \right) \times \mu \times (\mathbf{S}_{34})_{13} \tag{10.13}$$

$$(\mathbf{f}_{stab})_2 = \left(\sum_{\beta=3}^{4} h_{\beta,y} \times \gamma_\beta^T \right) \times \left[(\lambda + 2 \times \mu) \times (\mathbf{S}_{34})_{11} + \lambda \times (\mathbf{S}_{34})_{22} \right] + \cdots$$
$$\cdots + \left(\sum_{\beta=3}^{4} h_{\beta,x} \times \gamma_\beta^T \right) \times \mu \times (\mathbf{S}_{34})_{12} + \left(\sum_{\beta=3}^{4} h_{\beta,z} \times \gamma_\beta^T \right) \times \mu \times (\mathbf{S}_{34})_{23} \tag{10.14}$$

$$(\mathbf{f}_{stab})_3 = \left(\sum_{\beta=3}^{4} h_{\beta,x} \times \gamma_\beta^T \right) \times \mu \times (\mathbf{S}_{34})_{13} + \left(\sum_{\beta=3}^{4} h_{\beta,y} \times \gamma_\beta^T \right) \times \mu \times (\mathbf{S}_{34})_{23} + \cdots$$
$$\cdots + \left(\sum_{\beta=3}^{4} h_{\beta,z} \times \gamma_\beta^T \right) \times E \times (\mathbf{S}_{34})_{33} \tag{10.15}$$

Appendix D: Hyperelastoplastic constitutive law description

In continuum mechanics arise two trends of constitutive behavior law; hypoelastoplastic and hyperelastoplastic, as described in Simo & Hughes (1998). Hypoelastoplastic constitutive law is established in terms of stress rate induced by material deformation. The related formulation needs to stay independent of the frame and thus objective. Many developments helped to perform the formulation in large deformation context by making it energy consistent. Another school of thought drove to the hyperelastoplastic theory where stresses and strains are calculated from energy derivatives remaining by definition energy consistent. This is that last formulation which has been used in the present work and developed into a spatial coordinates system.

Cauchy stress tensor

The hyperelastoplastic model developed by Matei (2011) is briefly presented in the following lines. A crucial point of that work remains in the consideration of material history between two configurations, for example the configuration n and the configuration $n+1$. In the framework of an Eulerien description, let us consider an arbitrary q point of a domain Ω located at coordinates $\mathbf{X}$ expressed in the global coordinates system $\mathbf{X}(X,Y,Z)$. It is possible to attach to this arbitrary q point a co-rotational coordinates system $\mathbf{x}(x\ ,y\ ,z\ )$, as details in Table 4.1 and Table 5.1, which describes the material strain state in the current configuration. This hyperelastoplastic constitutive law is then defined in such a co-rotational coordinates system, $\mathbf{x}^n\left(x^n,y^n,z^n\right)$ at the old configuration n and $\mathbf{x}^{n+1}\left(x^{n+1},y^{n+1},z^{n+1}\right)$ at the new configuration $n+1$ as illustrated in Figure 7.1. This has the advantage to avoid possible parasitic effect due to rigid body rotation which could occur in case of large rotation states.

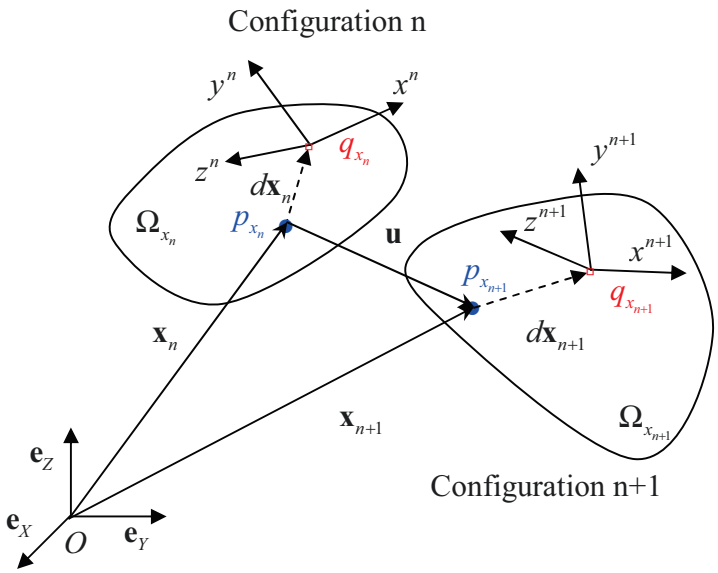

Figure 7.1: Rotated frame and time increments

The Cauchy stress tensor $\underset{\sim}{\boldsymbol{\sigma}}_{n+1}$ is calculated from the derivative of an objective Helmholtz free energy ψ described in Matei (2011):

$$\psi = \psi\left(q, \mathbf{C}(q)\right) \tag{11.1}$$

where the objective tensor $\mathbf{C}$ is calculated using only stretch tensor $\mathbf{U}$ as:

$$\mathbf{C} = \mathbf{U}^T \times \mathbf{U} \tag{11.2}$$

and takes the form:

$$\underset{\sim}{\boldsymbol{\sigma}}_{n+1} = \frac{\underset{\sim}{\boldsymbol{\Pi}}_{n+1}}{\det\left(\underset{\sim}{\mathbf{F}}^{elast}_{n+1}\right)} \tag{11.3}$$

where $\underset{\sim}{\boldsymbol{\Pi}}_{n+1}$ is the Kirchhoff stress tensor at configuration $n+1$, $\det\left(\underset{\sim}{\mathbf{F}}^{elast}_{n+1}\right)$ is the determinant of $\underset{\sim}{\mathbf{F}}^{elast}_{n+1}$ the strain tensor derivatives at configuration $n+1$ expressed as:

$$\underset{\sim}{\boldsymbol{\Pi}}_{n+1} = \det\left(\underset{\sim}{\mathbf{F}}^{elast}_{n+1}\right) \times \underset{\sim}{P}^{hydro}_{n+1} \times \mathbf{I} + \mu \times dev\left(\underset{\sim}{\overline{\mathbf{B}}}^{elast}_{n+1}\right) \tag{11.4}$$

with $P_{\underset{\sim}{n+1}}^{hydro}$ the hydrostatic pressure, $\mathbf{I}$ the identity matrix, μ the shear modulus and $\bar{\mathbf{B}}_{\underset{\sim}{n+1}}^{elast}$ the elastic left Cauchy-Green deviatoric part at configuration $n+1$ which is objective since it only depends on stretch tensor.

Elasticity

The classical 3D isotropic elasticity matrix $\mathbf{H}$ is used. It takes the form:

$$\mathbf{H} = \begin{bmatrix} \lambda+2\mu & \lambda & \lambda & 0 & 0 & 0 \\ \lambda & \lambda+2\mu & \lambda & 0 & 0 & 0 \\ \lambda & \lambda & \lambda+2\mu & 0 & 0 & 0 \\ 0 & 0 & 0 & \mu & 0 & 0 \\ 0 & 0 & 0 & 0 & \mu & 0 \\ 0 & 0 & 0 & 0 & 0 & \mu \end{bmatrix} \tag{11.5}$$

where the Lamé's coefficients are $\lambda = \frac{E.\nu}{(1+\nu)\times(1-2\times\nu)}$ and $\mu = \frac{E}{2.(1+\nu)}$ with E the Young's modulus .

Plasticity

In order to give a simple definition of plasticity concept, let us consider a loaded field Ω with a given material. This field Ω is subject to some deformation ε_{ij} due the applied load which can be split into a linear or reversible part ε_{ij}^{elast} and a plastic or irreversible part ε_{ij}^{plast} as presented in equation (11.6):

$$\varepsilon_{ij} = \varepsilon_{ij}^{elast} + \varepsilon_{ij}^{plast} \tag{11.6}$$

Mathematically, this phenomenon of plasticity can be described considering that the elastic and plastic domains are separated by a load surface described by a load function f as illustrated in Figure 7.2. This load function $f(\sigma)$, which general formulation for a perfectly plastic materials is presented in equation (11.7) while using an isotropic hardening defined in Simo & Hughes (1998). It depends on the stress level and is known as the yield condition or flow criterion since it characterizes the material behavior. If $f(\sigma)\langle 0$ the

material remains elastic; if $f(\sigma)=0$ the material is considered perfectly plastic; if $f(\sigma)\rangle 0$ the material is plastic.

$$f=\|\sigma\|-\sigma_y \tag{11.7}$$

where $\|\sigma\|$ is the norm of the Cauchy stress and σ_y is the flow stress.

In the same idea, the plastic strain rate $\dot{\varepsilon}_{ij}^{plast}$, also known as consistency parameter, $\Delta\gamma$ can indicate whether or not there is material plastification: if $\dot{\varepsilon}_{ij}^{plast}=0$ there is no plastic deformation ; if $\dot{\varepsilon}_{ij}^{plast}\neq 0$ there is material plastification.

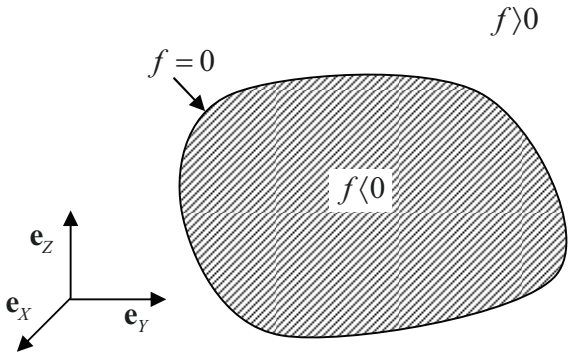

Figure 7.2: Load surface concept

The isotropic hardening model presented above is simplified compared with the hardening models determined with experimental tests since material stress / strain characteristic changes caused by microscopic stresses and known as Bauschinger effect are ignored. The kinematics hardening model, described in Simo & Hughes (1998), is another classical hardening model which describes an improved hardening compared with isotropic hardening, since it considers the displacement of the center of the load surface depending on plastification. The variable θ called “back stress” is then introduced to characterize this displacement and equation (11.7) becomes:

$$f=\|\sigma-\theta\|-\sigma_y \tag{11.8}$$

Translating the previous concept in terms of finite element analysis, let us introduce two consecutive configurations Ω_n and Ω_{n+1}. A classical method to calculate the Cauchy stress field $\boldsymbol{\sigma}_{n+1}$ is to use the technique known as return mapping algorithm. A key point of this technique is that a trial stress $\boldsymbol{\sigma}_{n+1}^{elast}$ is calculated making an elastic prediction from configuration Ω_n to Ω_{n+1}. Then the trial load function f_{n+1}^{trial} is calculated introducing the trial stress $\boldsymbol{\sigma}_{n+1}^{elast}$ into equation (11.8). The trial material state at configuration $n+1$ (elastic or plastic) is then verified checking the sign of the trial load function f_{n+1}^{trial}. If $f_{n+1}^{trial}\langle 0$, the material state stays in the elastic field which means that the elastic prediction was correct and then $\boldsymbol{\sigma}_{n+1}=\boldsymbol{\sigma}_{n+1}^{elast}$. However, if $f_{n+1}^{trial}\rangle 0$ the material state remains in the plastic field and as a consequence the elastic prediction is incorrect. In this case, a plastic correction is applied by orthogonal projection of the trial stress $\boldsymbol{\sigma}_{n+1}^{elast}$ onto the updated load surface as illustrated in Figure 7.3. In the present work, the Kirchhoff stress tensor $\mathbf{S}$ is used to calculate the stress state at configuration $n+1$. As in Matei (2011), the stress field in the new configuration is shown in equation (11.9):

$$\mathbf{S}_{n+1}=\mathbf{S}_{n+1}^{trial}-2\times\frac{\mu}{3}\times trace\left(\mathbf{B}_{n+1}^{elast}\right)\times\Delta\gamma\times sign\left(\mathbf{S}_{n+1}\right) \tag{11.9}$$

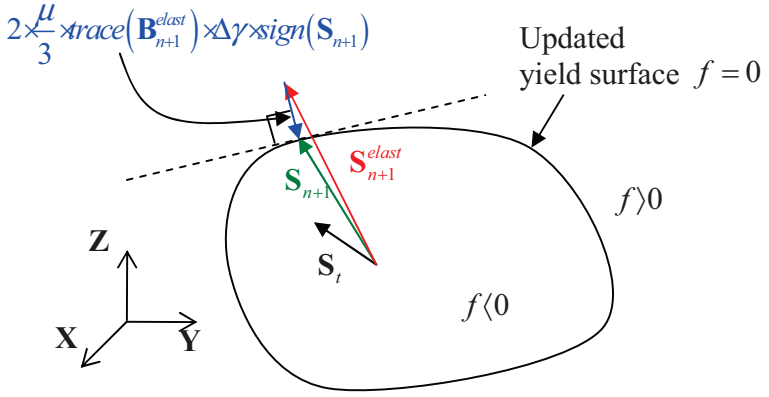

Figure 7.3: Return mapping concept

In the present work, the SH8RSe element has been combined with an ABAQUS/VUMAT type routine based on the work of Matei (2011), which has given accurate results in metallic THF context. Material behavior can then describe isotropic and anisotropic hardening, respectively from Simo & Hughes (1998) and Lemaître & Chaboche (2001), in equation (11.10) and (11.11).

$$f(\mathbf{S}) = \|\mathbf{S}\| - \sqrt{\frac{2}{3}} \times \sigma_H\left(\varepsilon^{plast}\right) \tag{11.10}$$

$$f(\mathbf{S}) = \|\mathbf{S} - \theta\| - \sqrt{\frac{2}{3}} \times \sigma_H\left(\varepsilon^{plast}\right) \tag{11.11}$$

The implemented isotropic non-linear hardening σ_H from Voce and from Simo described in Simo & Hughes (1998) are presented respectively in equations (11.12) and (11.13).

$$\sigma_H\left(\varepsilon^{plast}\right) = \sigma_y + K_1 \times \left(1 - e^{-K_s \times \varepsilon^{plast}}\right) \tag{11.12}$$

$$\sigma_H\left(\varepsilon^{plast}\right) = \sigma_y + K_0 \times \varepsilon^{plast} + K_1 \times \left(1 - e^{-K_s \times \varepsilon^{plast}}\right) \tag{11.13}$$

where ε^{plast} is the equivalent plastic strain, σ_H is the material hardening limit and K_0, K_1, K_s are other material parameters.